Preparation and Optimization of Novel Visible-Light-Active Photocatalysts for Waste-Water Treatment

Rong Ran

Thesis submitted to the

Faculty of Graduate and Postdoctoral Studies

in partial fulfillment of the requirements

for the Doctorate in Philosophy in Chemical Engineering

Department of Chemical and Biological Engineering

Faculty of Engineering

University of Ottawa

Abstract

Photocatalysis is a series of advanced light-induced redox reaction processes resulting in the degradation and mineralization of organic pollutants in the presence of oxygen and water. Due to their capability to destroy contaminants under mild conditions, photocatalytic processes have attracted considerable attention in the field of waste-water treatment. However, photocatalytic reactions using the traditional TiO_2 photocatalyst suffer from low energy efficiencies under solar irradiation. This low efficiency in the utilization of solar energy lies in its incapability in absorbing visible lights and also the high recombination rate of photo-excited species in photocatalysts. In addition, difficulties in the separation of fluids from micro- or nano-scale catalysts in large scale systems substantially impact cost efficiency in practice. In this thesis, strategies are explored which address these issues in order to improve the feasibility of solar photocatalysis. Two branches of photocatalytic transition metal-oxide semiconductor materials are investigated, namely bismuth-based and silver-based multi-phase heterogeneous photocatalysts. This research is focused on the design of visible-light-active metal-oxide photocatalysts to increase the absorption of visible light and to decrease the rates of electron-hole recombination, resulting in a high photocatalytic efficiency in regards to the degradation of organic pollutants. $BiVO_4$ powder, synthesized from freshly made potassium metavanadate was prepared via hydrothermal treatment, characterized and experimentally investigated for the degradation of rhodamine B under visible light irradiation. The crystal structures and the specific surface areas of the composites, based on $BiVO_4$ single phase crystal structures, are discussed. A multi-phase silver species ($Ag_2O/Ag_3VO_4/Ag_4V_2O_7$) photocatalyst was synthesized by adjusting the molar ratio of silver to vanadium (Ag to V) via hydrothermal method. The stabilities of as-prepared silver species composites regarding crystal structural changes due to photocatalytic reactions are investigated. Multi-phase silver species composites assisted with graphene oxide ($GO\text{-}Ag_2O/Ag_3VO_4/AgVO_3$) were synthesized at room temperature, and exhibited high visible-light photocatalytic activities regarding the degradation of model organic pollutants. The effect of graphene oxide addition on the photoactivity and on the photocorrosion of silver species composites under VLI is explored. The synergistic roles of each individual phase incorporated into the multi-phase composites are discussed regarding the photocatalytic performance.

Résumé

Le terme photocatalyse fait référence à la série de réactions oxido-réductrices induites par la lumière qui mène à la dégradation et la minéralisation de polluants organiques en présence d'eau et d'oxygène. Étant donné la possibilité de dégrader ces polluants sans avoir un effet important sur l'environnement, il n'est pas surprenant que cette technologie ait généré un intérêt considérable pour le traitement des eaux usagées. L'efficacité des procédés traditionnels utilisant TiO_2 comme catalyseur est toutefois très basse lorsque la lumière solaire est utilisée, un phénomène expliqué par le fait que le catalyseur est incapable d'absorber la lumière du spectre visible, et par le taux élevé de recombinaison des espèces photo-excitées dans le catalyseur. La séparation des fluides et des micro- et nano-particules de catalyseur demeure difficile et présente un obstacle économique important à surmonter. La présente thése etudie ces difficultés et vise à améliorer l'efficacité du processus de photocatalyse solaire. Deux types de matériaux semiconducteurs photocatalytiques à base d'oxides métalliques furent étudiés, notamment des composés hétérogènes à base de bismuth ou d'argent. La recherche présentée traite en particulier du design de photocatalyseurs à base d'oxides métalliques activés par la lumière visible, ayant comme objectifs d'augmenter l'absorption de lumière visible des photocatalyseurs, et la diminution des taux de recombinaison de vides électroniques, afin d'améliorer l'efficacité de dégradation de polluants organiques. De la poudre de $BiVO_4$ fut préparée par traitement hydrothermique en utilisant du metavanadate de potassium synthétisé comme précurseur, et fut caractérisée et utilisée pour catalyser la dégradation de rhodamine B en présence de lumière visible. La crystallinité et l'aire de surface des composés à base de $BiVO_4$ homogène furent mesurées. Un photocatalyseur hétérogène à base d'argent ($Ag_2O/Ag_3VO_4/Ag_4V_2O_7$) fut synthétisé par traitement hydrothermique en ajustant le rapport molaire d'argent et de vanadium. La stabilité et les changements structurels de ces composés à base d'argent furent étudiés au fil d'une réaction photocatalytique. Des composés à phases multiples associés à de l'oxide de graphène ($GO\text{-}Ag_2O/Ag_3VO_4/AgVO_3$) furent aussi synthétisés à température ambiante, et démontrèrent des activités catalytiques élevées lors de la dégradation de polluants organiques. L'impact de l'oxide de graphène sur l'activité photocatalytique et sur la photocorrosion des composés à base d'argent lorsque exposé à la lumière visible fut étudié. Le rôle de chaque phase de ces composés hétérogènes fut étudié en terme de performance photocatalytique.

Statement of Contribution of Collaborators

I declare that I am the only author of this thesis. I designed the methodologies of three projects after proposing the related hypothesis. This design included the selection of host materials for each project, modification of the materials' crystallinities, particle sizes and morphologies achieved by various synthesis methods, preliminary and detailed characterization tests for these host materials, further photoactivity studies, as well as the roles of reactive species in the specific photocatalytic performances and mechanism studies. I set up the experimental devices with assistance from technicians (Louis G. Tremblay, Franco Ziroldo and Gérard Nina) in the Department of Chemical and Biological Engineering. I independently conducted all of the experiments and performed all of the data analysis myself, and I wrote all of the chapters present in the thesis. In addition, Joanne Gamage McEvoy, a Ph.D. and co-worker in my lab, helped provide academic advice for the characterization of materials and the stability of silver species described in Chapter 3 and Chapter 4 respectively. Joanne Gamage McEvoy provided support in the form of grammatical corrections to two of my papers described in Chapter 3 and Chapter 4. She and I also held discussions relating to the academic field. Therefore, she was listed as a co-author in the two journal papers related to this work. I acknowledged other sources of assistance in analyses and reviews which were relevant.

Dr. Zisheng (Jason) Zhang as my supervisor offered guidance throughout this thesis. He contributed editorially to the whole written work present in the thesis. Editorial contributions may also be attributed to Dr. Joanne Gamage McEvoy, who was a Ph.D. student in Dr. Zhang's group from May 2010-May 2014. Dr. Joanne Gamage McEvoy is listed as a co-author on the papers associated with the work present in Chapter 2-3.

Acknowledgements

I would like to thank my supervisor, Dr. Zisheng (Jason) Zhang, for offering me the precious opportunity of joining his research group, and for his great guidance, as well as his support throughout my Ph.D. study.

I would like to thank the Natural Sciences and Engineering Research Council of Canada (NSERC) for the research funding, and the China Scholarship Council for the Ph.D. scholarship I was holding throughout my study. In addition, I would also like to thank the University of Ottawa for the admission scholarship.

I am grateful for a number of people who provided invaluable aid to me throughout this project. I would like to thank Dr. Joanne Gamage McEvoy for her friendship and suggestions to my research work, as well as Scott Barry Proulx (research assistant in Dr. Jason (Zisheng) Zhang's group) and Gary Cui (research assistant in Dr. Christopher Lan's group) for the grammatical corrections to parts of my writing. I am also grateful for staff working at the Centre for Catalysis Research and Innovation (CCRI) at the University of Ottawa, who provided great help with the materials characterizations. I would like to give many thanks to Louis G. Tremblay, Franco Ziroldo and Gérard Nina for their technical support in the Department of Chemical and Biological Engineering.

I would like to acknowledge the work of undergraduate students Thaís B. Miranda and Liyang Yan who provided valuable contributions to parts of my work.

I would like to give thanks to all of my friends I met during my doctoral studies who always supported me and cheered me up whenever I needed positive strength. I would like to mention and thank my lab coworkers in CBY D510 and my colleagues in CBY D417 past and present, especially Joanne Gamage McEvoy, Gabriel Potvin, Licheng Peng, Zhiliang Yang and Xiangchao Meng et al. for all of their help.

Table of Contents

List of Figures

List of Tables

Nomenclature, Abbreviations and Symbols

Photocatalyst nomenclature

Ag_2O	silver oxide
α-Ag_3VO_4	alpha-silver vanadate
β-$AgVO_3$	beta-silver vanadate
$Ag_4V_2O_7$	silver pyrovanadate
m-$BiVO_4$	monoclinic bismuth vanadate
KVO_3	potassium metavanadate
KV_3O_8	potassium vanadate
GO	graphene oxide
RGO	reduced graphene oxide
P25	Degussa P25 TiO_2

Abbreviations

AO	ammonium oxalate
BQ	benzoquinone
CB	conduction band
CMC	carboxymethyl cellulose, sodium salt
CTAB	cetyltrimethylammonium bromide
DL	donor level

EDS	energy dispersive X-ray spectrometry
EDTA	ethylenediaminetetraacetic acid
FWHM	full width at half maximum
IF	impact factor
ICSD	Inorganic Crystal Structure Database
JCDPS	Joint Committee on Powder Diffraction Standards (now ICDD)
MB	methylene blue
MO	methyl orange
NHE	normal hydrogen electrode
NP	nanoparticle
RhB	rhodamine B
rpm	revolutions per minute
RT	room temperature
SEM	scanning electron microscopy
STEM	scanning transmission electron microscopy
SPR	surface plasmon resonance
TBA	tert-butyl alcohol
TEM	transmission electron microscopy
UV	ultraviolet
UV-Vis DRS	ultraviolet-visible diffuse reflectance spectra
VB	valence band

VLI	visible light irradiation
XRD	X-ray diffraction
XPS	X-ray photoelectron spectroscopy

Symbols

Roman

A	illuminated area (m^2)
C	concentration at reaction time t (mg/L)
C_o	initial pollutant concentration (mg/L)
D_p	crystallite size of particles (usually nm)
E_{bg}	band gap energy (eV)
eV	electron volts
k	sphericity constant (usually taken as 0.9 for XRD)
K	adsorption coefficient of reactant in Langmuir-Hinshelwood expression (L/mg)
k'	pseudo-first order rate constant in Langmuir-Hinshelwood expression (L/min)
k_r	reaction rate constant in Langmuir-Hinshelwood expression (mg/(L·min))
t	irradiation time (min)
J	flux of photos (Einstein·m^{-2}·s^{-1})
V	volume of pollutant solution (m^3)

Greek

$\beta_{1/2}$	the peak width at half-maximum height of the sample and the equipment broadening
θ	Bragg angle (°)
λ	wavelength of light (nm)
ξ	apparent photonic efficiency (mol·Einstein^{-1})

SECTION I INTRODUCTION

Chapter 1

Introduction

1.1 Introduction

Photocatalysis concerns a series of advanced light-induced oxidation processes involving the generation and subsequent reaction of electron-hole pairs in a photocatalyst which has been excited by photons. This includes a series of redox reactions resulting in the degradation and mineralization of organic pollutants in the presence of oxygen and water [1]. Photocatalysis has attracted plenty of attention to the fields of environmental protection and clean energy, and could be widely employed in many real-world applications.

Photocatalytic activity was first popularized by the famous study of the 'Honda-Fujishima effect' on photoelectrochemical water splitting using a single-crystal titania electrode [2], which has been broadly used in many applications, including water cleavage, domestic and industrial wastewater treatment, air cleaning, and self-cleaning surfaces [3]. However, photocatalysis processes encounter low quantum efficiencies using traditional TiO_2 photocatalysts, which is the primary limitation of widely using sunlight energy. The band gap of TiO_2 (> 3.0 eV) [4] limits its light absorption to ultraviolet irradiation, which only constitutes approximately 4% of the solar spectrum, whereas visible light accounts for 43% and is the principal component of indoor artificial illumination [5-9], and only approximately 5% of radiation that reaches the earth contains UV light [10]. In addition, the lower efficiencies of traditional binary metal-oxide photocatalysts (e.g. TiO_2) are attributed to the high rate of electron-hole recombination after photo-assisted separation. In order to develop highly-active photocatalysts, second-generation visible-light-sensitive photocatalysts of ternary metal oxides obtained via environmentally-

friendly synthesis processes have been increasing in popularity recently. Approaches to improve photocatalytic efficiency and reusability have been studied, such as the development of bismuth-based and silver-based oxide visible-light-driven photocatalysts with lower band energies to enhance visible-light absorbance [4, 11, 12], and the development of modifications to silver-based oxide photocatalysts by means of heterogeneous structures to increase the surface area of photocatalyst composites, and to facilitate the degradation of organic pollutants under VLI [13].

In this thesis, further study about the modification of visible-light-driven bismuth-based and silver-based oxide photocatalysts, as well as novel, highly-active multi-phase heterogeneous photocatalysts is proposed to enhance the efficiency of visible-light-induced photocatalytic activity, as well as to facilitate the ideal application of modified photocatalysts to wastewater treatment. The mechanism associated with the proposed photocatalyst composites in application is also discussed.

1.2 Objectives

The main objective of this project was to synthesize novel visible-light-driven ternary metal oxide photocatalytic composites to be applied to the degradation of organic dyes in wastewater treatment. Two branches of ternary metal oxide-based composites were explored, namely bismuth-based and silver-based multi-phase, heterogeneous photocatalysts. The following three sub-objectives were proposed in order to make some contributions to addressing three progressive issues:

1) The experimental investigation of novel single phase crystal structures based on bismuth ternary metal-oxide photocatalysts was implemented. This aimed to improve the crystallinities of crystal structures and the specific surface areas of composites for the photocatalytic degradation of organic dyes under VLI.
2) A novel multi-phase silver species ($Ag_2O/Ag_3VO_4/Ag_4V_2O_7$) photocatalyst prepared by adjusting the molar ratio of silver to vanadium (Ag to V) via the hydrothermal method was explored, which aimed to improve the separation and transfer of photoexcited charges, and to overcome limitations caused by defects in a single phase.
3) The modification of novel multi-phase silver ($Ag_2O/Ag_3VO_4/AgVO_3$) photocatalysts incorporated with graphene oxide sheets was investigated, and the effect of graphene

oxide addition on the visible-light-driven photoactivity and on the photocorrosion of silver species composites due to the degradation of organic components was studied, aiming to improve the protection of catalysts from photocorrosion during redox reactions under VLI.

As such, the synthesis, characterization, experimental investigation, results, analyses and mechanism of photocatalytic performance used in the degradation of model organic pollutants were implemented and investigated as the basis of this project.

The main contribution of the project to research lies in the development of novel visible-light-driven photocatalysts with enhanced photocatalytic performances for wastewater treatment. The novelty of the project was in synthesizing multifunctional photocatalysts with multiphase, multimorphological features in order to improve the efficiency of visible-light-driven photocatalysis, and to protect catalysts from photocorrosion during these redox reactions.

1.3 Hypothesis

The proposed projects focus on the development of visible-light active photocatalysts for wastewater treatment. Specifically, the photocatalytic degradation of organic pollutants under visible light irradiation is expected to improve using novel visible-light-driven ternary photosensitive metal-oxide-based particles. In this thesis, these particles are namely bismuth-based and silver-based multiphase heterogeneous photocatalysts. The highly active, visible-light-driven, novel photocatalysts are defined when the following characteristics are satisfied:

1) Photocatalysts are semiconductors with a short band gap energy (E_{bg} < 3.1 eV). Since a band gap energy larger than 3.0 eV can only absorb UV light, which accounts for 5% of the solar spectrum, much of the visible light accounting for a large portion of the sunlight is not used.

2) Photocatalysts possess high crystallinities in their crystal structures. Acrystal structure is a unique arrangement of atoms, ions or molecules in a crystalline liquid or solid. The crystal lattice can be thought of as an array of ‘small boxes’ infinitely repeating in all

three spatial directions (the structure of atoms). The higher the crystalline quality is, the smaller the number of defects that are observed.

3) Photocatalysts possess particles with large surface areas. Large surface areas could improve the adsorption−desorption process, resulting in the increase of adsorption of organic pollutants onto photocatalysts particles. These adsorbed organic compounds could then be decomposed during redox reactions and eventually mineralized into CO_2 and H_2O in the presence of oxygen and water.

4) Photocatalysts possess small particle sizes. As the particle size becomes smaller, the distance that photogenerated charges have to migrate to reaction sites on the surface becomes shorter and results in a decrease in the probability of recombination [12].

5) Anti-photocorrosion protection for photocatalysts has managed to maintain a high photocatalytic efficiency in visible-light-driven photosystems.

The accomplishment of novel multi-phase photocatalysts with heterojunctions is supported by fundamental knowledge, such as the theory of the structure of atoms and knowledge of photoelectrochemistry. The fabrication of highly-active visible-light-driven photocatalysts relies on the exploration of synthesis methods modified with various conditions, which results in highly-active photocatalytic performances with regards to the degradation of organic pollutants. A flow chart of the proposed hypothesis, including the associated sub-objectives and logical flow is attached in Appendix A.

1.4 Connection among three projects

The promising ternary semiconductors with short band gap energies and highly-active visible-light driven photosensitizations were selected as the host materials applied to the improvement of photocatalytic activity with regards to the degradation of organic pollutants in different projects, which was the common connection in making contributions to the academic field.

1.5 Thesis structure

1.5.1 General structure

Aside from the introduction, the background and literature review as well as the conclusion sections, this thesis consists of three major sections which include the main aspects of the project undertaken as well as significant results and discussion. These three chapters are independently presented based on journal paper format, and represent the core of the project throughout. These three chapters are three research articles, two of which are published in scholarly journals, and are included in the thesis with the permission of the co-authors and the related publishers with copyrights. The third article has been submitted for publication.

1.5.2 Chapter contents

The details of the thesis structure concerned are presented below. The academic contributions related are listed as well, including the impact factor (IF) of the journals where relevant articles are published.

Chapter 1: Introduction

An overview and discussion of the project is exhibited, and the thesis objectives and research strategies are outlined.

Chapter 2: Background and literature review

The relevant background and literature associated with the project objectives are demonstrated with respect to presenting the most recent research on the relevant topics and to discovering the current academic gaps pertinent to the project.

Chapter 3: Synthesis and optimization of visible light active $BiVO_4$ photocatalysts for the degradation of RhB

A novel visible-light-driven photocatalyst based on monoclinic $BiVO_4$ is presented, synthesized, characterized, and investigated during the photocatalytic degradation of rhodamine B (RhB)

under VLI. In addition, the experimental investigation of crystal structure details and the relevant mechanism for photocatatlysis are proposed.

Contributions:

- *Published paper*

Rong Ran, Joanne Gamage McEvoy, Zisheng Zhang, Synthesis and optimization of visible light active $BiVO_4$ photocatalysts for the degradation of RhB, International Journal of Photoenergy (IF, 2012 = 2.663). DOI:10.1155/2015/612857.

- *Conference presentation*

Rong Ran, Joanne Gamage McEvoy, Zisheng Zhang, Synthesis and optimization of visible light active $BiVO_4$ photocatalysts for the degradation of RhB, 64th Canadian Society for Chemical Engineering, Niagara Falls, Canada, Oct. 19-22, 2014.

Chapter 4: $Ag_2O/Ag_3VO_4/Ag_4V_2O_7$ heterogeneous photocatalyst prepared by a facile hydrothermal synthesis with enhanced photocatalytic performance under visible light irradiation

A novel heterogeneous multi-phase $Ag_2O/Ag_3VO_4/Ag_4V_2O_7$ photocatalyst is proposed, characterized, and investigated to enhance the visible-light-induced photocatalytic performance for the degradation of a model organic pollutant (rhodamine B). The molar ratio of silver to vanadium (Ag to V) based on the as-prepared materials is studied. In addition, the stability of the as-prepared composite is discussed based on photocatalytic activity, and the mechanism of visible light activity is presented.

- *Published paper*

Rong Ran, Joanne Gamage McEvoy, Zisheng Zhang, $Ag_2O/Ag_3VO_4/Ag_4V_2O_7$ heterogeneous photocatalyst prepared by a facile hydrothermal synthesis with enhanced photocatalytic performance under visible light irradiation, Materials Research Bulletin (IF, 2014 = 2.288), 74 (2016) 140–150. DOI:10.1016/j.materresbull.2015.08.028.

Chapter 5: Facile preparation of novel graphene oxide-$Ag_2O/Ag_3VO_4/AgVO_3$ heterogeneous photocatalysts with high photocatalytic performance under visible light irradiation

A series of novel graphene oxide-assisted, heterogeneous multi-phase and multi-morphological $Ag_2O/Ag_3VO_4/AgVO_3$ photocatalysts are proposed, characterized, and investigated to improve visible-light-induced photocatalytic efficiency towards the degradation of model organic compounds (rhodamine B and methyl orange). In addition, the stability of the as-prepared composites and the protection of silver species catalysts from photocorrosion during redox reactions are discussed. A mechanism based on the photocatalytic performance is proposed and interpreted.

- *Published paper*

Rong Ran, Zisheng Zhang, Facile preparation of novel graphene oxide-$Ag_2O/Ag_3VO_4/AgVO_3$ heterogeneous photocatalysts with high photocatalytic performance under visible light irradiation, Applied Catalysis B (IF, 2014 = 7.435) (Under review)

Chapter 6: Discussion and conclusions

Discussion and conclusions are summarized based on the presented works done in this thesis. The contributions to the academic field and novelties of this thesis are highlighted, while suggestions for future studies are also included.

Appendix A: Flow chart of hypothesis

The prepared flow chart of the hypothesis aims to demonstrate an intuitive design of the three research projects. Strategies highlighted in the flow chart include one objective, two branches and three different projects shown in the red boxes, whereas the synthesis methods, theoretical factors, related parameters and experimental results are shown in the black boxes.

Appendix B: Terminologies used in photocatalysis

The clarification of various concepts involved in photocatalytic processes is given in Appendix B, including relevant definitions for terminologies such as the solar radiation spectrum, mole of photons, radiation intensity, spectral distribution of the lamp, the selection of the distance from the photoreactor, apparent photonic efficiency, band gap, valence band and conduction band, heterojunction, graphene oxide, as well as the host materials in the three projects.

Appendix C: Sample calculations

The related sample calculations mentioned in the thesis and Appendix B are given in Appendix C, which are involved in experimental results from previous studies discussed in the three research articles present in Chapter 3, Chapter 4 and Chapter 5 respectively.

1.6 References

[1] B. Ohtani, Photocatalysis by inorganic solid materials: Revisiting its definition, concepts, and experimental procedures, Adv. Inorg. Chem. 63 395-430.

[2] A. Fujishima, K. Honda, Electrochemical photolysis of water at a semiconductor electrode, Nature 238 (1972) 37-38.

[3] M.R. Hoffmann, S.T. Martin, W. Choi, D.W. Bahnemann, Environmental applications of semiconductor photocatalysis, Chem. Rev. 95 (1995) 69-96.

[4] A. Walsh, Y. Yan, M.N. Huda, M.M. Al-Jassim, S.-H. Wei, Band edge electronic structure of $BiVO_4$: Elucidating the role of the Bi s and V d orbitals, Chem. Mater. 21 (2009) 547-551.

[5] M. Gratzel, Photoelectrochemical cells, Nature 414 (2001) 338-344.

[6] D. Chatterjee, S. Dasgupta, Visible light induced photocatalytic degradation of organic pollutants, J. Photochem. Photobiol., C 6 (2005) 186-205.

[7] H. Li, G. Liu, X. Duan, Monoclinic $BiVO_4$ with regular morphologies: Hydrothermal synthesis, characterization and photocatalytic properties, Mater. Chem. Phys. 115 (2009) 9-13.

[8] Y. Li, W. Wang, X. Qiu, L. Song, H.M. Meyer Iii, M.P. Paranthaman, G. Eres, Z. Zhang, B. Gu, Comparing Cr, and N only doping with (Cr, N)-codoping for enhancing visible light reactivity of TiO_2, Appl. Catal., B 110 (2011) 148-153.

[9] H. Jiang, H. Dai, X. Meng, L. Zhang, J. Deng, Y. Liu, C.T. Au, Hydrothermal fabrication and visible-light-driven photocatalytic properties of bismuth vanadate with multiple morphologies and/or porous structures for methyl orange degradation, J. Environ. Sci. 24 (2012) 449-457.

[10] B.R. Das, UV radiation protective clothing, The open Text.J. 3 (2010) 14-21.

[11] A. Kudo, K. Ueda, H. Kato, I. Mikami, Photocatalytic O_2 evolution under visible light irradiation on $BiVO_4$ in aqueous $AgNO_3$ solution, Catal. Lett. 53 (1998) 229-230.

[12] A. Kudo, Y. Miseki, Heterogeneous photocatalyst materials for water splitting, Chem. Soc. Rev. 38 (2009) 253-278.

[13] M. Zhu, P. Chen, M. Liu, Graphene oxide enwrapped Ag/AgX (X = Br, Cl) nanocomposite as a highly efficient visible-light plasmonic photocatalyst, ACS Nano 5 (2011) 4529-4536.

SECTION II: NOVEL VISIBLE-LIGHT-DRIVEN PHOTOCATALYSTS BASED ON BISMUTH-BASED AND SILVER-BASED TERNARY METAL-OXIDE COMPOSITES

Chapter 2

Background and literature review

2.1 Background

2.1.1 Development of photocatalysis

The field of photocatalysis was energized by Fujishima's famous study on photoelectrochemical water splitting [1]. Photocatalysis consists of a series of advanced light-induced oxidation processes involving the generation of and subsequent reaction of electron-hole pairs in a photocatalyst (a semiconductor in general) when excited by photons. The photoexcited electrons and holes (e^--h^+) are formed on the photoexcited photocatalysts under light irradiation when excessive energy is applied to the band gap (E_{bg}). In this scenario, the photogenerated e^--h^+ pairs formed in the photocatalysts either separate and move freely onto the surface of composites, (i.e. the photoexcited electrons jump to the conduction band (CB), while holes stay on the valence band (VB)), or they recombine as the energy emission under the internal electric field due to the characteristics of the components [2]. Once the successful separation of the photoexcited e^--h^+ pairs occurrs, the separated electrons and holes can be trapped and may react with adsorbed water, oxygen and organic pollutants. Intermediates of the pollutants could be further mineralized into CO_2 and H_2O [3]. The complete photocatalysis process is presented in Figure 2.1.

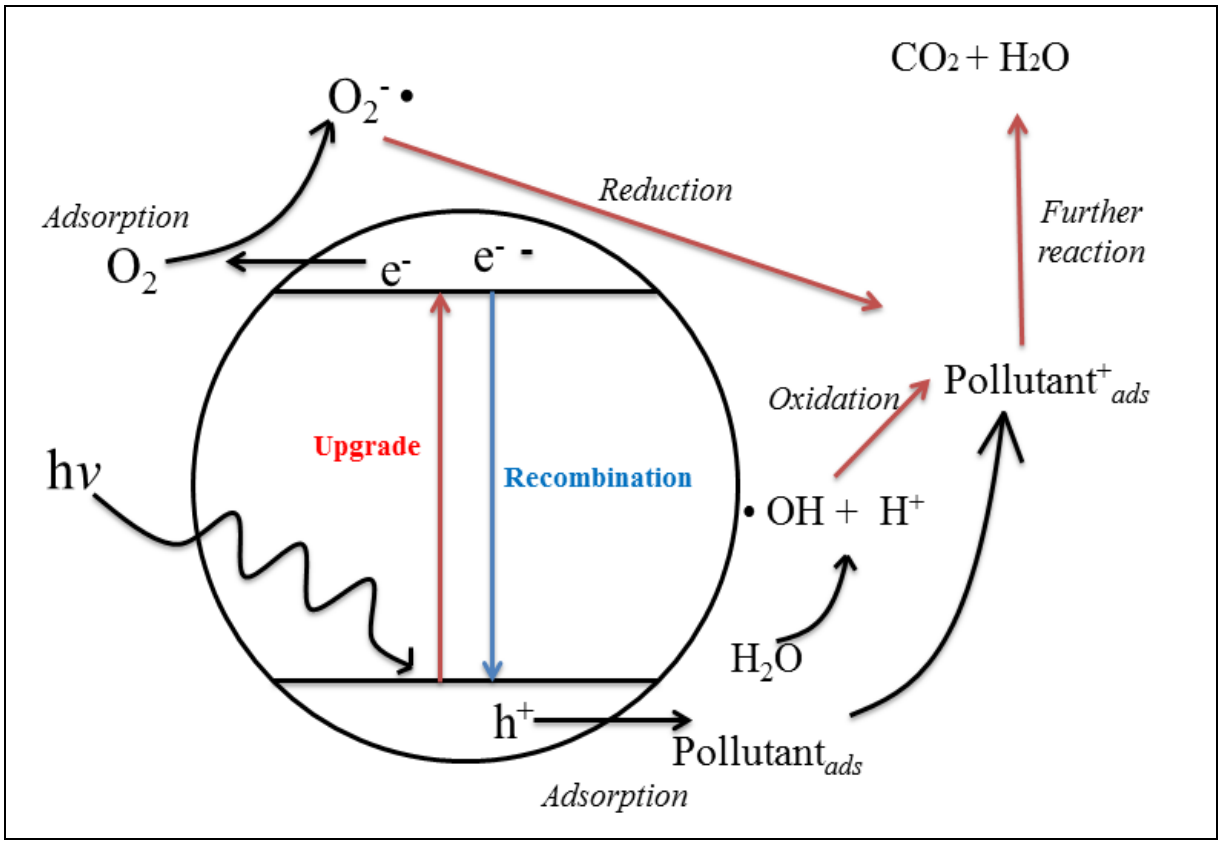

Figure 2.1: Photocatalysis process of the degradation of pollutants on a semiconductor.

2.1.2 Application studies

Development of the application of photocatalysis is the ultimate goal in a series of studies aiming to improve photocatalytic efficiency. Photocatalytic processes have drawn much attention in regards to the diverse applications of photocatalysis, such as the detoxification of effluents, the destruction of microorganisms including bacteria, the inactivation of cancer cells, superhydrophilic self-cleaning, the production of hydrogen fuel including photo-splitting of water to produce hydrogen gas, the elimination of inorganic/organic gaseous pollutants or odour control, the fixation of nitrogen, and the synthesis of organic fuels [4]. The purpose of this Ph.D. project is to apply photocatalysis to degrade contaminants using synthesized novel photocatalyst composites. Some important applications to wastewater treatment have been highlighted in this thesis.

2.1.3 Challenges in photocatalysis

Presently, the main challenge presented by photocatalysis process is to make economically viable and industrially available. Photocatalytic reactions using traditional TiO_2-based photocatalysts suffer from low energy efficiencies under solar irradiation. This occurs since the band gap of TiO_2 (> 3.0 eV) limits its light absorption to ultraviolet irradiation, which only constitutes approximately 4% of the solar spectrum. However, visible light accounts for 43%, and is the principal component of indoor artificial illumination. A solar spectral distribution is shown in Figure 2.2 [5], and only ~5% of radiation which reaches the earth contains UV light [6].

The limited efficiency of the current process includes several aspects: lower efficiency utilization of sunlight, electron-hole recombination, difficulties in the development of multi-phase photocatalytic reactors and industrialization. The greatest challenges to improving reactor design include finding a simple and convenient method to separate fluids, and implementing micro- or nano-scaled catalysts in large-scale systems. Since an immobilized-bed reactor is the preferred choice in the field of photocatalysis, much consideration must be given to efficient mixing rules with the effects of mass transfer, reaction kinetics, optimal illuminated specific surface area, and catalyst immobilization considered as factors which can be modified to improve efficiency [7]. High band gap energies of semiconductors (such as the band gap energy of TiO_2 > 3.2 eV) [8], defects in semiconductors causing high electron-hole recombination [9-11], lower surface areas of photocatalysts resulting in inefficient adsorption-desorption equilibriums [12-16], lower crystallinities of crystal structures and large particle sizes [17, 18] are all factors which experimentally reduce the efficiency of photocatalytic performance under light irradiation [19].

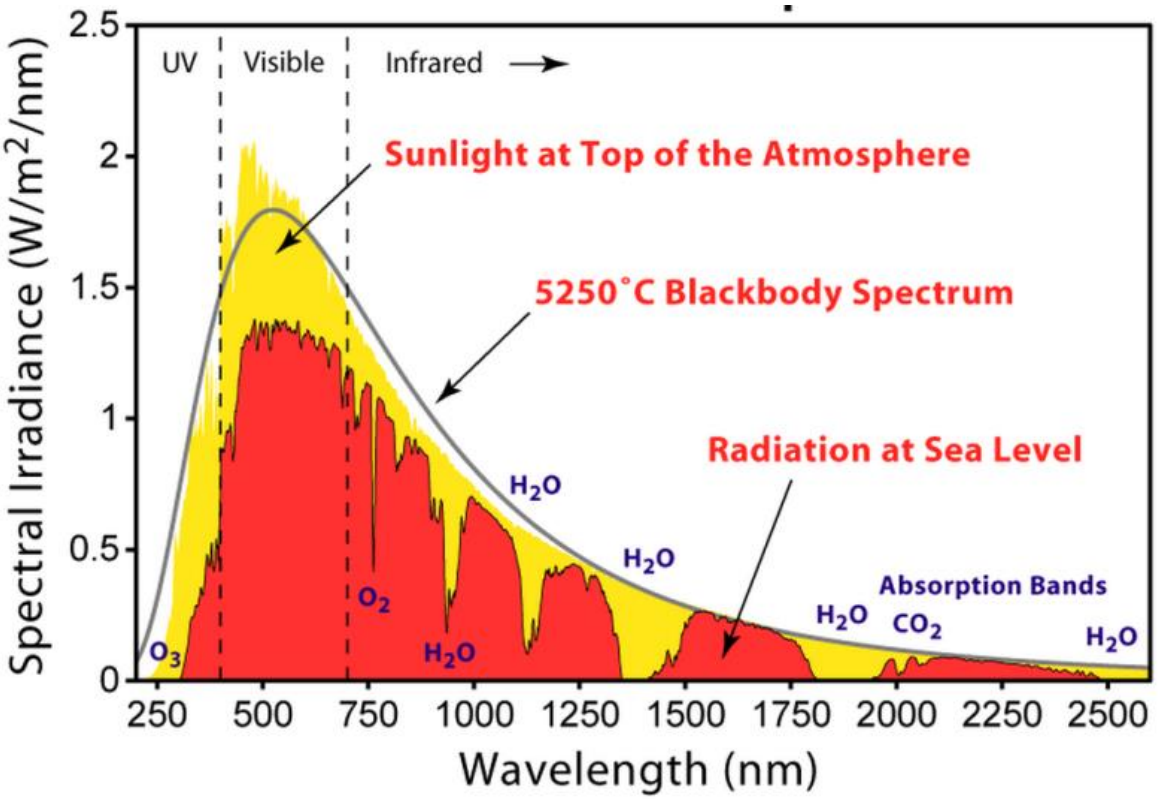

Figure 2.2: Solar spectral distribution (ASTM Standard C 33).

2.1.4 Strategies in development of highly-active photocatalysis

2.1.4.1 General objectives

A highly efficient photocatalysis process is required to improve the degradation of contaminants in the photosystem. Herein, two major strategies are presented:

A: Optimization of photoreactor design in order to distribute sun light irradiation.

B: Development of visible-light-induced photocatalysts to utilize a greater portion of solar radiation.

Many designs of photoreactors have modified and improved the utilization of solar light by optimizing pathways from traditional solar collectors using compound parabolic photoreactors, parabolic trough photoreactors, or optical fiber photoreactors [20]. Other configurations such as multi-annular series flow reactors [21] and fluidised-bed photoreactors [22] have been

investigated to facilitate the mixing of reactants and catalysts, giving rise to high-efficiency adsorption-desorption equilibriums.

Moreover, the development of visible-light-induced photocatalysts has been recognized as the other critical approach for increased performance under visible-light irradiation. Besides the modification of traditional photocatalysts (e.g. TiO_2), many second-generation photocatalysts with lower band gap energies [23] have been investigated, leading to significant progress towards enhancing photocatalytic activities by improving the absorbance of solar radiation. This includes the development of ternary metal-oxide photocatalysts [24], in which absorbance of a significant portion of the visible light spectrum supplies the majority of photocatalytic activity applied to the treatment of wastewater. Related strategies have been applied, namely:

1) Decreasing electron-hole recombination.
2) Band engineering design (tuning band gap), co-catalysts and the assistance of photosensitizer.
3) Facilitating the adsorbability of organic components to photocatalysts via increased surface area.

2.1.4.2 Decreasing electron-hole recombination

Strategies for inhibiting electron-hole recombination which have been seen in literature include developing novel ternary metal-oxide photocatalysts, optimizing the quality of crystal structures and fabricating heterogenerous junctions in photocatalyst composites. The development of ternary metal-oxides with transition metals was a favourable alternative route resulting in highly efficient photocatalysts used to degrade pollutants [9].

Photocatalysts such as $BiVO_4$ [25], Bi_2WO_6 [26], Bi_2MoO_6 [27], Ag_3VO_4 [28], $AgNbO_3$ [29], $Ag_4V_2O_7$ [30], β-$AgVO_3$ [31], $AgMO_2$ (M = Al, Ga, In) [32, 33], Ag_2CO_3 [34], and Ag_3PO_4 [35] and $SnNb_2O_6$ [36] have all exhibited high photocatalytic performances under visible light irradiation (VLI). Due to the intrinsic optical properties of ternary metal-oxide photocatalysts with low band gap energies (average 2.4-2.5 eV), they are able to absorb a wide range of visible light [37]. In addition, the mobility of photogenerated charges was also improved, attributed to the incorporation of various elements in ternary metal oxides, thus preventing electron-hole recombination via charge-separation mechanisms [38]. The difference of band gap energies

between traditional binary semiconductors and promising ternary semiconductors is given in Figure 2.3.

Another approach that has been explored is to increase the quality of crystal structures for photocatalysts. Crystallinity and particle size strongly affect the recombination of photogenerated electrons and holes; the stronger the crystalline quality is, the smaller the amount of defects. Larger particle sizes increase the distance that photogenerated electrons and holes would have to migrate to reach the reaction sites on the surface, resulting in an increase in the probability of recombination [9].

Forming a heterogeneous junction of photocatalysts is another promising alternative route for the separation of photoexcited charges. Photocatalysts such as $CuBi_2O_4$-$BiVO_4$ (p-n type) and the modified structure $Cu/CuBi_2O_4$-CoPi/$BiVO_4$ [39], in which both photogenerated electrons in $BiVO_4$ and holes in $CuBi_2O_4$ were successfully separated, due to the combination of electrons in the $BiVO_4$ with holes in the $CuBi_2O_4$. Multi-layer structure photocatalysts have also emerged, such as carbon-modified $BiVO_4$ microtubes embedded with Ag nanoparticles (BVO@C/AgMTs) [40], hollow olive-shaped $BiVO_4$ and n-p core-shell $BiVO_4@Bi_2O_3$ [41], as well as hollow core-shell ZrO_2@Void@$BiVO_4$ [42] with highly efficient photocatalytic activities.

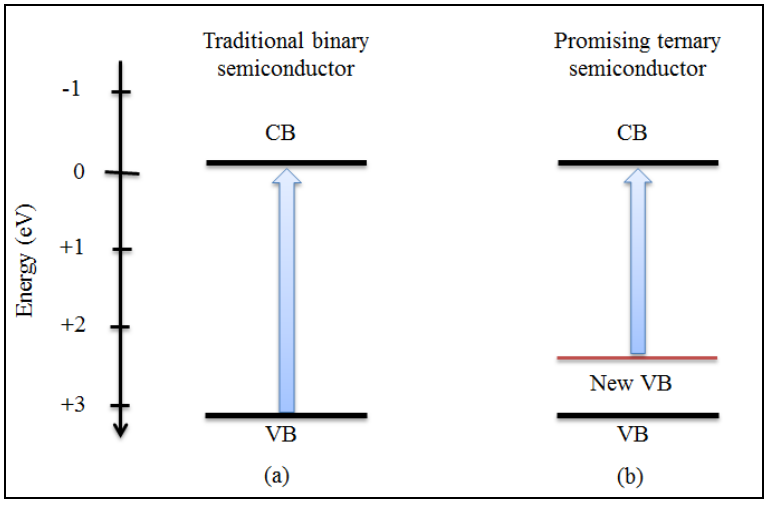

Figure 2.3: Strategies of band engineering for design of visible-light-induced photocatalysts (a) Traditional binary semiconductor (b) Promising ternary semiconductor.

2.1.4.3 Band engineering design, co-catalysts and photosensitizers' assistance

Routes for achieving red-shift absorption of photocatalysts include employing band engineering design, assisting with co-catalysts and using photosensitizers to extend excitation wavelengths.

Many approaches use metallic or non-metallic elements to conduct reliable and repeatable metal ion implantation, resulting in the increase of visible light absorption attributed to the narrowed band gaps. As such, transition metals are able to form an electron donor level (DL) via doping $BiVO_4$ with transition metals, such as Copper-doped $BiVO_4$ (Cu-$BiVO_4$) [43], cobalt-doped $BiVO_4$ (Co-$BiVO_4$) [44] and Ni-doped $BiVO_4$ (Ni-$BiVO_4$) [45]. Some noble metals may also be involved in the doping of photocatalysts, such as Pd-doped $BiVO_4$ (Pd/$BiVO_4$) [46], Pt-doped $BiVO_4$ (Pt/$BiVO_4$) [47] and Au-doped $BiVO_4$ (Au/$BiVO_4$) [48] composites. In addition, there are also non-metallic element-doped composites such as N-doped $BiVO_4$ [49], fluoride-doped $BiVO_4$ [50] and B-doped $BiVO_4$ [51].

Other pathways of extending excitation wavelengths have also been investigated. Methylene blue (MB), methyl orange (MO) and rhodamine B (RhB) were used to sensitize the carriers and to facilitate the transfer of charges via injection of the photoexcited electrons from the conduction bands of dyes into those of photocatalysts such as $BiVO_4$ [52-54] and α-Ag_3VO_4 [51, 55-57]. In addition, a sensitizer with co-catalysts of Fe_2O_3, Co_3O_4 or CuO onto $BiVO_4$ [58] was studied and resulted in the improvement of photocatalytic performance under VLI. The related mechanisms of band engineering design upon dopant-type and sensitized-type photocatalysts are given in Figure 2.4.

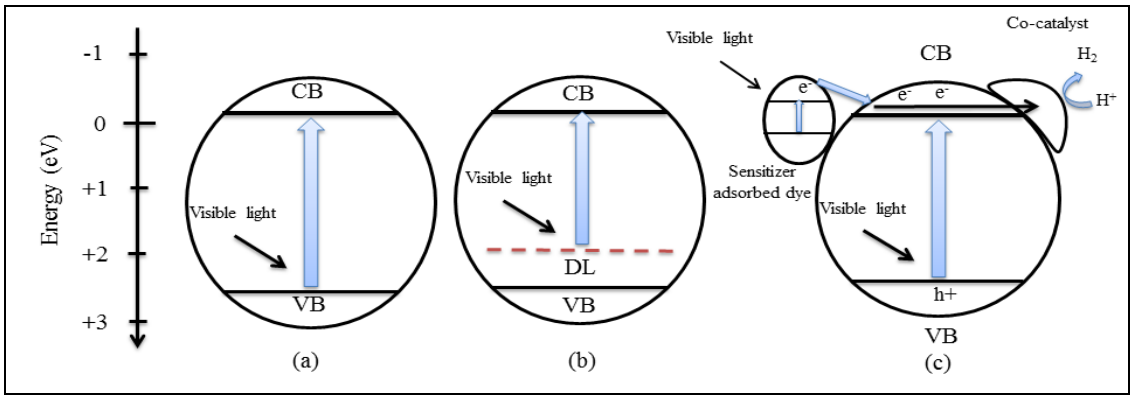

Figure 2.4: The changed band gap structure of photocatalysts compounds (a) unchanged type (b) dopant-type (c) co-catalysts & sensitized-type.

2.1.4.4 Facilitating the adsorability of organic components to photocatalysts via increased surface area

The surface area of a photocatalyst plays a key role in the surface-reaction photocatalytic activity system, influencing the adsorption-desorption equilibrium of organic components to photocatalyst composites involved in the reactions under light irradiation, and also influencing the reaction rate. Hence, an increase in catalyst surface area is required in high photocatalytic activity systems. This is achieved through various approaches, such as decreasing the particle size from micro-scale to nano-scale composites [59], dispersing photocatalysts onto large surface area substrates such as graphene oxide sheets [60, 61], graphene sheets [62], reduced graphene oxide [63], SiO_2 [64, 65] etc., synthesizing heterogeneous structures, and preparing porous [66] or shell-layered structures [67] using templates.

As for photocatalysts composites synthesized via highly adsorbent substrates such as graphene oxide sheets or graphene sheets, the synergistic effect between graphene oxide sheets or graphene sheets and catalyst composites results in a remarkable improvement in photocatalytic performance. This synergy has attracted considerable research interest in functionalized GO-assisted photocatalysts due to their large specific surface areas, strong adsorption capabilities and high quantity of reactive sites for surface modification reactions [68].

2.2 Thermodynamic analysis of photocatalysis

Photocatalysis involved in thermodynamics is classified into two different categories, namely: 'down-hill' and 'up-hill' reactions. Degradation, such as that mediated through the photo-oxidation of organic compounds, is generally a down-hill reaction which proceeds irreversibly. In this process, a photocatalyst works in the presence of oxygen and water to produce O_2^-, HO_2, OH•, and H^+ as active species for redox reactions through adsorbed dissolved O_2 and H_2O which are reduced and oxidized into these species, respectively, by photogenerated electron-hole pairs formed on the photocatalyst. This photocatalytic degradation process is associated with a negative change in the Gibbs free energy, and is thus classified as a 'down-hill' photo-induced reaction, as shown in Figure 2.5. In contrast, water splitting into H_2 and O_2 is accompanied by a large positive change in the Gibbs free energy (ΔG^0 = 237 kJ/mol) and is classified as an 'up-hill' reaction [69].

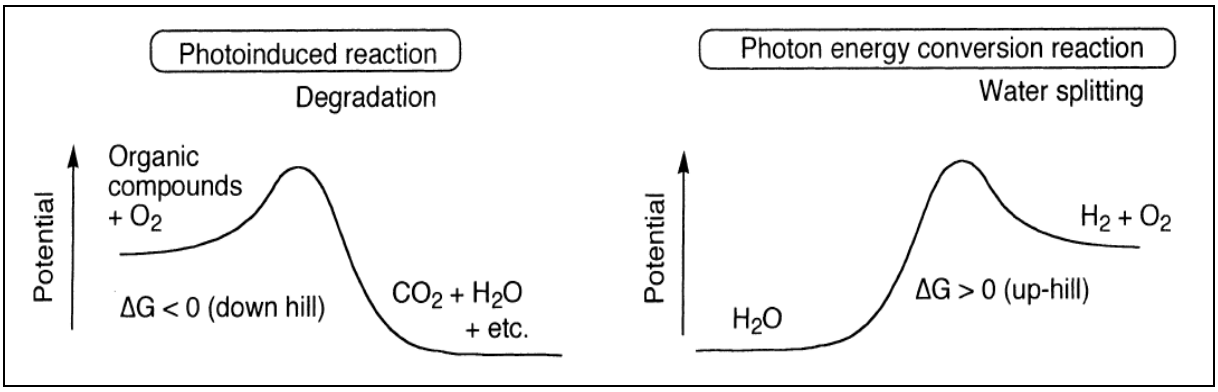

Figure 2.5: Energy changes associated with photocatalytic reactions.

In this project, photocatalytic oxidation and reduction processes were studied for the degradation of organic model pollutants. These processes preferentially occur at the interface of the heterogeneous phase (e.g. rhodamine B (RhB) (liquid) – $BiVO_4$ (solid)) under VLI [70], and are therefore surface reactions. The thermodynamics and kinetics for adsorption-desorption processes involved in the photocatalytic oxidation of organic pollutants should be further investigated.

As was previously noted, the change in Gibbs free energy (ΔG) is negative ($\Delta G < 0$) for oxidative and reductive decomposition of organic compounds under aerobic conditions, and the reaction releases energy. Therefore, it does not need to absorb extrinsic energy according to the laws of thermodynamics [71]. The change in Gibbs free energy can be defined as:

$$\Delta G = \Delta G^\circ + RT \ln K \quad (2.1)$$

where ΔG is the change in Gibbs free energy (kJ mol^{-1}); ΔG° is the change in Gibbs free energy of standard-state reactions (kJ mol^{-1}); K is the equilibrium constant (dimensionless), T is the absolute temperature (K); R is the gas constant (kJ $(mol\ K)^{-1}$). At equilibrium, ΔG is 0 (kJ mol^{-1}), so the equation becomes:

$$\Delta G^\circ = -RT \ln K \quad (2.2)$$

At constant temperature, the change in Gibbs free energy can be defined as:

$$\Delta G = \Delta H - T\Delta S \quad (2.3)$$

where ΔH is the change in enthalpy ($kJ \cdot mol^{-1}$), ΔS is the change in entropy ($kJ \cdot (mol \cdot K)^{-1}$). In the case of photocatalytic redox reactions, the reaction occurs exothermically at room temperature, so the exothermical equation is suitable for identifying the value of Gibbs energy change in terms of the change in enthalpy and change in entropy of the final products.

The final mineralization products of photocatalytic redox reaction are CO_2 (gas) and H_2O (liquid), and the standard-state Gibbs free energies of formation for these components are -393.5 $kJ \cdot mol^{-1}$ and -285.8 $kJ \cdot mol^{-1}$ respectively. Therefore, the overall change in Gibbs free energy for the overall reaction is negative ($\Delta G < 0$), and it is a spontaneous process. During photocatalytic redox processes, adsorbed dissolved oxygen molecules, H_2O and pollutant intermediates react with photoexcited electron-hole pairs on the photocatalyst surface, resulting in the eventual mineralization of pollutants into CO_2 and H_2O. The amount of dissolved oxygen molecules in water at room temperature (T = 25 ^oC) is approximately 8.25 $mg \cdot L^{-1}$ and is thought to be similar for very dilute dye solutions ($C_0 < 10^{-3}$ $mol \cdot L^{-1}$) [72]. The whole adsorption-desorption process occurs in the liquid-solid heterogeneous phase (H_2O (liquid), O_2 (liquid), pollutants (liquid) and $BiVO_4$ (soild)). Taking a RhB (liquid) – $BiVO_4$ (solid) heterogeneous system as an example, a schematic illustrating the thermodynamics of the photocatalytic degradation of RhB in the presence of $BiVO_4$ is shown in Figure 2.6 [73, 74]:

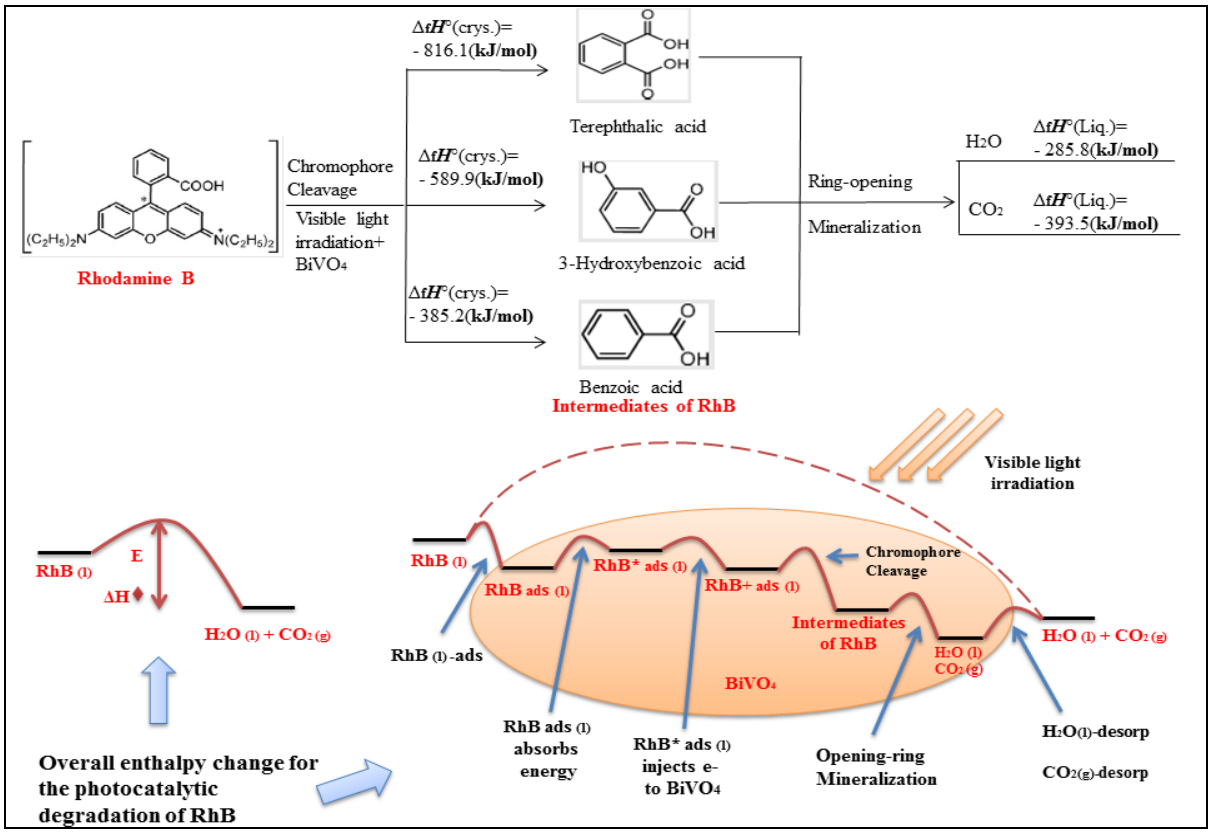

Figure 2.6: Schematic of thermodynamic processes occuring in the photocatalytic degradation of rhodamine B.

2.3 Kinetic analysis of photocatalysis

2.3.1 Adsorption-desorption processes

Adsorption is a surface-based process and results in the formation of an adsorbate film on the surface of the adsorbent. Taking liquid-solid and gas-solid heterogeneous surfaces as examples, the solid surface captures molecules in the gas or liquid phase with free surface unsaturated valence bonds, which concentrate those captured molecules at the interface of the heterogeneous phase in order to reduce the Gibbs free energy of the solid surface.

Desorption is a phenomenon in which a substance is released from or through a surface in an opposite process to adsorption, where the Gibbs free energy of the solid surface increases. Adsorption is generally classified as physisorption (characteristic of weak van der Waals forces) and chemisorption (characteristic of covalent bonding) [75]. Typically, the adsorption-desorption processes occuring in photocatalysis are mainly physisorption because this type of process

occurs more readily, allowing for ease of desorption of products and intermediates. In contrast, the binding effect of chemisorption is very strong and does not result in the ready desorption of products, and is likely more permanent [76, 77]. It should be noted that the adsorbed compounds on the surface of the photocatalyst do not react in the absence of light irradiation due to the absence of electron-hole pairs, indicating that a strictly catalytic process does not take place. The photogenerated electron-hole pairs provide the main active sites for photocatalytic reactions, owing to their high energies, and because they facilitate the formation of radicals which allow for further redox reactions to occur.

2.3.2 Heterogeneous reactions on active sites of ternary metal-oxide photocatalysts

In the case of photocatalysis mediated by ternary metal-oxide photocatalysts such as bismuth and sliver ternary oxide-based photocatatalyst composites, e.g. $BiVO_4$ and Ag_3VO_4 proposed in this thesis, adsorption-desorption sites occur on the heterogeneous surface of the photocatalysts, and the overall photosystem consists of a heterogeneous system with solid photocatalysts and aqueous pollutants. Under the assumption of Langmuir adsorption, only a monolayer is formed at maximum adsorption, and active sites for the reaction are found at the adsorption-desorption sites [78].

Given the existence of adsorption and active sites on the surface of $BiVO_4$ and Ag_3VO_4, according to Oshikiri et al.[79], it could be inferred that bismuth (Bi) and oxygen (O) sites favourably adsorb H_2O (liquid) molecules, while vanadium (V) sites favourably adsorb O_2 (liquid) in the whole photocatalytic oxidation and reduction processes. Therefore, V is expected to be an active reduction site, whereas oxidation could occur at either a Bi or an O site because of the electronic structure of $BiVO_4$ [80-82]. In this process, a photoexcited hole is expected to spread and move closer to the Bi and O atoms. Bi and O compose the VB of $BiVO_4$ with namely the Bi 6s-O 2p orbitals. The excited electron prefers to be close to the V atoms, making the CB of V act like a 3d orbital. Because of the similar situation for Ag_3VO_4, it could be deduced that silver (Ag) and O atoms, composing Ag 4d-O 2p orbitals, could serve as sites for adsorbing H_2O (liquid) molecules and act as active oxidation sites, while V atoms of V 3d orbitals could adsorb O_2 (liquid) and act as active reduction sites [83, 84].

Since the solution pH strongly influences the surface charge of the photocatalyst, adsorption of the model pollutant is highly pH-dependent [85]. $BiVO_4$ is a n-type photocatalyst [86] with a negatively charged surface, which exhibits strong adsorption towards cationic model pollutants possessing positive charges in acidic media due to electrostatic interactions, such as with rhodamine B (RhB) [85], methyl orange (MO) [87], methylene blue (MB) [88] and phenol [89]. In contrast, Ag_3VO_4 is a p-type photocatalyst [84] and exhibits strong adsorption towards pollutants possessing negative surface charges in alkaline media such as anionic model pollutants like Basic Blue 3 (BB3) [90].

The whole heterogeneous photocatalytic reaction undergoes three main steps, namely: adsorption of reactants (in the dark), surface reaction (upon light irradiation), and desorption of products (also under irradiation). Taking a RhB (liquid) – $BiVO_4$ (solid) heterogeneous system as an example, a schematic of the whole adsorption-photocatalytic reaction-desorption process including thermodynamic and kinetic considerations is shown in Figure 2.7 [69, 77]:

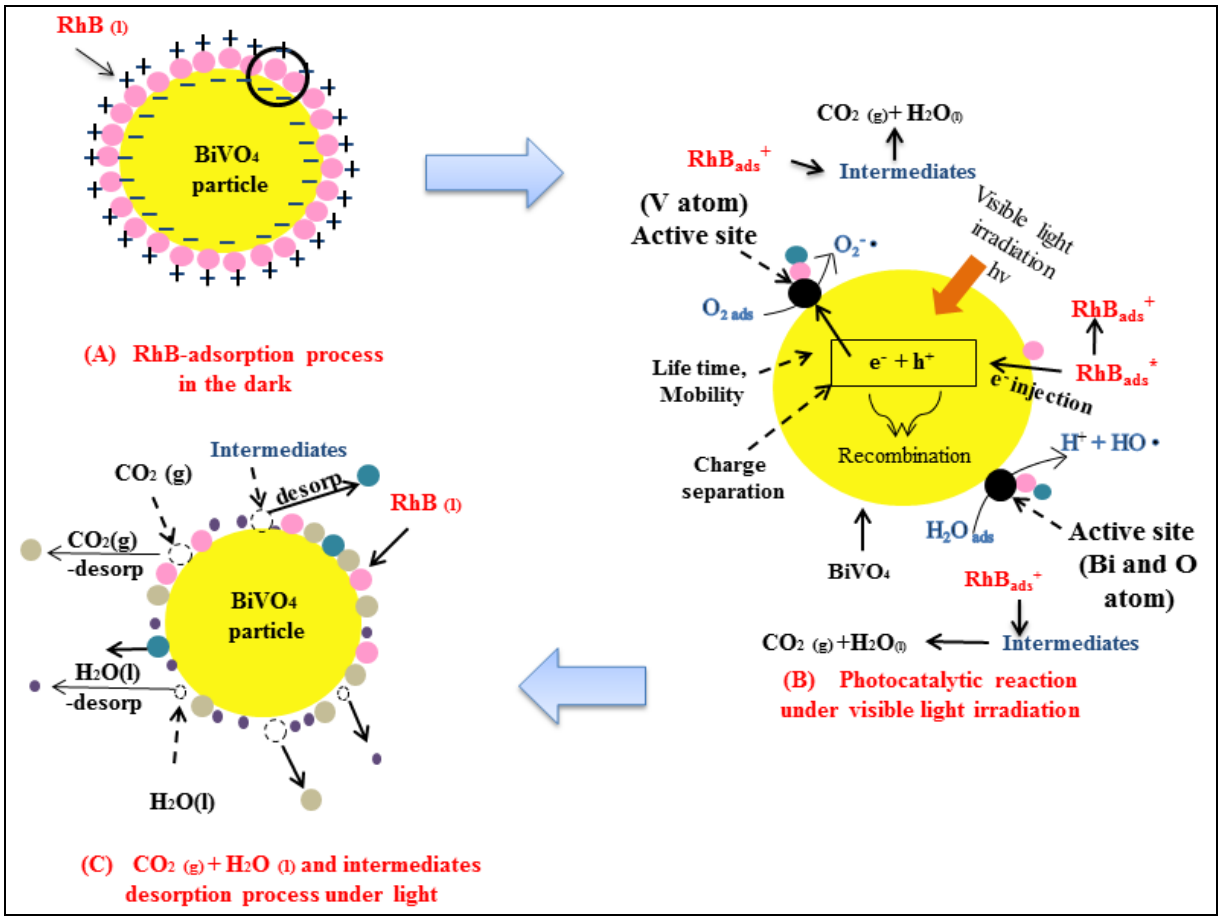

Figure 2.7: Schematic of the adsorption-photocatalytic reaction-desorption process for RhB in the presence of $BiVO_4$.

As seen from Figure 2.7(A), an adsorbate film forms on $BiVO_4$ in the dark, and an exothermic process occurs due to the reduced Gibbs free energy of the solid surface and electrostatic attractions. In addition, active sites in photocatalysis are defined as where the redox reaction occurs with photoexcited electron-hole pairs. Figure 2.7(B) shows that after absorbing photons with energies exceeding the band gap energy of the photocatalyst, photoexcited electron-hole pairs form in the bulk of $BiVO_4$, and these e-h pairs can be separated and can migrate to the surface of $BiVO_4$, where they can move freely. When the e-h pairs move to the adsorption sites on the surface of $BiVO_4$ and come in contact with adsorbed pollutants, dissolved O_2 (liquid) and H_2O (liquid), the redox reaction occurs. After a series of redox reactions mediated by the photocatalytic radical species, intermediates of RhB are formed, and may further react and eventually mineralize into CO_2 (gas) and H_2O (liquid). Figure 2.7(C) shows the desorption of intermediates and final products CO_2 (gas) and H_2O (liquid) from the surface of $BiVO_4$ as an

endothermic process, ascribed to the increased Gibbs free energy of the solid surface. As seen in Figure 2.7(C), during the desorption process, the residual RhB molecules, intermediates, CO_2 (gas) and H_2O (liquid) coexist in the system.

Although parts of intermediates desorb after reacting with high-energy radicals, they can readsorb onto the surface of $BiVO_4$ due to electrostatic interactions. As shown in Figure 2.7(B), they can continue to react and become further mineralized into final products CO_2 (gas) and H_2O (liquid). These final products may eventually be desorbed from $BiVO_4$, as shown in Figure 2.7(C). After many cycling reactions between Figure 2.7(B) and Figure 2.7(C), all of the pollutants could be finally degraded into CO_2 (gas) and H_2O (liquid). The heterogeneous reactions are thought to take place at the interfacial boundary between the two phases (i.e. RhB (liquid) – $BiVO_4$ (solid)), where the aqueous RhB and photocatalyst $BiVO_4$ are in different phases. For Ag_3VO_4 particles, the adsorption process is thought to occur similarly to that in $BiVO_4$ particles.

Photocatalytic reactions are distinct from those which occur in heterogeneous catalysis, in which, active sites refer to the specific surface active sites on the catalysts. While active sites in photocatalysis are defined as where the redox reaction occurs with photoexcited electron-hole pairs, these e-h pairs can move freely on the surface of homogeneous photocatalysts. Therefore, the density or concentration of active sites for visible-light-induced photocatalysis is distributed over the entire (photo) catalyst surface, and is described as a function of the available area [91]. Photocatalysis also varies from traditional catalysis because it does not accelerate the rate of reaction as catalysis does. In catalytic systems, the reactions of interest occur slowly even if the catalyst was not present in the system. However, in photocatalysis, no reaction takes place in the absence of a photocatalyst, even over very prolonged periods of time. In this sense, photocatalysis does not follow the traditional definition of a catalytic reaction, and may be considered more appropriately as a ‘photo-assisted’ process [92].

2.3.3 Crystal structure, crystallinity and particle size

Crystal structure, crystallinity and particle size also strongly affect the recombination rate of photogenerated electrons and holes. Different crystal structures have different band gap energies, which can affect the utilization of sunlight, and result in different performances of the

photocatalytic degradation of organic pollutants. The higher the crystalline quality is, the smaller the amount of defects that are present. These defects are of importance because they serve as recombination centers between photogenerated electrons and holes, resulting in a decrease in photocatalytic activity. Therefore, both a high crystallinity and a high specific surface area are integrally required in high-performance photocatalysts [9].

Crystallinity refers to the degree of structural order in a solid. In a crystal, the atoms or molecules are arranged in a regular, periodic manner and the higher the crystalline quality is, the lower the number of defects that are present. Amorphous materials which have boundary edges could also act as recombination centres [93]. Furthermore, particle size would also affect surface area, and as the particle size decreases, the distance (i.e. lifetime in Figure 2.7) that photogenerated electrons and holes have to migrate to reaction sites on the surface becomes shorter, decreasing the probability of recombination [9].

Nano-scale materials are generally favourable for heterogeneous photocatalysis, since a higher specific surface area can be obtained with a smaller particle size. For example, the specific surface of nano-scaled monoclinic-$BiVO_4$ (m-$BiVO_4$) particles, fabricated via hydrothermal method, is roughly 15 $m^2 \cdot g^{-1}$ [18], which is much better than that of $BiVO_4$ particles (0.3 to 4.2 $m^2\ g^{-1}$) fabricated by other methods such as combustion, sonochemical and solid-state reactions [94, 95]. As for the hydrothermal method, it not only provides excellent chemical homogeneity, but also allows for the rigorous control of physical properties with unique stable morphologies (e.g. spherical, cubic, fibrous and plate-like), phases, crystal sizes (from a few nanometers to tens of microns), as well as specific surface areas at low reaction temperatures and pressures [96-98].

2.3.4 Kinetic modeling

The Langmuir description of adsorption provides the most common equation, and is applied to kinetic modeling for quantitative analysis of the adsorption-desorption process due to its simplicity and its ability to fit a variety of adsorption data. It is based on four major assumptions [99]:

1) All of the adsorption sites are equivalent and each site can only accommodate one molecule.
2) The surface is energetically homogeneous and adsorbed molecules do not interact.

3) There are no phase transitions.
4) At the maximum adsorption, only a monolayer is formed. Adsorption only occurs at localized sites on the surface, and not with other adsorbates.

Heterogeneous reactions occur due to the presence of photoexcited electron-hole pairs in the photosystem. To investigate the kinetics of model pollutant degradation, Langmuir-Hinshelwood kinetics can be used to quantitatively approximate the reaction, and is the most commonly used expression for the description of heterogeneous catalytic processes [100]. In this project, the expression for a liquid-solid (e.g. RhB (liquid) – $BiVO_4$ (solid)) system is given by:

$$-\mathrm{d}C/\mathrm{d}t = k_r KC/(1+KC) \qquad (2.4)$$

Where C is the concentration of RhB (liquid) ($mg \cdot L^{-1}$), k_r is the reaction rate constant ($mg \cdot (L \cdot min)^{-1}$), K is the equilibrium constant for adsorption of RhB (liquid) onto $BiVO_4$ (solid), and t is the illumination time (min). This model assumes that the steps include the adsorption of RhB (liquid), the surface reaction at the interface of RhB ((liquid)) – $BiVO_4$ (solid), as well as the desorption of H_2O (liquid) and CO_2 (gas); where the reaction is the rate-limiting step. In the case of Eq. (2.4), the constants k_r and K can be calculated from the corresponding integrated expression. This equation can be integrated between the limits: $C = C_0$ at $t = 0$ and $C = C$ at $t = t$. The integrated expression is given by:

$$\ln(C_0/C) + K(C_0-C) = k_r K \cdot t \qquad (2.5)$$

It has been suggested that at very dilute concentrations ($C_0 < 10^{-3}$ $mol \cdot L^{-1}$; with $C_0 = 1.04 \times 10^{-5}$ ($mol \cdot L^{-1}$) of RhB (liquid) in this project), KC becomes $<<1$, and the reaction is of apparent first order [101]. With respect to limits: $C = C_0$ at $t = 0$ and $C = C$ at $t = t$, and when the initial concentration is sufficiently small, the L-H expression reduces to pseudo-first order kinetics and is given by:

$$\ln(C_0/C) = k_r Kt = k't \qquad (2.6)$$

Where k' represents the pseudo-first order rate constant. A plot of $\ln(C_0/C)$ as a function of illumination time yields a straight line with a slope corresponding to the pseudo-first order constant, and is used as a criterion for the comparison of photocatalyst activity.

2.4 Literature review on photocatalysis

2.4.1 Overview of the ternary oxide photocatalysts

Modification of ternary metal-oxide photocatalysts and novel highly-active visible-light-induced photocatalysts were investigated to enhance the photocatalysis efficiency under VLI. This project may provide a new photocatalytic perspective on the facilitation of the practical applications of photocatalysts to environmental issues. In this project, bismuth and sliver ternary oxide-based photocatatalysts as the main objectives were studied and divided into three programs in order to solve three academic issues sequentially, which are the:

1) Improvement of crystallinity of crystal structures and specific surface area of composites based on $BiVO_4$ single phase crystal structure.
2) Improvement of separation and transfer of photoexcited charges, as well as the inhibition of defects in single phase based on silver species composites.
3) Improvement of protection of catalysts from photocorrosion during redox reactions under VLI based on silver species composites.

For further discussion of these issues, photocatalytic activities were investigated while degrading of organic pollutants. It was found that photocatalytic performance could be enhanced by the following means: facile synthesis processes; highly active starting materials; heterojunction multi-phase photocatalysts with various morphologies and the incorporation of functionalized high surface area substrates, such as graphene oxides. The following chapters present literature related to the development of ternary oxide photocatalysts based on bismuth and silver ternary oxide-based photocatalysts. Strategies referring to improvements of photocatalytic activity and to novelties of academic studies are highlighted. The aim of the discussion is to provide references to the undertaken projects.

2.4.2 Development of the functionalized ternary metal-oxide composite photocatalysts

The development of functionalized ternary meta-oxide based photocatalysts is one of the many strategies used in band engineering design in which tuning the band gap can enhance photocatalytic efficiency and feasibility in the visible light spectrum. Strategies involving the enhancement of photocatalytic activity and applications will be reviewed.

2.4.2.1 Overview of the strategies of photocatalytic enhancement

Functionalized ternary metal-oxide composites combine two different kinds of metal cations and oxygen anions (i.e. $A_xB_yO_z$), demonstrating the characteristics of photosensitization under sunlight irradiation [9, 37, 102].

Functionalized ternary oxides have been developed to overcome the intrinsic limitations of binary metal oxides. Some favourable ternary oxides have been found to exhibit high photocatalytic performances under VLI. An example would be Bi with d^{10} ion; Bi_2WO_6 has been reported to exhibit photocatalytic activity towards O_2 evolution under VLI (λ > 420 nm) due to the low band gap energy of 2.8 eV [26]. Shimodaira et al. [27] have shown that Bi_2MoO_6 with a 2.70 eV band gap at a low-temperature phase showed an intense absorption band in the visible light region, and also exhibited photocatalytic activity for O_2 evolution from an aqueous silver nitrate solution under VLI. $Bi_2Mo_3O_{12}$ with a band gap of 2.88 eV [27] was also reported to show the photocatalytic activity towards O_2 evolution under VLI.

Many researchers have shown that $BiVO_4$ with a 2.4 eV band gap energy not only demonstrates a photocatalytic performance in O_2 evolution from aqueous solutions containing Ag^+ as an electron scavenger under VLI (λ > 520 nm), but it also displays a photocatalytic activity towards the degradation of organic pollutants in wastewater treatment under VLI [25, 52, 103]. Other photocatalysts such as Bi_3O_4Cl (band gap = 2.79 eV) [104], Bi_3SbO_7 (band gap = 2.71 eV) [105], and $CaBi_2O_4$ (band gap = 3.08 eV) [106] have also been reported as highly efficient ternary metal-oxide photocatalysts.

Ag elements with d^{10} ions have attracted much attention due to enhanced optical properties in photocatalysis. Silver vanadate has attracted much interest due to its special band structures.

Konta et al. [10] reported that silver vanadate powders with different compositions mainly consist of α-$AgVO_3$, β-$AgVO_3$, $Ag_4V_2O_7$ and Ag_3VO_4. Only the monoclinic scheelite Ag_3VO_4 with band gaps of 2.2-2.5 eV [28, 107] showed an excellent photocatalytic performance towards the evolution of O_2 from silver nitrate solution under VLI. Recent work using β-$AgVO_3$ nanowires synthesized via hydrothermal method with 2.25 eV band gap energy showed excellent photocatalytic performances towards the degradation of RhB under VLI [108]. Other photocatalysts with Nb elements (d^0 ions) such as $AgNbO_3$ (band gap = 2.8 eV) [29], and $SnNb_2O_6$ (band gap = 2.3 eV) [36] have also been reported in literature.

Compared to TiO_2, the valence bands of ternary metal-oxide semiconductors consist of hybridizations of transition-metal orbits, in which levels of valence bands can be increased by the hybridization process [109], resulting in the narrower band gaps of semiconductors. The photocatalysts with narrower band gaps could facilitate the transfer of electrons from the VB to the CB of a photocatalyst, resulting in the photocatalytic oxidation reaction, which could be used to efficiently degrade pollutants.

2.4.2.2 Applications to photocatalytic degradation

Studies involving photocatalysis generally use dyes such as methylene blue (MB), rhodamine B (RhB), methyl orange (MO) and azodye acid red B (ARB) as model organic pollutants for degradation under VLI. The industry standard in photocatalytic performance is currently based on applying state-of-the-art techniques to the degradation of organic model pollutants in order to improve the highly efficient utilization of solar radiation towards photocatalytic degradation.

Ternary metal oxides as ideal semiconductor catalysts have been applied to the photocatalytic degradation of organic pollutants and solar-driven hydrogen/oxygen production due to their low cost and stability in aqueous solution. Selected studies reported that metal cations involving transition metals as well as some main group metals with d^{10} ions such as silver (Ag) and bismuth (Bi) [9], could overcome the limitation of a high band gap energy. As such, the functionalized ternary oxides serve an important role in wastewater decontamination [9, 37, 102].

The $BiVO_4$ monoclinic structure in nanosheets around 10-40 nm thick was investigated by Zhang et al. [110], indicating high photocatalytic activity towards the degradation of RhB under VLI. Its photocatalytic performance was explored and it was verified that the photocatalysis

enhancement can be attributed to the nano-scale particle sizes, which were induced by adding sodium dodecyl benzene sulfonate (SDBS) as a morphology-directing template during hydrothermal synthesis. The degradation of RhB using morphologically diverse monoclinic $BiVO_4$ (m-$BiVO_4$) was also studied by Zhao et al. [111], who demonstrated that a hyper-branched structure of $BiVO_4$ was successfully prepared via a surfactant-free hydrothermal route, which led to a high photocatalytic activity towards the degradation of RhB. In addition, a study regarding the degradation of MB over $BiVO_4$ in a nanoplate-stacked, star-like shape was reported by Sun et al. [52], indicating 91% degradation of MB under VLI within 25 min. The removal of MO by $BiVO_4$ under VLI was reported by Li et al. [54], which indicated that both cetyltrimethylammonium bromide (CTAB) and pH affected the morphology of $BiVO_4$, and impacted the photocatalytic efficiency towards the degradation of MO.

Selected studies of the degradation of organic dye pollutants using silver ternary oxide photocatalysts were investigated as well. The photocatalytic efficiency towards decolouration of azodye acid red B (ARB) was increased by using the monoclinic structure Ag_3VO_4 according to the results reported by Hu et al. [28]. The degradation of RhB on nanoscale Ag_3VO_4 samples was investigated by Zhang et al. [112]. Results showed that polyethyleneglycol assisted in the synthesis of nanoscale particles, which led to a much higher photocatalytic degradation of RhB than the commercial photocatalyst titanium dioxide P25 under VLI.

Ag_3VO_4/TiO_2/graphene nanocomposites with multi-dye degradation effects were successfully fabricated, and displayed much higher photocatalytic performances while degradading MO and RhB [51] compared to Ag_3VO_4/TiO_2 and TiO_2/GR nanocomposites under VLI. It suggested that the high performance can be attributed to the synergistic effects of graphene with the capacity of storing and shuttling electrons. Also, the results improved efficiency for the separation of photogenerated electron-hole pairs compared to the heterojunction between Ag_3VO_4 and TiO_2. Therefore, high photocatalytic performances towards the degradation of organic pollutants can be improved with the assistance of heterogeneous junctions and large surface area substrates.

2.4.3 Development of active bismuth-based ternary composite photocatalysts

Active bismuth-based ternary photocatalysts have been studied as promising materials for photocatalysis due to their lower band gap energies. The environmentally friendly, non-toxic

properties of bismuth-based ternary photocatalysts presenting excellent photosensitization have attracted much interest. With great potential for converting photon energy into chemical energy, bismuth-based ternary photocatalysts are capable of decomposing organic contaminants and of facilitating O_2 evolution under VLI [9, 113, 114]. Bismuth vanadate ($BiVO_4$) as one of the bismuth-based ternary photocatalysts has attracted widespread interests for photocatalytic activity due to its functionalized characteristics [18]. It is reviewed in the following sections.

2.4.3.1 Overview and strategies of photocatalytic enhancement

$BiVO_4$ is one of the most promising semiconductors which possess some favourable properties: it is a non-toxic yellow pigment [115, 116] that is ferroelastic [117-119], and exhibits acousto-optical properties [120] and possesses ionic conductivity [121, 122]. These properties demonstrate that $BiVO_4$ exhibits desirable photocatalytic activity towards the degradation of organic pollutants under VLI. $BiVO_4$ has three main crystal forms with monoclinic scheelite (m-$BiVO_4$), tetragonal zircon (t-z-$BiVO_4$), and tetragonal scheelite (t-s-$BiVO_4$) [123, 124], of which m-$BiVO_4$ with a short band gap of 2.4 eV is one of the most promising visible-light-driven photocatalysts [37, 125].

$BiVO_4$ has been reported to be a direct band gap semiconductor [126], and the presence of unoccupied V 3d states in $BiVO_4$ coupled with O 2p and Bi 6p levels results in low-energy direct transitions [37]. Some new methods have been employed to prepare $BiVO_4$ other than the traditionally used solid-state reactions [25, 86], including sonochemical routes [95, 127], room temperature aqueous processes [123], molten salt methods [128], hydrothermal processes [129-131], chemical bath depositions [132, 133], organic decomposition methods [103, 134], combustion synthesis methods [94], and co-precipitation processes [135].

In order to increase the efficiency of photo-degradation for organic pollutants by increasing the speed of light transmission, various morphologies such as flower-like [125], flake-ball, flake [136], cuboid-like or plate-like [54] structures have been reported. However, most of the synthetic methods cannot produce $BiVO_4$ materials with both a high crystallinity and a high surface area [94, 95]. In order to optimize the photocatalytic properties of m-$BiVO_4$, research is focused on employing templates and surfactants such as silica (KIT-6), CTAB and CMC [135], as well as starting materials made from organic polymers and inorganic salts [137]. Although

photoactivity is improved using these methods, they cannot satisfy the requirements of both high crystallinity and high surface area required in high performance photocatalysts [138, 139]. Additionally, impurities may be generated which could block the active sites of $BiVO_4$, and decrease the overall photocatalytic activity.

Some studies involving optimum starting materials were conducted, and revealed that potassium vanadium oxide, particularly KVO_3 or K_3VO_8, is a promising alternative starting material for preparing m-$BiVO_4$ with high activity [81, 140]. Kelmers [141] prepared KVO_3 by dissolving equimolar amounts of K and V as KOH and V_2O_5 respectively. Recently, Mieczysław Trypuć et al. [142] reported one preparation of KVO_3 based on KCl and V_2O_5 in the presence of steam. Liu, et al. [143] also reported that m-$BiVO_4$ particles were synthesized using $NaVO_3$ or V_2O_5 via the hydrothermal method (at optimized synthesis conditions of 140 °C and 200 °C) and two single morphologies with plate form and rod-like particles were obtained, respectively.

2.4.3.2 Modification of m-$BiVO_4$ photocatalyst composites with high photocatalytic performance

Studies involving the modification of the $BiVO_4$ structure have been conducted. ZnO was loaded on $BiVO_4$ reported by Neves et al. [144], which demonstrated that ZnO/$BiVO_4$ microparticles were hollow-ZnO microparticles filled with $BiVO_4$. These loading strategies were developed and applied to photocatalysis. Transition metal elements used as favourable modification materials have attracted much attention. Fe_2O_3, Co_3O_4 and CuO were reported to be the favourite candidates loaded on $BiVO_4$, resulting in high photocatalytic decolouration efficiencies of MB dye under VLI [58]. Non-metallic elements such as carbon (C) have also been investigated recently. Carbon-loaded $BiVO_4$ was investigated by Lee et al. [145]. The results showed notable photocatalytic activity towards the degradation of RhB under VLI.

Doping has been increasing in popularity recently as another approach to modification. Doping $BiVO_4$ with metallic elements and non-metallic elements or with related oxide compounds has been investigated concurrently. Metallic compounds such as palladium (Pd) doped $BiVO_4$ (Pd/$BiVO_4$) [46], platinum (Pt) doped $BiVO_4$ (Pt/ $BiVO_4$) [47], Copper (Cu) doped $BiVO_4$ (Cu-doped $BiVO_4$) [43], Eu-, Gd- and Er-doped $BiVO_4$ [146], gold (Au) doped $BiVO_4$ (Au/$BiVO_4$) [48], as well as cobalt (Co) and nickel (Ni) doped $BiVO_4$ (Co-$BiVO_4$, Ni-$BiVO_4$) [45] were

investigated and were shown to successfully improve photocatalytic activity towards the degradation of organic pollutants including RhB, MO and MB under VLI. In addition, non-metallic elements including fluoride-doped $BiVO_4$ [50] and boron (B) as the dopant of $BiVO_4$ [51] were also investigated and showed correspondingly high photoactivities with regards to the degradation of dye components under VLI.

2.4.4 Development of active silver-based ternary composite photocatalysts

The development of functionalized silver-based ternary composites has attracted much attention to photocatalysis used for pollutant degradation and water splitting [9, 37]. Literature pertinent to the investigation of silver-based ternary composites is addressed in the following sections.

2.4.4.1 Overview of the strategies of photocatalytic enhancement

Numerous silver ternary metal-oxide photocatalysts have been reported in literature, such as Ag_3VO_4 [28], $Ag_4V_2O_7$ [30], β-$AgVO_3$ [31], $AgNbO_3$ [29], $AgMO_2$ (M = Al, Ga, In) [32, 33], Ag_2CO_3 [34], and Ag_3PO_4 [35], all of which have been found to exhibit enhanced photocatalytic performances under VLI compared to the traditional TiO_2 photocatalyst [147].

The early studies of Ag_3VO_4 published by Saxena et al. [148], which were related to the potentiometric determination of vanadium as silver orthovanadate, resulted in a surge of studies of Ag_3VO_4 pertinent to electronic properties, such as the phase transition of photoinduced effects [149], bonding characteristics [150] and the electronic structures of Ag_3VO_4 [83]. Konta et al. [10] reported that Ag_3VO_4 as a photosensitizer had a large VB in the content of silver, which resulted in holes photogenerated in Ag_3VO_4 which oxidized H_2O to form O_2 under VLI. Therefore, Ag_3VO_4 has been identified as one of several promising photocatalysts under VLI and could be widely applied to research work involved in wastewater treatment. Several methods have been reported for the synthesis of Ag_3VO_4 such as solid-state reactions [10, 151], precipitation [28], coprecpitation [112] and hydrothermal treatment [152]. In addition, other silver speices photocatalysts such as Ag_2O [153] also showed high photocatalytic performances towards the degradation of organic pollutants under VLI.

2.4.4.2 Modification of silver vanadate composites with high photocatalytic performances

Single-phase photocatalysts may increase the recombination rate of photogenerated e-h pairs because of the defects of grain boundaries serving as the recombination centers to impede the separation of charge species [9-11]. The modification of heterojunction photocatalysts increases the photocatalytic activity attributed to the matched band potentials among each phase, and to high transfer efficiency of charges at the interface as well [154].

The rare earth metals loaded on Ag_3VO_4, i.e. RE^{3+}-Ag_3VO_4, (RE = Nd, Sm, and Eu) served as early modifications of single phase silver species photocatalysts reported by Xu et al. [155], which indicated that RE^{3+}-Ag_3VO_4 with 2 wt% RE^{3+} led to the highest visible-light-driven performance towards the degradation of RhB among all loading amounts. One year later, Gd_2O_3/Ag_3VO_4 was investigated by Sun et al. [156], and it was shown that Gd_2O_3/Ag_3VO_4 with 3 wt% Gd^{3+} resulted in the highest enhancement of RhB degradation under VLI. La_2O_3, NiO (p-type) [157] and Co_3O_4 (p-type) [82] modified Ag_3VO_4 particles have been reported by Xu et al. [158], Hu et al. [159] and Zhang et al. [160] respectively. All of these modified La_2O_3-Ag_3VO_4, NiO/Ag_3VO_4 and Co_3O_4/Ag_3VO_4 particles were synthesized via wet impregnation processes, indicating high photocatalytic activities towards the degradation of organic dyes under VLI. $ZnFe_2O_4$/Ag_3VO_4 heterojunction structure composites with a 50 nm average diameter scale have been proposed by Zhang et al. [56], with results that indicated an outstanding performance of the photocatalytic decolouration of RhB over 50 min.

A novel Ag_3VO_4/AgBr/Ag plasmonic photocatalyst was fabricated via an anion-exchange reaction reported by Zhu et al. [55], which enhanced photocatalytic activity for the decolouration of RhB within 20 min compared to pure Ag_3VO_4, Ag_3VO_4/AgBr, and Ag/AgBr under VLI. A similar study of $AgVO_3$@AgBr@Ag nanobelt heterostructured plasmonic photocatalysts was reported by Sang et al [161], who demonstrated that highly efficient plasmonic photocatalysts, fabricated via a multi-step synthesis route that included a hydrothermal process, an ion-exchange reaction, and a photo-induced reduction, showed a superior performance towards the degradation of RhB under VLI. In addition, the plasmonic photocatalyst Ag@Ag_3VO_4 reported by Wang et al. [57] exhibited a high activity towards the degradation of RhB under VLI.

2.4.5 Development of graphene oxide-assisted photocatalysis

The development of graphene oxide-assisted (GO-assisted) hybrid photocatalyst composites applied to photocatalysis has recently emerged and has received considerable attention. Literature pertinent to the studies of GO-assisted photocatalysts is presented in the following sections.

2.4.5.1 Overview of characteristics of graphene oxide in photocatalysis

GO is a highly oxidative form of graphene consisting of a variety of oxygen functionalities [162]. The most notable model for the structure of GO was developed by Lerf-Klinowski, which indicated that the carbon plane in GO is decorated with hydroxyl and epoxy (1,2-ether) functional groups, carboxylic acids as well as organic carbonyl defects [60, 163]. These functional groups of GO disrupt the sp^2 bonding network, resulting in the electrical insulating characteristics of GO [164]. However, the conductivity can be partially recovered by restoring the π-network via chemical, thermal, or electrochemical reduction of GO to obtain reduced graphene oxide (RGO) [60].

GO is a wonderful candidate for the application to water purification due to the functional groups of GO such as hydroxyl, carbonyl, carboxyl and epoxide. GO dissolved in aqueous solution and formed functionalized hybrids with other photocatalyst composites, which results in high performance in water purification [165, 166]. In addition, the functional groups also offer reactive sites for surface modification reactions to improve functionalized GO-based materials for a wider range of applications [61]. GO also shows a high adsorption capacity for dyes. Usage of graphene sponges that present a high potential to remove cationic (MB, RhB) and anionic (MO) dyes from their aqueous solutions was investigated by Zhao et al. [167], whose results suggested that GO had a excellent binding affinity for dyes and aqueous solutions.

2.4.5.2 Overview of the strategies of photocatalytic enhancement over bismuth-based photocatalysts

Titanium dioxide TiO_2 (UV active), tungsten oxide WO_3 (visible-light-driven) and bismuth vanadate $BiVO_4$ (visible-light-driven) nanocomposites combined with RGO sheets were investigated and demonstrated improvements both in photocurrent generation and in

photoelectrocatalytic efficiencies [168]. Of these composites, bismuth ternary metal-oxide photocatalysts have attracted the most attention. GO-assisted $BiVO_4$ photocatalysts ($BiVO_4$/GO) were introduced by Dai et al. [169], who showed that photocatalysts with 1wt% GO produced the highest photocatalytic activities towards the degradation of MB under VLI, which suggests that the enhanced photocatalytic activity of $BiVO_4$/GO can be attributed to the synergetic effects of the strong visible-light absorption of $BiVO_4$ and the high electron capture of graphene oxide. Reduced graphene oxide-$BiVO_4$ (RGO-$BiVO_4$) was also reported in regards to the degradation of different organic pollutants. Yan et al. [170] reported that the produced RGO-$BiVO_4$ displayed an extremely high photocatalytic performance for the degradation of ciprofloxacin (CIP), more than pure $BiVO_4$ under VLI.

Other reduced graphene oxide-assisted photocatalyst composites also performed well in the degradation of organic pollutants, such as graphene-Bi_2WO_6 (G-BWO) composites [171, 172], graphene/Bi_2WO_6 [173], $BiOIO_3$/RGO nanocomposites [174], $Bi_{25}FeO_{40}$-graphene photocatalysts [175] and $BiPO_4$ nanoparticles combined with GO (GO-$BiPO_4$) [176], which exhibited increased photocatalytic activities both in degradation of organic pollutants and in water splitting under VLI.

2.4.5.3 Overview of the strategies of photocatalytic enhancement over silver-based photocatalysts

Silver halides have triggered interests of scholars when combined with graphene oxides and reduced graphene oxides. GO-assisted Ag/AgX (X = Br, Cl) nano-composites were produced via a water/oil process by Zhu et al. [177], who reported that the stability of a plasmonic photocatalyst was attributable to the combination of GO and hybrid nanoparticles, resulting in an amazing photocatalytic activity towards the degradation of MO pollutants under VLI.

The synthesis of GO-assisted silver halides has been achieved by various approaches, including a facile fabrication of GO-hybridized nanocomposite of Ag/AgBr/GO in a water/oil microemulsion [178] and Ag@AgCl/reduced GO (RGO) hybrids via a deposition-precipitation method [179], which both exhibited highly efficient photoactivities towards the photodegradation of organic pollutants under sunlight irradiation. The instability of silver oxide species photocatalysts manifests in the form of photocorrosion of the composites during

photocatalytic performances under VLI. This could be ascribed to the interstitial silver ions (Ag^+) combining with electrons in the absence of sacrificial reagents under VLI [180]. Therefore, metallic silver (Ag^0) as the reduced product of Ag^+ could block the active sites of photocatalysts and eventually decrease the photocatalytic activity [181]. For instance, Ag_3PO_4 [180], Ag_2O [153], Ag_2CO_3 [34], and Ag_3VO_4 [182] showed high photocatalytic activities towards the degradation of organic pollutants under VLI; however, photocorrosion occurred during the photocatalytic performance, decreasing visible-light-driven photocatalytic activity towards the degradation of organic pollutants. Hence, great efforts have been made to improve the stability of silver species in the application of the degradation of organic pollutants.

Scholars have made progress to improve the stability of Ag_3PO_4 by combining it with GO or RGO via electrostatic interactions [183] or by a simple precipitation method [8, 180]. The results indicated high photocatalytic performances for the degradation of organic components such as RhB, MB, and MO under VLI, suggesting that GO and RGO can be used as protective substrates that partially inhibit the photocorrosion of Ag_3PO_4. In addition, some GO-based visible-light-driven plasmonic photocatalysts such as Ag/Ag_3PO_4/GO nanostructure composites [184] and graphene oxide-loaded Ag_3PO_4@AgCl hybridized composites [185] have been investigated, demonstrating improved photocatalytic activities both in the degradation of organic pollutants and in water splitting.

Other silver species were also protected from photocorrison when applied to photocatalysis, including novel Ag_2O/GO nanocomposites [186], Ag_2CO_3 coupled with graphene-oxide composites (GO/Ag_2CO_3) [187], RGO-Ag_3VO_4 nanocomposites [188], Ag_3VO_4/TiO_2/graphene nanocomposites [51], from which GO may serve as an electron collector and a transporter to promote the separation of photoexcited electron-hole pairs, and to efficiently decrease the possibility of electron and hole recombination. An increase in visible light absorption and a corresponding improvement in photocatalytic activity under VLI were also observed.

2.5 Conclusions

In this chapter, features, prospects, and current challenges in photocatalysis were mentioned and highlighted in the background for the design of the undertaken projects.

General designs were provided and discussed to enhance photocatalytic efficiencies both in wastewater treatment and water splitting. Literature review pertinent to bismuth-based and silver-based visible-light-driven photocatalysts mainly for the photocatalytic degradation of organic pollutants was provided, with the goal of enhancing photocatalytic activity under VLI in the undertaken projects.

2.6 References

[1] A. Fujishima, K. Honda, Electrochemical photolysis of water at a semiconductor electrode, Nature 238 (1972) 37-38.

[2] S. Ghasemi, A. Esfandiar, S. Rahman Setayesh, A. Habibi-Yangjeh, A. Iraji zad, M.R. Gholami, Synthesis and characterization of TiO_2-graphene nanocomposites modified with noble metals as a photocatalyst for degradation of pollutants, Appl. Catal., A 462-463 (2013) 82-90.

[3] D.F. Ollis, C. Turchi, Heterogeneous photocatalysis for water purification: Contaminant mineralization kinetics and elementary reactor analysis, Environ. Prog. 9 (1990) 229-234.

[4] H. Changseok, A. Joel, C.P. Suresh, F. Rachel, F. Polycarpos, J.A. Byrne, S.M.D. Patrick, C. Hyeok, J. Wenjun, O.S. Kevin, D.D. Dionysios, Chapter green nanotechnology: Development of nanomaterials for environmental and energy applications, in, J. Am. Chem. Soc., 2013, pp. 201-229.

[5] D. Chatterjee, S. Dasgupta, Visible light induced photocatalytic degradation of organic pollutants, J. Photochem. Photobiol., C 6 (2005) 186-205.

[6] B.R. Das, UV radiation protective clothing, The open Text.J. 3 (2010) 14-21.

[7] D. Devilliers, Semiconductor photocatalysis: Still an active research area despite barriers to commercialization, Energeia (CAER-University of Kentucky Center for Applied Energy Research) 17 (2006) 1-3.

[8] Y. Ao, P. Wang, C. Wang, J. Hou, J. Qian, Preparation of graphene oxide-Ag_3PO_4 composite photocatalyst with high visible light photocatalytic activity, Appl. Surf. Sci. 271 (2013) 265-270.

[9] A. Kudo, Y. Miseki, Heterogeneous photocatalyst materials for water splitting, Chem. Soc. Rev. 38 (2009) 253-278.

[10] R. Konta, H. Kato, H. Kobayashi, A. Kudo, Photophysical properties and photocatalytic activities under visible light irradiation of silver vanadates, Phys. Chem. Chem. Phys. 5 (2003) 3061-3065.

[11] X. Tao, Q. Hong, T. Xu, F. Liao, Highly efficient photocatalytic performance of graphene-Ag_3VO_4 composites, J. Mater. Sci.-Mater. Electron. 25 (2014) 3480-3485.

[12] C. Dong, K.-L. Wu, X.-W. Wei, X.-Z. Li, L. Liu, T.-H. Ding, J. Wang, Y. Ye, Synthesis of graphene oxide-Ag_2CO_3 composites with improved photoactivity and anti-photocorrosion, CrystEngComm 16 (2014) 730-736.

[13] C. Belver, C. Adán, S. García-Rodríguez, M. Fernández-García, Photocatalytic behavior of silver vanadates: Microemulsion synthesis and post-reaction characterization, Chem. Eng. J. 224 (2013) 24-31.

[14] Q. Xiang, J. Yu, B. Cheng, H.C. Ong, Microwave-hydrothermal preparation and visible-light photoactivity of plasmonic photocatalyst Ag-TiO_2 nanocomposite hollow spheres, Chem. Asian J. 5 (2010) 1466-1474.

[15] B. Neppolian, H.C. Choi, S. Sakthivel, B. Arabindoo, V. Murugesan, Solar/UV-induced photocatalytic degradation of three commercial textile dyes, J. Hazard. Mater. 89 (2002) 303-317.

[16] D. Peng, Z. Min, X. Zhonglei, C. Lihong, Synthesis of the $ZnGa_2S_4$ nanocrystals and their visible-light photocatalytic degradation property, J. Nanomater. 2015 (2015) 7.

[17] J. Yan, G. Wu, N. Guan, L. Li, Z. Li, X. Cao, Understanding the effect of surface/bulk defects on the photocatalytic activity of TiO_2: Anatase versus rutile, Phys. Chem. Chem. Phys. 15 (2013) 10978-10988.

[18] Y. Zhou, K. Vuille, A. Heel, B. Probst, R. Kontic, G.R. Patzke, An inorganic hydrothermal route to photocatalytically active bismuth vanadate, Appl. Catal., A 375 (2010) 140-148.

[19] ASTM Standard C33, Specification for Concrete Aggregates (2003).

[20] R.J. Braham, A.T. Harris, Review of major design and scale-up considerations for solar photocatalytic reactors, Ind. Eng. Chem. Res. 48 (2009) 8890-8905.

[21] G.E. Imoberdorf, A.E. Cassano, H.A. Irazoqui, O.M. Alfano, Optimal design and modeling of annular photocatalytic wall reactors, Catal. Today 129 (2007) 118-126.

[22] M. Lim, V. Rudolph, M. Anpo, G.Q. Lu, Fluidized-bed photocatalytic degradation of airborne styrene, Catal. Today 131 (2008) 548-552.

[23] A. Walsh, S.-H. Wei, Y. Yan, M.M. Al-Jassim, J.A. Turner, M. Woodhouse, B.A. Parkinson, Structural, magnetic, and electronic properties of the Co-Fe-Al oxide spinel system: Density-functional theory calculations, Phys. Rev. B 76 (2007) 165119.

[24] M. Woodhouse, G.S. Herman, B.A. Parkinson, Combinatorial approach to identification of catalysts for the photoelectrolysis of water, Chem. Mater. 17 (2005) 4318-4324.

[25] A. Kudo, K. Ueda, H. Kato, I. Mikami, Photocatalytic O_2 evolution under visible light irradiation on $BiVO_4$ in aqueous $AgNO_3$ solution, Catal. Lett. 53 (1998) 229-230.

[26] A. Kudo, S. Hijii, H_2 or O_2 evolution from aqueous solutions on layered oxide photocatalysts consisting of Bi^{3+} with $6s^2$ configuration and d^0 transition metal ions, Chem. Lett. (1999) 1103-1104.

[27] Y. Shimodaira, H. Kato, H. Kobayashi, A. Kudo, Photophysical properties and photocatalytic activities of bismuth molybdates under visible light irradiation, J. Phys. Chem. B 110 (2006) 17790-17797.

[28] X. Hu, C. Hu, Preparation and visible-light photocatalytic activity of Ag_3VO_4 powders, J. Solid State Chem. 180 (2007) 725-732.

[29] H. Kato, H. Kobayashi, A. Kudo, Role of Ag^+ in the band structures and photocatalytic properties of $AgMO_3$ (M: Ta and Nb) with the perovskite structure, J. Phys. Chem. B 106 (2002) 12441-12447.

[30] J. Wang, X. Yang, J. Chen, J. Xian, S. Meng, Y. Zheng, Y. Shao, D. Li, Photocatalytic activity of novel $Ag_4V_2O_7$ photocatalyst under visible light irradiation, J. Am. Ceram. Soc. 97 (2014) 267-274.

[31] S. Zhang, W. Li, C. Li, J. Chen, Synthesis, characterization, and electrochemical properties of $Ag_2V_4O_{11}$ and $AgVO_3$ 1-D nano/microstructures, J. Phys. Chem. B 110 (2006) 24855-24863.

[32] Y. Maruyama, H. Irie, K. Hashimoto, Visible light sensitive photocatalyst, delafossite structured α-$AgGaO_2$, J. Phys. Chem. B 110 (2006) 23274-23278.

[33] S. Ouyang, N. Kikugawa, D. Chen, Z. Zou, J. Ye, A systematical study on photocatalytic properties of $AgMO_2$ (M = Al, Ga, In): Effects of chemical compositions, crystal structures, and electronic structures, J. Phys. Chem. C 113 (2009) 1560-1566.

[34] G. Dai, J. Yu, G. Liu, A new approach for photocorrosion inhibition of Ag_2CO_3 photocatalyst with highly visible-light-responsive reactivity, J. Phys. Chem. C 116 (2012) 15519-15524.

[35] Y. Bi, H. Hu, S. Ouyang, G. Lu, J. Cao, J. Ye, Photocatalytic and photoelectric properties of cubic Ag_3PO_4 sub-microcrystals with sharp corners and edges, Chem. Commun. 48 (2012) 3748-3750.

[36] Y. Hosogi, K. Tanabe, H. Kato, H. Kobayashi, A. Kudo, Energy structure and photocatalytic activity of niobates and tantalates containing Sn(II) with a $5s^2$ electron configuration, Chem. Lett. 33 (2004) 28-29.

[37] A. Walsh, Y. Yan, M.N. Huda, M.M. Al-Jassim, S.-H. Wei, Band edge electronic structure of $BiVO_4$: Elucidating the role of the Bi s and V d orbitals, Chem. Mater. 21 (2009) 547-551.

[38] S. Murugesan, M.N. Huda, Y. Yan, M.M. Al-Jassim, V. Subramanian, Band-engineered bismuth titanate pyrochlores for visible light photocatalysis, J. Phys. Chem. C 114 (2010) 10598-10605.

[39] M. Nishikawa, S. Hiura, Y. Mitani, Y. Nosaka, Enhanced photocatalytic activity of $BiVO_4$ by co-grafting of metal ions and combining with $CuBi_2O_4$, J. Photochem. Photobiol., A 262 (2013) 52-56.

[40] M. Zhang, C. Shao, X. Li, P. Zhang, Y. Sun, C. Su, X. Zhang, J. Ren, Y. Liu, Carbon-modified $BiVO_4$ microtubes embedded with Ag nanoparticles have high photocatalytic activity under visible light, Nanoscale 4 (2012) 7501-7508.

[41] M.L. Guan, D.K. Ma, S.W. Hu, Y.J. Chen, S.M. Huang, From hollow olive-shaped $BiVO_4$ to n-p core-shell $BiVO_4@Bi_2O_3$ microspheres: Controlled synthesis and enhanced visible-light-responsive photocatalytic properties, Inorg. Chem. 50 (2011) 800-805.

[42] B. Yao, M. Liu, Z. Ma, C. Wang, Synthesis and characterization of hollow core-shell $ZrO_2@void@BiVO_4$ visible-light photocatalyst, Adv. Mater.Res. 148-149 (2011) 1331-1338.

[43] J. Suo, L. Liu, F. Yang, Preparation of supported Cu-$BiVO_4$ photocatalyst and its application in oxidative removal of toluene in air, Chin. J. Catal. 30 (2009) 323-327.

[44] B. Zhou, X. Zhao, H. Liu, J. Qu, C.P. Huang, Visible-light sensitive cobalt-doped $BiVO_4$ (Co-$BiVO_4$) photocatalytic composites for the degradation of methylene blue dye in dilute aqueous solutions, Appl. Catal., B 99 (2010) 214-221.

[45] B. Zhou, X. Zhao, H. Liu, J. Qu, C.P. Huang, Synthesis of visible-light sensitive M-$BiVO_4$ (M=Ag, Co, and Ni) for the photocatalytic degradation of organic pollutants, Sep. Purif. Technol. 77 (2011) 275-282.

[46] L. Ge, Synthesis and characterization of novel visible-light-driven Pd/$BiVO_4$ composite photocatalysts, Mater. Lett. 62 (2008) 926-928.

[47] L. Ge, Preparation and characterization of novel visible light sensitive Pt/$BiVO_4$ photocatalysts, J. Inorg. Mater. 23 (2008) 449-453.

[48] A. Zhang, J. Zhang, Characterization and photocatalytic properties of Au/$BiVO_4$ composites, J. Alloys Compd. 491 (2010) 631-635.

[49] M. Wang, Q. Liu, Y. Che, L. Zhang, D. Zhang, Characterization and photocatalytic properties of N-doped $BiVO_4$ synthesized via a sol-gel method, J. Alloys Compd. 548 (2013) 70-76.

[50] H. Jiang, H. Dai, J. Deng, Y. Liu, L. Zhang, K. Ji, Porous F-doped $BiVO_4$: Synthesis and enhanced photocatalytic performance for the degradation of phenol under visible-light illumination, Solid State Sci. 17 (2013) 21-27.

[51] M. Wang, H. Zheng, Q. Liu, C. Niu, Y. Che, M. Dang, High performance B doped $BiVO_4$ photocatalyst with visible light response by citric acid complex method, Spectrochim. Acta, Part A 114 (2013) 74-79.

[52] S. Sun, W. Wang, L. Zhou, H. Xu, Efficient methylene blue removal over hydrothermally synthesized starlike $BiVO_4$, Ind. Eng. Chem. Res. 48 (2009) 1735-1739.

[53] G. Tan, L. Zhang, H. Ren, S. Wei, J. Huang, A. Xia, Effects of pH on the hierarchical structures and photocatalytic performance of $BiVO_4$ powders prepared via the microwave hydrothermal method, ACS Appl. Mater. Interfaces 5 (2013) 5186-5193.

[54] H. Li, G. Liu, X. Duan, Monoclinic $BiVO_4$ with regular morphologies: Hydrothermal synthesis, characterization and photocatalytic properties, Mater. Chem. Phys. 115 (2009) 9-13.

[55] Q. Zhu, W.S. Wang, L. Lin, G.Q. Gao, H.L. Guo, H. Du, A.W. Xu, Facile synthesis of the novel Ag_3VO_4/AgBr/Ag plasmonic photocatalyst with enhanced photocatalytic activity and stability, J. Phys. Chem. C 117 (2013) 5894-5900.

[56] L. Zhang, Y. He, P. Ye, Y. Wu, T. Wu, Visible light photocatalytic activities of $ZnFe_2O_4$ loaded by Ag_3VO_4 heterojunction composites, J. Alloys Compd. 549 (2013) 105-113.

[57] G. Wang, Y. Ren, G.J. Zhou, J.P. Wang, H.F. Cheng, Z.Y. Wang, J. Zhan, B.B. Huang, M.H. Jiang, Synthesis of highly efficient visible light $Ag@Ag_3VO_4$ plasmonic photocatalysts, Surf. Coat. Technol. 228, Supplement 1 (2013) S283-S286.

[58] H. Xu, H. Li, C. Wu, J. Chu, Y. Yan, H. Shu, Preparation, characterization and photocatalytic activity of transition metal-loaded $BiVO_4$, Mater. Sci. Eng., B 147 (2008) 52-56.

[59] M. Shang, W. Wang, L. Zhou, S. Sun, W. Yin, Nanosized $BiVO_4$ with high visible-light-induced photocatalytic activity: Ultrasonic-assisted synthesis and protective effect of surfactant, J. Hazard. Mater. 172 (2009) 338-344.

[60] D.R. Dreyer, S. Park, C.W. Bielawski, R.S. Ruoff, The chemistry of graphene oxide, Chem. Soc. Rev. 39 (2010) 228-240.

[61] V. Singh, D. Joung, L. Zhai, S. Das, S.I. Khondaker, S. Seal, Graphene based materials: Past, present and future, Prog. Mater Sci. 56 (2011) 1178-1271.

[62] Y. Fu, X. Sun, X. Wanga, $BiVO_4$-graphene catalyst and its high photocatalytic performance under visible light irradiation, Mater. Chem. Phys. 131 (2011) 325-330.

[63] Y.H. Ng, A. Iwase, A. Kudo, R. Amal, Reducing graphene oxide on a visible-light $BiVO_4$ photocatalyst for an enhanced photoelectrochemical water splitting, J. Phys. Chem. Lett. 1 (2010) 2607-2612.

[64] Y. Zhang, X. Su, G. Hou, S. Bi, F. Guo, Z. Mei, Characterization and photocatalytic properties of porous $BiVO_4$-SiO_2 composites, in: Adv. Mater. Res., 2011, pp. 1267-1271.

[65] L.J. Ci, S.Y. Zhang, Y.J. Zhang, Preparation and optical properties of $BiVO_4/SiO_2$ composite, Rengong Jingti Xuebao/Journal of Synthetic Crystals 39 (2010) 797-801.

[66] B. Yao, M. Liu, Z. Ma, C. Wang, Synthesis and characterization of hollow core-shell ZrO_2@void@$BiVO_4$ visible-light photocatalyst, in: Adv. Mater. Res., 2011, pp. 1331-1338.

[67] M.-L. Guan, D.-K. Ma, S.-W. Hu, Y.-J. Chen, S.-M. Huang, From hollow olive-shaped $BiVO_4$ to n-p core-shell $BiVO_4$@Bi_2O_3 microspheres: Controlled synthesis and enhanced visible-light-responsive photocatalytic properties, Inorg. Chem. 50 (2010) 800-805.

[68] Q. Xiang, J. Yu, M. Jaroniec, Graphene-based semiconductor photocatalysts, Chem. Soc. Rev. 41 (2012) 782-796.

[69] A. Kudo, Photocatalyst materials for water splitting, Catal. Surv. Asia 7 (2003) 31-38.

[70] F. Chen, J. Zhao, H. Hidaka, Highly selective deethylation of rhodamine B: Adsorption and photooxidation pathways of the dye on the TiO_2/SiO_2 composite photocatalyst, Int. J. Photoenergy 5 (2003) 209-217.

[71] J. Yang , D. Wang , X. Zhou, C. Li, A theoretical study on the mechanism of photocatalytic oxygen evolution on $BiVO_4$ in aqueous solution, Chem. Eur. J. 19 (2013) 1320-1326.

[72] P. Mack, Dissolved oxygen and the three S's, River Monitoring Program (2003).

[73] W. Ranke, Y. Joseph, Determination of adsorption energies and kinetic parameters by isosteric methods, Phys. Chem. Chem. Phys. 4 (2002) 2483-2498.

[74] Z. He, C. Sun, S. Yang, Y. Ding, H. He, Z. Wang, Photocatalytic degradation of rhodamine B by Bi_2WO_6 with electron accepting agent under microwave irradiation: Mechanism and pathway, J. Hazard. Mater. 162 (2009) 1477-1486.

[75] L. Ferrari, J. Kaufmann, F. Winnefeld, J. Plank, Interaction of cement model systems with superplasticizers investigated by atomic force microscopy, zeta potential, and adsorption measurements, J. Colloid Interface Sci. 347 (2010) 15-24.

[76] S. Ghosh-Mukerji, H. Haick, Y. Paz, Controlled mass transport as a means for obtaining selective photocatalysis, J. Photochem. Photobiol., A 160 (2003) 77-85.

[77] C.-T. Hsieh, W.-S. Fan, W.-Y. Chen, J.-Y. Lin, Adsorption and visible-light-derived photocatalytic kinetics of organic dye on Co-doped titania nanotubes prepared by hydrothermal synthesis, Sep. Purif. Technol. 67 (2009) 312-318.

[78] O. Deutschmann, H. Knözinger, K. Kochloefl, T. Turek, Heterogeneous catalysis and solid catalysts, 1. Fundamentals, in: Ullmann's Encyclopedia Ind. Chem., Wiley-VCH Verlag GmbH & Co. KGaA, 2000.

[79] M. Oshikiri, M. Boero, Water molecule adsorption properties on the $BiVU_4$ (100) surface, J. Phys. Chem. B 110 (2006) 9188-9194.

[80] A. Walsh, G.W. Watson, D.J. Payne, R.G. Edgell, J. Guo, P.-A. Glans, T. Learmonth, K.E. Smith, Electronic structure of the α and δ phases of Bi_2O_3: A combined ab initio and X-ray spectroscopy study, Phys. Rev. B 73 (2006) 235104.

[81] A. Kudo, K. Omori, H. Kato, A novel aqueous process for preparation of crystal form-controlled and highly crystalline $BiVO_4$ powder from layered vanadates at room temperature and its photocatalytic and photophysical properties, J. Am. Chem. Soc. 121 (1999) 11459-11467.

[82] M. Long, W. Cai, J. Cai, B. Zhou, X. Chai, Y. Wu, Efficient photocatalytic degradation of phenol over $Co_3O_4/BiVO_4$ composite under visible light irradiation, J. Phys. Chem. B 110 (2006) 20211-20216.

[83] M.R. Dolgos, A.M. Paraskos, M.W. Stoltzfus, S.C. Yarnell, P.M. Woodward, The electronic structures of vanadate salts: Cation substitution as a tool for band gap manipulation, J. Solid State Chem. 182 (2009) 1964-1971.

[84] G. Trimarchi, H. Peng, J. Im, A.J. Freeman, V. Cloet, A. Raw, K.R. Poeppelmeier, K. Biswas, S. Lany, A. Zunger, Using design principles to systematically plan the synthesis of hole-conducting transparent oxides: Cu_3VO_4 and Ag_3VO_4 as a case study, Phys. Rev. B: Condens. Matter 84 (2011).

[85] J. Zhao, C. Chen, W. Ma, Photocatalytic Degradation of Organic Pollutants Under Visible Light Irradiation, Top Catal 35 (2005) 269-278.

[86] I.C. Vinke, J. Diepgrond, B.A. Boukamp, K.J. Vries de, A.J. Burggraaf, Bulk and electrochemical properties of $BiVO_4$, Solid State Ionics 57 (1992) 83-89.

[87] T.P. Thao, H.-C. Kao, R.-S. Juang, J.C.-W. Lan, Kinetic characteristics of biodegradation of methyl orange by pseudomonas putida mt_2 in suspended and immobilized cell systems, J. Taiwan Inst. Chem. Eng. 44 (2013) 780-785.

[88] S. Chakrabarti, B.K. Dutta, Photocatalytic degradation of model textile dyes in wastewater using ZnO as semiconductor catalyst, J. Hazard. Mater. 112 (2004) 269-278.

[89] S. Lathasree, A.N. Rao, B. SivaSankar, V. Sadasivam, K. Rengaraj, Heterogeneous photocatalytic mineralisation of phenols in aqueous solutions, J. Mol. Catal. A: Chem. 223 (2004) 101-105.

[90] A.R. Amani-Ghadim, A. Olad, S. Aber, H. Ashassi-Sorkhabi, Comparison of organic dyes removal mechanism in electrocoagulation process using iron and aluminum anodes, Environ. Prog. Sustainable Energy 32 (2013) 547-556.

[91] H.T. Chang, N.-M. Wu, F. Zhu, A kinetic model for photocatalytic degradation of organic contaminants in a thin-film TiO_2 catalyst, Water. Res. 34 (2000) 407-416.

[92] N. Serpone, A.V. Emeline, Suggested terms and definitions in photocatalysis and radiocatalysis, Int. J. Photoenergy 4 (2002) 91-131.

[93] P.D. Eufinger K., H. Poelman, D. Gryse R., G.B. Marin, TiO_2 thin films for photocatalytic applications, Thin Solid Films: Process & Appl. (2008) 189-227.

[94] H.-q. Jiang, H. Endo, H. Natori, M. Nagai, K. Kobayashi, Fabrication and photoactivities of spherical-shaped $BiVO_4$ photocatalysts through solution combustion synthesis method, J. Eur. Ceram. Soc. 28 (2008) 2955-2962.

[95] L. Zhou, W. Wang, S. Liu, L. Zhang, H. Xu, W. Zhu, A sonochemical route to visible-light-driven high-activity $BiVO_4$ photocatalyst, J. Mol. Catal. A: Chem. 252 (2006) 120-124.

[96] W.S. Nam, G.Y. Han, A photocatalytic performance of TiO_2 photocatalyst prepared by the hydrothermal method, Korean J. Chem. Eng. 20 (2003) 180-184.

[97] J. Ovenstone, Preparation of novel titania photocatalysts with high activity, J. Mater. Sci. 36 (2001) 1325-1329.

[98] W.J. Dawson, Hydrothermal synthesis of advanced ceramic powders, Am. Ceram. Soc. Bull. 67 (1988) 1673-1678.

[99] M.R.B. Leszek Czepirski, Ewa Komorowska-Czepirska, Some generalization of Langmuir adsorption isotherm, Inernet J. Chem. 3 (2000).

[100] K.V. Kumar, K. Porkodi, F. Rocha, Langmuir–Hinshelwood kinetics–A theoretical study, Catal. Commun. 9 (2008) 82-84.

[101] J.M. Herrmann, Heterogeneous photocatalysis: Fundamentals and applications to the removal of various types of aqueous pollutants, Catal. Today 53 (1999) 115-129.

[102] L.-W. Zhang, Y.-J. Wang, H.-Y. Cheng, W.-Q. Yao, Y.-F. Zhu, Synthesis of porous Bi_2WO_6 thin films as efficient visible-light-active photocatalysts, Adv. Mater. 21 (2009) 1286-1290.

[103] K. Sayama, A. Nomura, T. Arai, T. Sugita, R. Abe, M. Yanagida, T. Oi, Y. Iwasaki, Y. Abe, H. Sugihara, Photoelectrochemical decomposition of water into H_2 and O_2 on porous $BiVO_4$ thin-film electrodes under visible light and significant effect of Ag ion treatment, J. Phys. Chem. B 110 (2006) 11352-11360.

[104] X. Lin, T. Huang, F. Huang, W. Wang, J. Shi, Photocatalytic activity of a Bi-Based oxychloride Bi_3O_4Cl, J. Phys. Chem. B 110 (2006) 24629-24634.

[105] X. Lin, F. Huang, W. Wang, Z. Shan, J. Shi, Methyl orange degradation over a novel Bi-based photocatalyst Bi_3SbO_7: Correlation of crystal structure to photocatalytic activity, Dyes Pigm. 78 (2008) 39-47.

[106] W. Luo, J. Tang, Z. Zou, J. Ye, Preparation and photophysical properties of some oxides in Ca-Bi-O system, J. Alloys Compd. 455 (2008) 346-352.

[107] C.M. Huang, G.T. Pan, L.C. Chen, T.C.K. Yang, W.S. Chang, Effects of synthesis conditions on the crystalline phases and photocatalytic activities of silver vanadates via hydrothermal method, in: Mater. Res. Soc. Symp. Proc., San Francisco, CA; United States, 2009, pp. 13-18.

[108] J. Xu, C. Hu, Y. Xi, B. Wan, C. Zhang, Y. Zhang, Synthesis and visible light photocatalytic activity of β-$AgVO_3$ nanowires, Solid State Sci. 14 (2012) 535-539.

[109] J. Tang, Z. Zou, J. Ye, Efficient photocatalytic decomposition of organic contaminants over $CaBi_2O_4$ under visible-light irradiation, Angew. Chem. Int. Ed. 43 (2004) 4463-4466.

[110] L. Zhang, D. Chen, X. Jiao, Monoclinic structured $BiVO_4$ nanosheets: Hydrothermal preparation, formation mechanism, and coloristic and photocatalytic properties, J. Phys. Chem. B 110 (2006) 2668-2673.

[111] Y. Zhao, Y. Xie, X. Zhu, S. Yan, S. Wang, Surfactant-free synthesis of hyperbranched monoclinic bismuth vanadate and its applications in photocatalysis, gas sensing, and lithium-ion batteries, Chem. Eur. J. 14 (2008) 1601-1606.

[112] Y. Zhang, H. Ding, F. Liu, S. Wei, S. Liu, D. He, F. Xiao, Synthesis of nanosized Ag_3VO_4 particles and their photocatalytic activity for degradation of rhodamine B under visible light, Chin. J. Catal. 29 (2008) 783-787.

[113] L. Zhang, Y. Zhu, A review of controllable synthesis and enhancement of performances of bismuth tungstate visible-light-driven photocatalysts, Catal. Sci. Technol. 2 (2012) 694-706.

[114] H. Fu, C. Pan, W. Yao, Y. Zhu, Visible-light-induced degradation of rhodamine B by nanosized Bi_2WO_6, J. Phys. Chem. B 109 (2005) 22432-22439.

[115] L. Ren, L. Jin, J.B. Wang, F. Yang, M.Q. Qiu, Y. Yu, Template-free synthesis of $BiVO_4$ nanostructures: I. Nanotubes with hexagonal cross sections by oriented attachment and their photocatalytic property for water splitting under visible light, Nanotechnol. 20 (2009) 115603.

[116] K. Shantha, K.B.R. Varma, Preparation and characterization of nanocrystalline powders of bismuth vanadate, Mater. Sci. Eng., B 60 (1999) 66-75.

[117] J.D. Bierlein, A.W. Sleight, Ferroelasticity in $BiVO_4$, Solid State Commun. 16 (1975) 69-70.

[118] A.R. Lim, S.Y. Jeong, Ferroelastic phase transition of $BiVO_4$ single crystals with prominent W-domain walls by stress-strain hysteresis measurements, J. Intell. Mater. Syst. Struct. 21 (2010) 915-920.

[119] W.I.F. David, Ferroelastic phase transition in $BiVO_4$: III. Thermodynamics, J. Phys. C: Solid State Phys. 16 (1983) 5093-5118.

[120] C. Manolikas, S. Amelinckx, Ferroelastic domains in $BiVO_4$, Phys. Status Solidi A 60 (1980) 167-172.

[121] P.R. Bodart, Y. Dumazy, J.P. Amoureux, C. Fernandez, Orientation of electric field gradient and chemical shift tensors in $BiVO_4$ at room temperature by 51V NMR, Magn. Reson. Chem. 37 (1999) 223-226.

[122] T.H. Yeom, C. Rudowicz, S.H. Choh, D.G. McGavin, Monoclinic spin hamiltonian analysis of EPR spectra of Mn^{2+} in $BiVO_4$ single crystals, Phys. Status Solidi B 198 (1996) 839-851.

[123] S. Tokunaga, H. Kato, A. Kudo, Selective preparation of monoclinic and tetragonal $BiVO_4$ with scheelite structure and their photocatalytic properties, Chem. Mater. 13 (2001) 4624-4628.

[124] A.R. Lim, S.H. Choh, J. Min Su, Prominent ferroelastic domain walls in $BiVO_4$ crystal, J. Phys. Condens. Matter 7 (1995) 7309-7323.

[125] L. Zhou, W. Wang, L. Zhang, H. Xu, W. Zhu, Single-crystalline $BiVO_4$ microtubes with square cross-sections: Microstructure, growth mechanism, and photocatalytic property, J. Phys. Chem. C 111 (2007) 13659-13664.

[126] W.E. Morgan, W.J. Stec, J.R. Van Wazer, Inner-orbital binding-energy shifts of antimony and bismuth compounds, Inorg. Chem. 12 (1973) 953-955.

[127] N.A. Dhas, K.S. Suslick, Sonochemical preparation of hollow nanospheres and hollow nanocrystals, J. Am. Chem. Soc. 127 (2005) 2368-2369.

[128] C. Li, G. Pang, S. Sun, S. Feng, Phase transition of $BiVO_4$ nanoparticles in molten salt and the enhancement of visible-light photocatalytic activity, J. Nanopart. Res. 12 (2010) 3069-3075.

[129] L. Zhang, J. Long, W. Pan, S. Zhou, J. Zhu, Y. Zhao, X. Wang, G. Cao, Efficient removal of methylene blue over composite-phase $BiVO_4$ fabricated by hydrothermal control synthesis, Mater. Chem. Phys. 136 (2012) 897-902.

[130] D. Ke, T. Peng, L. Ma, P. Cai, K. Dai, Effects of hydrothermal temperature on the microstructures of $BiVO_4$ and its photocatalytic O_2 evolution activity under visible light, Inorg. Chem. 48 (2009) 4685-4691.

[131] T. Yang, D. Xia, Self-assembly of highly crystalline spherical $BiVO_4$ in aqueous solutions, J. Cryst. Growth 311 (2009) 4505-4509.

[132] J.B. Liu, H. Wang, H.M. Zhang, W.X. Zhang, H. Yan, Preparation of oriented $BiVO_4$ thin film by chemical bath deposition, J. Phys. Chem. B 23 (2007) 1299-1302.

[133] M.C. Neves, T. Trindade, Chemical bath deposition of $BiVO_4$, Thin Solid Films 406 (2002) 93-97.

[134] A. Galembeck, O.L. Alves, $BiVO_4$ thin film preparation by metalorganic decomposition, Thin Solid Films 365 (2000) 90-93.

[135] U.M. García-Pérez, S. Sepúlveda-Guzmán, A. Martínez-De La Cruz, Nanostructured $BiVO_4$ photocatalysts synthesized via a polymer-assisted coprecipitation method and their photocatalytic properties under visible-light irradiation, Solid State Sci. 14 (2012) 293-298.

[136] Q. Chen, M. Zhou, D. Ma, D. Jing, Effect of preparation parameters on photoactivity of $BiVO_4$ by hydrothermal method, J. Nanomater 2012 (2012).

[137] F. Rullens, A. Laschewsky, M. Devillers, Bulk and thin films of bismuth vanadates prepared from hybrid materials made from an organic polymer and inorganic salts, Chem. Mater. 18 (2006) 771-777.

[138] S. Obregón, A. Caballero, G. Colón, Hydrothermal synthesis of $BiVO_4$: Structural and morphological influence on the photocatalytic activity, Appl. Catal., B 117-118 (2012) 59-66.

[139] A. Kudo, K. Omori, H. Kato, A novel aqueous process for preparation of crystal form-controlled and highly crystalline $BiVO_4$ powder from layered vanadates at room temperature and its photocatalytic and photophysical properties, J. Am. Chem. Soc. 121 (1999) 11459-11467.

[140] L. Sui, L. Yu, Y. Zhang, Surface and catalytic properties of K/V Catalysts coating on porous Al_2O_3 substrate, J. Dispersion Sci. Technol. 28 (2007) 285-289.

[141] A.D. Kelmers, Compounds in the system $KVO_3 \cdot V_2O_5$, J. Inorg. Nucl. Chem. 23 (1961) 279-283.

[142] M. Trypuć, Z. Torski, U. Kiełkowska, Experimental determination of the optimum conditions of KVO_3 synthesis based on KCl and V_2O_5 in the presence of steam, Ind. Eng. Chem. Res. 40 (2001) 1022-1025.

[143] J. Liu, H. Wang, S. Wang, H. Yan, Hydrothermal preparation of $BiVO_4$ powders, Mater. Sci. Eng., B 104 (2003) 36-39.

[144] M.C. Neves, T. Trindade, Preparation of hollow shells of zinc oxide/bismuth (III) vanadate, Mater. Res. Bull. 38 (2003) 1013-1020.

[145] D.K. Lee, I.-S. Cho, S. Lee, S.-T. Bae, J.H. Noh, D.W. Kim, K.S. Hong, Effects of carbon content on the photocatalytic activity of $C/BiVO_4$ composites under visible light irradiation, Mater. Chem. Phys. 119 (2010) 106-111.

[146] A.P. Zhang, J.Z. Zhang, Synthesis and activities of ln-doped $BiVO_4$ (Ln = Eu, Gd and Er) photocatalysts, Chin.J. Inorg. Chem. 25 (2009) 2040-2047.

[147] A. Kubacka, M. Fernández-García, G. Colón, Advanced nanoarchitectures for solar photocatalytic applications, Chem. Rev. 112 (2011) 1555-1614.

[148] R.S. Saxena, O.P. Sharma, Potentiometric determination of vanadium as silver orthovanadate, Talanta 11 (1964) 863-866.

[149] T. Hirono, H. Koizumi, T. Yamada, T. Nishi, Photoinduced effect on the phase transition in Ag_3VO_4 thin films, Thin Solid Films 149 (1987) L85-L88.

[150] K.S. Raju, M.K. Pour Seydei, S.A. Suthanthiraraj, Bonding characteristics in silver vanadate: an XPS study, Mater. Lett. 19 (1994) 65-68.

[151] S. Kittaka, S. Nishida, T. Ohtani, Mechanochemical reactions between Ag_2O and V_2O_5 to form crystalline silver vanadates, J. Solid State Chem. 169 (2002) 139-142.

[152] C.-M. Huang, G.-T. Pan, Y.-C.M. Li, M.-H. Li, T.C.K. Yang, Crystalline phases and photocatalytic activities of hydrothermal synthesis Ag_3VO_4 and $Ag_4V_2O_7$ under visible light irradiation, Appl. Catal., A 358 (2009) 164-172.

[153] W. Jiang, X. Wang, Z. Wu, X. Yue, S. Yuan, H. Lu, B. Liang, Silver oxide as superb and stable photocatalyst under visible and near-infrared light irradiation and its photocatalytic mechanism, Ind. Eng. Chem. Res. 54 (2015) 832-841.

[154] X. Lin, J. Xing, W. Wang, Z. Shan, F. Xu, F. Huang, Photocatalytic activities of heterojunction semiconductors $Bi_2O_3/BaTiO_3$: A strategy for the design of efficient combined photocatalysts, J. Phys. Chem. C 111 (2007) 18288-18293.

[155] H. Xu, H. Li, L. Xu, C. Wu, G. Sun, Y. Xu, J. Chu, Enhanced photocatalytic activity of Ag_3VO_4 loaded with rare-earth elements under visible-light irradiation, Ind. Eng. Chem. Res. 48 (2009) 10771-10778.

[156] G. Sun, H. Xu, H. Li, H. Shu, C. Liu, Q. Zhang, Fabrication and characterization of visible-lightinduced photocatalyst Gd_2O_3/Ag_3VO_4, React. Kinet. Mech.Catal. 99 (2010) 471-484.

[157] L. Ren, Y.-P. Zeng, D. Jiang, The improved photocatalytic properties of P-type NiO loaded porous TiO_2 sheets prepared via freeze tape-casting, Solid State Sci. 12 (2010) 138-143.

[158] H. Xu, H. Li, G. Sun, J. Xia, C. Wu, Z. Ye, Q. Zhang, Photocatalytic activity of La_2O_3-modified silver vanadates catalyst for rhodamine B dye degradation under visible light irradiation, Chem. Eng. J. 160 (2010) 33-41.

[159] X. Hu, C. Hu, Selective photocatalytic degradation of azodyes in NiO/Ag_3VO_4 suspension, J. Chem. Technol. Biotechnol. 85 (2010) 1522-1527.

[160] L. Zhang, Y. He, P. Ye, W. Qin, Y. Wu, T. Wu, Enhanced photodegradation activity of rhodamine B by Co_3O_4/Ag_3VO_4 under visible light irriadiation, Mater. Sci. Eng., B 178 (2013) 45-52.

[161] Y. Sang, L. Kuai, C. Chen, Z. Fang, B. Geng, Fabrication of a visible-light-driven plasmonic photocatalyst of $AgVO_3$@AgBr@Ag nanobelt heterostructures, ACS Appl. Mater. Interfaces 6 (2014) 5061-5068.

[162] S. Chowdhury, R. Balasubramanian, Recent advances in the use of graphene-family nanoadsorbents for removal of toxic pollutants from wastewater, Adv. Colloid Interface Sci. 204 (2014) 35-56.

[163] A. Lerf, H. He, M. Forster, J. Klinowski, Structure of graphite oxide revisited, J. Phys. Chem. B 102 (1998) 4477-4482.

[164] D. Krishnan, F. Kim, J. Luo, R. Cruz-Silva, L.J. Cote, H.D. Jang, J. Huang, Energetic graphene oxide: Challenges and opportunities, Nano Today 7 (2012) 137-152.

[165] G. Eda, M. Chhowalla, Chemically derived graphene oxide: Towards large-area thin-film electronics and optoelectronics, Adv. Mater. 22 (2010) 2392-2415.

[166] P. Steurer, R. Wissert, R. Thomann, R. Mülhaupt, Functionalized graphenes and thermoplastic nanocomposites based upon expanded graphite oxide, Macromol. Rapid Commun. 30 (2009) 316-327.

[167] J. Zhao, W. Ren, H.M. Cheng, Graphene sponge for efficient and repeatable adsorption and desorption of water contaminations, J. Mater. Chem. 22 (2012) 20197-20202.

[168] Y.H. Ng, A. Iwase, N.J. Bell, A. Kudo, R. Amal, Semiconductor/reduced graphene oxide nanocomposites derived from photocatalytic reactions, Catal. Today 164 (2011) 353-357.

[169] G. Dai, J. Liu, S. Liu, Y. Liang, X. Huang, Fabrication of rodlike $BiVO_4$/graphene oxide photocatalyst with highly visible-light photocatalytic activity, Kuei Suan Jen Hsueh Pao/Journal of the Chinese Ceramic Society 40 (2012) 1456-1460.

[170] Y. Yan, S. Sun, Y. Song, X. Yan, W. Guan, X. Liu, W. Shi, Microwave-assisted in situ synthesis of reduced graphene oxide-$BiVO_4$ composite photocatalysts and their enhanced photocatalytic performance for the degradation of ciprofloxacin, J. Hazard. Mater. 250-251 (2013) 106-114.

[171] E. Gao, W. Wang, M. Shang, J. Xu, Synthesis and enhanced photocatalytic performance of graphene-Bi_2WO_6 composite, Phys. Chem. Chem. Phys. 13 (2011) 2887-2893.

[172] Z. Sun, J. Guo, S. Zhu, L. Mao, J. Ma, D. Zhang, A high-performance Bi_2WO_6-graphene photocatalyst for visible light-induced H_2 and O_2 generation, Nanoscale 6 (2014) 2186-2193.

[173] J. Zhang, Z.H. Huang, Y. Xu, F. Kang, Hydrothermal synthesis of graphene/Bi_2WO_6 composite with high adsorptivity and photoactivity for Azo dyes, J. Am. Ceram. Soc. 96 (2013) 1562-1569.

[174] T. Xiong, F. Dong, Y. Zhou, M. Fu, W.-K. Ho, New insights into how RGO influences the photocatalytic performance of $BiOIO_3$/RGO nanocomposites under visible and UV irradiation, J. Colloid Interface Sci. 447 (2015) 16-24.

[175] A. Sun, C. Song, F. Jiang, H. Chen, Hydrothermal preparation and visible light photocatalytic activity of $Bi_{25}FeO_{40}$-graphene nanocomposite, in: ICMREE 2013, 2013, pp. 658-661.

[176] H. Lv, X. Shen, Z. Ji, D. Qiu, G. Zhu, Y. Bi, Synthesis of graphene oxide-$BiPO_4$ composites with enhanced photocatalytic properties, Appl. Surf. Sci. 284 (2013) 308-314.

[177] M. Zhu, P. Chen, M. Liu, Graphene oxide enwrapped Ag/AgX (X = Br, Cl) nanocomposite as a highly efficient visible-light plasmonic photocatalyst, ACS Nano 5 (2011) 4529-4536.

[178] M. Zhu, P. Chen, M. Liu, Ag/AgBr/Graphene oxide nanocomposite synthesized via oil/water and water/oil microemulsions: A comparison of sunlight energized plasmonic photocatalytic activity, Langmuir 28 (2012) 3385-3390.

[179] H. Zhang, X. Fan, X. Quan, S. Chen, H. Yu, Graphene sheets grafted Ag@AgCl hybrid with enhanced plasmonic photocatalytic activity under visible light, Environ. Sci. Technol. 45 (2011) 5731-5736.

[180] P. Dong, Y. Wang, B. Cao, S. Xin, L. Guo, J. Zhang, F. Li, Ag_3PO_4/reduced graphite oxide sheets nanocomposites with highly enhanced visible light photocatalytic activity and stability, Appl. Catal., B 132-133 (2013) 45-53.

[181] Y. Bi, S. Ouyang, J. Cao, J. Ye, Facile synthesis of rhombic dodecahedral AgX/Ag_3PO_4 (X = Cl, Br, I) heterocrystals with enhanced photocatalytic properties and stabilities, Phys. Chem. Chem. Phys. 13 (2011) 10071-10075.

[182] C. Belver, C. Adán, S. García-Rodríguez, M. Fernández-García, Photocatalytic behavior of silver vanadates: Microemulsion synthesis and post-reaction characterization, Chem. Eng. J. 224 (2013) 24-31.

[183] Q. Liang, Y. Shi, W. Ma, Z. Li, X. Yang, Enhanced photocatalytic activity and structural stability by hybridizing Ag_3PO_4 nanospheres with graphene oxide sheets, Phys. Chem. Chem. Phys. 14 (2012) 15657-15665.

[184] M.S. Zhu, P.L. Chen, M.H. Liu, Visible-light-driven Ag/Ag_3PO_4-based plasmonic photocatalysts: Enhanced photocatalytic performance by hybridization with graphene oxide, Chin. Sci. Bull. 58 (2013) 84-91.

[185] M. Cao, P. Wang, Y. Ao, C. Wang, J. Hou, J. Qian, Preparation of graphene oxide-loaded Ag_3PO_4@AgCl and its photocatalytic degradation of methylene blue and O_2 evolution activity under visible light irradiation, Int. J. Hydrogen Energy 40 (2015) 1016-1025.

[186] Z. Ji, X. Shen, J. Yang, Y. Xu, G. Zhu, K. Chen, Graphene oxide modified Ag_2O nanocomposites with enhanced photocatalytic activity under visible-light irradiation, Eur. J. Inorg. Chem. (2013) 6119-6125.

[187] Y. Song, J. Zhu, H. Xu, C. Wang, Y. Xu, H. Ji, K. Wang, Q. Zhang, H. Li, Synthesis, characterization and visible-light photocatalytic performance of Ag_2CO_3 modified by graphene-oxide, J. Alloys Compd. 592 (2014) 258-265.

[188] D.P. Das, A. Samal, J. Das, A. Dash, H. Gupta, One-Pot fabrication of RGO-Ag_3VO_4 nanocomposites by in situ photoreduction using different sacrificial agents: High selectivity toward catechol synthesis and photodegradation ability, Photochem. Photobiol. 90 (2014) 57-65.

Chapter 3

Synthesis and optimization of visible light active $BiVO_4$ photocatalysts

Rong Ran, Joanne Gamage McEvoy, Zisheng Zhang

International Journal of Photoenergy

Abstract

In this work, monoclinic $BiVO_4$ powders were synthesized via a novel route using potassium metavanadate (KVO_3) prepared by calcination of K_2CO_3 and V_2O_5 as a starting material and followed by hydrothermal treatment, and were investigated as photocatalyst for the degradation of rhodamine B (RhB) under visible light irradiation. The synthesized $BiVO_4$ particles were characterized by X-ray diffraction (XRD), scanning electron microscopy (SEM), X-ray photoelectron spectroscopy (XPS), and UV-Vis light diffuse reflectance spectrophotometry (UV-Vis). The synthesis produced pure monoclinic $BiVO_4$ particles with multi-morphological features containing flower-like, flake-ball, flake, cuboid-like and plate-like shapes, and exhibited strong absorption in the visible light range. The $BiVO_4$ prepared via KVO_3 possessed excellent photocatalytic activity for the degradation of RhB under visible light. The performance of this catalyst was found to be superior to other $BiVO_4$ photocatalysts prepared via ammonium metavanadate (NH_4VO_3) using co-precipitation, combustion and calcination methods reported in literature, respectively.

Keywords: Hydrothermal synthesis, $BiVO_4$, Potassium metavanadate, Visible-light-induced photodegradation.

3.1 Introduction

Bismuth vanadate ($BiVO_4$) is a promising semiconductor for use in solar photocatalysis due to its efficient visible light absorption and other favorable properties such as its non-toxicity [1, 2]. $BiVO_4$ exists in three major crystal phases, namely, monoclinic scheelite, tetragonal zircon and tetragonal scheelite [3, 4]. Of these, monoclinic $BiVO_4$ possesses a band gap of 2.4 eV, making it the most appropriate $BiVO_4$ phase for applications to visible-light-induced photocatalysis [5, 6]. Solid state reactions are traditionally used for the synthesis of $BiVO_4$ [7, 8], however other synthesis methods such as sonochemical routes [9, 10], room temperature aqueous processes [3], molten salt methods [11], hydrothermal processes [12, 13], chemical bath depositions [14, 15], organic decompositions [16, 17], combustion synthesis [18], and co-precipitation processes [19] have been recently proposed and investigated.

In order to enhance the photodegradation efficiency of the composite, various $BiVO_4$ morphologies such as flower-like [5], flake-ball, flake [20], cuboid-like and plate-like [21] structures exhibiting enhanced surface area for photocatalysis have been reported . However, most of the synthesis methods investigated cannot result in the synthesis of $BiVO_4$ materials with both high crystallinity and high surface areas required for efficient photocatalytic reactions [9, 18]. In order to address these issues and to optimize the photocatalytic properties of monoclinic $BiVO_4$, certain research efforts have been focused on employing templates and surfactants such as silica (KIT-6) [22], CTAB [21], CMC [19], and starting materials made from organic polymers and inorganic salts [23]. However, the generated impurities from these methods may be responsible for the blockage of active sites on $BiVO_4$ particles, decreasing the overall photocatalytic activity.

In recent years, potassium vanadium oxides, particularly KVO_3 and K_3VO_8, have been reported as promising alternative starting materials for the preparation of monoclinic $BiVO_4$ [24, 25]. For example, Kelmers [26] prepared the KVO_3 precursor by dissolving equimolar amounts of K and V, as KOH and V_2O_5, respectively. KVO_3 was also previously prepared using KCl and V_2O_5 in the presence of steam [27]. Liu et al. [28] reported using $NaVO_3$ and V_2O_5 as two different vanadium sources to synthesize $BiVO_4$ particles via a hydrothermal method (at synthesis

conditions of 140 °C from $NaVO_3$ and 200 °C from V_2O_5), to obtain two different morphologies of $BiVO_4$ particles with a plate form and rod-like shapes, respectively.

In this work, a novel method for the preparation of monoclinic $BiVO_4$ via a KVO_3 starting material prepared by facile calcination of K_2CO_3 and V_2O_5 was investigated. The $BiVO_4$ synthesized via this route and subsequent hydrothermal synthesis was compared to a similar hydrothermally prepared $BiVO_4$ obtained via a NH_4VO_3 starting material. In addition, the $BiVO_4$ synthesized was compared to $BiVO_4$ synthesized by other methods reported in literature, such as co-precipitation, combustion, and calcination. Compared to the $BiVO_4$ obtained by all other synthesis methods, the as-prepared $BiVO_4$ synthesized via the novel route proposed exhibited enhanced photocatalytic activity for the degradation of model organic pollutant, rhodamine B (RhB), under visible light irradiation due to its desirable phase structure, morphologies, and surface areas. There have been no reports to date on the synthesis of monoclinic $BiVO_4$ powders via KVO_3 and the hydrothermal method, therefore the study of this material and its enhanced performance when prepared via this route contributes to the advancement of visible light photocatalysis using novel bismuth-based structures.

3.2 Experimental

3.2.1 Catalyst Synthesis

All chemicals used were of analytical purity. $BiVO_4$ was synthesized in a two-step procedure, where potassium metavanadate (KVO_3) was first prepared by calcination; followed by the hydrothermal synthesis of monoclinic $BiVO_4$ particles. In the first process, 0.38 g K_2CO_3 (Fisher Scientific, Certified ACS) and 0.5 g V_2O_5 (ACROS Organics, 99.6%) were dissolved in 35 ml deionized water (DW) under vigorous magnetic stirring. The resulting red solution was then poured into an evaporation dish and the obtained solid was dried at 50 °C in an oven overnight. The dry sample was then ground and annealed in air at 457 °C (730 K) for 5 h, resulting in a pink KVO_3 powder. To prepare $BiVO_4$, 1 mmol $Bi(NO_3)_3 \cdot 5H_2O$ and 0.1056 g of the prepared KVO_3 powder were mixed in 35 ml DW, and allowed to react under continuous stirring for 50 min to obtain a vivid yellow slurry. The pH of the slurry was then adjusted by adding 50 vol. % acetic acid, until a final pH of ~ 1 was reached. The slurry was then transferred

into a 45 ml Teflon-lined stainless steel autoclave and the reaction allowed to proceed at 200 °C for 24 h. The resulting solid was collected by filtration, washed with DW several times, and then dried in air overnight.

To investigate the influence of starting materials on the photocatalytic activity of $BiVO_4$ prepared via the hydrothermal method, two hydrothermal synthesis routes were investigated, namely via KVO_3 and via NH_4VO_3, respectively, as outlined in Table 3.1. In order to compare the morphologies, optical properties, and photocatalytic activities of $BiVO_4$ obtained by the proposed hydrothermal synthesis to properties of $BiVO_4$ prepared via various other syntheses reported in the literature, a number of alternative synthesis methods were also explored, as outlined in Table 3.2. The nomenclature for the as-prepared $BiVO_4$ samples are given in Table 3.1 for two samples prepared via hydrothermal synthesis and Table 3.2 for samples prepared via other synthesis methods. It should be noted that the operating parameters selected for the various syntheses methods shown in Table 3.1 were adopted from the optimal parameters reported in the corresponding literatures.

Table 3.1: Synthesis parameters of $BiVO_4$ samples prepared via hydrothermal method

Sample (sample name)	**Reactants**	**pH of precursor slurry (pH control medium)**	**Temperature & Time**
$BiVO_4$ (H-140-8)	3 mmol $Bi(NO_3)_3$•5H_2O 2 mmol NH_4VO_3 2 M NH_4OH 35 ml deionized water (DW)	7 (2 M NH_4OH)	Hydrothermal 140 °C, 8 h [29].
$BiVO_4$ (C+H-200-24)	3 mmol $Bi(NO_3)_3$•5H_2O 0.38 g K_2CO_3 0.5 g V_2O_5 50 vol.% acetic acid 35 ml DW	1 (50 vol.% acetic acid)	Precursor Calcination 730 K (457 °C), 5 h; Hydrothermal 200 °C, 24 h [24].

Samples prepared via hydrothermal synthesis were denoted by the nomenclature $BiVO_4$ (H-XXX-XX), where XXX and XX refer to the treatment temperature and time, respectively; $BiVO_4$ (H-XXX-XX) and $BiVO_4$ (C+H-XXX-XX) denote samples prepared via hydrothermal and calcination & hydrothermal synthesis, respectively.

Table 3.2: Synthesis methods used and relevant parameters for the preparation of various $BiVO_4$ samples

Sample (sample name)	Synthesis method	Reactants	pH of precursor slurry (pH control medium)	Treatment Temperature & Time
$BiVO_4$ (Co-pre-350-24)	Co-precipitation [19]	30 mmol $Bi(NO_3)_3•5H_2O$ 30 mmol NH_4VO_3 4 M HNO_3 2 M NH_4OH 9% (Sodium Carboxymethylcellulose) CMC [a]	9 (2 M NH_4OH)	Calcination 350 °C, 24 h.
$BiVO_4$ (Comb-500-3)	Combustion [30]	2 mmol $Bi(NO_3)_3•5H_2O$ 2 mmol Citric acid 1 M HNO_3; 2 mmol NH_4VO_3 5 mmol citric acid	7.5 (2 M NH_4OH)	Calcination at 500 °C, 3 h.
$BiVO_4$ (Calc-450-5)	Calcination [24]	1 mmol $Bi(NO_3)_3•5H_2O$ 3 mmol K_2CO_3 5 mmol V_2O_5	1 (no pH adjustment)	Calcination 450 °C, 5 h.

a: 9% CMC weight percentages related to the total weight of prepared samples. Samples prepared via co-precipitation synthesis were denoted by the nomenclature $BiVO_4$ (Co-pre-YYY-YY), where YYY and YY refer to the treatment temperature and time, respectively; $BiVO_4$ (Comb-YYY-YY) and $BiVO_4$ (Calc-YYY-YY) denote samples prepared via combustion and calcination, respectively.

3.2.2 Characterization

X-ray powder diffraction (XRD) measurements were carried out on a Rigaku Ultima IV, in Bragg–Brentano geometry, using Cu Kα1 (λ = 0.15418 nm) radiation operating under 40 kV and 40 mA, and with a scanning range of 2θ from 10° to 70°. Scanning electron microscopy (SEM) images were obtained with a JEOL JSM-7500F field emission SEM operated at 2.00 kV. X-ray photoelectron spectroscopy (XPS) was conducted on a Kratos Analytical Axis Ultra DLD instrument with mono-chromated Al X-rays at 140 W. The powder UV-Vis diffuse reflectance spectra (DRS) were recorded on a Thermo Evolution 300 UV/Vis spectrophotometer equipped with a Praying Mantis diffuse reflectance accessory, and the spectra were collected at a scan rate of 240 $nm \cdot min^{-1}$.

3.2.3 Photocatalytic activity

Photocatalytic performance was quantified by the decomposition of RhB (Sigma-Aldrich) as a model organic pollutant under visible light irradiation. A device in the photocatalytic activity test was shown in Figure 3.1. A slurry reactor was placed in a reflective housing to prevent outside light from entering the reactor, and inside light from exiting the system.

A 300-W ELH tungsten halide bulb (Ushio) was used as a light source with a 410 nm cut-off filter (Kenko Zeta, λ > 410 nm, transmittance > 90%) to provide visible light irradiation. The light source was placed at a distance of 15 cm from the top of the slurry. The corresponding irradiation was measured using a quantum meter (Biospherical QSL-2100; 400 nm < λ < 700 nm), and was found to be approximately 4.7×10^{-3} $Einstein \cdot m^{-2} \cdot s^{-1}$. Cooling was provided by an external cooling jacket, and temperature of the reaction was controlled to 22 °C ± 2.

Before illumination, 0.1 gram of photocatalyst dispersed into 150 mL of RhB solution (5 $mg \cdot L^{-1}$) was allowed to reach adsorption-desorption equilibration under continuous magnetic stirring at 340 rpm for 30 min in the dark. Irradiation was then provided for 2 h for each photocatalytic degradation trial. Samples were withdrawn at 20 min time intervals and separated by centrifugation at 10×10^3 rpm for 3 min in an accuSpin Micro 17 (Fisher Scientific) microcentrifuge to remove the suspended catalyst, and the supernatant fluid was analyzed by monitoring the peak absorbance (λ = 552 nm for RhB) via a Genysys 10-UV spectrophotometer

(Geneq Inc.). A standard curve for RhB was prepared and the concentration determined by the measured absorbance and the Beer-Lambert Law. UV/Vis analysis of RhB samples was obtained via a Biochrom Ultrospec 60 UV/Vis spectrophotomer.

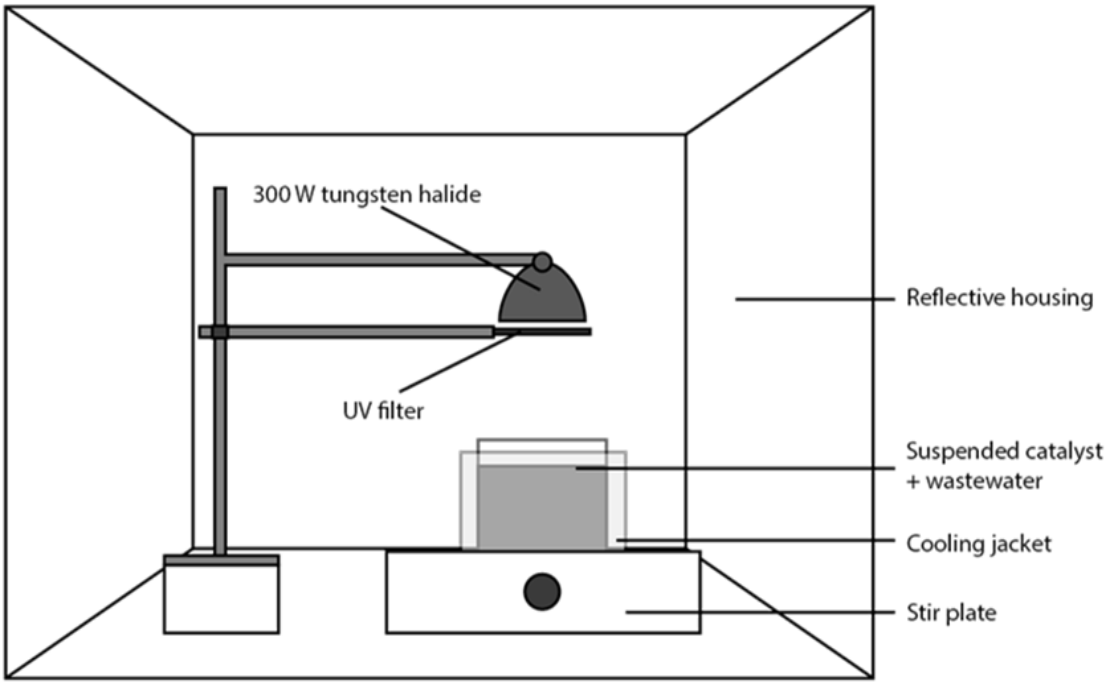

Figure 3.1 A device in the photocatalytic activity test

Quenching tests were performed by the addition of appropriate reactive species scavengers. 2 mg Benzoquinone (BQ) (reagent-grade ≥ 98%, Sigma Aldrich) was used to trap superoxide radicals (O_2^-•), 0.15 g ammonium oxalate (AO) (ACS, Sigma-Aldrich) was used as the holes scavenger, and 3 ml tert-butyl alcohol (TBA) (ACS, Sigma-Aldrich) was used to trap hydroxyl radicals (•OH), respectively.

3.3 Results and discussion

3.3.1 XRD analysis

The XRD pattern for the KVO_3 material obtained by calcination of K_2CO_3 and V_2O_5 is shown in Figure 3.2. The diffraction peaks of KVO_3 could be well indexed to the orthorhombic phase (JCPDS Card No.00-033-1052).

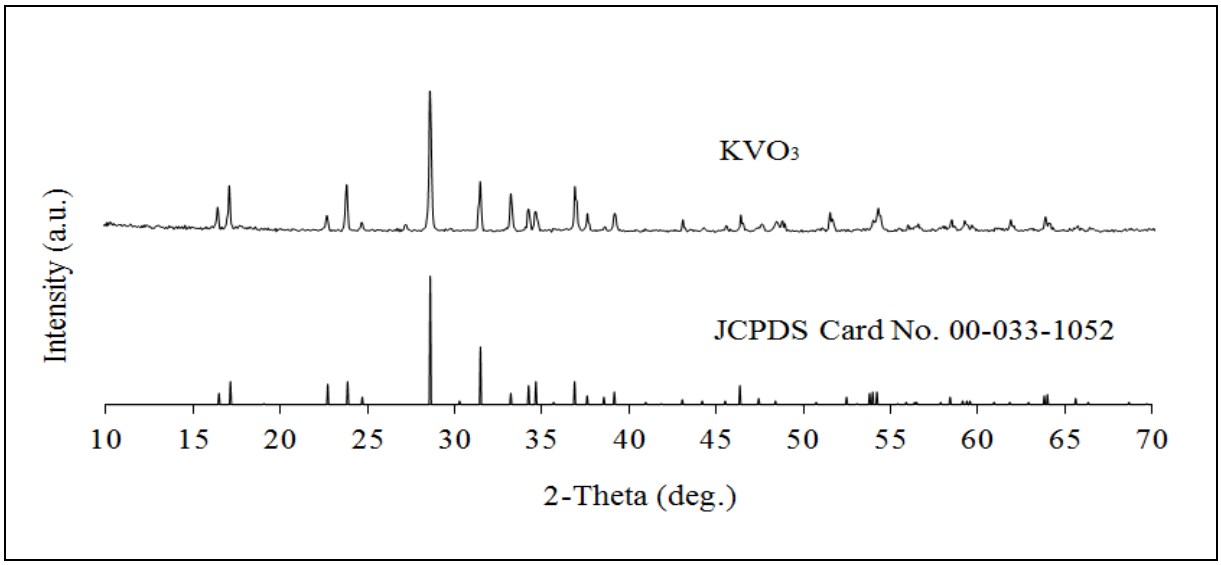

Figure 3.2: XRD pattern of KVO_3 powder synthesized from K_2CO_3 and V_2O_5 via calcination in air at 457 °C (730 K) for 5 h, the pattern of orthorhombic KVO_3 (JCPDS Card No.00-033-1052) is shown for reference.

As shown in Figure 3.2, the XRD pattern for the prepared KVO_3 was well-indexed to the reference pattern, indicating that pure KVO_3 particles with orthorhombic structure resulted from calcination of K_2CO_3 and V_2O_5 in air at 457 °C (730 K) for 5 h.

XRD pattern of $BiVO_4$ obtained via various synthesis methods are shown in Figure 3.3. For all the prepared photocatalysts, all of the diffraction peaks could be well indexed to the monoclinic scheelite phase of $BiVO_4$ (JCPDS Card No.01-083-1699) with the exception of the $BiVO_4$ (H-140-8) synthesized via hydrothermal method, which was indexed to a tetragonal structure (JCPDS Card No.00-014-0133), but also exhibited monoclinic reflections.

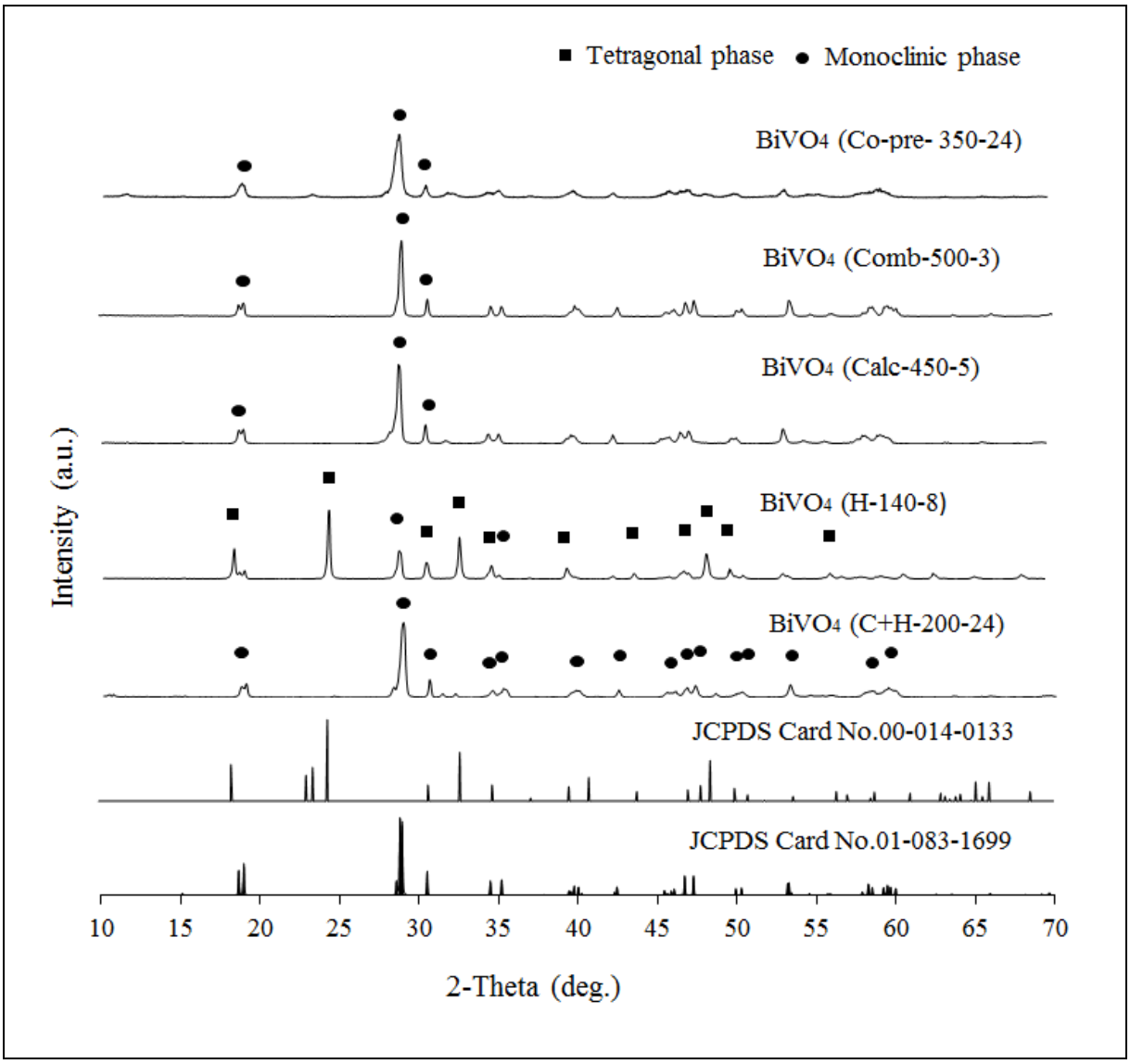

Figure 3.3: XRD patterns of $BiVO_4$ samples synthesized by various methods and conditions (according to Table 3.1 and Table 3.2). Reference tetragonal and monoclinic $BiVO_4$ are shown for comparison according to JCPDS Card No.00-014-0133 and 01-083-1699, respectively.

The major reflections observed for the monoclinic $BiVO_4$ structure occurred at 28.8° and 28.9°, and the major diffraction peak of the tetragonal $BiVO_4$ structure (JCPDS Card NO.00-014-0133) occurred at 24.4°. As shown in Figure 3.3, the XRD pattern of $BiVO_4$ (H-140-8) possessed mixed phases of both tetragonal and monoclinic structures, as evidenced by the characteristic peaks observed at both 24.4° and 28.8°, respectively. According to the relative intensities of these reflections, the tetragonal structure was thought to be the dominant phase present.

All other prepared samples exhibited pure monoclinic structure, and were well-indexed to the expected reflections according to JCPDS Card No.01-083-1699. The $BiVO_4$ sample prepared via co-precipitation (Co-pre-350-24) was observed to possess lower crystallinity due to the long calcination process used. Sintering was thought to occur at 350 °C when the sample was annealed for 24 h, which caused the growth of crystalline sizes and consequent decrease of surface area [31]. It was also previously reported in literature that low crystallinity could lead to an increase in the amounts of defects formed relative to the crystalline quantities produced [32]. This low crystallinity and large particle size was found to lead to lower photocatalytic activity [31, 33].

From the results obtained, the simple calcination process could not be used for the preparation of highly crystalline $BiVO_4$ materials. In contrast, the $BiVO_4$ prepared by combustion and calcination (Comb-500-3 and Calc-450-5, respectively) possessed higher crystallinities. The XRD patterns obtained from $BiVO_4$ samples prepared via hydrothermal synthesis (H-140-8 and C+H-200-24, respectively) indicated that the resulting crystalline structures were dependent on the temperature and time used in the synthesis. However, the $BiVO_4$ (C+H-200-24) sample prepared via the novel route proposed using KVO_3 as the starting material resulted in the formation of a highly crystalline, monoclinic structure which was thought to be advantageous for photocatalysis. The pattern obtained also suggested that higher temperatures and longer reaction times were favorable for the formation of monoclinic $BiVO_4$.

The crystalline size was estimated from the Scherrer formula [34] (Eq. 1):

$$D_p = \frac{k\lambda}{\beta_{1/2}\cos\theta} \qquad (3.1)$$

where D_p is the crystalline size; λ is the wavelength of the X-ray radiation (λ = 0.15418 nm); k is the sphericity constant (usually taken as 0. 9); $\beta_{1/2}$ is the peak width at half-maximum height of the sample after subtraction for equipment broadening. In Eq. 1, the values of 2θ were 28.95° for monoclinic $BiVO_4$ and 24.37° for tetragonal $BiVO_4$, respectively. The crystalline sizes of $BiVO_4$ prepared via various syntheses are shown in Table 3.4.

The molar ratio of bismuth to vanadium was thought to influence the formation of monoclinic $BiVO_4$. Therefore, the molar ratio of Bi:V was kept at 3:2 during hydrothermal synthesis (C+H-200-24) to ensure the formation of monoclinic $BiVO_4$, and provide sufficient vanadium for the stoichiometric conversion from tetragonal to monoclinic $BiVO_4$ [24]. On the basis of our experiments, relevant chemical reactions were formulated as follows:

$$K_2CO_3 + V_2O_5 \xrightarrow[457\ °C\ for\ 5\ h]{Calcination} 2\ KVO_3 + CO_2\ \uparrow \qquad (3.2)$$

$$2\ KVO_3 + 3\ Bi(NO_3)_3 \bullet 5H_2O \xrightarrow[Hvdrothermal]{200\ °C\ for\ 24\ h} BiVO_4 \qquad (3.3)$$

$$Bi(NO_3)_3 + H_2O \leftrightharpoons 2\ HNO_3 + BiONO_3 \qquad (3.3a)$$

$$10\ KVO_3 + 4\ H^+ \rightarrow V_{10}O^{6-}_{28} + 10\ K^+ + 2\ H_2O \qquad (3.3b)$$

$$10\ K^+ + 3\ V_{10}O^{6-}_{28} + 8\ H^+ \leftrightarrow 10\ KV_3O_8 + 4\ H_2O \qquad (3.3c)$$

$$3\ BiONO_3 + V_3O_8^- + H_2O \leftrightharpoons 3\ BiVO_4 + 3\ NO_3^- + 2\ H^+ \qquad (3.3d)$$

$$CH_3COOH + NO_3^- \leftrightharpoons CH_3COO^- + HNO_3 \qquad (3.4)$$

According to Kudo et al. [24] and Liu et al. [28], the formation of $BiVO_4$ was sensitive to temperature and pH of the aqueous medium. The authors indicated that high temperature (~ 200 °C) might facilitate the conversion of excess BiO^+ to the monoclinic structure, by the adsorption on the tetragonal $BiVO_4$ crystals. In addition, under pH ~ 1, the interaction of BiO^+ cations with VO_3^- present in KVO_3 was thought to be much stronger than with VO_3^- in NH_4VO_3, due to Coulombic attractions.

The increase of the KVO_3 solubility in water is greater than that of NH_4VO_3 over a temperature range 293 K to 323 K [35], which may have also contributed to providing more VO_3^- for the generation of $BiVO_4$. Furthermore, VO_3^- in KVO_3 was reported to be converted to an intermediate product of vanadate ions (i.e. $V_{10}O^{6-}_{28}$) during the hydrothermal process by increasing temperature, to eventually form a stable KV_3O_8 phase [36], as shown in (3.3b) and

(3.3c). This phase could serve as an inorganic morphology control agent during the synthesis [24].

The pH value was also thought to influence growth process and the morphology of $BiVO_4$ particles, and the pH for the precursor slurry of $BiVO_4$ was ~ 1 due to the hydrolyses of $Bi(NO_3)_3 \cdot 5H_2O$ [24]. The final pH of the $BiVO_4$ precursor slurry was kept at ~ 1 by adding 50 vol.% acetic acid (acidity $pK_a = 4.76$). Acetic acid was thought to play the following roles during the synthesis:

(1) Adjusted concentrations between Bi (III) and V (V), acting as a morphology controlling agent for $BiVO_4$ [37].

(2) Promoted the conversion from tetragonal $BiVO_4$ to monoclinic $BiVO_4$ crystals resulting in pure monoclinic $BiVO_4$ particles.

(3) Preferentially formed pure monoclinic $BiVO_4$ particles with nanoscaled average crystalline sizes [33].

3.3.2 SEM analysis

The microstructure and morphology of synthesized $BiVO_4$ particles were investigated by SEM, and the images obtained are shown in Figure 3.4 and Figure 3.5.

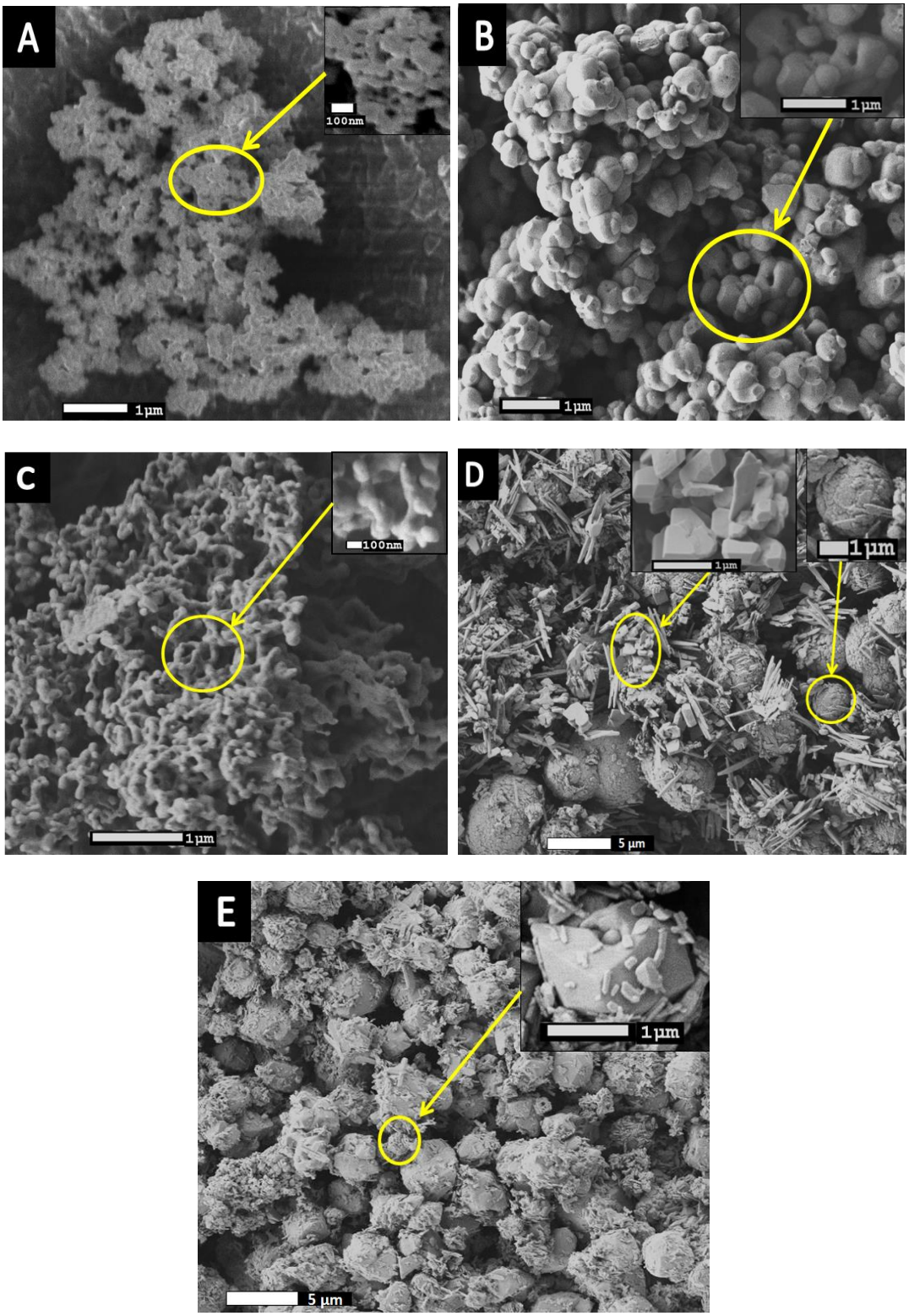

Figure 3.4: SEM images of $BiVO_4$ samples obtained from various synthesis methods: (A) co-precipitation (B) combustion (C) calcination (D) hydrothermal (E) calcination & hydrothermal method.

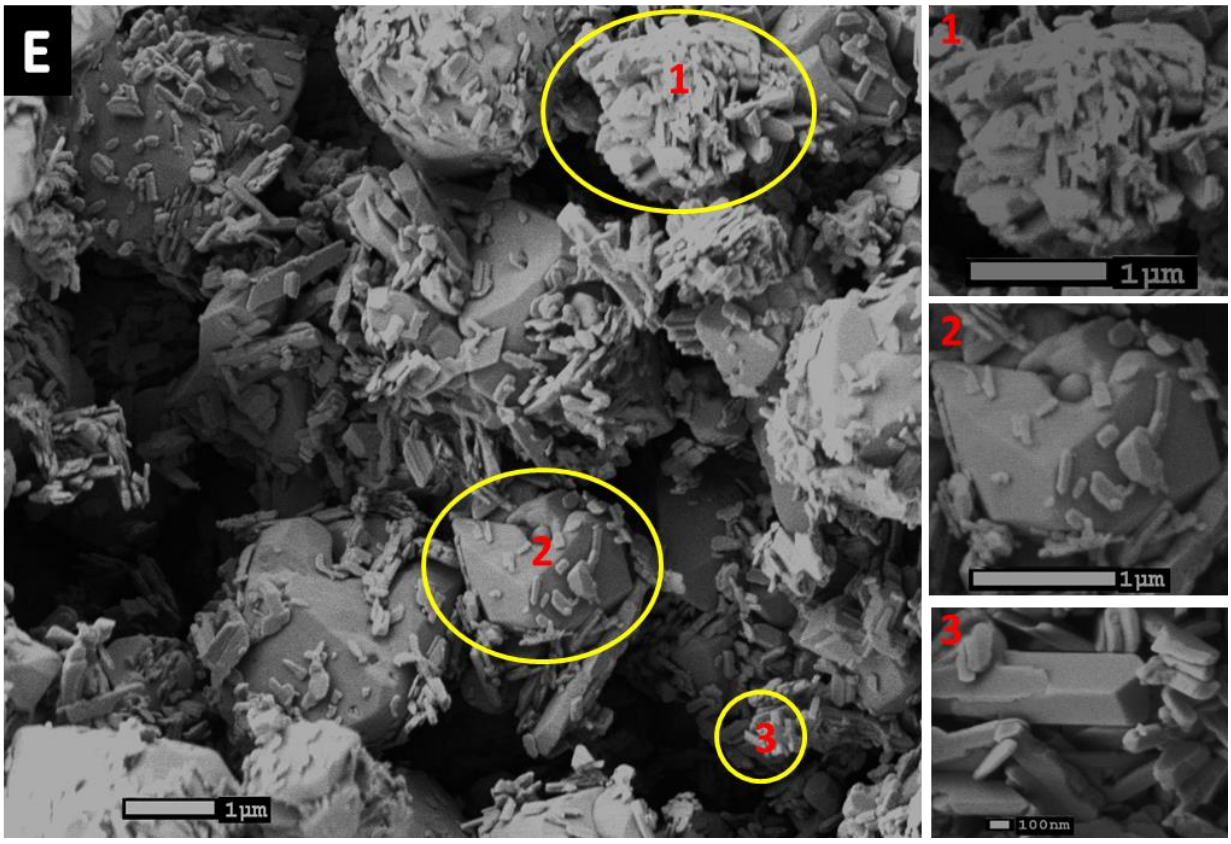

Figure 3.5: SEM image of $BiVO_4$ (E) showing various morphologies.

From Figures 3.4A, 3.4B, and 3.4C, the as-obtained samples prepared using various methods were observed to be quasi-spherical with 100 nm nanoscale length. As shown in the inset of Figure 3.4A, clusters of sintered particles were distinctly observed for the sample prepared via co-precipitation instead of individual balls, and this was thought to be due to severe sintering, as expected from the XRD results obtained (Figure 3.3 $BiVO_4$ (Co-pre-350-24)). Comparison of Figures 3.4A, 3.4B and 3.4C indicated that the synthesized $BiVO_4$ particles exhibited good morphology evolution which was mainly attributed to shorter calcination times at higher calcination temperatures [24, 38]. From Figure 3.4B, the morphology was observed to be composed of nanoscale balls without severe sintering. However, because of the drawbacks associated to calcination synthesis, the surface area of $BiVO_4$ particles formed using the combustion method declined to some extent, which was thought to negatively influence the photocatalytic activity.

As seen in Figures 3.4D and 3.4E, excellent flake-ball superstructures could be observed for the samples prepared by hydrothermal synthesis. As shown in the inset of Figure 3.4D, the

morphological evolution of the $BiVO_4$ particles from nanoscale flakes and squares to balls with rough surfaces was likely due to the effect of the hydrothermal aqueous system, in which the strong surface-charge driven forces influenced the resulting photocatalyst structures [39, 40].

As the treatment time increased, part of these nanoscale crystals agglomerated to balls. As such, shorter reaction times were thought to provide inadequate surface-charge driven forces for the formation of smooth balls in the hydrothermal processes. Nevertheless, the surface area of $BiVO_4$ particles rapidly increased with treatment time, and multi-morphological features of $BiVO_4$ particles were distinctly observed. If various reaction times were used in conjunction with different temperatures, multi-morphological features of $BiVO_4$ particles were reported be more diverse in one system [41]. For instance, flake-ball superstructures with obvious edges were observed in Figure 3.4E (see Figure 3.4inset), which agreed well with the $BiVO_4$ monoclinic structure seen in the XRD pattern (Figure 3.3. $BiVO_4$ (C+H-200-24)).

To investigate $BiVO_4$ (C+H-200-24), additional SEM imaging was performed, and the results are shown in Figure 3.5. The multi-morphological features observed in the superstructure are highlighted in the insets, where inset 1, 2 and 3 indicate flower-like [5], flake-ball and flake [20], cuboid-like, plate-like structures [21] respectively, which were present in the same system. Iwase and Kudo [37] reported that the edge surfaces of the plate-like and well-crystallized particles of monoclinic $BiVO_4$ were highly active sites for photocatalytic oxidation reactions. Therefore, monoclinic $BiVO_4$ particles with multi-morphological features were thought to be advantageous for photocatalysis due to the increased surface area, resulting in promoting adsorption of dyes onto the photocatalysts, and their subsequent photodegradation.

3.3.3 XPS analysis

In order to explore the chemical and electronic states of $BiVO_4$, XPS analysis of a representative sample ($BiVO_4$ (C+H-200-24)) was performed, and the results from the full-scan spectrum are shown in Figure 3.6(a). The corresponding high resolution XPS spectra patterns are presented in Figures 3.6(b), 3.6(c) and 3.6(d), for the Bi 4f, V 2p, O 1s and C 1s states, respectively. The spectrum of the C 1s was attributed to the adsorbed carbon present in the samples.

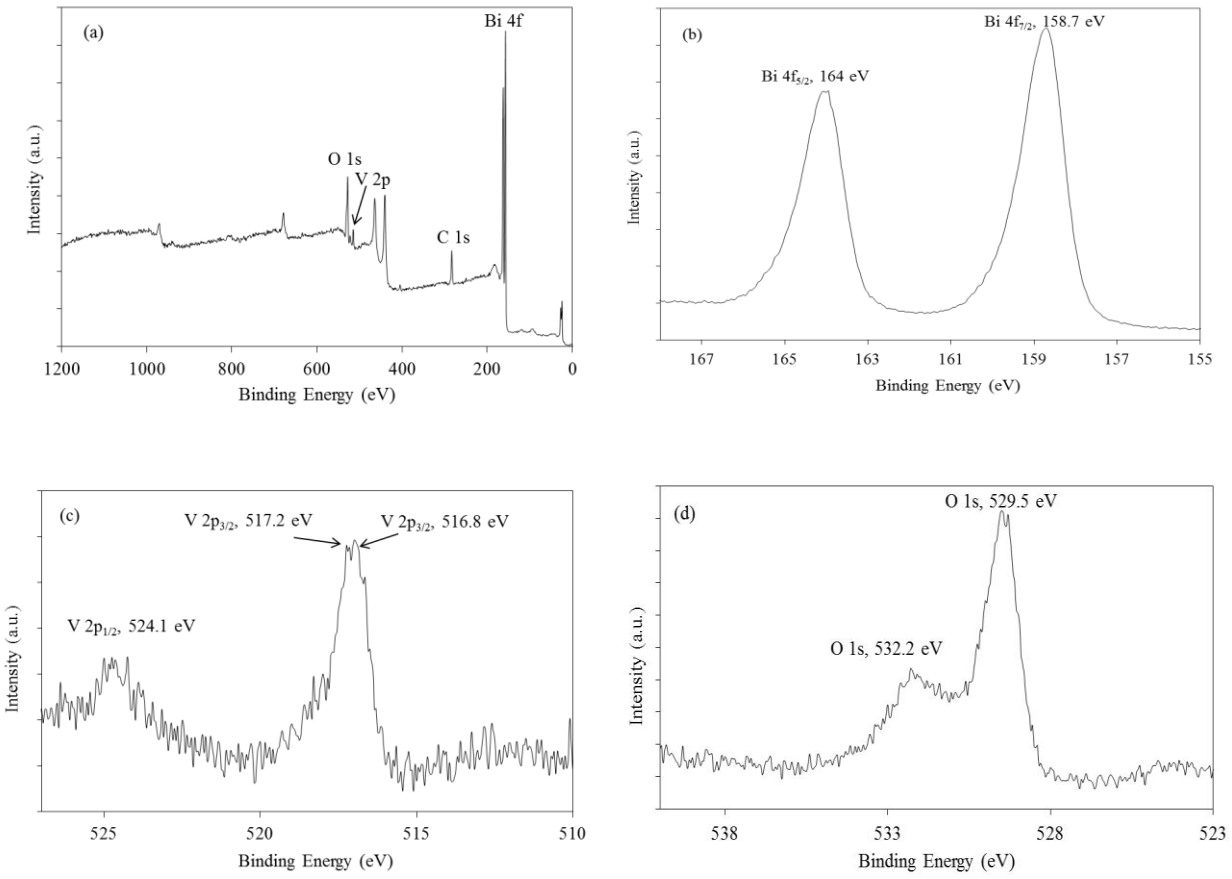

Figure 3.6: Full scan XPS spectrum of $BiVO_4$ (C+H-200-24) and high resolution spectra of Bi 4f, V 2p and O 1s. (a) full scan of $BiVO_4$, (b) Bi 4f, (c) V 2p and (d) O 1s.

From Figure 3.6(b), the spectra of Bi species were seen to exhibit two symmetric peaks centered at 158.7 eV and 164 eV, (for spin-orbit splitting characteristic of Bi $4f_{7/2}$ and Bi $4f_{5/2}$, respectively) which corresponded to characteristic signals of Bi^{3+} [42-44]. The observed V $2p_{3/2}$ peak (Figure 3.6(c)) was composed of two components at binding energies of 516.8 eV and 517.2 eV, which were assigned to the V^{4+} and V^{5+} species, respectively, in terms of the V $2p_{3/2}$ orbital [43, 45].

Interestingly, as shown in Figure 3.6(c), the difference in intensity for those two species was small. Accounting for electroneutrality, $BiVO_4$ (C+H-200-24) had an apparent oxygen deficiency filled with V^{4+} species [46] incorporated with V^{5+} species on the surface of $BiVO_4$ in dynamic equilibrium, in which the lost oxygen groups were thought to be consumed to create extra hydroxyl groups on the surface of $BiVO_4$, and these hydroxyl groups generated may have caused the presence of oxygen vacancies [46]. The amount of lost oxygen was determined by the molar

ratio of V^{4+}/V^{5+} in the whole system [43, 45, 47]. Furthermore, the peak at a binding energy of 524.1 eV was attributed to the V $2p_{½}$ orbital. As seen in Figure 3.6(d), the O 1s spectral peak located at 530 eV was composed of two separate peaks at binding energies of 529.5 eV and 532.1 eV. The former peak was characteristic of oxidic species such as O^-, O_2^- or O^{2-} in an effective oxide over-layer [48], and was attributable to oxygen vacancies in $BiVO_{4-\delta}$ [43]. The latter O 1s peak was assigned to lattice oxygen of $BiVO_4$ crystallites, resulting from interfacial hydroxyl groups (i.e. OH radicals) or molecularly adsorbed water in the system [44, 48, 49].

$BiVO_4$ is a direct band gap semiconductor [6, 42], which is favourable for retaining low energy direct transitions. In addition to the crystal structure observed, the electronic structure of a semiconductor material affects the photocatalytic activity [50, 51]. For monoclinic $BiVO_4$, as an n-type material [8], V 3d orbitals preferentially formed the conduction band (CB), whereas Bi 6s and O 2p orbitals favoured the composition of a hybridized valence band (VB) [52], where charge transfer occurred from the Bi 6s and O 2p hybrid orbitals to the V 3d orbitals under photoexcitation. The hybridization of the Bi 6s and O 2p levels created a desirably dispersed VB, which could enable the mobility of photoexcited holes [32], resulting in a high activity of photocatalytic oxidation towards organic pollutants [22].

3.3.4 Optical properties of $BiVO_4$

As seen in Figure 3.7, the UV-Vis spectra of all $BiVO_4$ samples exhibited intrinsic absorption in the visible light region attributed to the characteristic features of $BiVO_4$ (both monoclinic and tetragonal phases), which was related to the band-band transition of a semiconductor with a direct band gap [6, 31, 52].

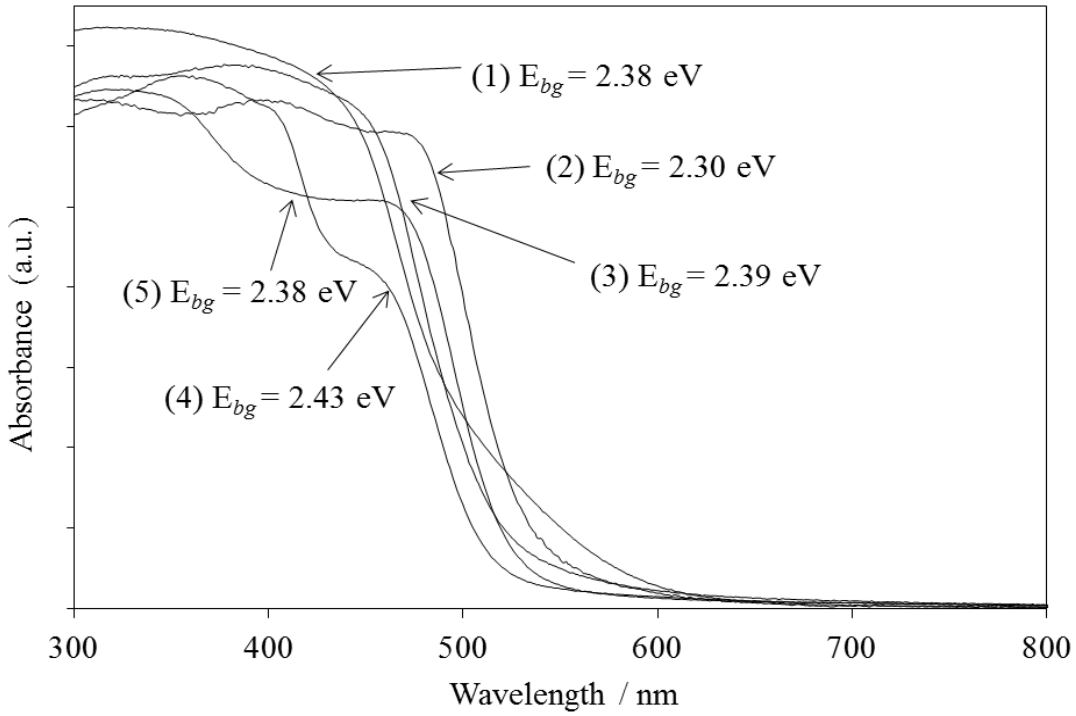

Figure 3.7: UV-Vis diffuse reflectance spectra (DRS) of $BiVO_4$ samples prepared via various synthesis methods (1) $BiVO_4$ (Co-pre-350-24), (2) $BiVO_4$ (Comb-500-3), (3) $BiVO_4$ (Calc-450-5), (4) $BiVO_4$ (H-140-8) and (5) $BiVO_4$ (C+H-200-24).

The band gaps of the prepared samples were estimated from the DRS data, where respective band gap energies (E_{bg}, eV) were estimated using the following equation:

$$\lambda = 1240/E_{bg} \qquad (3.5)$$

where λ is the maximum wavelength of absorption by photocatalysts (nm), and E_{bg} is the estimated band gap of photocatalysts (eV).

The calculated band gap energies were 2.38, 2.30, 2.39, 2.43 and 2.38 eV for the $BiVO_4$ (Co-pre-350-24), $BiVO_4$ (Comb-500-3), $BiVO_4$ (Calc-450-5), $BiVO_4$ (H-140-8) and $BiVO_4$ (C+H-200-24) samples, respectively. All of $BiVO_4$ particles prepared via various synthesis methods had strong absorption in the visible light range (λ < 510 nm). From the SEM presented in Figure 3.4B, the $BiVO_4$ (Comb-500-3) sample had the largest agglomerate size due to the severe sintering, and this was thought to have caused the band gap of 2.30 eV observed. In contrast, the $BiVO_4$ (Co-pre-350-24), $BiVO_4$ (Calc-450-5), $BiVO_4$ (H-140-8), and $BiVO_4$ (C+H-200-24) samples were all

present as smaller particles, and exhibited band gaps of 2.38, 2.39, 2.43 and 2.38 eV, respectively.

It has been reported in literature that the band gap of a semiconductor increases with an absorption shift to shorter wavelengths due to decreased individual particle size [53, 54]. In accordance with this, a decrease in the light absorption was observed for $BiVO_4$ (H-140-8), $BiVO_4$ (C+H-200-24), and was thought to be due to the formation of flakes of several hundred nanometers in diameter on the surface of $BiVO_4$ (Figure 3.4 and Figure 3.5), which caused the scattering of light [55].

3.3.5 Photocatalytic activity of $BiVO_4$

3.3.5.1 Photodegradation of RhB

RhB is a basic red xanthene dye with a high water solubility, and its molecular formula is $C_{28}H_{31}ClN_2O_3$ [56]. The structure of RhB is shown in Figure 3.8 for reference.

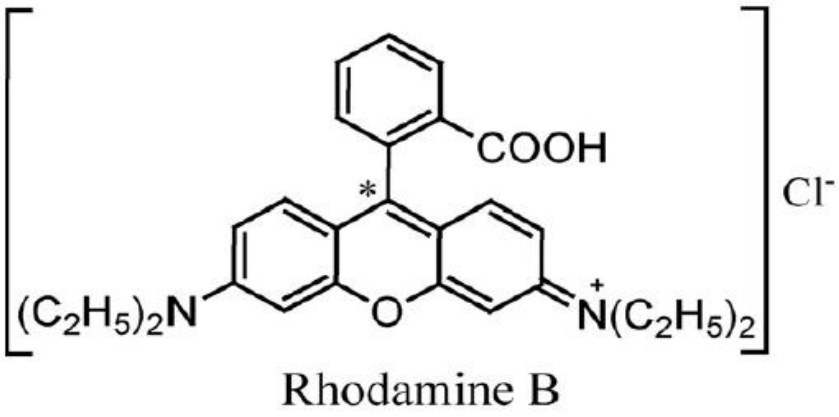

Figure 3.8: Structure of RhB

RhB is widely applied as a model target organic pollutant to study photoactivity. The results of the adsorption-desorption equilibration and visible-light-induced photoactivity in the presence of various prepared $BiVO_4$ samples are shown in Figure 3.9.

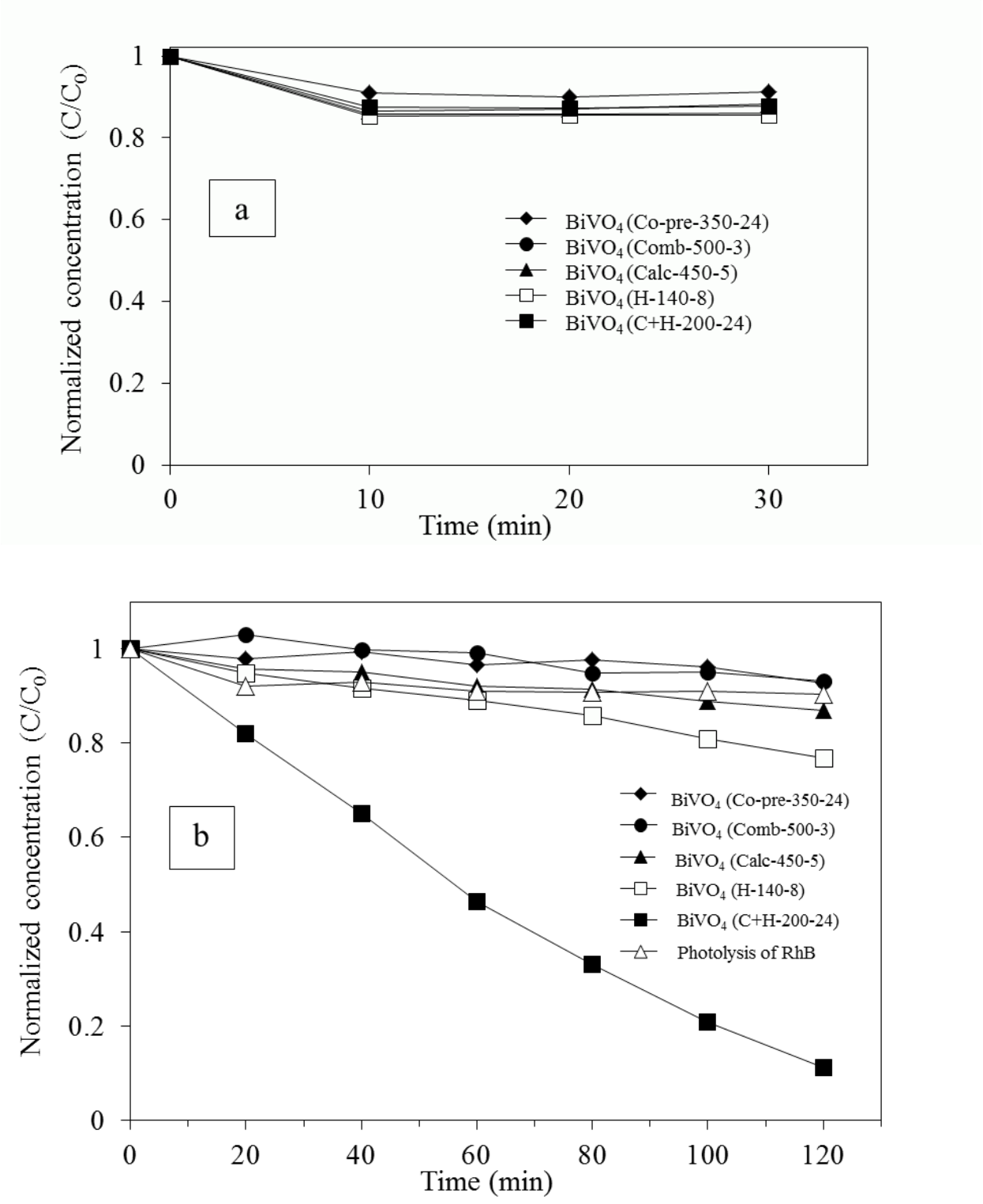

Figure 3.9: (a): adsorption reaction of RhB in the presence of various $BiVO_4$ samples in the absence of light over 30 min; (b): Photocatalytic degradation of RhB (5 $mg \cdot L^{-1}$) in the absence of and presence of various $BiVO_4$ samples under visible-light irradiation for 2 h.

To achieve adsorption-desorption equilibration, the adsorption reaction of RhB in the presence of various $BiVO_4$ samples was performed over 30 min in the absence of light, the results of which shown in Figure 3.9(a). It can be seen that adsorptions of 8.8%, 14%, 11.7%, 14.4%, 12.3% onto photocatalysts corresponding to co-precipitation, combustion, calcination, hydrothermal and calcination & hydrothermal methods, respectively.

To investigate the self-degradation of RhB, a control test for photolysis in the absence of $BiVO_4$ samples was performed under visible light irradiation. This self-degradation was found to contribute up to 9.6% in 2 h of irradiation (Figure 3.9(b)), and as such may have induced a self-sensitized process. However, compared to the results obtained in the presence of $BiVO_4$ samples, the degree of RhB self-degradation due to photolysis was thought to have a relatively low contribution to the overall degradation observed in the presence of a photocatalytic process.

The RhB degradation by $BiVO_4$ (C+H-200-24) was up to 88% in 2 h in contrast, and represented a higher removal capacity of than both photolysis and the other $BiVO_4$ samples prepared, where degradation of 7.2%, 6.9%, 13% and 23% corresponding to $BiVO_4$ (Co-pre-350-24), $BiVO_4$ (Comb-500-3), $BiVO_4$ (Calc-450-5) and $BiVO_4$ (H-140-8), respectively, were observed, as shown in Figure 3.9(b). This indicated that $BiVO_4$ (C+H-200-24) was comparatively more active than other $BiVO_4$ samples, and the increase in activity observed was thought to be due to the optimal synthesis method (calcination & hydrothermal) and optimal starting material (KVO_3) used in the hydrothermal process. These factors acted in concert to create an overall optimized catalyst, which exhibited improved adsorption-desorption kinetics of RhB on the surface of $BiVO_4$ particles, as well as an improvement in the visible light absorption and photocatalytic degradation. In addition to the photoactivity observed, the adsorption of RhB by the prepared $BiVO_4$ samples also influenced the degradation.

As a cationic dye in acidic media, the adsorption of RhB onto a photocatalyst required the presence of anionic catalysts with negative surface charges in order to facilitate photodegradation [57]. As a n-type material [8], $BiVO_4$ was a desirable anionic catalyst with respect to the photodegradation of RhB, because it could adsorb the RhB molecules by Coulombic attractions and also provided extra electrons and created an excess of negative (n-type) electron charge carriers.

3.3.5.2 Langmuir–Hinshelwood kinetics

To quantitatively compare the powders synthesized using various conditions, Langmuir–Hinshelwood kinetic analysis was applied to RhB degradation in the presence of $BiVO_4$ particles. Here the simplification to a pseudo-first-order reaction model is given by the following:

$$ln\left(\frac{C_0}{C}\right) = k_r \times K\mathrm{t} = k'\mathrm{t} \qquad (3.6)$$

where C_0 and C are the initial RhB concentration ($mol \cdot L^{-1}$) and concentration at reaction time t (min), respectively. k_r is the reaction rate constant ($mg\ (L \cdot min)^{-1}$), K is the adsorption coefficient of the reactant onto catalyst ($L \cdot mg^{-1}$), k' is pseudo-first order rate constant in Langmuir-Hinshelwood expression (min^{-1}), and t is the irradiation time (min). The reaction is expressed by the pseudo first order equation if adequately dilute initial concentrations are used($C_0 < 10^{-3}$ $mol \cdot L^{-1}$) [58]. In our experiments, the C_0 was adequately small ($C_0 = 1.04 \times 10^{-5}$ $mol \cdot L^{-1}$). Hence, k' could be used to describe the pseudo-first order rate constant, and was obtained from the gradient of the line of $ln(C_0/C)$ versus time t. The pseudo first order constant was used as a criterion for the comparison of the photoactivity of the catalysts. Taking the initial 20 min of degradation into account, the comparison of rate constants obtained is given in Table 3.3.

Table 3.3: Pseudo-first order rate constants *k'* using Langmuir-Hinshelwood kinetics for various $BiVO_4$ samples

Sample	Degradation rate constants k' (min^{-1})
$BiVO_4$ (Co-pre-350-24)	0.00102
$BiVO_4$ (Comb-500-3)	-0.00149
$BiVO_4$ (Calc-450-5)	0.00219
$BiVO_4$ (H-140-8)	0.00260
$BiVO_4$ (C+H-200-24)	0.0142

Note: Sample naming follows the previous convention described in Table 3.1 and Table 3.2.

As seen from Table 3.3, all samples exhibited photocatalytic activity for the degradation of RhB to some extent. Of these prepared samples, $BiVO_4$ (C+H-200-24) showed the highest degradation rate of $k' = 0.0142$ (min^{-1}). Therefore, the pseudo-first order rate constant of $BiVO_4$

(C+H-200-24) agreed well with the corresponding result of photocatalytic degradation shown in Figure 3.9.

3.3.5.3 Apparent photonic efficiency

It has been reported that apparent photonic efficiency can be applied to determining the effectiveness of photon utilization. The initial reaction within 20 min was considered to be linear, and the photonic efficiency at 20 min was taken as the reference for comparsion of photocatalytic activities among $BiVO_4$ samples. The formula for apparent photonic efficiency is given according to the following [59]:

$$\xi = \frac{V \Delta C}{J A \Delta t} \qquad (3.7)$$

where ξ is the apparent photonic efficiency (i.e. the ratio of reaction rate and incident light intensity), V is the solution volume (m^3), ΔC is the change in the concentration ($mol \cdot m^{-3}$), J is the flux of photons ($Einstein \cdot m^{-2} \cdot s^{-1}$), A is the illuminated area (m^2) and Δt is the change in time (min).

The results of photonic efficiency agreed well with the first order kinetic constants obtained by Langmuir-Hinshelwood analysis. $BiVO_4$ (C+H-200-24) was found to possess superior photonic effiency to the other samples, with the maximum photonic efficiency of 0.0131. The calculated values of apparent photonic efficiencies, crystalline size and band gap of prepared catalysts are shown in Table 3.4.

Table 3.4: Properties and photocatalytic performance of $BiVO_4$ samples prepared via various synthesis methods

Sample	Crystalline size (nm)[b]	Band gap (eV) [c]	Apparent photonic efficiency ξ
$BiVO_4$ (Co-pre-350-24)	16	2.38	0.000410
$BiVO_4$ (Comb-500-3)	37	2.30	0.000808
$BiVO_4$ (Calc-450-5)	30	2.39	0.00162
$BiVO_4$ (H-140-8)	51	2.43	0.00278
$BiVO_4$ (C+H-200-24)	25	2.38	0.0131

b: By Scherer formula; c: Estimated from the diffuse reflectance spectroscopy adsorption edge.

The results indicated that $BiVO_4$ (C+H-200-24) via optimized hydrothermal method gave the maximum *k*' value of 0.0142 min^{-1} corresponding to the highest degree of photocatalytic degradation of RhB, as shown in Figure 3.9. Table 3.3 also indicated that the rate constant of the $BiVO_4$ (C+H-200-24) sample was higher than the other samples prepared via hydrothermal method, indicating that the starting materials affected the overall photocatalytic activity observed.

3.3.5.4 RhB degradation

In order to investigate the RhB photocatalytic degradation, the changes of UV-vis spectrum during the decolorization of RhB under visible irradiation were investigated, and the results are shown in Figure 3.10.

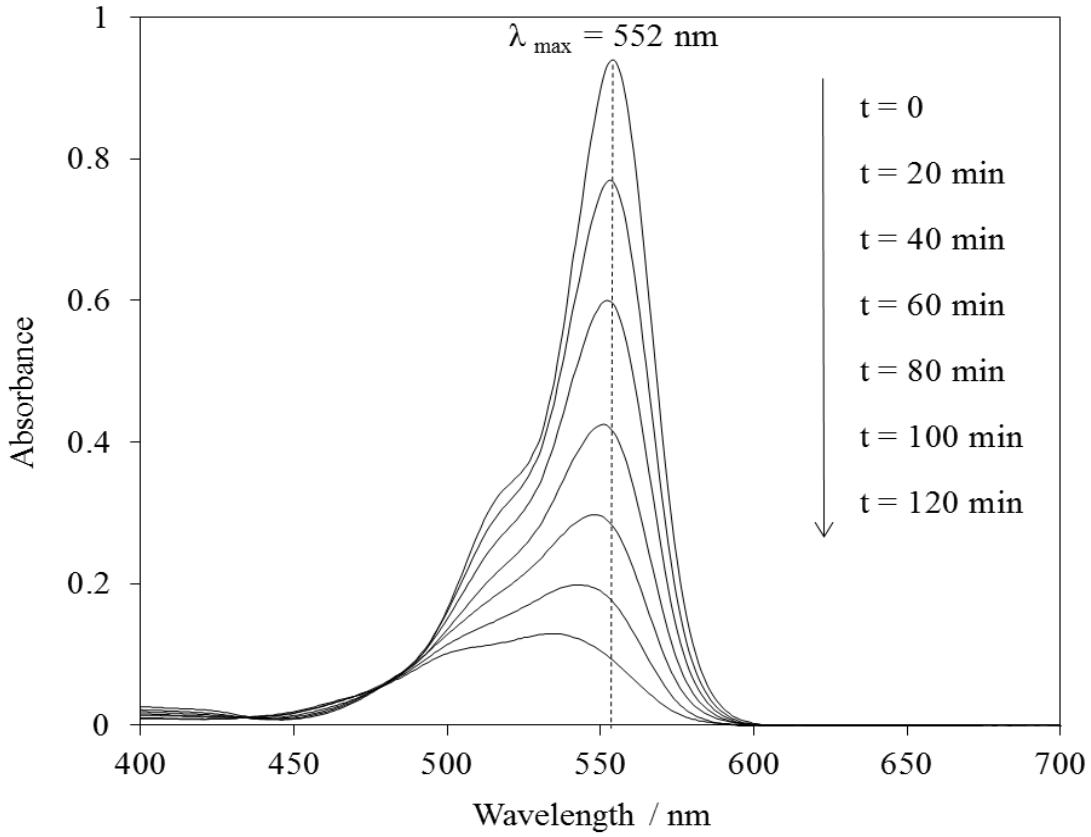

Figure 3.10: UV-Vis spectra of RhB upon photodegradation by $BiVO_4$ (C+H-200-24).

As seen in Figure 3.10, the intensity of characteristic absorption peak at 552 nm diminished rapidly with time, and had gradually hypsochromic shifts of absorption bands from 552 nm to 535 nm, in agreement with the results reported in literature [60, 61]. The decline of RhB at its maximum absorption wavelength was attributable to the cleavage of the whole conjugated chromophore structure, while the small shifts from 552 nm to 535 nm implied the stepwise N-de-ethylation of RhB. Generally, those two competitive pathways were thought to occur throughout the whole degradation process. However, from Figure 3.10, the high initial concentration of RhB under visible light irradiation may have slowed the production of N-deethylated intermediates.

The main reason may be due to the carboxyl group preferentially adsorbing on the surface of $BiVO_4$, rather than that of the diethyl-amino group at the weak acidic conditions [62], from which, the active oxygen species mainly attacked the conjugated chromophore ring structure and resulted in the cleavage of the ring structure of RhB in the presence of $BiVO_4$. Therefore, the observed absorption shifts were thought to be relatively negligible compared to the decrease in

peak absorbance due to the cleavages of the whole conjugated chromophore. Further decomposition of the de-ethylated intermediates was thought to occur with longer and continuous treatment under visible light irradiation, as reported in literature [57].

3.3.5.5 Recyclability and durability of photocatalytic activity for $BiVO_4$ particles

Recyclability of photocatalyst is an important factor for the assessment of practical utilization and scalability of the catalyst. For the recyclability runs, the photocatalyst were separated by centrifugation without washing after each run, and the degraded RhB supernatant was removed, and fresh RhB solution added. To assess the recyclability and durability of $BiVO_4$ (C+H-200-24) sample for photocatalytic degradation, four runs of recycling experiments were conducted, and the results are shown in Figure 3.11.

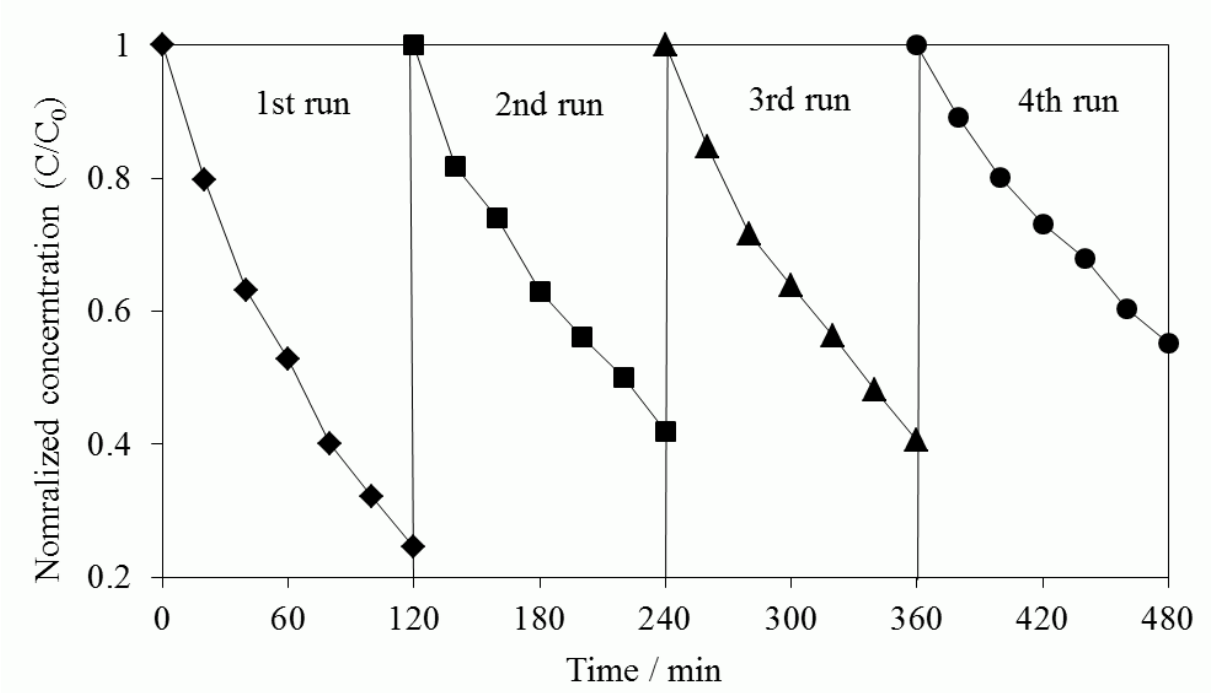

Figure 3.11: Recycling experiments for the photocatalytic degradation of RhB.

From the results obtained, the concentration of RhB was seen to obviously decrease in each cycle, implying that $BiVO_4$ (C+H-200-24) could exhibit some degree of visible-light-induced photoactivity in four successive cycling experiments without regeneration. Despite this, some loss of photoactivity after recycling was observed, and the activity in the first run was greater than that observed in the sequential uses at the end of 2 h visible light irradiation for the second

to fourth run, respectively. The 45% degradation of RhB observed in the final run indicated that some activity was still maintained by the catalyst, although active sites were thought to be possibly blocked by the intermediates from decomposed RhB [63, 64].

3.3.5.6 Role of reactive species

The photocatalytic degradation of organic pollutants is generally induced by reaction with reactive species such as h^+, •OH and O_2^-•, which are generated on the surface of photocatalysts upon irradiation [57]. To further investigate the impact of various reactive species on the photocatalytic degradation reactions, the influence of numerous additives were studied on photodegradation of RhB. Reactive species scavengers (including BQ, AO and TBA) were employed, and their effect in suppressing photocatalytic degradation of RhB in the presence of $BiVO_4$ was studied. The results are shown in Figure 3.12.

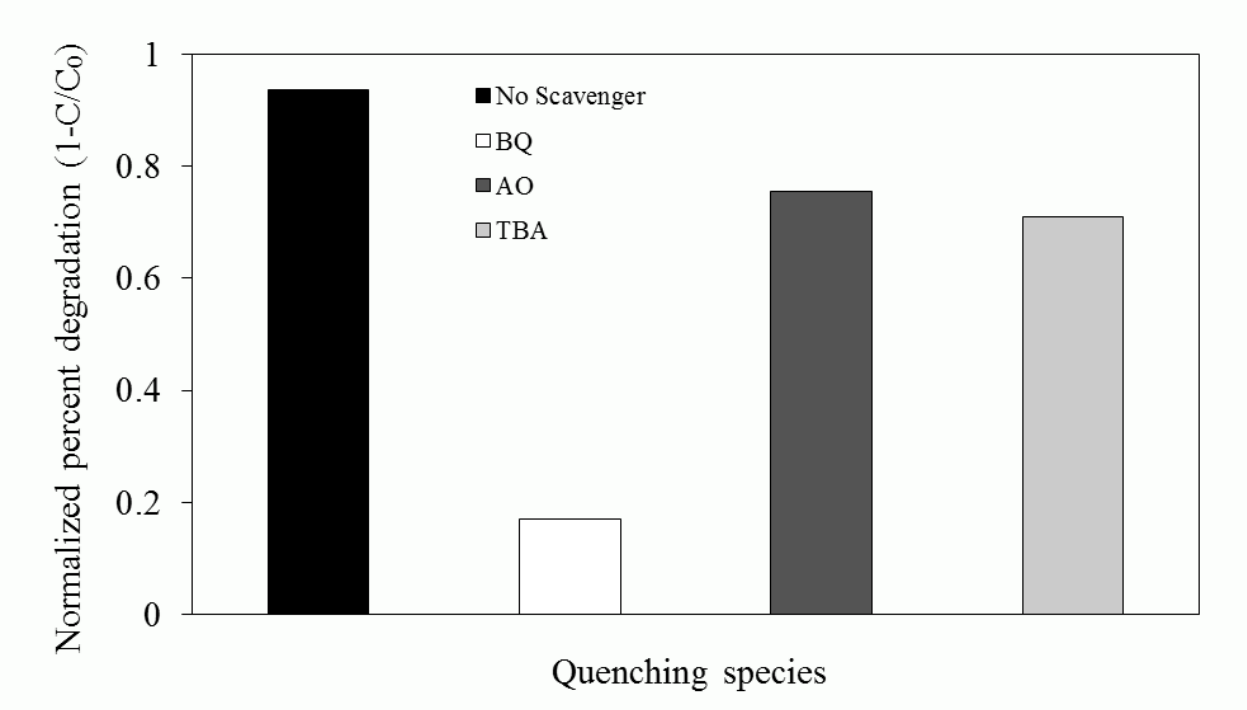

Figure 3.12: Quenching tests for photocatalytic degradation of RhB on $BiVO_4$ (C+H-200-24) under different conditions with VLI.

From Figure 3.12, it was found that, without scavengers, the photocatalytic degradation of RhB on $BiVO_4$ (C+H-200-24) was ~ 88% after 2 hours. 2 mg BQ as a scavenger of O_2^-• was added in the photocatalytic system [65, 66] causing the photodegradation of RhB on $BiVO_4$ (C+H-200-24)

to decrease significantly, reducing the degradation to 17%. This suggested that O_2^-• played a significant role in the photocatalytic degradation mechanism of RhB over $BiVO_4$. 0.15 g of AO was used as a hole scavenger [67, 68]. This addition caused a degradation of RhB up to 75%, with little change from the unquenched test. 3 ml TBA was added into the photodegradation system as an •OH scavenger [69], and resulted in a 71% RhB degradation. From the results of the quenching tests, the degradation of RhB by $BiVO_4$ under visible light irradiation was thought to be mainly attributed O_2^-•, where the •OH and holes species played a lesser role in the process.

3.3.5.7 Mechanism of photocatalytic activity

To characterize the photodegradation pathways of the dye pollutant in the absence and presence of $BiVO_4$ under visible light irradiation, considering the results obtained from the photolytic and photocatalytic degradation study, as well as the quenching tests, respectively, the following scheme was proposed:

$$RhB_{ads} + \text{visible light} \rightarrow RhB^*_{ads} \quad (3.8)$$

$$RhB^*_{ads} + BiVO_4 \rightarrow BiVO_{4(\text{injected } e^-)} + RhB^+_{ads} \quad (3.9a)$$

$$BiVO_{4(\text{injected } e^-)} + O_{2(\text{surface - adsorbed})} \rightarrow BiVO_4 + O_2^-\bullet \quad (3.10a)$$

$$BiVO_4 + \text{visible light} \rightarrow h^+ + e^- \quad (3.9b)$$

$$e^- + O_2 \rightarrow O_2^-\bullet \quad (3.10b)$$

$$h^+ + H_2O \rightarrow \bullet OH \quad (3.11)$$

$$RhB^+_{ads} + O_2^-\bullet \text{ or } \bullet OH \text{ radicals } (3.12) \rightarrow \text{peroxides or hydroxylated…intermediates} \rightarrow \text{degraded or mineralized products [57, 70].}$$

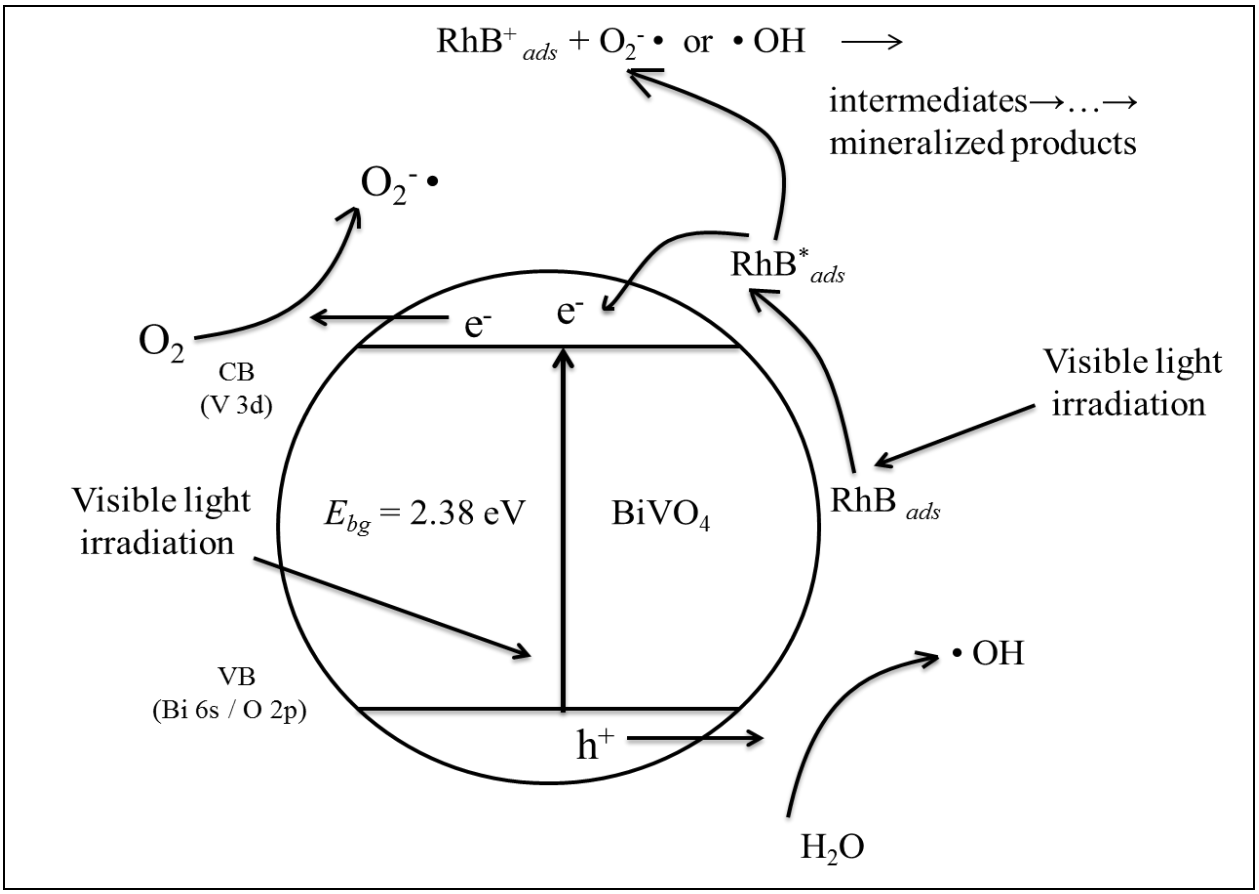

Figure 3.13: Photocatalytic mechanism of $BiVO_4$ (C+H-200-24) over RhB under visible light irradiation.

In accordance with reactions (3.8)-(3.12) and Figure 3.13, the amount of adsorbed RhB and surface-adsorbed molecular oxygen were significant parameters which were dependent on the degree of initial excitation of dye molecules and the yield of molecular oxygen such as O_2^-• and •OH, which were assumed to be responsible for the dye degradation. From the viewpoint of enhancing photocatalytic degradation of RhB, an optimized photocatalyst with higher adsorption-desorption kinetics of dye was also necessary.

In our research, the optimized $BiVO_4$ (C+H-200-24) was able to satisfy these requirements due to its high crystallinity, lower defects content, lower band gap of 2.38 eV and multi-morphological features resulting in high visible-light-induced photocatalytic activity for RhB degradation. In addition, reaction (3.9a) and (3.9b) were presumed to occur simultaneously, because $BiVO_4$ particles with a direct band gap around 2.4 eV [42] could be easily excited by visible light. Concurrently, the electron injected from the excited RhB^*_{ads} into the conduction band of $BiVO_4$ facilitated the stepwise degradation of RhB^+_{ads}, while the injected electron on the

conduction band reduced surface-adsorbed oxidants (e.g. O_2) (3.10a). Meanwhile, reactions (3.10b) and (3.11) occurred sequentially due to sufficient high-energy e^- and h^+ presented in the system. Furthermore, self-photosensitization of dye occurred during the whole visible-light induced photodegradation process via oxidizing O_2^{-}• or •OH radicals in accordance with reaction (3.12) [70], implying that photosensitization was a possible route due to the photolysis. Despite this, the optimized $BiVO_4$ (C+H-200-24) particles exhibited a much higher overall capability for photocatalytic activity presented in Figure 3.9, where $BiVO_4$ particles acting both as electron donors and as electron carriers played a critical role in transporting electrons to acceptors in order to achieve photocatalytic reactions under visible light irradiation, and these holes and electrons reacted with adsorbed RhB both directly and indirectly, improving the photocatalytic degradation of RhB.

3.4 Conclusion

Fine monoclinic $BiVO_4$ particles were synthesized through a facile hydrothermal method using the synthesized potassium metavanadate (KVO_3) as precursor. The synthesized $BiVO_4$ (C+H-200-24) particles had a high crystallinity and multi-morphological features, and they exhibited good visible-light-induced photocatalytic activity for the degradation of RhB. A maximum pseudo-first order degradation rate of 0.0142 min^{-1} was observed for $BiVO_4$ (C+H-200-24). Comparison of the photoactivity observed using samples prepared by various synthesis methods and conditions indicated that adsorption-desorption kinetics, particle size, crystallinity, morphology and optical properties of photocatalysts all influenced the photoactivity obtained. The hydrothermal synthesis promoted the reaction between $Bi(NO_3)_3 \cdot 5H_2O$ and KVO_3, and the interaction of BiO^+ cations with VO_3^- from KVO_3 was thought to be much stronger than from NH_4VO_3 due to the electrostatic forces present during the synthesis. Additionally, the hydrothermal method facilitated the production of more interfacial •OH radicals on $BiVO_4$ particles, promoting reactions between electrons (or holes) and the adsorbed species on $BiVO_4$ particles such as adsorbed O_2 and H_2O, in order to prevent photoexcited electrons and holes from recombining, facilitating photocatalytic decomposition.

3.5 Acknowledgments

This work was funded by the Natural Sciences and Engineering Research Council of Canada (NSERC).The authors would like to thank the Center for Catalysis Research and Innovation and the Department of Earth Sciences at the University of Ottawa for help with sample characterization, and the China Scholarship Council for the financial support.

3.6 References

[1] K. Shantha, K.B.R. Varma, "Preparation and characterization of nanocrystalline powders of bismuth vanadate," *Mater. Sci. Eng., B* vol. 60, pp. 66-75, 1999.

[2] L. Ren, L. Jin, J.B. Wang, F. Yang, M.Q. Qiu, Y. Yu, "Template-free synthesis of $BiVO_4$ nanostructures: I. Nanotubes with hexagonal cross sections by oriented attachment and their photocatalytic property for water splitting under visible light," *Nanotechnol.*, vol. 20, pp. 115603, 2009.

[3] S. Tokunaga, H. Kato, A. Kudo, "Selective preparation of monoclinic and tetragonal $BiVO_4$ with scheelite structure and their photocatalytic properties," *Chem. Mater.*, vol. 13, pp. 4624-4628, 2001.

[4] A.R. Lim, S.H. Choh, J. Min Su, "Prominent ferroelastic domain walls in $BiVO_4$ crystal," *J. Phys. Condens. Matter*, vol. 7, pp. 7309-7323, 1995.

[5] L. Zhou, W. Wang, L. Zhang, H. Xu, W. Zhu, "Single-crystalline $BiVO_4$ microtubes with square cross-sections: Microstructure, growth mechanism, and photocatalytic property," *J. Phys. Chem. C*, vol. 111, pp. 13659-13664, 2007.

[6] A. Walsh, Y. Yan, M.N. Huda, M.M. Al-Jassim, S.-H. Wei, "Band edge electronic structure of $BiVO_4$: Elucidating the role of the Bi s and V d orbitals," *Chem. Mater.*, vol. 21, pp. 547-551, 2009.

[7] A. Kudo, K. Ueda, H. Kato, I. Mikami, "Photocatalytic O_2 evolution under visible light irradiation on $BiVO_4$ in aqueous $AgNO_3$ solution," *Catal. Lett.*, vol. 53, pp. 229-230, 1998.

[8] I.C. Vinke, J. Diepgrond, B.A. Boukamp, K.J. Vries de, A.J. Burggraaf, "Bulk and electrochemical properties of $BiVO_4$," *Solid State Ionics*, vol. 57, pp. 83-89, 1992.

[9] L. Zhou, W. Wang, S. Liu, L. Zhang, H. Xu, W. Zhu, "A sonochemical route to visible-light-driven high-activity $BiVO_4$ photocatalyst," *J. Mol. Catal. A: Chem.*, vol. 252, pp. 120-124, 2006.

[10] N.A. Dhas, K.S. Suslick, "Sonochemical preparation of hollow nanospheres and hollow nanocrystals," *J. Am. Chem. Soc.*, vol. 127, pp. 2368-2369, 2005.

[11] C. Li, G. Pang, S. Sun, S. Feng, "Phase transition of $BiVO_4$ nanoparticles in molten salt and the enhancement of visible-light photocatalytic activity," *J. Nanopart. Res.*, vol. 12, pp. 3069-3075, 2010.

[12] D. Ke, T. Peng, L. Ma, P. Cai, K. Dai, "Effects of hydrothermal temperature on the microstructures of $BiVO_4$ and its photocatalytic O_2 evolution activity under visible light," *Inorg. Chem.*, vol. 48, pp. 4685-4691, 2009.

[13] T. Yang, D. Xia, "Self-assembly of highly crystalline spherical $BiVO_4$ in aqueous solutions," *J. Cryst. Growth*, vol. 311, pp. 4505-4509, 2009.

[14] J.B. Liu, H. Wang, H.M. Zhang, W.X. Zhang, H. Yan, "Preparation of oriented $BiVO_4$ thin film by chemical bath deposition," *J. Phys. Chem. B*, vol. 23, pp. 1299-1302, 2007.

[15] M.C. Neves, T. Trindade, "Chemical bath deposition of $BiVO_4$," *Thin Solid Films*, vol. 406, pp. 93-97, 2002.

[16] K. Sayama, A. Nomura, T. Arai, T. Sugita, R. Abe, M. Yanagida, T. Oi, Y. Iwasaki, Y. Abe, H. Sugihara, "Photoelectrochemical decomposition of water into H_2 and O_2 on porous $BiVO_4$ thin-film electrodes under visible light and significant effect of Ag ion treatment," *J. Phys. Chem. B*, vol. 110, pp. 11352-11360, 2006.

[17] A. Galembeck, O.L. Alves, "$BiVO_4$ thin film preparation by metalorganic decomposition," *Thin Solid Films*, vol. 365, pp. 90-93, 2000.

[18] H. Jiang, H. Endo, H. Natori, M. Nagai, K. Kobayashi, "Fabrication and photoactivities of spherical-shaped $BiVO_4$ photocatalysts through solution combustion synthesis method," *J. Eur. Ceram. Soc.*, vol. 28, pp. 2955-2962, 2008.

[19] U.M. García-Pérez, S. Sepúlveda-Guzmán, A. Martínez-De La Cruz, "Nanostructured $BiVO_4$ photocatalysts synthesized via a polymer-assisted coprecipitation method and their photocatalytic properties under visible-light irradiation," *Solid State Sci.*, vol. 14, pp. 293-298, 2012.

[20] Q. Chen, M. Zhou, D. Ma, D. Jing, "Effect of preparation parameters on photoactivity of $BiVO_4$ by hydrothermal method," *J. Nanomater*, vol. 2012, pp. 2012.

[21] H. Li, G. Liu, X. Duan, "Monoclinic $BiVO_4$ with regular morphologies: Hydrothermal synthesis, characterization and photocatalytic properties," *Mater. Chem. Phys.*, vol. 115, pp. 9-13, 2009.

[22] G. Li, D. Zhang, J.C. Yu, "Ordered mesoporous $BiVO_4$ through nanocasting: A superior visible light-driven photocatalyst," *Chem. Mater.*, vol. 20, pp. 3983-3992, 2008.

[23] F. Rullens, A. Laschewsky, M. Devillers, "Bulk and thin films of bismuth vanadates prepared from hybrid materials made from an organic polymer and inorganic salts," *Chem. Mater.*, vol. 18, pp. 771-777, 2006.

[24] A. Kudo, K. Omori, H. Kato, "A novel aqueous process for preparation of crystal form-controlled and highly crystalline $BiVO_4$ powder from layered vanadates at room temperature and its photocatalytic and photophysical properties," *J. Am. Chem. Soc.*, vol. 121, pp. 11459-11467, 1999.

[25] L. Sui, L. Yu, Y. Zhang, "Surface and catalytic properties of K/V catalysts coating on porous Al_2O_3 substrate," *J. Dispersion Sci. Technol.*, vol. 28, pp. 285-289, 2007.

[26] A.D. Kelmers, "Compounds in the system $KVO_3 \bullet V_2O_5$," *J. Inorg. Nucl. Chem.*, vol. 23, pp. 279-283, 1961.

[27] M. Trypuć, Z. Torski, U. Kiełkowska, "Experimental determination of the optimum conditions of KVO_3 synthesis based on KCl and V_2O_5 in the presence of steam," *Ind. Eng. Chem. Res.*, vol. 40, pp. 1022-1025, 2001.

[28] J. Liu, H. Wang, S. Wang, H. Yan, "Hydrothermal preparation of $BiVO_4$ powders," *Mater. Sci. Eng., B*, vol. 104, pp. 36-39, 2003.

[29] C.-M. Huang, G.-T. Pan, Y.-C.M. Li, M.-H. Li, T.C.K. Yang, "Crystalline phases and photocatalytic activities of hydrothermal synthesis Ag_3VO_4 and $Ag_4V_2O_7$ under visible light irradiation," *Appl. Catal., A*, vol. 358, pp. 164-172, 2009.

[30] Z. Zhang, W. Wang, M. Shang, W. Yin, "Photocatalytic degradation of rhodamine B and phenol by solution combustion synthesized $BiVO_4$ photocatalyst," *Catal. Commun.*, vol. 11, pp. 982-986, 2010.

[31] J. Yan, G. Wu, N. Guan, L. Li, Z. Li, X. Cao, "Understanding the effect of surface/bulk defects on the photocatalytic activity of TiO_2: anatase versus rutile," *Phys. Chem. Chem. Phys.*, vol. 15, pp. 10978-10988, 2013.

[32] A. Kudo, Y. Miseki, "Heterogeneous photocatalyst materials for water splitting," *Chem. Soc. Rev.*, vol. 38, pp. 253-278, 2009.

[33] Y. Zhou, K. Vuille, A. Heel, B. Probst, R. Kontic, G.R. Patzke, "An inorganic hydrothermal route to photocatalytically active bismuth vanadate," *Appl. Catal., A*, vol. 375, pp. 140-148, 2010.

[34] J. Yu, A. Kudo, "Effects of structural variation on the photocatalytic performance of hydrothermally synthesized $BiVO_4$," *Adv. Funct. Mater.*, vol. 16, pp. 2163-2169, 2006.

[35] M. Trypuć, D.I. Stefanowicz, "Solubility in the $KVO_3 + NH_4VO_3 + H_2O$ system," *J. Chem. Eng. Data*, vol. 42, pp. 1140-1144, 1997.

[36] H.T. Evans, S. Block, "The crystal structures of potassium and cesium trivanadates," *Inorg. Chem.*, vol. 5, pp. 1808-1814, 1966.

[37] A. Iwase, A. Kudo, "Photoelectrochemical water splitting using visible-light-responsive $BiVO_4$ fine particles prepared in an aqueous acetic acid solution," *J. Mater. Chem.*, vol. 20, pp. 7536-7542, 2010.

[38] W. Yin, W. Wang, M. Shang, L. Zhou, S. Sun, L. Wang, "$BiVO_4$ hollow nanospheres: Anchoring synthesis, growth mechanism, and their application in photocatalysis," *Eur. J. Inorg. Chem.*, vol. 2009, pp. 4379-4384, 2009.

[39] J. Joo, B.Y. Chow, M. Prakash, E.S. Boyden, J.M. Jacobson, "Face-selective electrostatic control of hydrothermal zinc oxide nanowire synthesis," *Nat. Mater.*, vol. 10, pp. 596-601, 2011.

[40] C. Hariharan, "Photocatalytic degradation of organic contaminants in water by ZnO nanoparticles: Revisited," *Appl. Catal., A*, vol. 304, pp. 55-61, 2006.

[41] W. Yu, J. Wang, Z. Gou, W. Zeng, W. Guo, L. Lin, "Hydrothermal synthesis of vanadium pentoxide nanostructures and their morphology control," *Ceram. Int.*, vol. 39, pp. 2639-2643, 2013.

[42] W.E. Morgan, W.J. Stec, J.R. Van Wazer, "Inner-orbital binding-energy shifts of antimony and bismuth compounds," *Inorg. Chem.*, vol. 12, pp. 953-955, 1973.

[43] H. Jiang, H. Dai, X. Meng, L. Zhang, J. Deng, Y. Liu, C.T. Au, "Hydrothermal fabrication and visible-light-driven photocatalytic properties of bismuth vanadate with multiple morphologies and/or porous structures for methyl orange degradation," *J. Environ. Sci.*, vol. 24, pp. 449-457, 2012.

[44] Q. Jia, K. Iwashina, A. Kudo, "Facile fabrication of an efficient $BiVO_4$ thin film electrode for water splitting under visible light irradiation," *Proc. Natl. Acad. Sci. U.S.A.*, vol. 109, pp. 11564-11569, 2012.

[45] W. Liu, S.Y. Lai, H. Dai, S. Wang, H. Sun, C.T. Au, "Oxidative dehydrogenation of n-butane over mesoporous VO_x /SBA-15 catalysts," *Catal. Lett.*, vol. 113, pp. 147-154, 2007.

[46] G. Wang, Y. Ling, X. Lu, F. Qian, Y. Tong, J.Z. Zhang, V. Lordi, C. Rocha Leao, Y. Li, "Computational and photoelectrochemical study of hydrogenated bismuth vanadate," *J. Phys. Chem. C*, vol. 117, pp. 10957-10964, 2013.

[47] W.E. Slink, P.B. DeGroot, "Vanadium-titanium oxide catalysts for oxidation of butene to acetic acid," *J. Catal.*, vol. 68, pp. 423-432, 1981.

[48] G.U. Kulkarni, C.N.R. Rao, M.W. Roberts, "Nature of the oxygen species at Ni(110) and Ni(100) surfaces revealed by exposure to oxygen and oxygen-ammonia mixtures: Evidence for the surface reactivity of O-type species," *J. Phys. Chem.*, vol. 99, pp. 3310-3316, 1995.

[49] P.M. Blass, X.L. Zhou, J.M. White, "Coadsorption and reaction of water and potassium on silver(III)," *J. Phys. Chem.*, vol. 94, pp. 3054-3062, 1990.

[50] D. Wang, J. Tang, Z. Zou, J. Ye, "Photophysical and photocatalytic properties of a new series of visible-light-driven photocatalysts $M_3V_2O_8$ (M = Mg, Ni, Zn)," *Chem. Mater.*, vol. 17, pp. 5177-5182, 2005.

[51] H. Fu, C. Pan, W. Yao, Y. Zhu, "Visible-light-induced degradation of rhodamine B by nanosized Bi_2WO_6," *J. Phys. Chem. B*, vol. 109, pp. 22432-22439, 2005.

[52] J. Tang, Z. Zou, J. Ye, "Efficient photocatalytic decomposition of organic contaminants over $CaBi_2O_4$ under visible-light irradiation," *Angew. Chem. Int. Ed.*, vol. 43, pp. 4463-4466, 2004.

[53] A. Henglein, "Nanoclusters of semiconductors and metals: Colloidal nano-particles of semiconductors and metals: Electronic structure and processes," *Ber. Bunsenges. Phys. Chem.*, vol. 101, pp. 1562-1572, 1997.

[54] D. Beydoun, R. Amal, G. Low, S. McEvoy, "Role of nanoparticles in photocatalysis," *J. Nanopart. Res.*, vol. 1, pp. 439-458, 1999.

[55] J. Yu, H. Yu, B. Cheng, X. Zhao, J.C. Yu, W. Ho, "The effect of calcination temperature on the surface microstructure and photocatalytic activity of TiO_2 thin films prepared by liquid phase deposition," *J. Phys. Chem. B*, vol. 107, pp. 13871-13879, 2003.

[56] W. Sun, J. Li, G. Mele, Z. Zhang, F. Zhang, "Enhanced photocatalytic degradation of rhodamine B by surface modification of ZnO with copper (II) porphyrin under both UV–vis and visible light irradiation," *J. Mol. Catal. A: Chem.*, vol. 366, pp. 84-91, 2013.

[57] J. Zhao, C. Chen, W. Ma, "Photocatalytic degradation of organic pollutants under visible light irradiation," *Top. Catal.*, vol. 35, pp. 269-278, 2005.

[58] J.-M. Herrmann, "Heterogeneous photocatalysis: Fundamentals and applications to the removal of various types of aqueous pollutants," *Catal. Today*, vol. 53, pp. 115-129, 1999.

[59] C. Baumanis, D.W. Bahnemann, "TiO_2 thin film electrodes: Correlation between photocatalytic activity and electrochemical properties," *J. Phys. Chem. C*, vol. 112, pp. 19097-19101, 2008.

[60] S. Horikoshi, A. Saitou, H. Hidaka, N. Serpone, "Environmental remediation by an integrated microwave/UV illumination method. V. Thermal and nonthermal effects of microwave radiation on the photocatalyst and on the photodegradation of Rhodamine-B under UV/Vis radiation," *Environ. Sci. Technol.*, vol. 37, pp. 5813-5822, 2003.

[61] Z. He, C. Sun, S. Yang, Y. Ding, H. He, Z. Wang, "Photocatalytic degradation of rhodamine B by Bi_2WO_6 with electron accepting agent under microwave irradiation: Mechanism and pathway," *J. Hazard. Mater.*, vol. 162, pp. 1477-1486, 2009.

[62] F. Chen, J. Zhao, H. Hidaka, "Highly selective deethylation of rhodamine B: Adsorption and photooxidation pathways of the dye on the TiO_2/SiO_2 composite photocatalyst," *Int. J. Photoenergy*, vol. 5, pp. 209-217, 2003.

[63] L. Jing, B. Xin, F. Yuan, B. Wang, K. Shi, W. Cai, H. Fu, "Deactivation and regeneration of ZnO and TiO_2 nanoparticles in the gas phase photocatalytic oxidation of n-C_7H_{16} or SO_2," *Appl. Catal., A*, vol. 275, pp. 49-54, 2004.

[64] M. Long, W. Cai, J. Cai, B. Zhou, X. Chai, Y. Wu, "Efficient photocatalytic degradation of phenol over $Co_3O_4/BiVO_4$ composite under visible light irradiation," *J. Phys. Chem. B*, vol. 110, pp. 20211-20216, 2006.

[65] M. Stylidi, D.I. Kondarides, X.E. Verykios, "Visible light-induced photocatalytic degradation of Acid Orange 7 in aqueous TiO_2 suspensions," *Appl. Catal., B*, vol. 47, pp. 189-201, 2004.

[66] P. Raja, A. Bozzi, H. Mansilla, J. Kiwi, "Evidence for superoxide-radical anion, singlet oxygen and OH-radical intervention during the degradation of the lignin model compound (3-methoxy-4-hydroxyphenylmethylcarbinol)," *J. Photochem. Photobiol., A*, vol. 169, pp. 271-278, 2005.

[67] H. Lin, H. Ye, S. Chen, Y. Chen, "One-pot hydrothermal synthesis of $BiPO_4$/$BiVO_4$ with enhanced visible-light photocatalytic activities for methylene blue degradation," *RSC Adv.*, vol. 4, pp. 10968-10974, 2014.

[68] W. Li, D. Li, W. Zhang, Y. Hu, Y. He, X. Fu, "Microwave synthesis of $Zn_xCd_{1-x}S$ nanorods and their photocatalytic activity under visible light," *J. Phys. Chem. C*, vol. 114, pp. 2154-2159, 2010.

[69] J. Wang, X. Yang, J. Chen, J. Xian, S. Meng, Y. Zheng, Y. Shao, D. Li, "Photocatalytic activity of novel $Ag_4V_2O_7$ photocatalyst under visible light irradiation," *J. Am. Ceram. Soc.*, vol. 97, pp. 267-274, 2014.

[70] T. Wu, G. Liu, J. Zhao, H. Hidaka, N. Serpone, "Photoassisted degradation of dye pollutants. V. self-photosensitized oxidative transformation of rhodamine B under visible light irradiation in aqueous TiO_2 dispersions," *J. Phys. Chem. B*, vol. 102, pp. 5845-5851, 1998.

Chapter 4

$Ag_2O/Ag_3VO_4/Ag_4V_2O_7$ heterogeneous photocatalyst prepared by a facile hydrothermal synthesis with enhanced photocatalytic performance under visible light irradiation

Rong Ran, Joanne Gamage McEvoy, Zisheng Zhang

Material Research Bulletin

Abstract

A novel $Ag_2O/Ag_3VO_4/Ag_4V_2O_7$ photocatalyst was synthesized by adjusting the molar ratio of silver-vanadium (Ag-V) in a facile hydrothermal method to obtain multi-phase $Ag_2O/Ag_3VO_4/Ag_4V_2O_7$ photocatalyst. The photocatalytic activity of the prepared samples was quantified by the degradation of rhodamine B (RhB) model organic pollutant under visible light irradiation. Compared to pure Ag_3VO_4, $Ag_4V_2O_7$ and P25 TiO_2, respectively, the as-synthesized multi-phase $Ag_2O/Ag_3VO_4/Ag_4V_2O_7$ powders gave rise to a significantly higher photocatalytic activity, achieving up to 99% degradation of RhB in 2 h under visible light. This enhanced photocatalytic performance was attributed to the effect of the multi-phase $Ag_2O/Ag_3VO_4/Ag_4V_2O_7$ photocatalyst and the surface plasmon resonance (SPR) of the incorporated metallic silver (Ag^0) nanoparticles (NPs) generated during the photocatalysis, as evidenced by post-use characterization, resulting in improved visible light absorption and electron-hole (e^--h^+) separation. A mechanism was proposed for the photocatalytic degradation of RhB on the surface of $Ag_2O/Ag_3VO_4/Ag_4V_2O_7$.

Keywords: Photocatalysis, Multi-phase $Ag_2O/Ag_3VO_4/Ag_4V_2O_7$, Silver vanadate, Multi-morphology.

4.1 Introduction

Strategies for the development of ternary metal oxides have been investigated in recent years as an alternate route for the fabrication of highly efficient photocatalysts, which can be used for photocatalytic degradation and water splitting applications [1-4]. Numerous ternary metal-oxide photocatalysts have been reported in literature, such as Ag_3VO_4 [5], $Ag_4V_2O_7$ [6], β-$AgVO_3$ [7], $AgNbO_3$ [8], $AgMO_2$ (M = Al, Ga, In) [9, 10], Ag_2CO_3 [11] , and Ag_3PO_4 [12] and have been found to exhibit enhanced photocatalytic performance under visible light irradiation (VLI), compared to the traditional TiO_2 photocatalyst [13].

Despite these research efforts, single phase ternary metal-oxide photocatalysts tend to suffer from poor visible light absorption due to the number of grain boundaries present [1, 14]. These defects usually serve as recombination centers, and impede the effective transfer of the photogenerated electrons (e^-) and holes (h^+) to adsorbed organic pollutants by trapping the separated charge species [1, 14, 15]. In addition, large specific surface area is a prerequisite for the effective photocatalytic degradation of organic pollutants, as it contributes to increasing the transfer rate of photogenerated charges, improving carrier separation, and increasing surface reactivity during adsorption-desorption equilibration [16-20].

An approach to improving photocatalytic performance under VLI has been in the development and preparation of heterogeneous photocatalysts based upon silver species. For example, Xue et al [21] reported that novel Ag_2O/N-doped helical carbon nanotubes (Ag_2O/N–HCNTs) were successfully synthesized via a simple co-precipitation of N–HCNTs and Ag_2O, respectively, which gave rise to the high photocatalytic performance towards degradation of methylene blue (MB) and showed good stability in multiple degradation cycles under visible light irradiation. Similarly, Wang et al. [22] investigated Ag_2O/Ag_3PO_4 heterostructured photocatalyst prepared by ion-exchange synthesis of Ag_3PO_4 and subsequent precipitation. The heterostructures prepared exhibited a much higher degradation of methyl orange (MO) and phenol than the pure Ag_3PO_4, and possessed good stability in the aqueous photosystem under VLI. Highly efficient p-n junction Ag_2O-decorated flower-like ZnO photocatalyst exhibited high photoactivity towards MO under ultraviolet (UV) irradiation by transferring photogenerated carriers and suppressing the e-h recombination rate [23]. Zhou et al. [24] reported that the photocatalytic activity of

Ag_2O/TiO_2 nanobelts' heterostructure was attributed to the Ag_2O NPs scattered uniformly on the surface of TiO_2, giving rise to the higher photocatalytic decomposition of MO under both UV and VLI. However, the conventional syntheses employed to prepare these heterostructure-containing visible-light-induced photocatalysts are multi-step, time-consuming procedures.

In this work, we propose a facile approach to obtain multi-phase $Ag_2O/Ag_3VO_4/Ag_4V_2O_7$ photocatalyst with high photocatalytic performance under VLI, fabricated via a hydrothermal process and changing the ratio of elements employed in the synthesis procedure. The prepared photocatalysts were then studied for the degradation of RhB organic dye. The novel heterogeneous $Ag_2O/Ag_3VO_4/Ag_4V_2O_7$ photocatalyst could improve the utilization of light to enhance the degradation of organic pollutants via the synergistic effects among these three photosensitive phases. To the best of our knowledge, this approach to the preparation of multi-phase $Ag_2O/ Ag_3VO_4/Ag_4V_2O_7$ has not yet been reported.

4.2 Experimental

4.2.1 Synthesis

Multi-phase $Ag_2O/Ag_3VO_4/Ag_4V_2O_7$ photocatalyst was synthesized via hydrothermal method using potassium metavanadate (KVO_3) and silver nitrate as starting materials. KVO_3 was prepared by calcination, where 0.38 g K_2CO_3 (Fisher Scientific, Certified ACS) and 0.5 g V_2O_5 (ACROS Organics, 99.6%) were dissolved in 35 mL deionized water (DW) under vigorous magnetic stirring. The resulting red solution was poured into an evaporation dish, and dried overnight at 50 °C in an oven (Sheldon Manufacturing, Inc. Model No: 1350 GM). The dry sample was then ground in an agate mortar and annealed in air at 457 °C (730 K) for 5 h, yielding a pink KVO_3 powder.

To prepare the multi-phase $Ag_2O/Ag_3VO_4/Ag_4V_2O_7$ powders, the molar ratio of silver to vanadium (Ag to V) used was 6:1.5. 15 mL of as-prepared KVO_3 solution was heated in a water bath at 60 °C for 3 min, and 60 mL of 0.1 M $AgNO_3$ (Fisher Scientific, Certified ACS) was then added dropwise and allowed to react under continuous stirring for 30 min to obtain an orange-yellow slurry. The pH of the resulting slurry was then adjusted by adding 1M KOH, until a final pH of 7 was reached, as measured by a pH meter (Fisher Scientific, accumet basic, AB 15 pH

meter). The slurry was then transferred into 45 mL Teflon-lined stainless steel autoclave reactors, and the reaction was allowed to proceed at 140 °C for 8 h. The resulting solid was collected by filtration, washed five times with DW, and dried in an oven at 110 °C for 6 h. The temperatures and times selected for the hydrothermal process were based upon the study by Huang et al. [25].

For comparison, pure Ag_3VO_4 was also prepared via the described method, but applying a molar ratio of Ag - V of 3: 1. Single phase $Ag_4V_2O_7$ (Ag - V of 3: 1) was also similarly prepared, but adding Cetyltrimethyl Ammonium Bromide (CTAB, $C_{19}H_{49}BrN$) (ACROS Chemical, 99 + %) as a structural agent at a molar ratio of 0.05:1 (CTAB: silver), in accordance with the report of Huang et al. [25, 26].

4.2.2 Characterization

Powder X-ray diffraction (XRD) measurements were carried out in Bragg–Brentano geometry on a Rigaku Ultima IV apparatus with Cu Kα1 (λ = 0.15418 nm) radiation, operating at 40 kV and 44 mA, and with a scanning range of 2θ from 15° to 70°. Transmission electron microscopy (TEM) images were obtained using an FEI (formerly Phillips) Tecnai G2 F20 field emission transmission electron microscope at an acceleration voltage of 200 keV. Scanning electron microscopy (SEM) images were obtained with a Tescan VegaII XMU electron microscope operated at 20 kV, with Au/Pd alloy coated samples (coated with an Anatech Hummer VII sputter coater). SEM-EDS was performed using an energy dispersive X-ray detector. X-ray photoelectron spectroscopy (XPS) was conducted on a Kratos Analytical Axis Ultra DLD instrument with mono-chromated Al X-rays at 140 W. The powder UV-Vis diffuse reflectance spectra (DRS) were recorded on a Thermo Evolution 300 UV/Vis spectrophotometer equipped with a Praying Mantis diffuse reflectance accessory, and the spectra were collected at a scan rate of 240 nm min^{-1}. UV/Vis spectra of RhB samples were obtained via a Biochrom Ultrospec 60 UV/Vis spectrophotometer.

4.2.3 Photocatalytic activity

Photocatalytic performance was quantified by the decomposition of RhB (Sigma-Aldrich) as a model organic pollutant under VLI. A slurry reactor was placed in a reflective housing to prevent outside light from entering the reactor, and inside light from exiting the system.

A 300-W ELH tungsten halide bulb (Ushio) was used as a light source with a 410 nm cut-off filter (Kenko Zeta, $\lambda > 410$ nm, transmittance > 90%) to provide visible light irradiation. The light source was placed at a distance of 15 cm from the top of the slurry. The corresponding irradiation was measured using a quantum meter (Biospherical QSL-2100; 400 nm < λ < 700 nm), and was found to be approximately 10.9×10^{-3} Einstein·m^{-2}·s^{-1}. Cooling was provided by an external cooling jacket, and the temperature of the reaction was controlled to 20 °C ± 2.

Before illumination, 0.15 g of photocatalyst dispersed into 150 mL of 15 mg·L^{-1} RhB solution was allowed to reach adsorption-desorption equilibrium under continuous magnetic stirring at 280 rpm for 30 min in the dark. Irradiation was then provided for 2 h. Samples were withdrawn at 15 min time intervals and separated by centrifugation at 10×10^3 rpm for 3 min in an accuSpin Micro 17 (Fisher Scientific) microcentrifuge to remove the suspended catalyst. The supernatant fluid was then analyzed by monitoring the peak absorbance (λ = 554 nm for RhB) with a Genysys 10-UV spectrophotometer (Geneq Inc.). A standard curve for RhB was prepared and the concentration was determined by the measured absorbance and the Beer-Lambert Law.

In the recyclability studies, the used, unwashed photocatalysts were separated by centrifugation after each run, the degraded RhB supernatant removed, and fresh 15 mg·L^{-1} RhB solution added. The roles of various reactive species were studied by employing reactive species scavengers (including tert-butyl alcohol (TBA) (Sigma-Aldrich, ACS), benzoquinone (BQ) (reagent-grade ≥ 98%, Sigma-Aldrich) and ammonium oxalate (AO) (ACS, Sigma-Aldrich)), using the same procedures and methodology described above.

4.3 Results and discussion

4.3.1 XRD analysis

The XRD pattern of the fresh, multi-phase photocatalyst obtained via hydrothermal synthesis is shown in Figure 4.1.

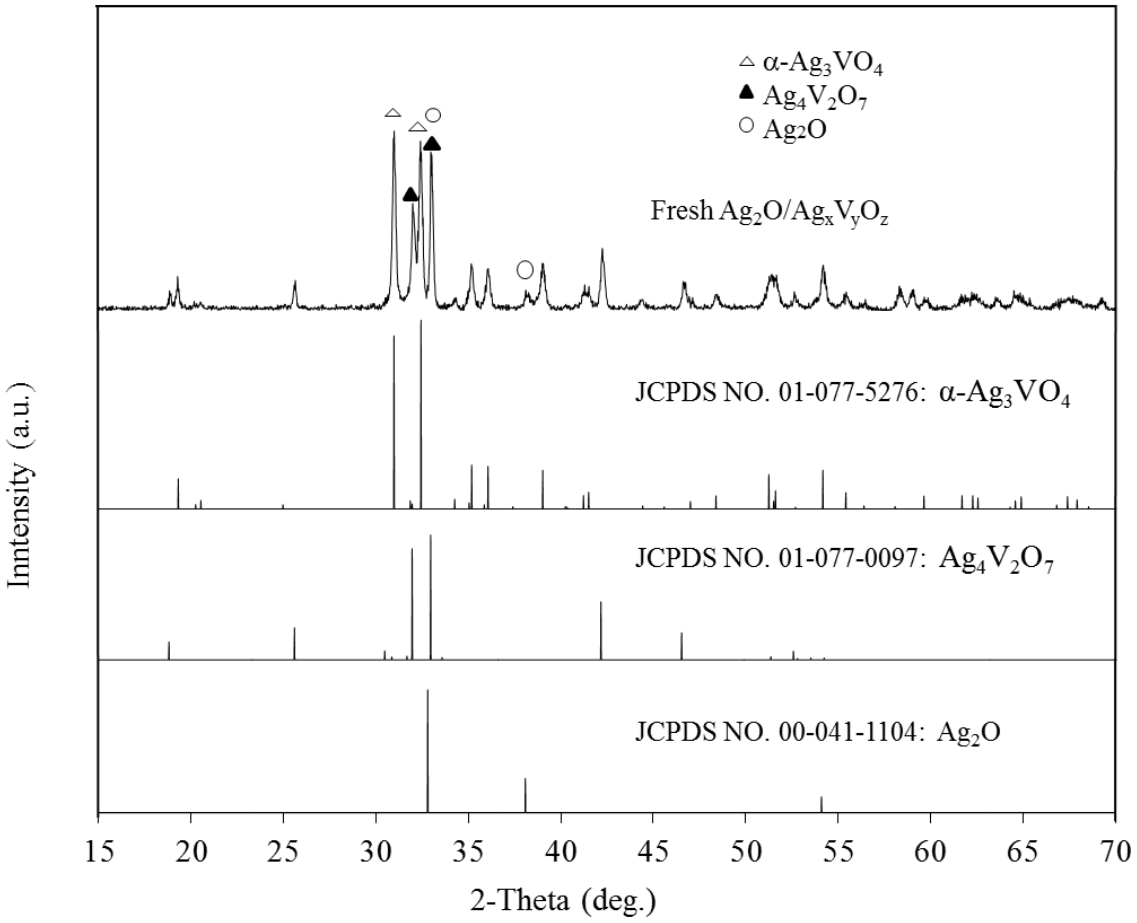

Figure 4.1: XRD pattern of fresh multi-phase $Ag_2O/Ag_3VO_4/Ag_4V_2O_7$ photocatalyst.

The pattern observed was found to exhibit features of the α-Ag_3VO_4 (JCPDS Card No. 01-077-5276), $Ag_4V_2O_7$ (JCPDS Card No.01-077-0097), and silver oxide phases (JCPDS Card No. 00-041-1104), respectively. The major reflections for the α-Ag_3VO_4 phase occurred at 32.42° (3 1 2) and 30.96° (1 1 2), while the major peaks of the $Ag_4V_2O_7$ structure were observed at 32.93° (0 4 0) and 31.93° (2 2 4), and the reflection of the silver oxide peaks was identified at 32.79° (1 1 1)

and 38.07° (2 0 0) with low intensity, suggesting that a low amount of Ag_2O was present in the fresh sample.

4.3.2 TEM analysis

As shown in Figures 4.2a and b, the fresh multi-phase $Ag_2O/Ag_3VO_4/Ag_4V_2O_7$ photocatalyst was observed to range from 0.5 μm to 4 μm, and was decorated with Ag_2O NPs clusters ranging from 50 nm to 180 nm; similar results were reported by Yang et al. [27].

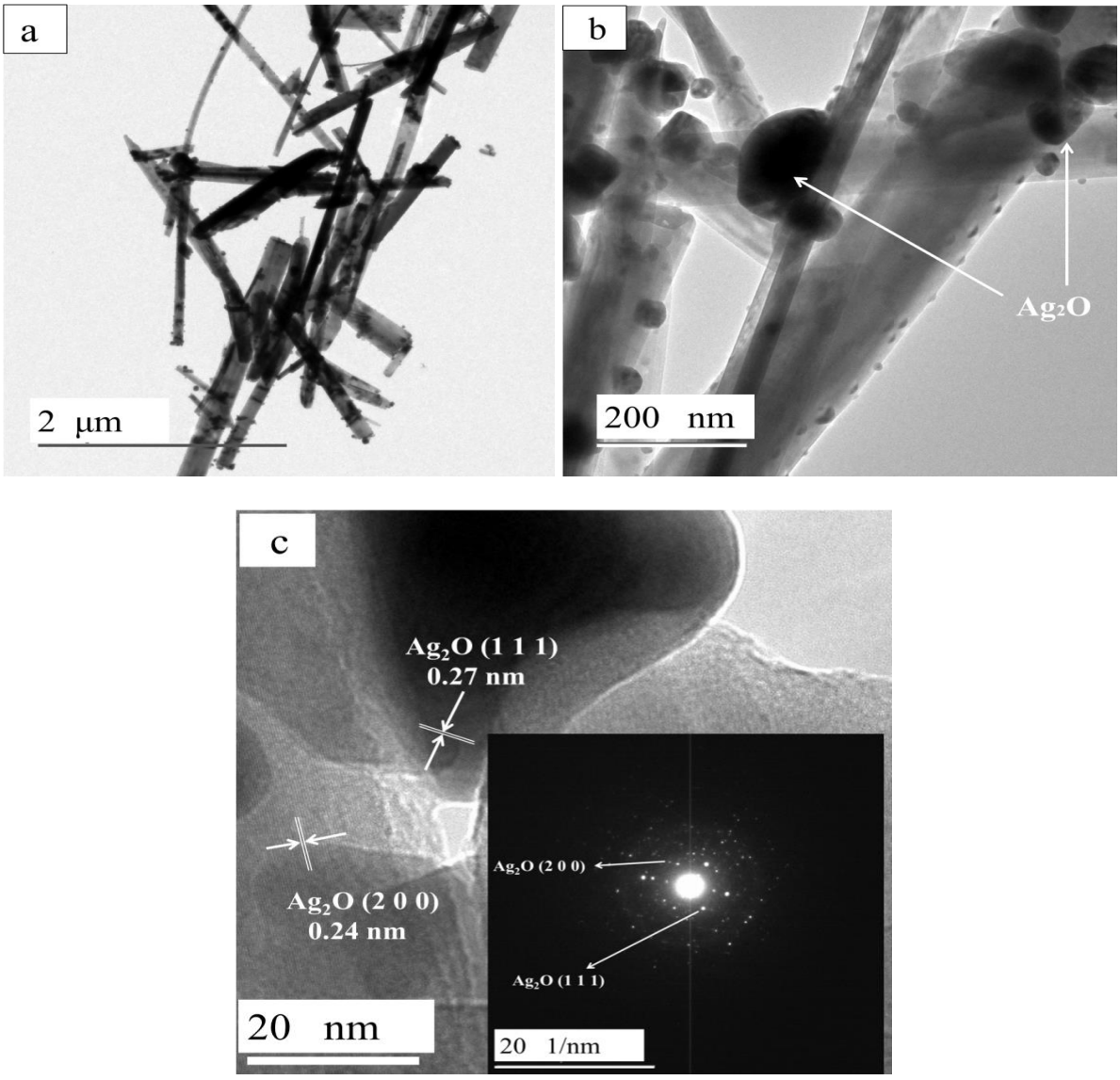

Figure 4.2: TEM images of (a and b) multi-phase $Ag_2O/Ag_3VO_4/Ag_4V_2O_7$; (c) high-resolution TEM of multi-phase $Ag_2O/Ag_3VO_4/Ag_4V_2O_7$ composite (SAED patterns shown inset).

As seen in Figure 4.2c, the high-resolution TEM (HRTEM) of the multi-phase $Ag_2O/Ag_3VO_4/Ag_4V_2O_7$ photocatalyst exhibited lattice spacings of 0.27 nm and 0.24 nm, which corresponded to *d-spacings* of Ag_2O (1 1 1) and (2 0 0) planes of silver oxide. Also, the selected area electron diffraction (SAED) patterns shown in the inset of Figure 4.2c further confirmed the crystal structure of Ag_2O present in the multi-phase crystalline structure of $Ag_2O/Ag_3VO_4/Ag_4V_2O_7$ photocatalyst, demonstrating that the as-prepared silver species sample was polycrystalline structure in nature. The rings were ascribed to diffraction from the (1 1 1) and (2 0 0) reflections of Ag_2O phase (JCPDS Card No. 00-041-1104), based on the calculated *d-spacings* of 2.73 Å and 2.36 Å, respectively.

4.3.3 SEM and EDS analyses

The morphologies present in the synthesized multi-phase $Ag_2O/Ag_3VO_4/Ag_4V_2O_7$ photocatalyst were explored by SEM. The corresponding EDS spectra were also studied to qualitatively investigate the components present in the $Ag_2O/Ag_3VO_4/Ag_4V_2O_7$ photocatalyst, and the results are shown in Figures 4.3a and 4.3b, respectively.

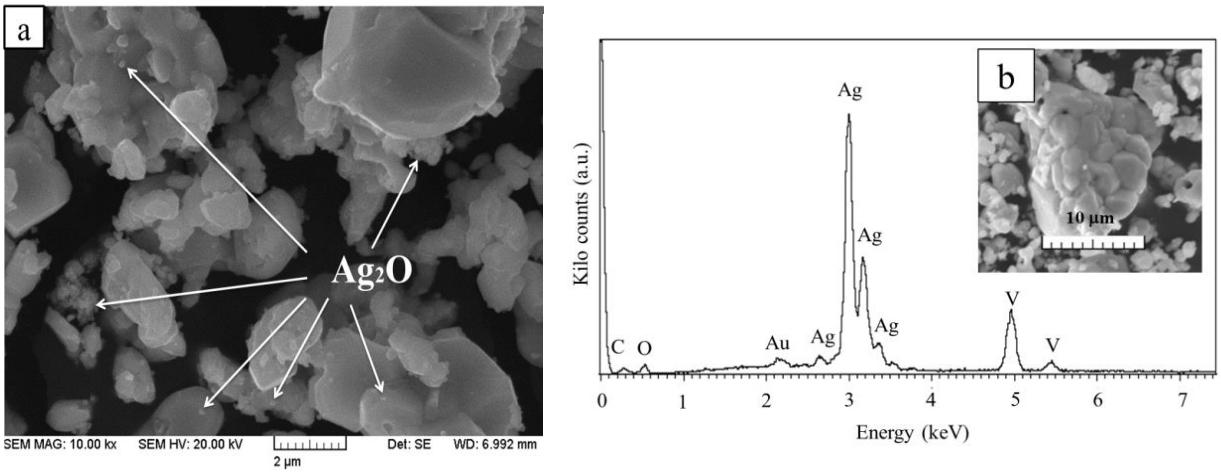

Figure 4.3: (a) SEM image of fresh multi-phase $Ag_2O/Ag_3VO_4/Ag_4V_2O_7$ photocatalyst and (b): corresponding EDS data.

As shown in Figure 4.3a, the fresh $Ag_2O/Ag_3VO_4/Ag_4V_2O_7$ photocatalyst exhibited plate-like morphology with size ranges from 0.5 µm to 4 µm, which agreed with the results reported by Pan et al. [28], and were sparsely decorated with Ag_2O NPs, agreed with the report by Zhou et al. [24] and the results observed from XRD and TEM. According to the results shown in Figure 4.3b,

EDS data showed that only the silver, vanadium and oxygen elements constituted the as-synthesized sample. The results indicated that no other elements occurred as impurities in the prepared $Ag_2O/Ag_3VO_4/Ag_4V_2O_7$. It should be noted that the Au peak occurred as a result of the sputter coating, and carbon was attributed to the adsorbed carbon present in the samples.

4.3.4 XPS analysis

To investigate the chemical and electronic states present in the prepared multi-phase photocatalyst, XPS analyses of the fresh $Ag_2O/Ag_3VO_4/Ag_4V_2O_7$ were conducted, and the corresponding high resolution XPS spectral patterns are shown in Figures 4.4a-c, for Ag 3d, V 2p and O 1s states, respectively.

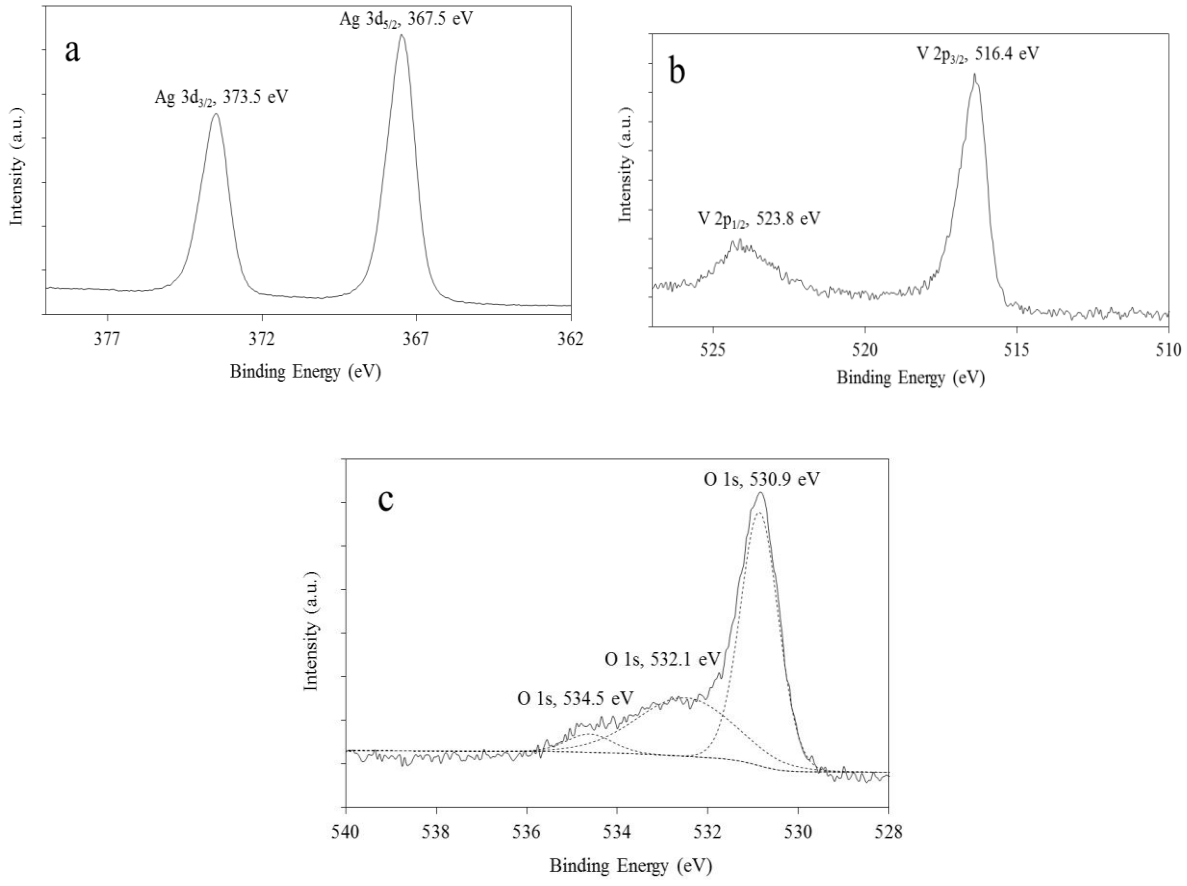

Figure 4.4: XPS spectra of (a) Ag 3d, (b) V 2p and (c) O 1s.

As shown in Figure 4.4a, the spectra of the Ag species exhibited two symmetric peaks located at binding energies of 367.5 eV and of 373.5 eV, with a separation of 6 eV, ascribed to the spin-

orbit splitting characteristic of Ag $3d_{5/2}$ and Ag $3d_{3/2}$, respectively, and corresponding to Ag^{+} [29, 30]. The binding energy observed at 367.5 eV and 373.5 eV indicated that silver was probably in the state of oxides [31], agreeing with the results in shown in XRD and SEM. No peaks attributable to Ag^{0} (located at 368.3 eV and 374.5 eV) [30, 32, 33] were observed, indicating that no Ag^{0} NPs existed in the fresh sample.

The observed peak shown in Figure 4.4b at a binding energy of 516.4 eV was attributed to the V $2p_{3/2}$ orbital, and that at 523.8 eV to the V $2p_{1/2}$ orbital, indicating that the vanadium was present in the form of V^{5+} [7], which corresponds well with the data expected from KVO_3 [34].

The oxygen peak in Figure 4.4c for the O 1s spectra was observed to be broad and was deconvoluted into three separate peaks (dashed lines in Figure 4.4c). The main peak occuring at binding energy of 530.9 eV was thought to be dominant, while the peaks located at binding energies of 532.1 eV and 534.5 eV were of lower intensity, and indicated that the oxygen species was not purely ionic but also contained metal-oxygen bonds with covalent characteristics [29]. The main peak at 530.9 eV was considered to be oxygen species in the presence of covalent mixing states. As reported in literature, the oxide ions, such as O^{2-}, would have given rise to a single Gaussian peak around 532 eV [29]. However, the results obtained indicated that the oxygen species present contained mainly covalent characteristics in the presence of dominant metal-oxygen bonds rather than pure oxide ionic states.

This covalent characteristic with metal-oxygen bonds promoted a shift of the broad oxygen peak observed, in which binding energies of 532.1 eV and 534.5 eV were attributed to the lattice oxygen in the multi-phase silver speices composite, and the absorbed oxygen, respectively [35]. Therefore, the results suggested the existence of covalent bonding including the Ag-O bonding [36] and between the vanadium and oxygen in the form of $(VO_4)^{3-}$ and $(V_2O_7)^{4-}$ species [29], respectively, which were also confirmed with the results in SAED patterns and EDS data present in the previous section.

4.3.5 Optical properties

In order to estimate the band gap energy of the fresh $Ag_2O/Ag_3VO_4/Ag_4V_2O_7$, UV-Vis diffuse reflectance spectra of the samples were investigated and the corresponding patterns indicating intrinsic absorption in the visible light region are shown in Figure 4.5.

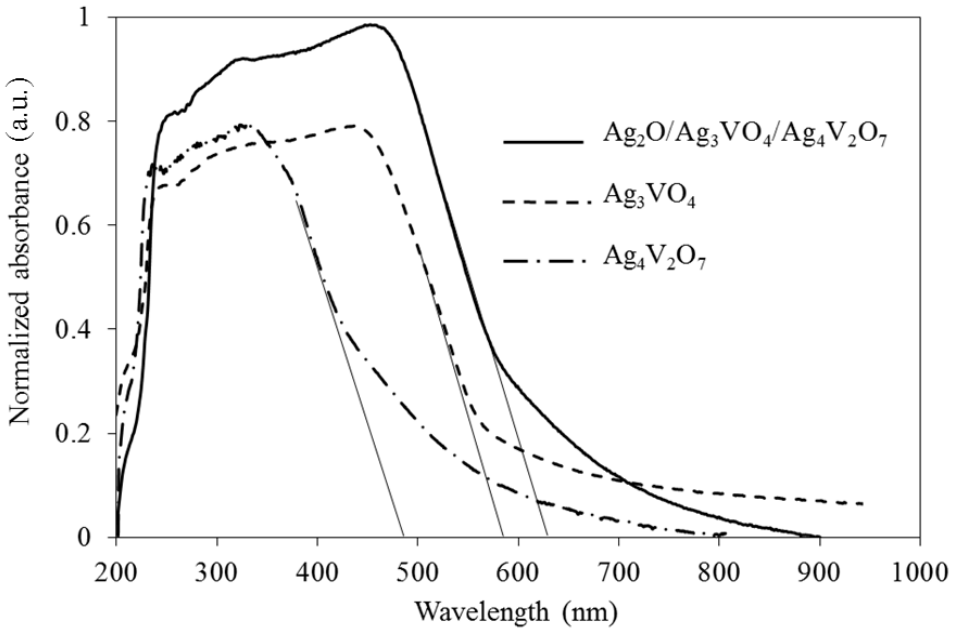

Figure 4.5: UV-Vis diffuse reflectance spectra (DRS) of various fresh samples.

The band gap energies of the as-prepared fresh catalysts were estimated by the DRS data and the following equation:

$$\lambda = 1240/E_{bg} \qquad (4.1)$$

Where λ is the maximum wavelength of absorption by photocatalysts (nm) (illustrated by the tangent lines in Figure 4.5), and E_{bg} is the estimated band gap energy of the photocatalysts (eV).

As shown in Figure 4.5, the onset of visible light absorption by $Ag_2O/Ag_3VO_4/Ag_4V_2O_7$ occurred around 625 nm, resulting in a calculated band gap energy of ~ 1.98 eV, which was smaller than that of both Ag_3VO_4 (E_{bg} = 2.1 eV) and $Ag_4V_2O_7$ (E_{bg} = 2.5 eV), agreeing with the results from literature [6, 25, 37]. This improved visible light absorption observed in the multi-

phase photocatalyst was thought to be due to the presence of Ag_2O (E_{bg} = 1.29 eV) [38], where more visible light could be absorbed by these incorporated species containing narrower band gap energy.

4.3.6 Photocatalytic activity of $Ag_2O/Ag_3VO_4/Ag_4V_2O_7$

4.3.6.1 Photodegradation of RhB

To quantify photocatalytic activity, RhB was used as a model organic pollutant in both the absence of light and under VLI, and the results obtained are shown in Figure 4.6.

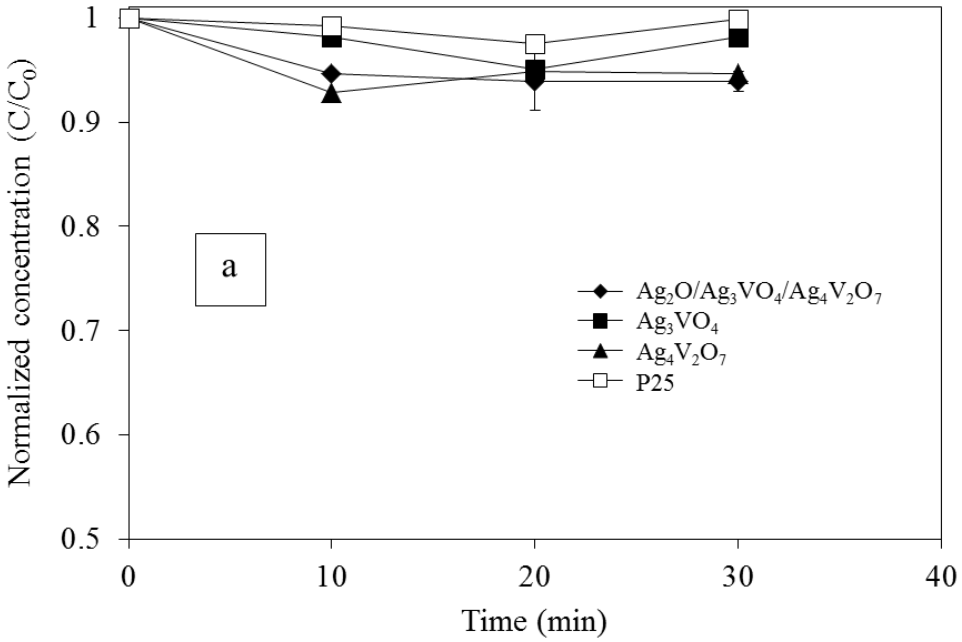

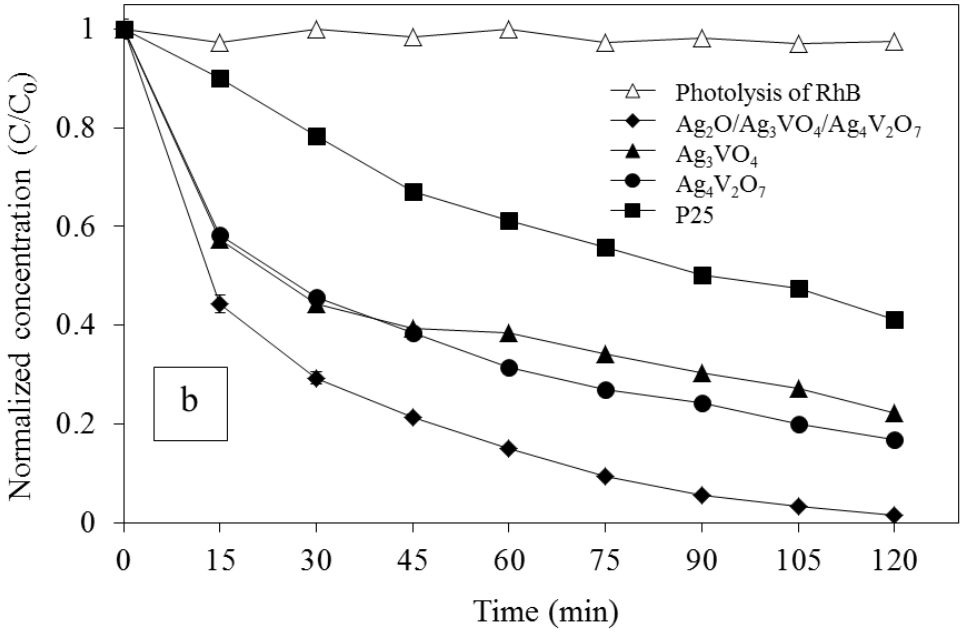

Figure 4.6: (a): adsorption reaction of RhB in the presence of various silver species samples in the absence of light over 30 min; (b): Photocatalytic degradation of RhB (15 mg·L^{-1}) in the presence of $Ag_2O/Ag_3VO_4/Ag_4V_2O_7$, Ag_3VO_4, $Ag_4V_2O_7$ and P25 as well as the photolysis of RhB under VLI for 2 h, respectively.

To achieve adsorption-desorption equilibration, the adsorption reaction of RhB in the presence of various silver species samples was performed over 30 min in the absence of light, the results of which are shown in Figure 4.6(a). It can be seen that adsorptions of 6.0%, 1.8%, 5.3% and 0.1% onto photocatalysts corresponding to $Ag_2O/Ag_3VO_4/Ag_4V_2O_7$, Ag_3VO_4, $Ag_4V_2O_7$, and P25 particles, respectively.

As shown in Figure 4.6(b), the photolysis control in the absence of photocatalyst was found to contribute approximately 2.4% self-degradation in 2 h under VLI. Due to this relatively small contribution, the effect of photolysis was thought to be negligible in the photocatalytic system. As seen in Figure 4.6, the $Ag_2O/Ag_3VO_4/Ag_4V_2O_7$ sample exhibited the highest photocatalytic activity compared to the other photocatalysts tested, giving 99% RhB decomposition in 2 h, while the Ag_3VO_4, $Ag_4V_2O_7$ and P25 TiO_2 affected 78%, 83% and 59% degradations in the same time period, respectively. The improved photocatalytic performance of the $Ag_2O/Ag_3VO_4/Ag_4V_2O_7$ compared to the other photocatalysts was thought to be attributed to the effects of the multi-phase $Ag_2O/Ag_3VO_4/Ag_4V_2O_7$ photocatalyst.

4.3.6.2 RhB degradation mechanism

To further investigate the mechanism of RhB photocatalytic degradation in the presence of $Ag_2O/Ag_3VO_4/Ag_4V_2O_7$, the changes to the UV-vis spectra of the dye during the photocatalytic reaction were investigated, and the results are shown in Figure 4.7.

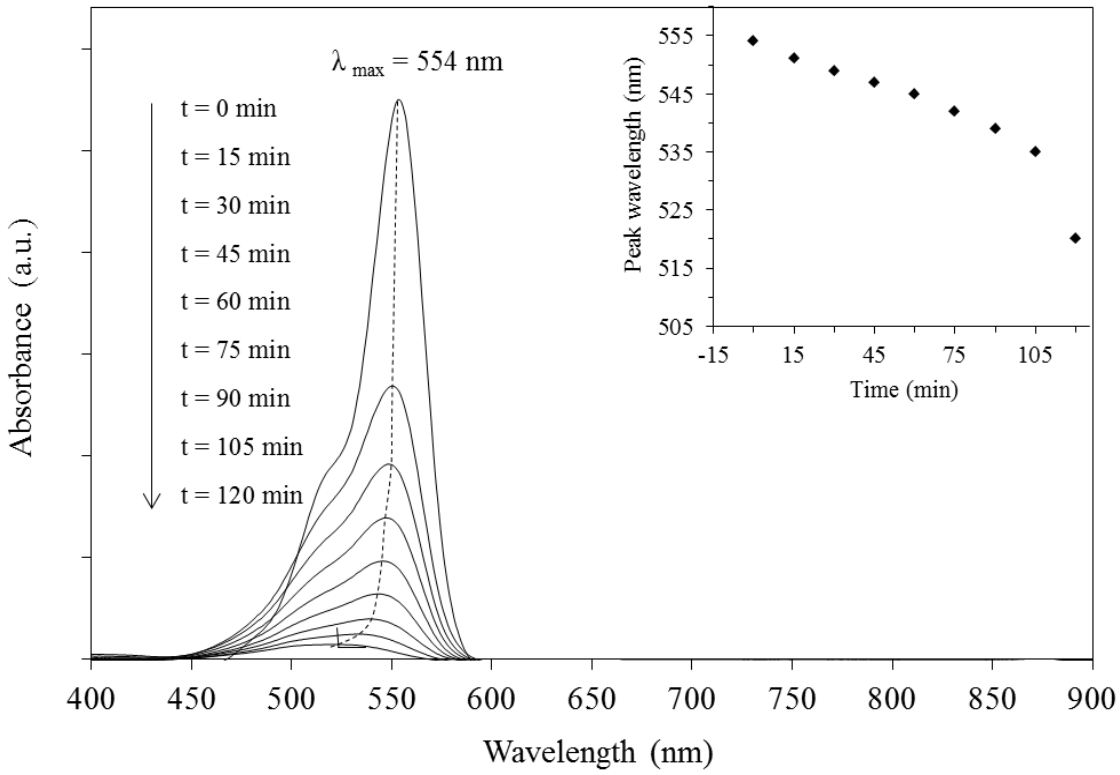

Figure 4.7: UV-Vis spectra of RhB during the course of photocatalytic degradation by $Ag_2O/Ag_3VO_4/Ag_4V_2O_7$.

As seen in Figure 4.7, the intensity of the characteristic absorption peak at 554 nm reduced significantly along the course of reaction, with progressive shifts of the absorption bands towards the blue region from 554 nm to 520 nm, in agreement with the results reported in literature on the photocatalytic degradation of RhB over TiO_2 and Bi_2WO_6 under visible light, respectively [39, 40]. Competitive reactions between the cleavage of the RhB chromophore ring structure and *N*-de-ethylation were thought to occur during the entire photocatalytic degradation process for RhB. From Figure 4.7, the decline at the maximum absorption wavelength of 554 nm was indicative of the cleavage of the whole conjugated chromophore structure of RhB, while the minor shifts from 554 nm to 520 nm were indicative of the stepwise *N*-de-ethylation of RhB. Of

these processes, the cleavage of the whole conjugated chromophore structure for RhB was thought to be predominant during the observed degradation process.

4.3.7 Stability of $Ag_2O/Ag_3VO_4/Ag_4V_2O_7$

4.3.7.1 Analyses of crystal structural changes

The multi-phase material synthesized consisted of dual-phase $Ag_3VO_4/Ag_4V_2O_7$ decorated with Ag_2O NPs at the surface. It was thought that the instability of the photocatalyst under the photocatalytic conditions was caused by the loss of crystallinity of dual-phase $Ag_3VO_4/Ag_4V_2O_7$ and the generation of Ag^0 NPs. Some Ag^+ ions from $Ag_4V_2O_7$ were thought to first react with the adsorbed hydroxyl ions (OH^-) to give rise to Ag_2O, as shown in reaction (4.2):

$$2\ Ag^+ + 2\ OH^- \rightarrow Ag_2O + H_2O\ [41, 42] \qquad (4.2)$$

Ag_2O were unstable with prolonged photocatalytic reaction under VLI, and some of Ag_2O could be reduced to Ag^0 NPs by receiving photogenerated electrons [38]:

$$Ag^+ + e^- \rightarrow Ag^0 \qquad (4.3)$$

With the increase of quantity of Ag^0 NPs, Ag_3VO_4 was thought to be converted to pyrovanadate ($Ag_4V_2O_7$) and some Ag_2O, under prolonged photocatalytic reaction. This is shown by the following reaction:

$$2\ Ag_3VO_4 \rightarrow Ag_4V_2O_7 + Ag_2O \qquad (4.4)$$

Accordingly, the loss of crystallinity of both Ag_3VO_4 and $Ag_4V_2O_7$ promoted the generation of Ag_2O and the increase of Ag^0 NPs, as reported by Belver et al. [17]. This process decreased the crystallinity of Ag_3VO_4 during photocatalytic reaction under VLI. Although the instability of Ag_3VO_4 facilitated the transformation of Ag^+ into Ag^0, resulting in the photocorrosion of Ag_3VO_4 in the absence of the electron acceptors, Ag^0 NPs with the SPR served as active photocatalytic sites for accepting photogenerated electrons and transferring them to the adsorbed oxygen, where more hydroxyl radicals were generated due to photogenerated holes that reacted with absorbed H_2O, which acted to enhanced photocatalytic reaction under VLI.

Structural changes to the multi-phase $Ag_2O/Ag_3VO_4/Ag_4V_2O_7$ photocatalyst occurred during the course of photocatalytic reaction, and were studied via a number of characterization techniques and investigations. The post-use characterization results are discussed in subsequent sections.

4.3.7.2 Post-use XRD analysis

In order to further investigate changes to the crystal structure of the multi-phase $Ag_2O/Ag_3VO_4/Ag_4V_2O_7$ photocatalyst upon exposure in the photoreactive system, XRD analyses were performed on the recycled catalysts. The post-use patterns obtained for various samples are shown in Figure 4.8.

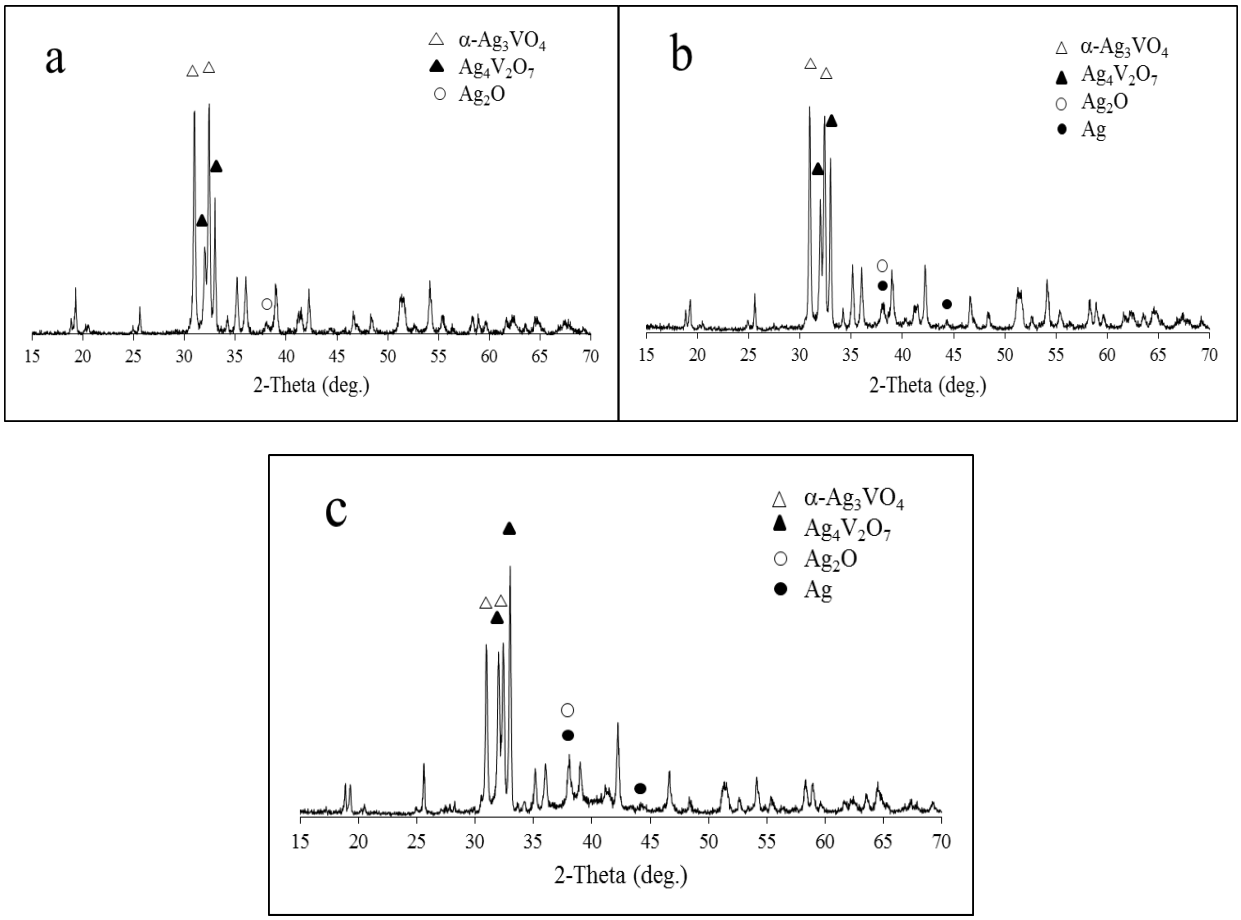

Figure 4.8: XRD patterns of various post-use multi-phase $Ag_2O/Ag_3VO_4/Ag_4V_2O_7$ photocatalysts; (a) recycled sample after a single use (rinsed with ethanol after use); (b) recycled sample after a single use (unwashed) and (c) recycled sample after three uses (unwashed).

Compared to the fresh sample shown in Figure 4.1, the XRD patterns obtained from the material recovered post-use and after recycling evidenced that structural changes occurred to

$Ag_2O/Ag_3VO_4/Ag_4V_2O_7$ in the photosystem. In the XRD pattern shown in Figure 4.8a, after reaction with 15 $mg{\cdot}L^{-1}$ RhB over 2 h, an obvious loss of crystallinity of the $Ag_4V_2O_7$ structure was observed, as evidenced in the decline of major peaks at 32.93° and 31.93°. This was thought to be due to the reported instability of $Ag_4V_2O_7$ under visible light irradiation [43]. The Ag^+ ions in $Ag_4V_2O_7$ reacted with the adsorbed OH^- ions to produce Ag_2O. In addition, some lattice Ag^+ of Ag_2O was thought to be reduced to the Ag^0 by receiving photogenerated electrons during the photocatalytic reaction [38]. This was evidenced by the Ag^0 phase discovered and the major reflections which occurred at 38.10° and 44.28° for Ag^0 in the pattern (JCPDS Card No. 01-071-4613), as shown in Figure 4.8b.

The produced Ag_2O phase was not stable in the presence of ethanol as well, and could be dissolved in ethanol after photocatalytic reaction according to the literature reported by Singh et al. [44] and Mehta and Singh [45] due to the solubilty of this phase in the solvent. As such, the used photocatalyst was rinsed with ethanol after recovery from the degraded RhB supernatant, and then recovered from the ethanol extract by centrifugation. By comparison of the rinsed photocatalyst and the unwashed photocatalyst after use, respectively, crystallinity changes and the characteristics of these post-use photocatalysts were observed. The loss of crystallinity of $Ag_4V_2O_7$ during photocatalysis was appreciable, as observed in Figure 4.8a.

The XRD pattern shown in Figure 4.8b represented that of the unwashed photocatalyst after a single use in the photosystem with 15 $mg{\cdot}L^{-1}$ RhB solution under VLI for 2 h. Comparison of Figure 4.8b with Figure 4.8a illustrates an obvious increase in the intensity of the diffraction peak for Ag^0 in the unwashed sample at 38.10°; and was thought to be due to more $Ag_4V_2O_7$ being photocorroded, so that more Ag^+ ions from $Ag_4V_2O_7$ were reduced to Ag^0 eventually with prolonged reaction under VLI. Furthermore, the intensity of the diffraction peaks of $Ag_4V_2O_7$ at 31.93° and 32.93° were much higher than the characteristic peaks for $Ag_4V_2O_7$ shown in Figure 4.8a. This was ascribed to the instability of Ag_3VO_4 with prolonged photocatalytic reaction in the presence of generated Ag^0 NPs, resulting in the conversion from Ag_3VO_4 to pyrovanadate ($Ag_4V_2O_7$), and a new generation of Ag_2O [17].

The XRD patterns of Figures 4.8b and c were used to further investigate these structural changes in the multi-phase $Ag_2O/Ag_3VO_4/Ag_4V_2O_7$ upon cyclic use. As shown in Figure 4.8c for the

recycled photocatalyst used three times, more Ag^0 NPs were generated upon prolonged reaction, as shown in the intensity of diffraction peaks at 38.10°. In addition, the loss of crystallinity of Ag_3VO_4 was more severe than the sample shown in Figure 4.8b, suggesting that Ag^+ ions in Ag_3VO_4 were both reduced to Ag^0 NPs and gave rise to the increase of $Ag_4V_2O_7$ phase, respectively.

4.3.7.3 Post-use SEM analysis

The morphologies of the synthesized multi-phase $Ag_2O/Ag_3VO_4/Ag_4V_2O_7$ photocatalysts after photocatalytic reactions were explored by SEM, in order to investigate the microstructure and morphology changes that occurred, and the images obtained are shown in Figure 4.9.

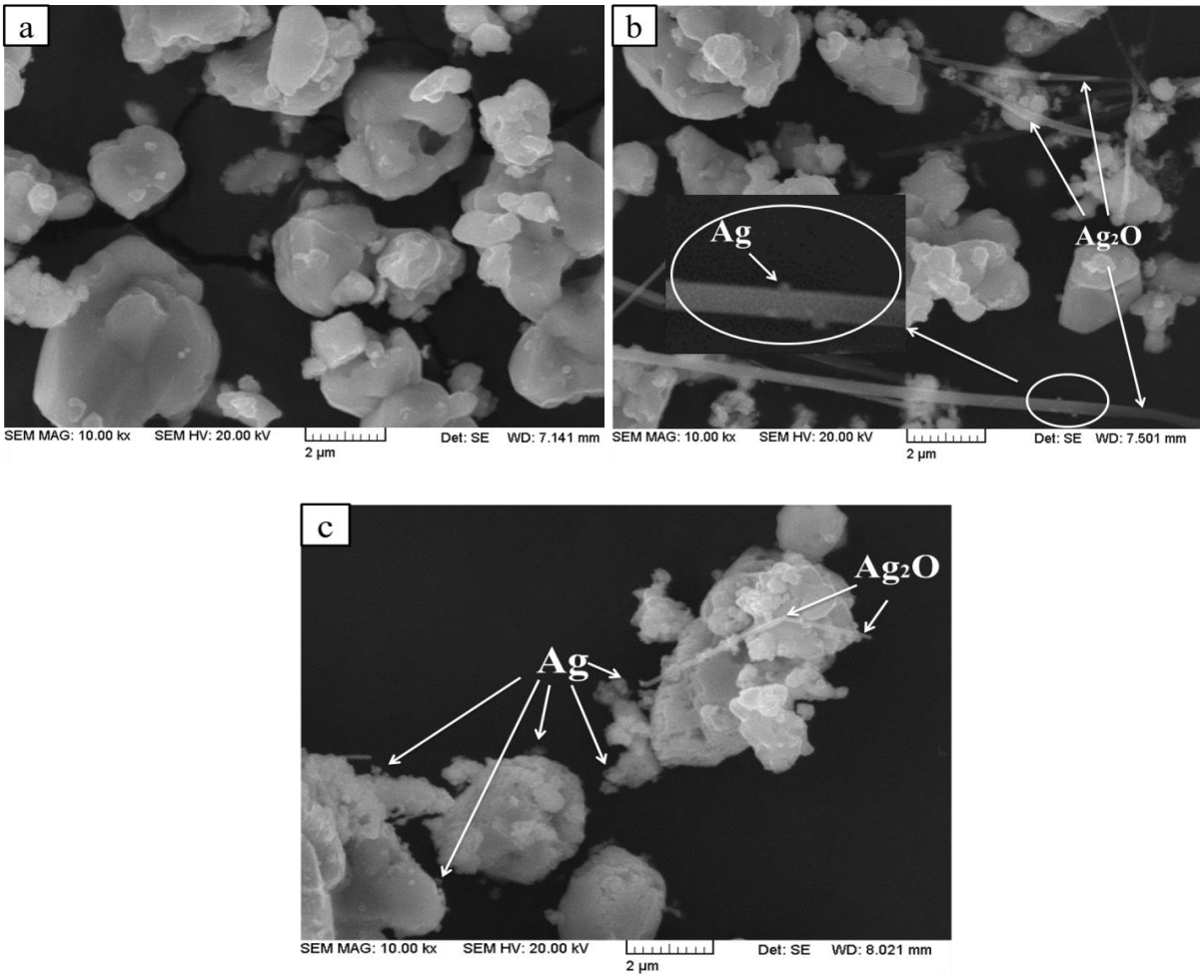

Figure 4.9: SEM images of various post-use multi-phase $Ag_2O/Ag_3VO_4/Ag_4V_2O_7$ photocatalysts; (a) recycled sample after a single use (rinsed with ethanol after use); (b) recycled sample after a single use (unwashed) and (c) recycled sample after three uses (unwashed).

No difference in morphologies was observed between Figure 4.3a and Figure 4.9a, indicating that the photocatalytic reaction towards dye degradation did not strongly impact the morphology of the catalyst. Comparison of Figures 4.9a–c indicated that multi-morphology of the synthesized photocatalysts emerged after use in the photocatalytic reaction, where more Ag^0 NPs were generated during the course of VLI, as confirmed by the XRD results obtained. In addition, a new generation of two-dimensional Ag_2O nanotubes (NTs) (width: 0.2 –0.4 μm; length: 4 –40 μm) was also observed in the unwashed samples (Figures 4.9b–c), which was mainly attributed to the loss of crystallinity of Ag_3VO_4 and $Ag_4V_2O_7$ under prolonged photocatalytic conditions [17]. As seen in Figures 4.9b–c, two-dimensional NTs were observed and were thought to be Ag_2O, based upon the results obtained by XRD. These Ag_2O NTs were not observed in the pure rinsed sample shown in Figure 4.9a, suggesting that the new generation of Ag_2O NTs resulted from both Ag_3VO_4 and $Ag_4V_2O_7$ after photocatalytic performance.

As shown in Figure 4.9c, more Ag^0 NPs were obtained in the unwashed recycled sample after three runs, while the amount of Ag_2O NTs decreased. This may indicate that the loss crystallinity of both Ag_3VO_4 and $Ag_4V_2O_7$ was severe after prolonged photocatalytic reaction, resulting in the generation of more Ag_2O NTs, while Ag_2O was unstable in the reducing ambient RhB solution under VLI, and gave rise to Ag^0 NPs [44], increasing the amount of Ag^0 NPs decorated on the multi-phase photocatalyst, in good agreement with the results from XRD.

4.3.7.4 Post-use XPS analysis

To investigate the changes of chemical and electronic states present in the multi-phase photocatalyst, XPS analyses of the post-use $Ag_2O/Ag_3VO_4/Ag_4V_2O_7$ were discussed, and the corresponding high resolution XPS spectral patterns are shown in Figures 4.10a–c, for Ag 3d, V 2p and O 1s states, respectively.

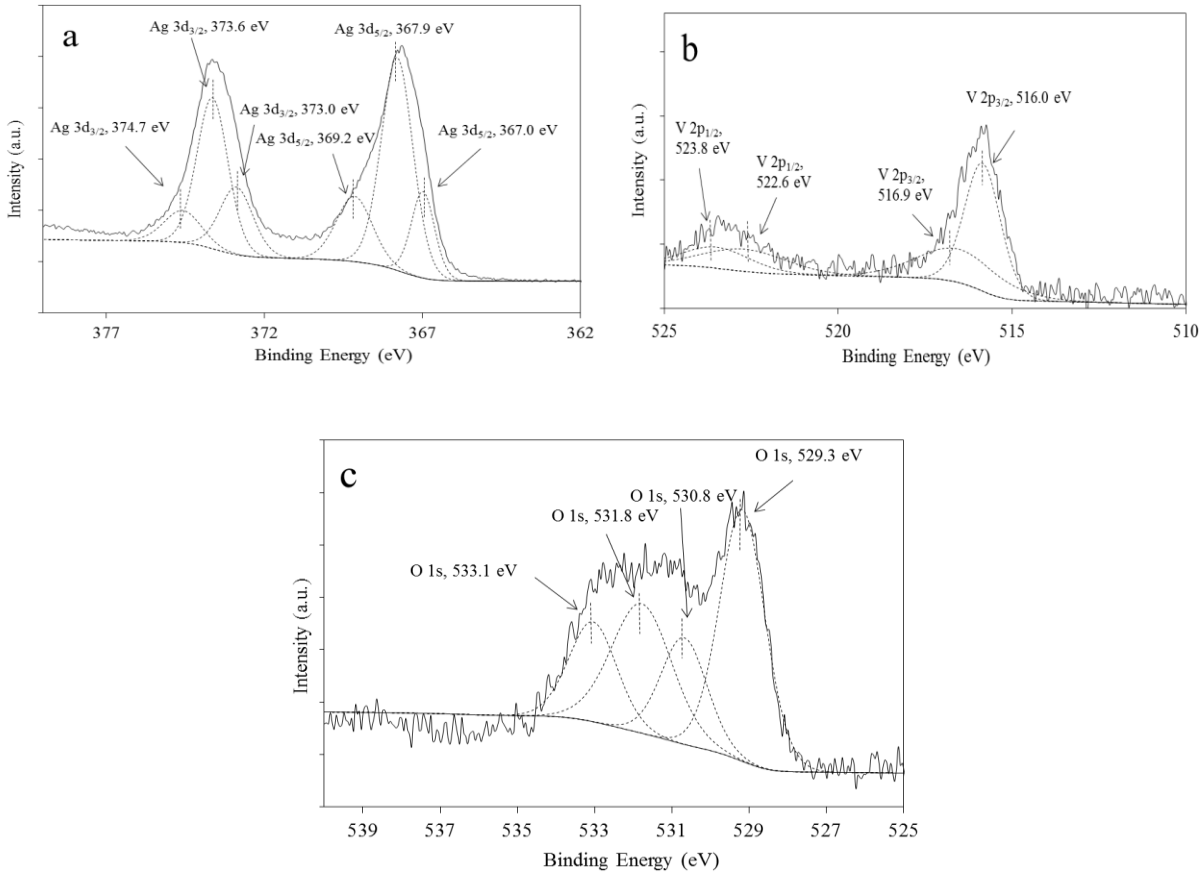

Figure 4.10: XPS spectra of post-use multi-phase $Ag_2O/Ag_3VO_4/Ag_4V_2O_7$ photocatalysts; (a) Ag 3d, (b) V 2p and (c) O 1s.

Comparing Ag 3d spectra in Figure 4.4 and Figure 4.10, the observed Ag 3d spectra of post-use sample changed markedly. The deconvolution of the Ag 3d was performed, and peaks assigned to three sets of individual peaks centered at 367.0 eV&373.0 eV, 367.9 eV&373.6 eV, and 369.2 eV&374.7 eV (dashed lines in Figure 4.10a) were obtained. Of these six peaks, the peaks at 367.0 eV&373.0 eV and 367.9 eV&373.6 eV were ascribed to the binding energies of Ag, corresponding to Ag^+, and peaks at 369.2 eV&374.7 eV were ascribed to the binding energies of Ag, corresponding to Ag^0 [30, 32, 46]. The chemical and electronic states of silver were thought to be changed during photocatalytic reactions under VLI, indicating that some Ag^+ species were reduced into metallic silver.

V $2p_{3/2}$ and V $2p_{1/2}$ spectra were observed to be broad in Figure 4.10b, and were deconvoluted into two pairs of individual peaks centered at 516.0 eV&522.6 eV, and 516.9 eV&523.8 eV

(dashed lines in Figure 4.10b), corresponding to V^{5+}, and corresponding well with the data from KVO_3 [34].

Photocatalytic reactions also influenced the chemical and electronic states of oxygen shown in Figure 4.10. O 1s spectra observed were changed noticeably, and deconvoluted into four separated peaks (dashed lines in Figure 4.10c), centered at 529.3 eV, 530.8 eV, 531.8 eV and 533.1 eV, respectively. Of these four peaks, peaks at 529.3eV, 530.8 eV and 531.8 eV were attributed to the lattice oxygen in the heterogeneous multi−phase photocatalysts, while the observed peak of O 1s at 533.1 eV was ascribed to the absorbed oxygen according to the literature [35].

4.3.7.5 Post-use optical properties

As shown in Figure 4.11, the UV-Vis diffuse reflectance spectra of post-use $Ag_2O/Ag_3VO_4/Ag_4V_2O_7$ samples also revealed intrinsic absorption in the visible light region.

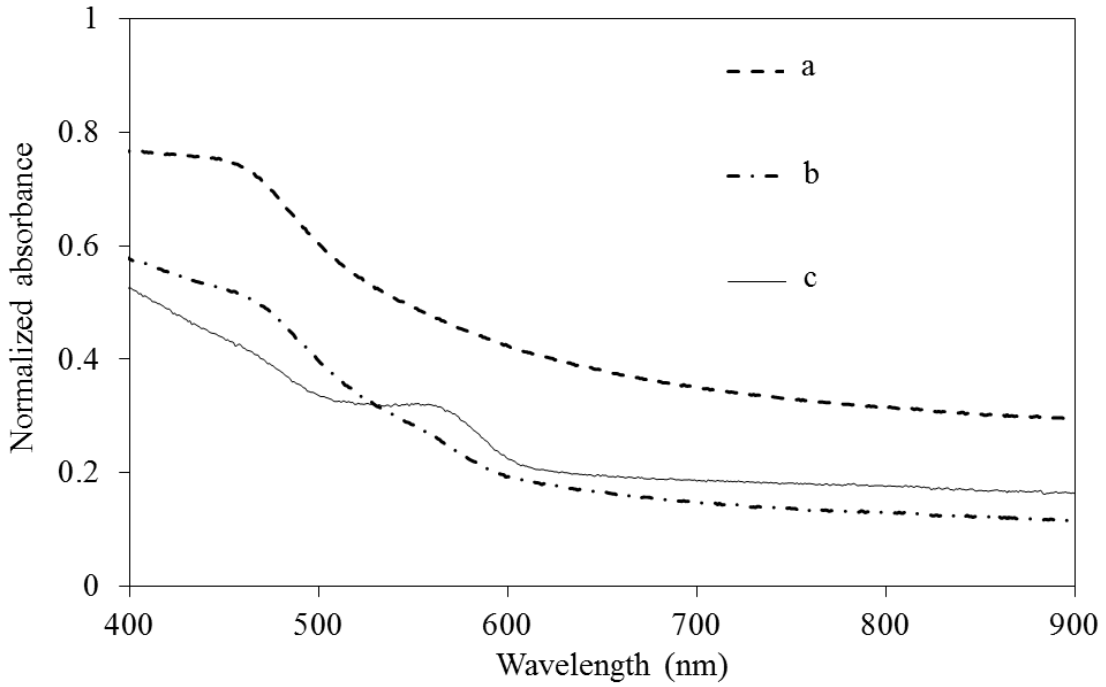

Figure 4.11: UV-Vis diffuse reflectance spectra (DRS) of post-use $Ag_2O/Ag_3VO_4/Ag_4V_2O_7$ samples prepared via hydrothermal method; (a) recycled sample after a single use (rinsed with ethanol after use); (b) recycled sample after a single use (unwashed) and (c) recycled sample after three uses (unwashed).

Compared to the fresh catalyst shown in Figure 4.5, no apparent absorption peaks of two spectra shown in Figures 4.11a–b were observed at longer wavelengths, indicating that Ag^0 NPs were

present in low quantities after a single use. However, as shown in Figure 4.11c, a noticeable broad peak at around 573 nm occurred in the absorption spectrum for the recycled sample used three times, and was thought to be due to the increased number of Ag^0 NPs present in the catalyst [47]. The broadening of the absorption peak was mainly due to the non-uniformity of the Ag^0 nanoparticle sizes and shapes [48]. These Ag^0 NPs both acted to increase the range of visible light absorption and to decrease the rate of recombination of e^--h^+ pairs [49] resulting in enhancing the efficiency of photogenerated e^--h^+ pairs capture by the adsorbed organic pollutants.

4.3.8 Role of reactive species testing

To further investigate the role of the reactive species impacting the photocatalytic degradation, quenching tests were applied to the degradation studies. Photocatalytic degradation of organic pollutants is caused by reaction with reactive species such as h^+, e^-, •OH and O_2•$^-$, which are generated on the surface of photocatalysts after irradiation [50]. The adsorption-desorption equilibration of RhB onto photocatalysts was achieved over 30 min in the absence of light, which was followed by the quenching tests for photocatalytic degradation of RhB by employing various radical species scavengers, and the results are shown in Figure 4.12a-b.

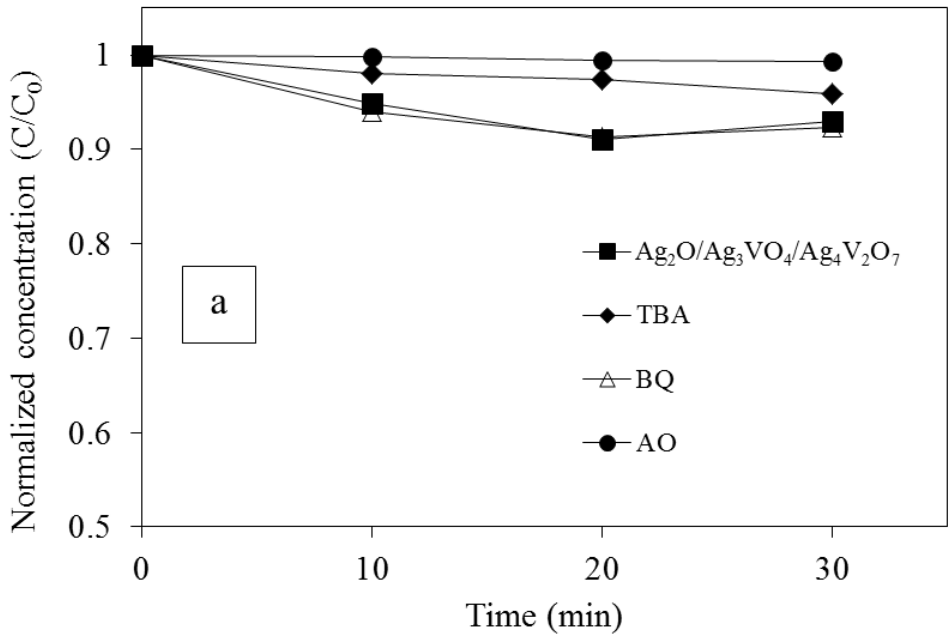

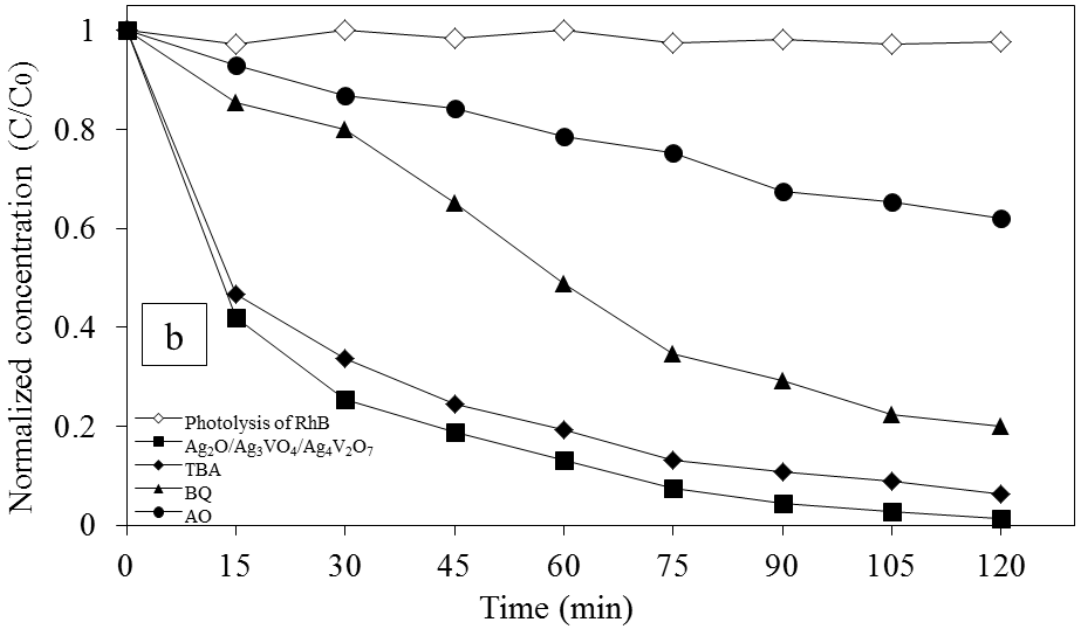

Figure 4.12: (a): adsorption reaction of RhB over 30 min in the absence of light; (b): quenching tests for photocatalytic degradation of RhB over $Ag_2O/Ag_3VO_4/Ag_4V_2O_7$ under different conditions with VLI.

To achieve adsorption-desorption equilibration, adsorption reactions of RhB in the presence of $Ag_2O/Ag_3VO_4/Ag_4V_2O_7$ composites were performed over 30 min in the absence of light, the results of which are shown in Figure 4.12a. This adsorption-desorption process resulted in the adsorptions of 7.0%, 4.1%, 7.6% and 0.7% onto photocatalysts shown in Figure 4.12a, corresponding to a no-scavenger system, as well as the scavengers of TBA, BQ, and AO used in the quenching tests, respectively.

As shown in Figure 4.12b, without scavengers, the photocatalytic degradation of RhB was 99% within 2 h. 3 mL TBA was added to the photocatalytic reaction system as the scavenger of •OH [6], resulting in a reduction in the degradation of RhB to 93% at the end of the 2 h reaction. 0.015 g BQ was used as a scavenger of $O_2•^-$ [51, 52], limiting the capture of photogenerated electrons by molecular oxygen (O_2) to generate $O_2•^-$, and causing the photodegradation of RhB on $Ag_2O/Ag_3VO_4/Ag_4V_2O_7$ to reduce to 80%. These results indicated that the photocatalytic reaction was less likely to be restricted by reducing the amount of •OH and $O_2•^-$. In contrast, by adding 0.15 g AO into the photocatalytic system [53, 54], the degradation was suppressed to 38% during the course of reaction, which indicated that holes played a major role in the

degradation mechanism for RhB. Therefore, holes were thought to dominate the mechanism of photocatalytic degradation of RhB under VLI for the prepared photocatalyst.

4.3.9 Mechanism of photocatalytic activity

A mechanism for RhB photodegradation in the presence of $Ag_2O/Ag_3VO_4/Ag_4V_2O_7$ under VLI was proposed, and the applicable reactions are given as follows:

$$Ag_2O + VLI \rightarrow Ag_2O\ (h^+ + e^-) \quad (4.5a)$$

$$Ag_3VO_4 + VLI \rightarrow Ag_3VO_4\ (h^+ + e^-) \quad (4.5b)$$

$$Ag_4V_2O_7 + VLI \rightarrow Ag_4V_2O_7\ (h^+ + e^-) \quad (4.5c)$$

$$h^+ + e^- \rightarrow \text{Heat} \quad (4.6)$$

$$Ag_4V_2O_7\ (e^-) + Ag_2O \rightarrow Ag_2O_{\ (\text{injected } e^-)} + Ag_4V_2O_7 \quad (4.7a)$$

$$Ag_3VO_4\ (e^-) + Ag_2O \rightarrow Ag_2O_{\ (\text{injected } e^-)} + Ag_3VO_4 \quad (4.7b)$$

$$Ag_3VO_4\ (h^+) + Ag_2O \rightarrow Ag_2O\ (h^+) + Ag_3VO_4 \quad (4.7c)$$

$$Ag_2O\ (h^+) + Ag_4V_2O_7 \rightarrow Ag_4V_2O_7\ (h^+) + Ag_2O \quad (4.7d)$$

$$Ag^+ (\text{in } Ag_2O) + e^- \rightarrow Ag \quad (4.8a)$$

$$Ag + VLI \rightarrow Ag\ (SPR) \quad (4.8b)$$

$$Ag\ (SPR) + Ag_4V_2O_7 \rightarrow Ag_4V_2O_{7\ (\text{injected } e^-)} + Ag^+\ (SPR) \quad (4.8c)$$

$$e^- + O_2 \rightarrow O_2\bullet^- \quad (4.9a)$$

$$h^+ + H_2O \rightarrow \bullet OH + H^+ \quad (4.9b)$$

$$4\ h^+ + 2\ H_2O \rightarrow 4\ H^+ + O_2 \quad (4.9c)$$

$$4\,h^+ + 2\,OH^- \rightarrow O_2 + 2\,H^+ \qquad (4.9d)$$

$$O_2\bullet^- + H^+ \rightarrow HO_2\bullet \qquad (4.10a)$$

$$HO_2\bullet + 2e^- + H^+ \rightarrow \bullet OH + OH^- \qquad (4.10b)$$

$$RhB_{\ ads} + VLI \rightarrow RhB^*_{\ ads} \qquad (4.11a)$$

$$RhB^*_{\ ads} - e^- \rightarrow RhB^+_{\ ads} + \bullet OH \rightarrow \text{intermediates} \rightarrow CO_2 + H_2O \qquad (4.11b)\ [40, 50]$$

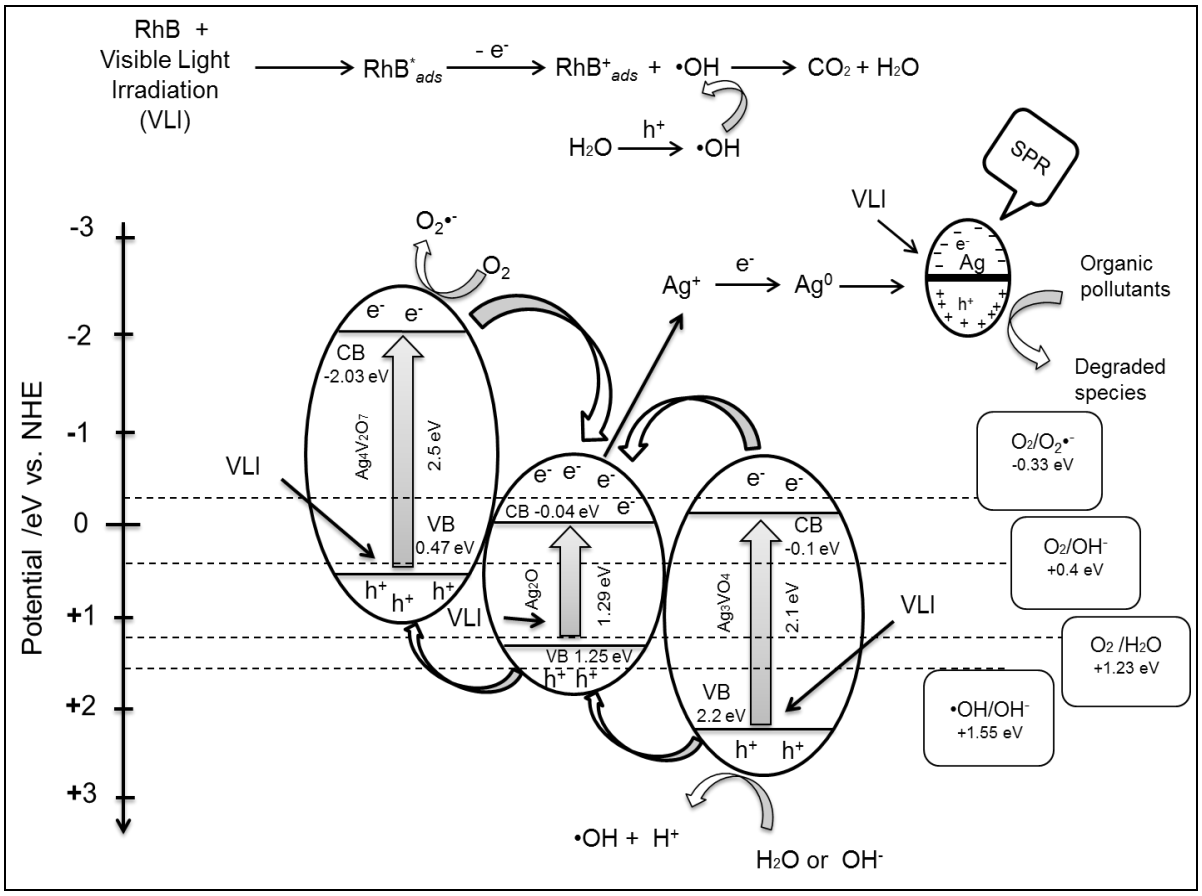

Figure 4.13: Photocatalytic mechanism of $Ag_2O/Ag_3VO_4/Ag_4V_2O_7$ over RhB under VLI.

In accordance with reactions (4.5)-(4.11) and Figure 4.13, the photocatalyst prepared consisted of multi-phase $Ag_2O/Ag_3VO_4/Ag_4V_2O_7$, namely Ag_3VO_4 /$Ag_4V_2O_7$ decorated with Ag_2O NPs. As seen from Figure 4.13, photocatalytic reaction was initiated by the absorption of photons from the visible light range with energy higher than the band gap energies of for Ag_2O, Ag_3VO_4 and $Ag_4V_2O_7$, causing the photogenerated e^--h^+ pairs to occur in the photoexcited

semiconductors, in accordance with reactions (4.5a-4.5c). In addition, reaction (4.6) showed that these e^--h^+ pairs could either separate and move freely on the surface of photocatalysts, or recombine as energy emission under the internal electric field caused by the heterosturcture, which occurred when the migration of e^--h^+ pairs was slow from the bulk to reaction sites at surface [1].

After the photoexcitation on the heterogenerous photocatalyst, the photogenerated electrons were promoted to the conduction band (CB) and the holes were left at the valence band (VB) of the photocatalyst, respectively. These electrons were transferred from the CB of $Ag_4V_2O_7$ to the CB of Ag_2O firstly (reaction 4.7a), meanwhile, some photogenerated electrons were shifted from the CB of Ag_3VO_4 to the CB of Ag_2O as well, due to the internal electric field (reaction 4.7b), because CB potential of $Ag_4V_2O_7$ (-2.03 eV vs. NHE) [6] and CB potential of Ag_3VO_4 (-0.1 eV vs. NHE) [37] were more negative than that of Ag_2O (-0.04 eV vs. NHE) [38]. In addition, the CB of $Ag_4V_2O_7$ was more negative than the standard redox potential of $O_2/O_2^{\bullet -}$ (-0.33 eV vs. NHE). Therefore, electrons were able to reduce the adsorbed O_2 to $O_2^{\bullet -}$ species (reaction 4.9a). However, an excess of electrons accumulated in the CB of Ag_2O rather than being captured by the adsorbed O_2 molecules due to the more positive CB potential of Ag_2O than that of $O_2/O_2^{\bullet -}$ (-0.33 eV vs. NHE).

The extra photogenerated electrons transferred to CB of Ag_2O could reduce Ag^+ to Ag^0 (reaction 4.8a), Ag^0 NPs exhibited SPR in the visible region, exciting e^--h^+ pairs on their surface. During the reaction processes, Ag^0 NPs exhibited higher absorption intensities in the visible region ($\lambda >$ 410 nm) by absorbing photons, in which, one Ag^0 nanoparticle could absorb one visible light photon resulting in the effectively polarized state by plasmon resonance of silver, causing effective separation of the SPR-excited electrons and holes [55] (reaction 4.8b). And these electrons were transferred from the SPR-excited Ag^0 NPs to CB of $Ag_4V_2O_7$ [56] (reaction 4.8c), while, holes caused more •OH by reacted with absorbed H_2O (reaction 4.9b). Therefore, more electrons transferred happened from the CB of $Ag_4V_2O_7$ to that of Ag_2O (reaction 4.7a) due to the plasmon resonance of silver.

Holes also migrated from the VB of Ag_3VO_4 to VB of Ag_2O then to VB of $Ag_4V_2O_7$ because of the internal electric field present, as shown in reactions (4.7c and 4.7d), accompanied with more

positive VB potential, Ag_3VO_4 preferentially oxidized OH^- to give •OH (•OH/OH^-, 1.55 eV vs. NHE) (reaction 4.9b), H_2O to give O_2 (O_2/H_2O, 1.23 eV vs. NHE) (reaction 4.9c), and OH^- to give O_2 (O_2/OH^-, 0.4 eV vs. NHE) (reaction 4.9d) [57]. Ag_2O was able to give rise to reactions 4.9c and 4.9d as well, due to the internal electric field present. In addition, holes transferred to VB of $Ag_4V_2O_7$ were trapped by OH^- ions originating from hydrolysis of H_2O at surface to yield O_2 and protons (H^+) (reaction 4.9d). Furthermore, the generated O_2•$^-$ radicals at CB of $Ag_4V_2O_7$ combined with the generated protons to yield HO_2• radicals (reaction 4.10a). Finally, additional •OH radicals were generated via HO_2• radicals reacting with both photoexcited electrons and protons (reaction 4.10b) [58].

During the whole photocatalytic degradation, photogenerated holes played a significant role of generating the strong oxidant •OH radicals, resulting in the direct oxidization of RhB (reactions 4.11a and 4.11b) [56] on the surface of $Ag_2O/Ag_3VO_4/Ag_4V_2O_7$. Therefore, this high photocatalytic performance was attributed to the positive effects between the photocatalysis of multi-phase $Ag_2O/Ag_3VO_4/Ag_4V_2O_7$ and SPR of Ag^0 NPs [56].

4.4 Conclusions

Multi-phase $Ag_2O/Ag_3VO_4/Ag_4V_2O_7$ photocatalyst was prepared through a facile hydrothermal method. Characterization tests indicated that dual-phase Ag_3VO_4 and $Ag_4V_2O_7$ were present in the system and were surface-decorated by Ag_2O NPs. Although each single phase (Ag_2O, $Ag_4V_2O_7$ and Ag_3VO_4), suffered from structural changes and loss of crystallinity in the photocatalytic system, the existence of the produced Ag^0 NPs induced positive effects of SPR on photocatalysis, which promoted an overall high photocatalytic performance towards the degradation of RhB under VLI. A new generation of Ag_2O nanotube-like structures and the increase of Ag^0 formed from the morphological changes that occurred under the photocatalytic reaction were observed. A mechanism was proposed for the photocatalytic degradation of RhB.

4.5 Acknowledgments

This work was funded by the Natural Sciences and Engineering Research Council of Canada (NSERC). The authors would like to thank Dr. Alexander Mommers at the Center for Catalysis Research and Innovation, and the Department of Earth Sciences at the University of Ottawa, as

well as Dr. Jianqun Wang at Carleton University for help with sample characterizations. The China Scholarship Council is also acknowledged for financial support.

4.6 References

[1] A. Kudo, Y. Miseki, Chem. Soc. Rev. 38 (2009) 253-278.

[2] A. Walsh, Y. Yan, M.N. Huda, M.M. Al-Jassim, S.-H. Wei, Chem. Mater. 21 (2009) 547-551.

[3] D.Y. Shahriari, N. Erdman, U.T.M. Haug, M.C. Zarzyczny, L.D. Marks, K.R. Poeppelmeier, J. Phys. Chem. Solids 64 (2003) 1437-1441.

[4] C. Linke, M. Jansen, Inorg. Chem. 33 (1994) 2614-2616.

[5] X. Hu, C. Hu, J. Solid State Chem. 180 (2007) 725-732.

[6] J. Wang, X. Yang, J. Chen, J. Xian, S. Meng, Y. Zheng, Y. Shao, D. Li, J. Am. Ceram. Soc. 97 (2014) 267-274.

[7] S. Zhang, W. Li, C. Li, J. Chen, J. Phys. Chem. B 110 (2006) 24855-24863.

[8] H. Kato, H. Kobayashi, A. Kudo, J. Phys. Chem. B 106 (2002) 12441-12447.

[9] Y. Maruyama, H. Irie, K. Hashimoto, J. Phys. Chem. B 110 (2006) 23274-23278.

[10] S. Ouyang, N. Kikugawa, D. Chen, Z. Zou, J. Ye, J. Phys. Chem. C 113 (2009) 1560-1566.

[11] G. Dai, J. Yu, G. Liu, J. Phys. Chem. C 116 (2012) 15519-15524.

[12] Y. Bi, H. Hu, S. Ouyang, G. Lu, J. Cao, J. Ye, Chem. Commun. 48 (2012) 3748-3750.

[13] A. Kubacka, M. Fernández-García, G. Colón, Chem. Rev. 112 (2011) 1555-1614.

[14] R. Konta, H. Kato, H. Kobayashi, A. Kudo, Phys. Chem. Chem. Phys. 5 (2003) 3061-3065.

[15] X. Tao, Q. Hong, T. Xu, F. Liao, J. Mater. Sci. - Mater. Electron. 25 (2014) 3480-3485.

[16] C. Dong, K.-L. Wu, X.-W. Wei, X.-Z. Li, L. Liu, T.-H. Ding, J. Wang, Y. Ye, CrystEngComm 16 (2014) 730-736.

[17] C. Belver, C. Adán, S. García-Rodríguez, M. Fernández-García, Chem. Eng. J. 224 (2013) 24-31.

[18] Q. Xiang, J. Yu, B. Cheng, H.C. Ong, Chem. Asian J. 5 (2010) 1466-1474.

[19] B. Neppolian, H.C. Choi, S. Sakthivel, B. Arabindoo, V. Murugesan, J. Hazard. Mater. 89 (2002) 303-317.

[20] D. Peng, Z. Min, X. Zhonglei, C. Lihong, J. Nanomater. 2015 (2015) 7.

[21] J. Xue, S. Ma, Y. Zhou, Z. Zhang, X. Wu, C. She, RSC Adv. 5 (2015) 3122-3129.

[22] P.Q. Wang, Y. Bai, P.Y. Luo, J.Y. Liu, Micro Nano Lett. 8 (2013) 340-344.

[23] L. Xu, B. Wei, W. Liu, H. Zhang, C. Su, J. Che, Nanoscale Res. Lett. 8 (2013) 1-16.

[24] W. Zhou, H. Liu, J. Wang, D. Liu, G. Du, J. Cui, ACS Appl. Mater. Interfaces 2 (2010) 2385-2392.

[25] C.-M. Huang, G.-T. Pan, Y.-C.M. Li, M.-H. Li, T.C.K. Yang, Appl. Catal., A 358 (2009) 164-172.

[26] C.-M. Huang, K.-W. Cheng, G.-T. Pan, W.-S. Chang, T.C.K. Yang, Chem. Eng. Sci. 65 (2010) 148-152.

[27] D. Yang, H. Liu, L. Liu, S. Sarina, Z. Zheng, H. Zhu, Nanoscale 5 (2013) 11011-11018.

[28] G.-T. Pan, M.-H. Lai, R.-C. Juang, T.-W. Chung, T.C.K. Yang, Ind. Eng. Chem. Res. 50 (2011) 2807-2814.

[29] K.S. Raju, M.K. Pour Seydei, S.A. Suthanthiraraj, Mater. Lett. 19 (1994) 65-68.

[30] W.-S. Wang, H. Du, R.-X. Wang, T. Wen, A.-W. Xu, Nanoscale 5 (2013) 3315-3321.

[31] H.S. Shin, H.C. Choi, Y. Jung, S.B. Kim, H.J. Song, H.J. Shin, Chem. Phys. Lett. 383 (2004) 418-422.

[32] M.S.A.S. Shah, M. Nag, T. Kalagara, S. Singh, S.V. Manorama, Chem. Mater. 20 (2008) 2455-2460.

[33] W. Liu, Y. Yu, L. Cao, G. Su, X. Liu, L. Zhang, Y. Wang, J. Hazard. Mater. 181 (2010) 1102-1108.

[34] D. Courcot, A. Ponchel, B. Grzybowska, Y. Barbaux, M. Rigole, M. Guelton, J.P. Bonnelle, Catal. Today 33 (1997) 109-118.

[35] Z. Sun, J. Guo, S. Zhu, L. Mao, J. Ma, D. Zhang, Nanoscale 6 (2014) 2186-2193.

[36] H.H. Huang, X.P. Ni, G.L. Loy, C.H. Chew, K.L. Tan, F.C. Loh, J.F. Deng, G.Q. Xu, Langmuir 12 (1996) 909-912.

[37] G. Trimarchi, H. Peng, J. Im, A.J. Freeman, V. Cloet, A. Raw, K.R. Poeppelmeier, K. Biswas, S. Lany, A. Zunger, Phys. Rev. B: Condens. Matter 84 (2011).

[38] W. Jiang, X. Wang, Z. Wu, X. Yue, S. Yuan, H. Lu, B. Liang, Ind. Eng. Chem. Res. 54 (2015) 832-841.

[39] Z. He, C. Sun, S. Yang, Y. Ding, H. He, Z. Wang, J. Hazard. Mater. 162 (2009) 1477-1486.

[40] T. Wu, G. Liu, J. Zhao, H. Hidaka, N. Serpone, J. Phys. Chem. B 102 (1998) 5845-5851.

[41] F.A.W. Cotton, Geoffrey, New York: Interscience. (1966) 1042.

[42] G. Wang, X. Ma, B. Huang, H. Cheng, Z. Wang, J. Zhan, X. Qin, X. Zhang, Y. Dai, J. Mater. Chem. 22 (2012) 21189-21194.

[43] R. Rotival, Y. Corvis, Y. Cartigny, P. Negrier, M. Marchivie, S. Massip, I. Gana, P. Lemoine, P. Espeau, CrystEngComm 15 (2013) 7970-7980.

[44] V.N. Singh, B. Rajmehta, R.K. Joshi, F.E. Kruis, J. Nanomater. 2007 (2007) 1-5.

[45] B.R. Mehta, V.N. Singh, Pramana-J. Phys 65 (2005) 949-958.

[46] P. Wang, B. Huang, Z. Lou, X. Zhang, X. Qin, Y. Dai, Z. Zheng, X. Wang, Chem. Eur. J. 16 (2010) 538-544.

[47] G. Li, K.H. Wong, X. Zhang, C. Hu, J.C. Yu, R.C.Y. Chan, P.K. Wong, Chemosphere 76 (2009) 1185-1191.

[48] X. Zhang, Y.L. Chen, R.-S. Liu, D.P. Tsai, Rep. Prog. Phys. 76 (2013) 046401.

[49] D. Zhang, F. Zeng, Res. Chem. Intermed. 36 (2010) 1055-1063.

[50] J. Zhao, C. Chen, W. Ma, Top. Catal. 35 (2005) 269-278.

[51] M. Stylidi, D.I. Kondarides, X.E. Verykios, Appl. Catal., B 47 (2004) 189-201.

[52] P. Raja, A. Bozzi, H. Mansilla, J. Kiwi, J. Photochem. Photobiol., A 169 (2005) 271-278.

[53] H. Lin, H. Ye, S. Chen, Y. Chen, RSC Adv. 4 (2014) 10968-10974.

[54] W. Li, D. Li, W. Zhang, Y. Hu, Y. He, X. Fu, J. Phys. Chem. C 114 (2010) 2154-2159.

[55] J. Gamage McEvoy, W. Cui, Z. Zhang, Appl. Catal., B 144 (2014) 702-712.

[56] Q. Zhu, W.S. Wang, L. Lin, G.Q. Gao, H.L. Guo, H. Du, A.W. Xu, J. Phys. Chem. C 117 (2013) 5894-5900.

[57] A.J. Bard, R. Parsons, J. Jordan, Marcel Dekker: New York (1985).

[58] S. Horikoshi, H. Hidaka, N. Serpone, Environ. Sci. Technol. 36 (2002) 1357-1366.

Chapter 5

Facile preparation of novel graphene oxide-$Ag_2O/Ag_3VO_4/AgVO_3$ heterogeneous photocatalysts with high photocatalytic performance under visible light irradiation

Rong Ran, Zisheng Zhang

Applied Catalysis B: Environmental

Abstract

A series of graphene oxide-assisted, multi-phase $Ag_2O/Ag_3VO_4/AgVO_3$ (GO-$Ag_2O/Ag_3VO_4/AgVO_3$) heterogeneous photocatalysts were synthesized via simple procedures at room temperature, and exhibited higher visible-light-driven photocatalytic performances with respect to the degradation of rhodamine B and methyl orange model organic pollutants compared to those of pure $Ag_2O/Ag_3VO_4/AgVO_3$ composites. The study of the influence of added graphene oxide (GO) on photocatalytic performance indicated that 1.2 wt% GO was an optimum amount to aid in the degradation of model organic pollutants, presenting the highest photoactive efficiency under visible light irradiation. The increased photoactivities of as-prepared GO photocatalyst composites were attributed to the effect of high surface area of GO in cooperation with multi-phase heterogeneous photocatalysts. From the photocatalytic activity, it can be inferred that GO could accelerate the adsorption and absorption abilities of as-prepared photocatalyst composites during photocatalytic performance, enhancing the separation of electron-hole (e-h) pairs compared to the pure sample. Moreover, GO as a sacrificial reagent in the photosystem was able to partially protect silver species composites from photocorrosion. A

possible mechanism was proposed for the photocatalytic degradation of organic dyes on the surface of GO-$Ag_2O/Ag_3VO_4/AgVO_3$.

Keywords: Multi-phase $Ag_2O/Ag_3VO_4/AgVO_3$, Multi-morphology photocatalyst, Graphene oxide, Visible-light-driven photocatalysis.

5.1 Introduction

Strategies have been investigated for the synthesis of metal-oxide photocatalysts with low band gap energies and increased visible-light-driven photocatalytic activities, which can be used to degrade organic pollutants [1-3]. Using single-phase photocatalysts, it has been reported that the increase in the recombination rate of photogenerated e-h pairs can be attributed to defects in the grain boundaries of photocatalyst serving as recombination centers to impede the separation of charged species [1, 4, 5]. Although heterojunction photocatalysts are capable of increasing their photocatalytic activities attributed to both the matched band potentials among each phase as well as the high transfer efficiencies of charges at the interface [6], the instability of silver species photocatalysts has manifested in the form of photocorrosion in the composites during photocatalytic performances under visible light irradiation (VLI). This could be ascribed to the combination of interstitial silver ions (Ag^+) with electrons in the absence of sacrificial reagents under VLI [7]. Metallic silver (Ag^0), as the reduced product of Ag^+, therefore blocks the active sites of photocatalysts and eventually decreases their photocatalytic activities [8]. For instance, Ag_2O [9], Ag_2CO_3 [10], Ag_3PO_4 [7], and Ag_3VO_4 [11] showed high photocatalytic activities with respect to the degradation of organic pollutants under VLI; however, photocorrosion occurred during photocatalytic performance, decreasing visible-light-driven photocatalytic activity towards the degradation of organic pollutants.

Graphene oxide (GO) is one of the more highly oxidative forms of graphene which have attracted much attention to the field of waste-water treatment [12, 13]. Functionalized GO-assisted photocatalysts have attracted considerable research interests due to their large specific surface areas, strong adsorption capabilities and their abundances of reactive sites for surface modification reactions [14]. The remarkable characteristics of GO not only allow functional groups such as those containing oxygen to effectively photodegrade pollutants, but also allow

GO to serve as a sacrificial reagent providing a possible protection to photocatalysts from photocorrosion during visible-light-driven photocatalysis [13].

The combination of GO with silver species composites has been rightfully increasing in popularity recently. Reports have shown that compounds such as Ag_2O [15], Ag_3PO_4 [16, 17], Ag_2CO_3 [18, 19] and Ag/AgX (X =Br, Cl) [20, 21], etc. have demonstrated improved photocatalytic activities towards the degradation of organic pollutants under VLI, indicating that the functionalized GO-assisted silver species composites facilitate visible-light-driven photocatalytic activity in several aspects. Firstly, the combination of GO with these composites improves both the efficiency of transferring charges (electrons and holes) at the interface of photocatalysts, and the mobility of photogenerated electrons and holes in photocatalysts [17, 22]. Secondly, adsorption of organic dyes was favoured at the interface of photocatalysts because of the strong π-π interactions between GO and organic molecules [23], suppressing the recombination of e-h pairs in photocatalysts due to the high electrical conductivity of GO. Thirdly, GO was incorporated with two or more particles resulting in the modification of the morphologies of photocatalysts [20, 24]. Hence, the fabrication of functionalized GO-assisted silver species photocatalysts presents a high potential for highly active visible-light-driven photocatalytic performances in the field of water purification.

In this study, a facile fabrication process is proposed to obtain visible-light-driven, multi-phase, heterogeneous $Ag_2O/Ag_3VO_4/AgVO_3$ photocatalysts in the presence of various quantities of GO, synthesized via simple chemical procedures at room temperature (RT). These prepared photocatalyst composites were then studied with regards to the photodegradation of model organic pollutants, i.e. rhodamine B (RhB) and methyl orange (MO), and then compared to the photodegradation performed by pure $Ag_2O/Ag_3VO_4/AgVO_3$. A possible mechanism for the photocatalytic degradation of organic dyes is discussed. The accelerated visible-light-driven photocatalytic activity towards the degradation of organic dyes was attributed to the synergistic effects between the three photosensitive phases and the characteristics of GO. Quite possibly, this could be the first report regarding the novel multi-phase heterogeneous GO-$Ag_2O/Ag_3VO_4/AgVO_3$ photocatalysts with highly active photocatalytic performances under VLI.

5.2 Experimental

5.2.1 Synthesis

GO-assisted multi-phase $Ag_2O/Ag_3VO_4/AgVO_3$ photocatalysts were prepared via simple procedures using potassium metavanadate (KVO_3), silver nitrate and GO as starting materials. KVO_3 was synthesized via calcination, in which 0.38 g K_2CO_3 (Fisher Scientific, Certified ACS) and 0.5 g V_2O_5 (ACROS Organics, 99.6%) were dissolved in 35 mL deionized water (DW) under strong magnetic stirring. The resultant solution was poured into an evaporation dish, and dried overnight at 50°C in an oven (Sheldon Manufacturing, Inc. Model No: 1350 GM). The dry sample was ground in an agate mortar and calcined in air at 457°C (730 K) for 5 h, yielding a pink KVO_3 powder. The molar ratio of silver to vanadium (Ag to V) used was 4:1.

To prepare the GO-assisted multi-phase $Ag_2O/Ag_3VO_4/AgVO_3$ powders, 15 mL of as-prepared 0.1 M KVO_3 aqueous solution was obtained after treatment in a water bath at 60°C for 3 min. Next, 60 mL of dispersion mixture containing 0.1 M $AgNO_3$ (Fisher Scientific, Certified ACS) and 4 $mg \cdot mL^{-1}$ GO (dispersion in H_2O, Sigma-Aldrich) was prepared under vigorous magnetic stirring for 1.5 h. Subsequently, the dispersion mixture containing $AgNO_3$ and GO was added dropwise to the KVO_3 solution and allowed to react under continuous stirring for 30 min to obtain a yellow slurry. The pH of the resulting slurry was then adjusted by adding 1 M KOH solution until a final pH of 7 was reached, as measured by a pH meter (Fisher Scientific, accumet basic, AB 15 pH meter), resulting in a dark-green slurry. The slurry was then maintained at RT overnight after 1 h magnetic stirring. The resulting solid was collected by centrifugation, washed four times with DW, and dried in air at RT overnight.

In the experiment, six GO-assisted samples were prepared with initial graphene oxide amounts of 0.5 wt%, 0.8 wt%, 1 wt%, 1.2 wt%, 1.5 wt% and 2.0 wt%, where the weight percentage is designated as the weight ratio of GO to silver composites. For comparison, pure silver composite was also synthesized via the previously described method without the addition of graphene oxide.

5.2.2 Characterization

Powder X-ray diffraction (XRD) measurements were carried out in Bragg-Brentano geometry on a Rigaku Ultima IV apparatus with Cu Kα1 (λ = 0.15418 nm) radiation, operating at 40 keV and 44 mA, and with a scanning range of 2θ from 15° to 70°. The morphologies of the prepared samples were obtained by scanning electron microscopy (SEM) (JEOL JSM-7500F field emission SEM), scanning transmission electron microscopy (STEM) (JEOL JSM-7500F field emission SEM), and transmission electron microscopy (TEM) (JEOL JEM-2100F field emission TEM operated at 120 KeV; FEI (formerly Phillips) Tecnai G2 F20 field emission TEM at an acceleration voltage of 200 keV). STEM-EDS was performed using an energy dispersive X-ray detector (JSM-7500F SEM). X-ray photoelectron spectroscopy (XPS) was conducted on a Kratos Analytical Axis Ultra DLD instrument with mono-chromated Al X-rays at 140 W. The powder UV-Vis diffuse reflectance spectra (DRS) were recorded on a Thermo Evolution 300 UV/Vis spectrophotometer equipped with a Praying Mantis diffuse reflectance accessory, and the spectra were collected at a scan rate of 240 nm min^{-1}. UV/Vis spectra of RhB samples were obtained using a Biochrom Ultrospec 60 UV/Vis spectrophotometer.

5.2.3 Photocatalytic activity

5.2.3.1 Photodegradation of RhB

Photocatalytic performance was quantified by the decomposition of RhB (Sigma-Aldrich) as a model organic pollutant under VLI. A slurry reactor was placed in a reflective housing unit to prevent external radiation from entering the reactor, as well as to prevent internal radiation from exiting the system.

A 300-W ELH tungsten halide bulb (Ushio) was used as a light source with a 410 nm cut-off filter (Kenko Zeta, λ > 410 nm, transmittance > 90%) to provide VLI. The light source was placed at a distance of 15 cm from the top of the slurry. The corresponding irradiation was measured using a quantum meter (Biospherical QSL-2100; 400 nm < λ < 700 nm), and was found to be approximately 10.9 × 10^{-3} Einstein·m^{-2}·s^{-1}. Cooling was provided by an external cooling jacket, and the temperature of the reaction was controlled to 20 ± 2°C.

Before illumination, 0.15 g of photocatalyst was dispersed into 150 mL of 15 $mg \cdot L^{-1}$ RhB solution and was allowed to reach adsorption-desorption equilibrium under continuous magnetic stirring at 280 rpm for 40 min in the absence of light. Irradiation was then provided for 45 min for each photocatalytic degradation trial. Liquid was taken every 5 min and separated by centrifugation at 10^4 rpm for 3 min in an accuSpin Micro 17 (Fisher Scientific) microcentrifuge to remove the suspended catalyst. The supernatant fluid was analyzed by monitoring the peak absorbance (λ = 554 nm for RhB) using a Genysys 10-UV spectrophotometer (Geneq Inc.). A standard curve for RhB was prepared and the concentration determined by the measured absorbance and the Beer-Lambert Law. UV/Vis analysis of RhB samples was accomplished with a Biochrom Ultrospec 60 UV/Vis spectrophotomer.

Quenching tests were performed through the addition of appropriate reactive species scavengers. A quantity of 0.015 g Benzoquinone (BQ) (reagent-grade ≥ 98%, Sigma Aldrich) was used to trap superoxide radicals (O^{2-}•), 0.15 g ammonium oxalate (AO) (ACS, Sigma-Aldrich) was used as the hole scavenger, and 3 ml tert-butyl alcohol (TBA) (ACS, Sigma-Aldrich) was used to trap hydroxyl radicals (•OH).

5.2.3.2 Photodegradation of MO

The photocatalytic degradation of MO (Fisher Scientific) induced by the GO-assisted multi-phase $Ag_2O/Ag_3VO_4/AgVO_3$ photocatalysts synthesized via KVO_3 was also investigated. The same parameters and methodologies that were seen in the RhB photocatalysis studies were applied, where the spectrophotometric analysis was performed at a peak absorbance of 463 nm. Quenching tests were also performed to investigate the roles of reactive species in photocatalysis, which was achieved through the addition of the same reactive species scavengers which were used in the RhB photocatalysis studies.

5.3 Results and discussion

5.3.1 XRD analysis

Figure 5.1 shows the XRD patterns of the fresh multi-phase and pure composites, as well as those assisted by graphene oxide, i.e. GO-$Ag_2O/Ag_3VO_4/AgVO_3$, in the presence of various quantities of GO obtained via simple chemical reactions.

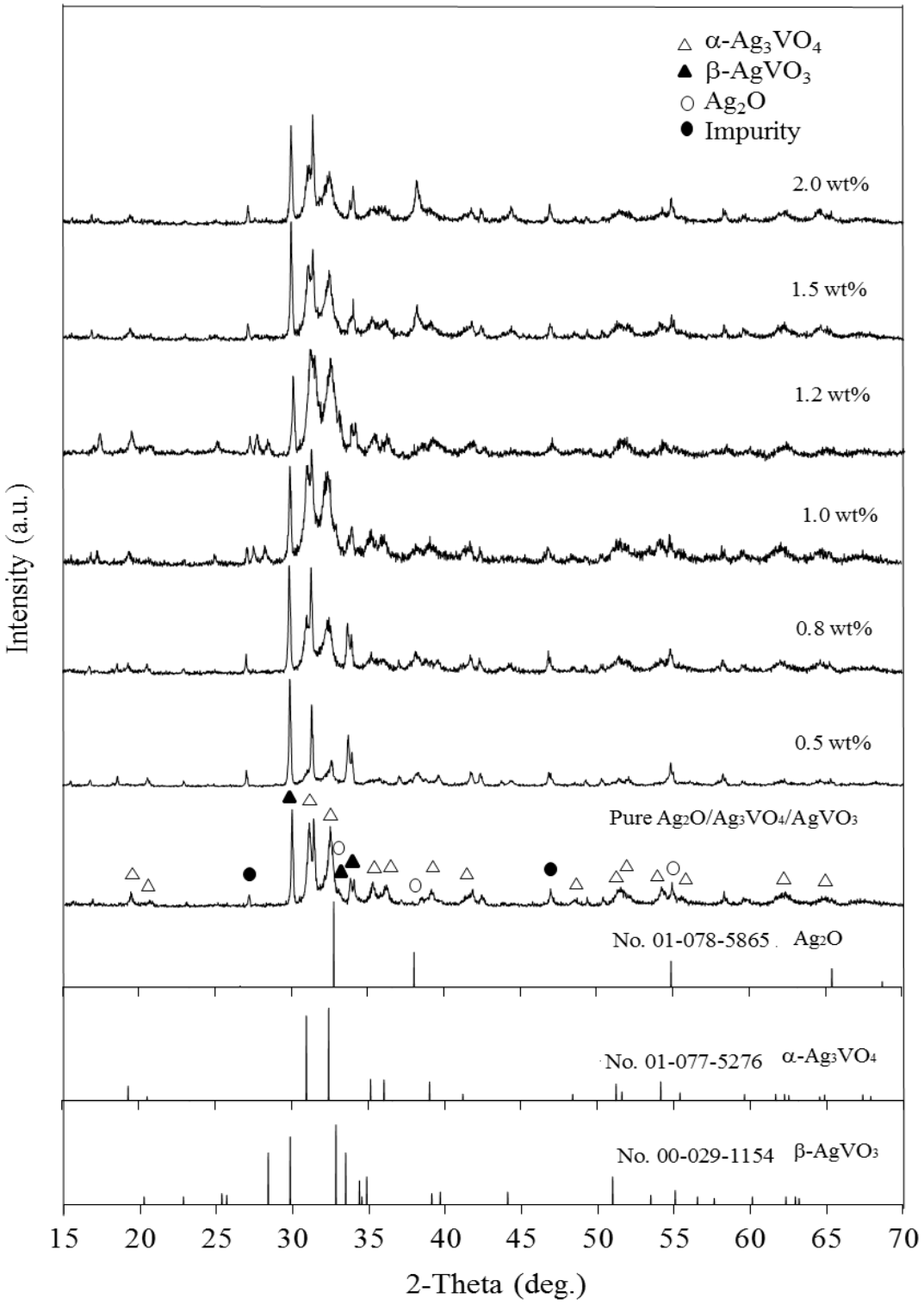

Figure 5.1: XRD patterns of fresh, multi-phase pure $Ag_2O/Ag_3VO_4/AgVO_3$ and GO-$Ag_2O/Ag_3VO_4/AgVO_3$ composites with various quantities of GO.

As seen in Figure 5.1, the patterns of multi-phase, pure and GO-assisted heterogeneous photocatalysts exhibited crystal structures including monoclinic α-Ag_3VO_4 phase (JCPDS Card No. 01-077-5276), monoclinic β-$AgVO_3$ phase (JCPDS Card No. 00-029-1154), and cubic silver oxide phase (JCPDS Card No. 01-078-5865), respectively. The diffraction peaks observed from the pure sample indicate that α-Ag_3VO_4 is the dominant phase in the heterogeneous composite due to the pH which was adjusted to 7. Major reflections for α-Ag_3VO_4 which occurred at 30.96° (1 1 2) and 32.42° (-3 1 2) agreed well with the results reported by Pan et al. [25]. Apart from α-Ag_3VO_4, β-$AgVO_3$ and Ag_2O are the other two main phases presented in the heterogeneous composites, and the major reflections for β-$AgVO_3$ and Ag_2O were identified at 29.84° (5 0 1), 32.85° (-4 1 1), 33.48° (-1 1 2) and 32.78° (1 1 1), 38.03° (2 0 0), 54.88° (2 2 0), respectively. In addition, two unknown diffraction peaks which emerged at 27.02° and 46.82° were identified as impurities according to the observed patterns.

Compared to the multi-phase pure heterogeneous composite, no significant differences in the diffraction peaks were found in the GO-assisted multi-phase heterogeneous photocatalysts, suggesting that the introduction of GO had little impact on the crystal structure of multi-phase $Ag_2O/Ag_3VO_4/AgVO_3$ [26], with the exception of the sample containing 0.5 wt% GO. The intensity of major peaks for α-Ag_3VO_4 at 30.96° and 32.42° decreased in the GO-assisted heterogeneous sample with 0.5 wt% GO, suggesting that the amount of GO had some influence on the formation of crystallinity in the crystal structure of α-Ag_3VO_4 during the preparation process. Furthermore, the amount of Ag_2O particles increased proportionally to the amount of GO in as-prepared composites, and the maximum amount of Ag_2O was observed in the 2.0 wt% GO-assisted sample shown in Figure 5.1. However, the major peaks for β-$AgVO_3$ at 29.84°, 32.85°and 33.48° showed little change, which indicates that the amount of GO had little impact on the formation of crystallinity in β-$AgVO_3$ during the synthesis. Moreover, no obvious GO peaks were detected, which can probably be ascribed to the low quantities of GO in the samples. The diffraction peak corresponding to GO was barely visible in the XRD pattern when hybridized with inorganic components due to the low diffraction intensity of GO [21].

5.3.2 SEM analysis

The microstructures and morphologies present in the prepared fresh, multi-phase pure $Ag_2O/Ag_3VO_4/AgVO_3$ composite, and composites with varying weight percentages of GO were investigated by SEM, and the results are shown in Figures 5.2a-g.

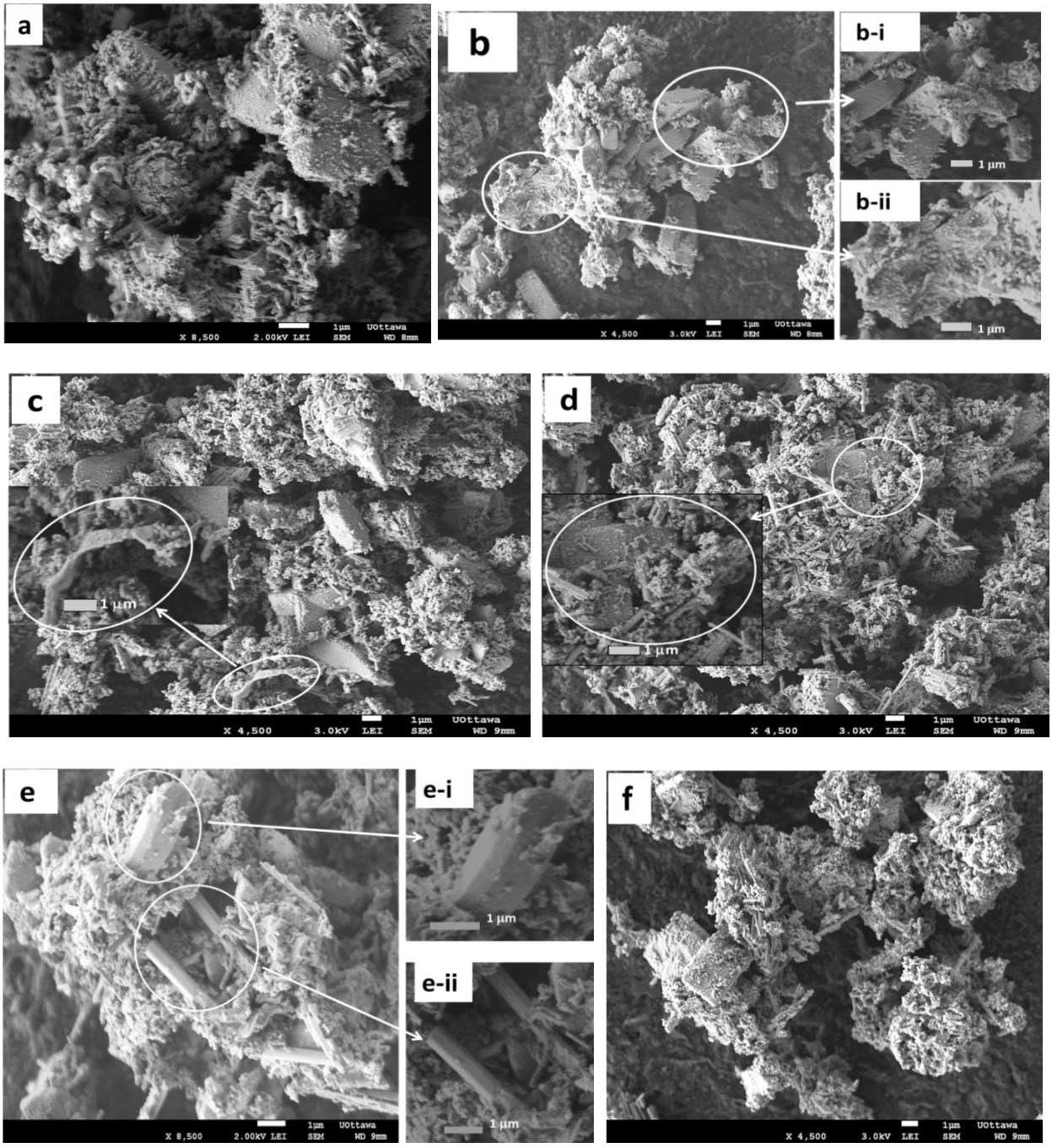

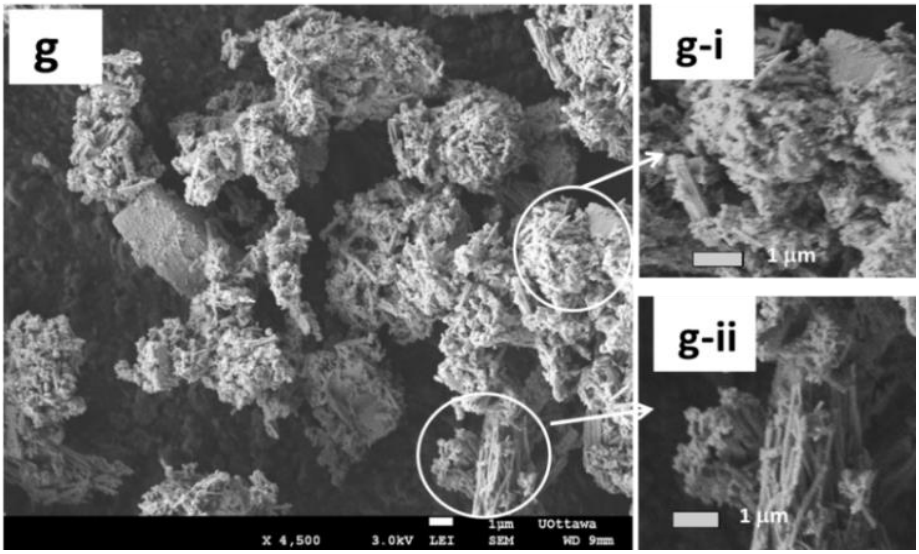

Figure 5.2: SEM images of fresh, multi-phase $Ag_2O/Ag_3VO_4/AgVO_3$ composites with various additions of GO. (a) pure composite; (b) 0.5 wt%; (c) 0.8 wt%; (d) 1 wt%; (e) 1.2 wt%; (f) 1.5 wt%; (g) 2.0 wt%.

As seen in Figures 5.2a–g, the as-obtained samples with different quantities of GO were observed to be multi-scale particles with multi-morphological features. In Figure 5.2a, multi-morphological structures composed of 2 μm-wide chunks and 3 μm-long dendritic-like plates can be seen, both of which were decorated with flake-like and nanoscale granular particles. The nanoscale granular particles were identified as Ag_2O nanoparticles (NPs) according to the XRD results, the results of which were corroborated with studies from relevant literatures [9, 27]. As such, multi-morphological structures could increase the surface areas of the as-prepared composites by increasing the adsorption efficiencies to promote solid-liquid heterogeneous photocatalytic reactions [8, 28, 29].

The morphologies of the as-prepared samples were slightly different at different quantities of GO. A comparison of Figures 5.2b, 5.2c and 5.2d shows obvious aggregations of those nanoparticles found in the as-obtained samples in the additions of 0.5 wt%, 0.8 wt% and 1 wt% GO respectively, indicating that the GO weight ratio may influence the dispersion of the multi-morphological structures during synthesis, possibly due to the electrostatic interactions between GO sheets and the multi-scale particles present in the system [12, 20]. In particular, many distinct monoclinic crystal structures emerged in the GO-assisted samples, highlighted in the inset of Figure 5.2b-i, which were identified as α-Ag_3VO_4 crystal structures. This agrees with the results obtained in the XRD patterns and in reports from other scholars [30, 31]. In addition, the

lamella sheet was observed and identified as GO in the system, and is highlighted in the inset of Figure 5.2b-ii, which was covered and filled with numerous nanoscale granular particles on the top, indicating that GO sheets as substrates offer large surface areas to distribute nanoscale particles rather than to agglomerate them together, resulting in the increased specific surface areas of the composites [14]. As such, the same morphology of GO was found and demonstrated in the inset of Figure 5.2c. Moreover, from Figure 5.2d, the elongated cylindrical-like structures were observed and identified as β-$AgVO_3$ crystals, which agrees well with XRD results and existing literature [25, 32], indicating that the morphological features of the as-prepared samples were influenced by the addition of GO.

In a comparison of Figures 5.2e, 5.2f and 5.2g, the apparent octagonal crystal structures were observed and highlighted in the insets of Figure 5.2e-i and Figure 5.2e-ii. Most notably, the 1.2 wt% GO sample was observed with three different morphologies: prismatic monoclinic crystals, elongated prismatic crystals, and nanoscale granular particles. This suggests that the yielded composites possess high crystallinities demonstrating multi-morphological features after simple chemical procedures with a quantity of 1.2 wt% GO. Nevertheless, many agglomerated structures are exhibited in Figure 5.2f and Figure 5.2g, which display prismatic monoclinic crystal structures encrusted by elongated cylindrical-like structures and nanoscale particles rather than yielding bare crystal structures. This suggests that larger surface areas on large prismatic monoclinic crystals were formed using GO as the carrier to distribute small crystal structures and nanoparticles. In addition, some elongated nanofibers emerged, highlighted in the inset of Figure 5.2g-ii, and were identified as β-$AgVO_3$. Therefore, the multi-morphological features of the prepared samples were attributed to the effects of the cooperation of GO with multi-phase composites, resulting in the increased specific surface areas of large crystal structures and giving rise to the high efficiencies of adsorption processes. This could eventually facilitate the obtainment of high photocatalytic degradation efficiencies with regards to organic dyes [8, 18].

5.3.3 STEM-EDS and TEM analyses

In order to further investigate the multi-morphology and the detailed structures of GO-assisted $Ag_2O/Ag_3VO_4/AgVO_3$ composites, STEM-EDS and TEM were employed to provide deeper analyses of the prepared samples. Results are shown in Figures 5.3a–e.

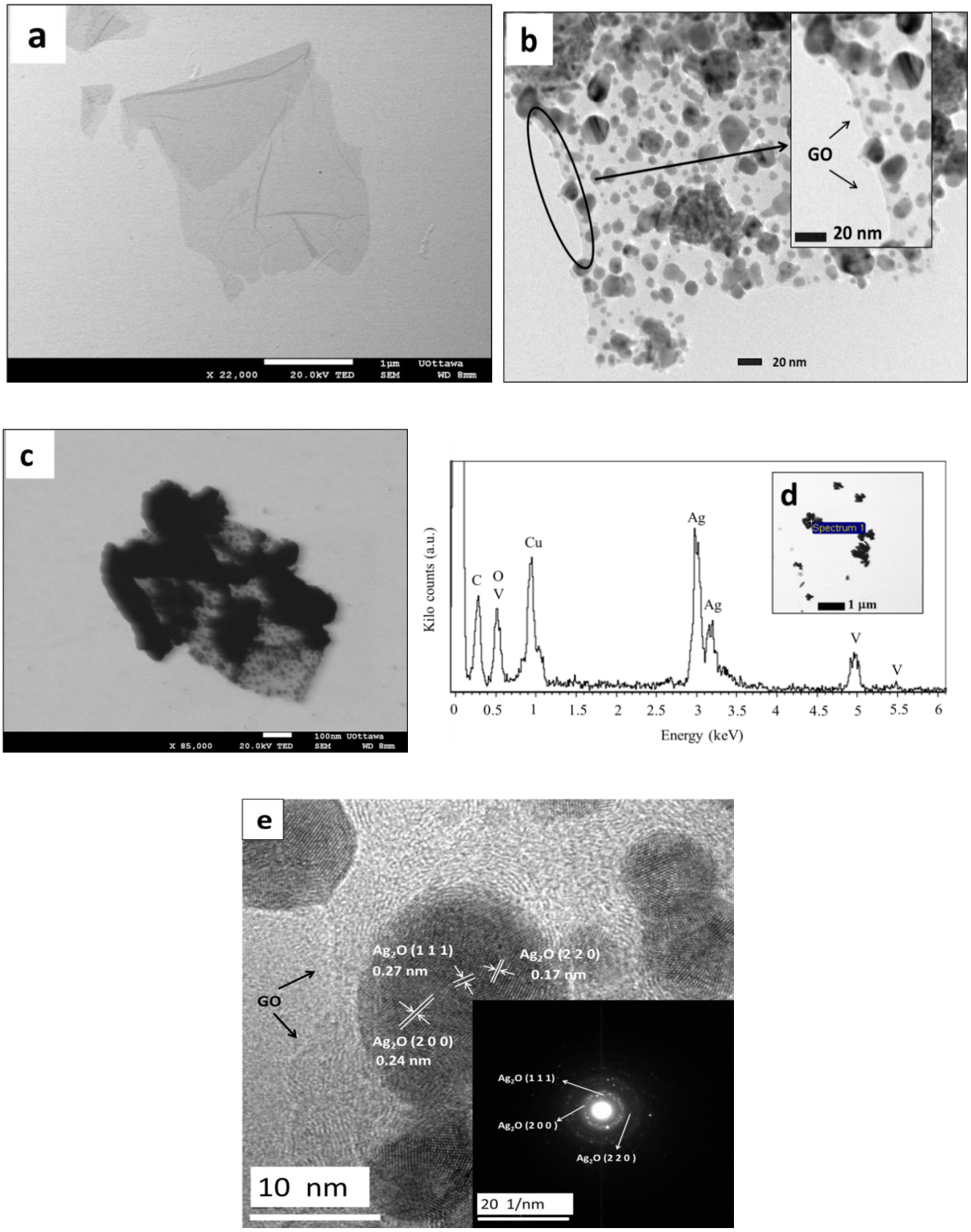

Figure 5.3: (a) STEM of GO sheets; (b and c) TEM and STEM images of the fresh 1.2 wt% GO-$Ag_2O/Ag_3VO_4/AgVO_3$ composite, respectively; and corresponding EDS data for (d) is shown; (e) high-resolution TEM of 1.2 wt% GO-$Ag_2O/Ag_3VO_4/AgVO_3$ composite and SAED patterns inset.

As shown in Figure 5.3a, GO sheets exhibited super-thin layers with microscale ranges, which agrees well with the images observed in Figure 5.2b-ii and Figure 5.2c. This indicates that GO increased the specific surface areas of composites, resulting in strong adsorption capabilities [14]. From the TEM image shown in Figure 5.3b, the noticeable distribution of multi-phase $Ag_2O/Ag_3VO_4/AgVO_3$ composites with the assistance of 1.2 wt% GO was observed, indicating that using GO sheets as the reticulate substrate resulted in an even distribution of nanoscale particles over large surface areas, preventing agglomeration. In addition, the distinct distribution of multi-morphological $Ag_2O/Ag_3VO_4/AgVO_3$ composites in various size ranges is exhibited in the STEM image found in Figure 5.3c and provides supporting evidence for the analyses performed in the previous SEM section. Furthermore, regarding the results shown in Figure 5.3d, EDS data indicated that the elemental composition of the as-obtained 1.2 wt% GO sample was primarily silver, vanadium, carbon and oxygen. It should be noted that the copper (Cu) peak occurred as a result of the sputter coating.

In Figure 5.3e, the high-resolution TEM image of the 1.2 wt% GO-$Ag_2O/Ag_3VO_4/AgVO_3$ photocatalyst exhibits lattice fringes of 0.27 nm, 0.24 nm and 0.17 nm, which correspond to the (1 1 1), (2 0 0) and (2 2 0) interlayer spacings (*d-spacings)* of Ag_2O, respectively. In addition, the selected area electron diffraction (SAED) patterns shown in the inset of Figure 5.3e further confirmed the crystal structure of Ag_2O present in the multi-phase crystalline structure of the $Ag_2O/Ag_3VO_4/AgVO_3$ photocatalyst. The rings were ascribed to diffraction from the (1 1 1), (2 0 0) and (2 2 0) reflections of the Ag_2O phase (JCPDS Card No. 01-078-5865), based on the calculated *d-spacings* of 2.73 Å, 2.36 Å, and 1.67 Å, respectively.

5.3.4 XPS analysis

The chemical and electronic states of the as-synthesized, fresh, multi-phase, pure samples, and multi-phase 1.2 wt% GO-$Ag_2O/Ag_3VO_4/AgVO_3$ composites were implemented via XPS analysis, and the obtained results are shown in Figures 5.4a-i and 5.4a-ii, 5.4b-i and 5.4b-ii, 5.4c-i and 5.4c-ii, as well as 5.4d-i and 5.4d-ii for Ag 3d, V 2p, O 1s and C 1s states, respectively. The obtained binding energies from XPS analysis were calibrated by referencing C 1s to 285 eV.

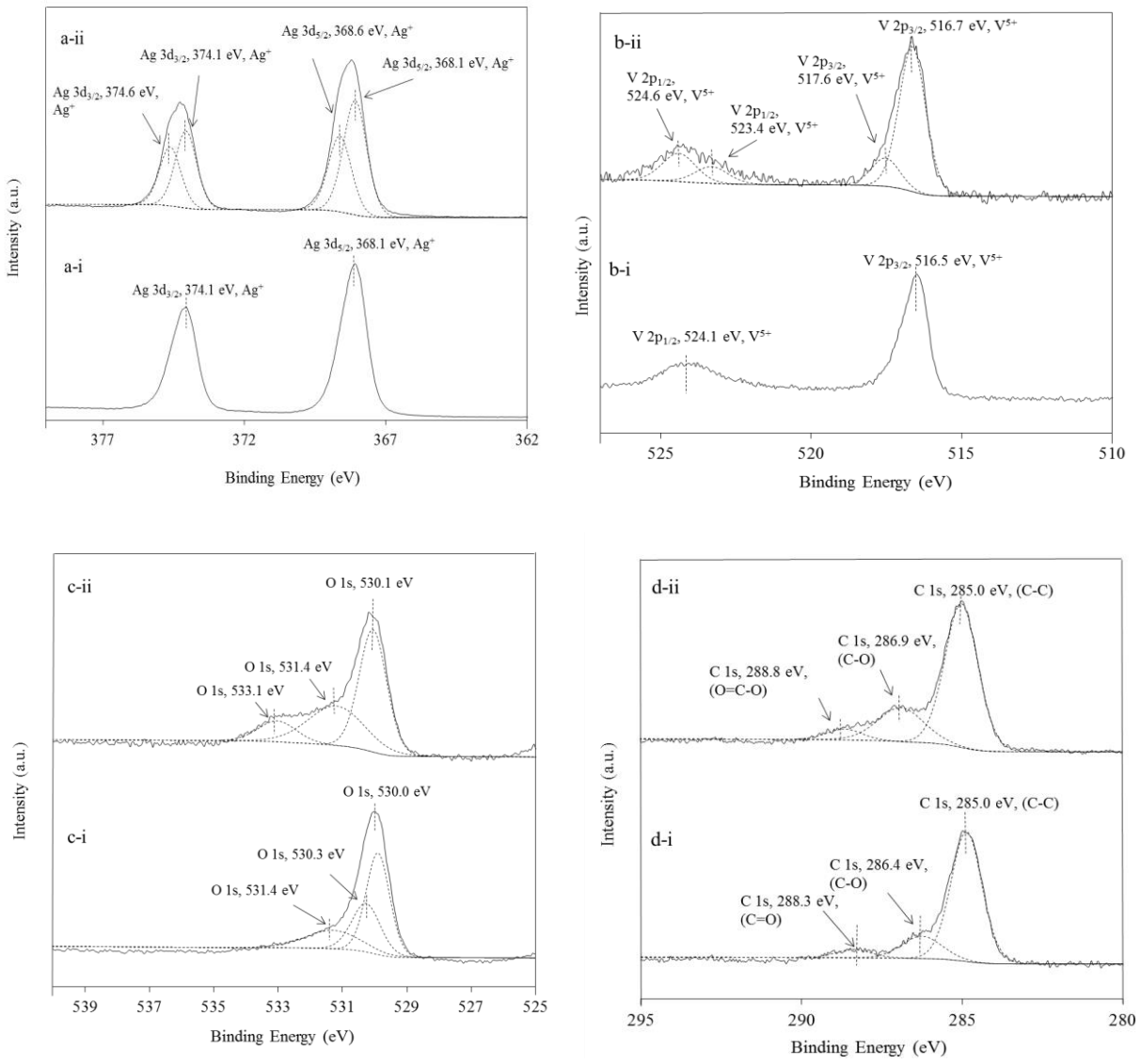

Figure 5.4: High-resolution XPS spectra of fresh, multi-phase pure (a-i, b-i, c-i and d-i) and 1.2 wt% GO-$Ag_2O/Ag_3VO_4/AgVO_3$ (a-ii, b-ii, c-ii and d-ii) composites; (a-i and a-ii): Ag 3d; (b-i and b-ii): V 2p; (c-i and c-ii): O 1s; (d-i and d-ii): C 1s.

In a comparison of the high-resolution spectra of pure samples and the 1.2 wt% GO sample observed in Figures 5.4a-i, 5.4b-i, 5.4c-i, and 4d-i as well as 5.4a-ii, 5.4b-ii, 5.4c-ii, and 5.4d-ii, the addition of GO slightly impacted the chemical and electronic states of the components in the GO-assisted sample. Two individual peaks observed centered at 368.1 eV and 374.1 eV in Figure 5.4a-i were assigned to the spin-orbit splitting characteristics of Ag $3d_{5/2}$ and Ag $3d_{3/2}$, respectively. However, the slight deconvolution spectra of Ag 3d (dashed lines in Figure 5.4a-ii) which occurred in the presence of the 1.2 wt% GO sample were centered at binding energies of 368.1 eV, 368.6 eV (ascribed to Ag $3d_{5/2}$), and binding energies of 374.1 eV, 374.6 eV (ascribed

to Ag $3d_{3/2}$). All of the Ag 3d peaks corresponded to Ag^{+} both in pure and 1.2 wt% GO samples, which agrees with results reported in literature [20, 33, 34]. A similar situation occurred with the peaks of V 2p. The observed peaks shown in Figure 5.4b-i were ascribed to V $2p_{3/2}$ at a binding energy of 516.5 eV, and V $2p_{1/2}$ centered at a binding energy of 524.1 eV. V 2p spectra shown in Figure 5.4b-ii were deconvoluted into two sets of peaks (dashed lines in Figure 5.4b-ii) centered at 516.7 eV, and 517.6 eV as well as 523.4 eV, and 524.6 eV. All such peaks were identified as V^{5+} corresponding well with the data from experiments with KVO_3 [35].

Figure 5.4c-i and Figure 5.4c-ii show that the O 1s spectra observed were broad and deconvoluted into three separated peaks (dashed lines in Figure 5.4c-i and Figure 5.4c-ii), centered at 530.0 eV, 530.3 eV, and 531.4 eV as well as 530.1 eV, 531.4 eV, and 533.1 eV for Figure 5.4c-i and Figure 5.4c-ii respectively. Of these six peaks, the peaks at 530.0 eV, 530.1 eV, 530.3 eV and 531.4 eV may be attributed to the lattice oxygen in the heterogeneous multi-phase photocatalysts, while the observed peak of O 1s at 533.1 eV was ascribed to absorbed oxygen [36].

Figure 5.4d-i shows three types of observed carbon, centered at 285.0 eV (C-C), 286.4 eV (C-O), and 288.3 eV (C=O) [24]. It should be noted that the obtained C 1s spectra were attributed to the adsorbed carbon present in the as-prepared pure composite. While slightly different deconvolutions occurred in the C 1s spectra of 1.2 wt% GO sample, Figure 5.4d-ii shows three separated peaks centered at 285.0 eV (C-C), 286.9 eV (C-O), and 288.8 eV (O=C-O) [18]. Therefore, the chemical and electronic states of multi-phase GO-assisted composites may be influenced by the addition of GO due to its electrical insulation via the disruption of sp^2 bonding networks [37].

5.3.5 Optical properties

In order to estimate the optical properties of the as-prepared fresh, multi-phase $Ag_2O/Ag_3VO_4/AgVO_3$ and GO-$Ag_2O/Ag_3VO_4/AgVO_3$ samples, UV-Vis diffuse reflectance spectra were explored, the results of which are shown in Figure 5.5:

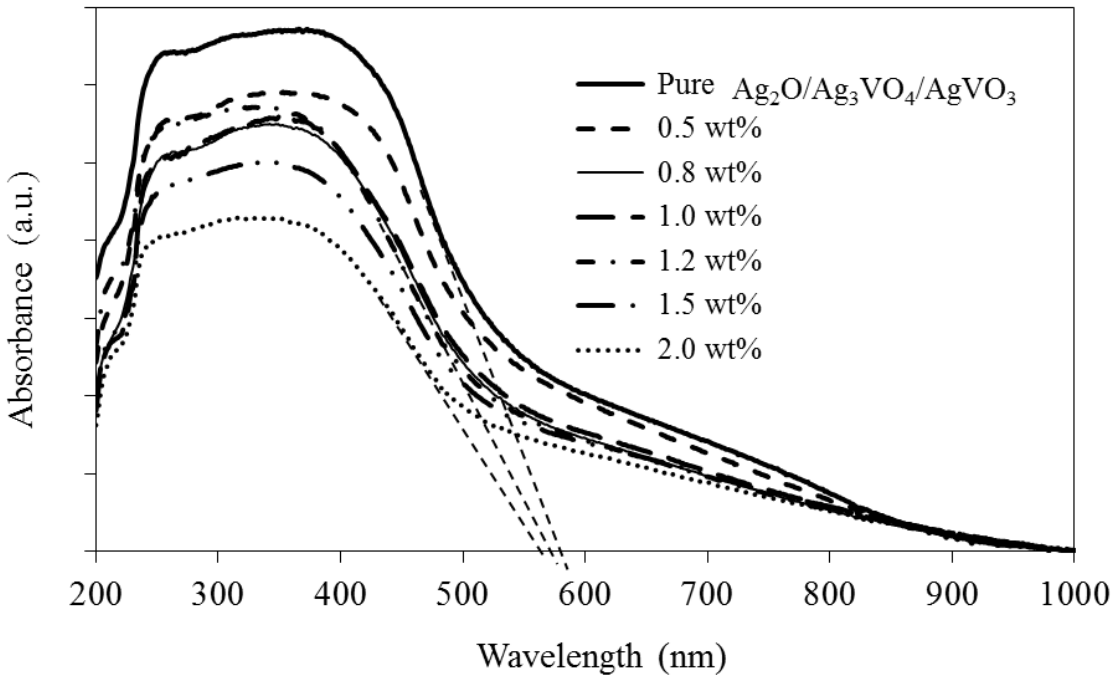

Figure 5.5: UV-vis DRS spectra of fresh samples with different quantities of GO.

No significant differences in the UV-Vis spectra of various samples were observed in Figure 5.5, indicating that the addition of GO had little impact on the optical properties of as-prepared samples in the visible light region (380 - 750 nm), primarily due to the functionalized optical properties of GO shown in the UV light region (absorption peak of GO at 230 nm) [38], which had proved to be weak in the visible light region. Hence, the optical properties of GO-assisted photocatalysts do not change substantially. In particular, the band gap energies of the as-synthesized fresh composites did not change substantially with the addition of GO. For this analysis, the band gap energies of the as-prepared composites were estimated using DRS results with the following formula:

$$\lambda = 1240/E_{bg} \qquad (5.1)$$

Where λ is the maximum wavelength of absorption by as-prepared samples (nm) (explained by the tangent dashed lines in Figure 5.5), and E_{bg} is the estimated band gap energy of the samples (eV).

As shown in Figure 5.5, ranges for the onset of visible light absorption by as-prepared samples were observed between 580 nm for pure $Ag_2O/Ag_3VO_4/AgVO_3$ and 565 nm for the 2.0 wt% GO sample, resulting in 580 nm (0 wt%), 578 nm (0.5 wt%), 570 nm (0.8 wt%), 572 nm (1.0 wt%), 570 nm (1.2 wt%), 568 nm (1.5 wt%) and 565 nm (2.0 wt%) corresponding to calculated band gap energies of 2.14 eV, 2.15 eV, 2.18 eV, 2.17 eV, 2.18 eV, 2.18 eV and 2.19 eV, respectively. Crucially, the calculated band gap energy of 2.18 eV was obtained for 1.2 wt% GO samples shown by the center dashed line. Therefore, the band gap energies of as-synthesized samples were less influenced by the amount of added GO.

5.3.6 Photocatalytic activity of organic components

5.3.6.1 Photodegradation of RhB

To quantify photocatalytic activity, RhB was used as a model organic pollutant in both the absence of light and under VLI, and the absorption spectra of RhB solution exposed to VLI were investigated over different periods of exposure. The corresponding results obtained are shown in Figures 5.6a, 5.6b and 5.6c.

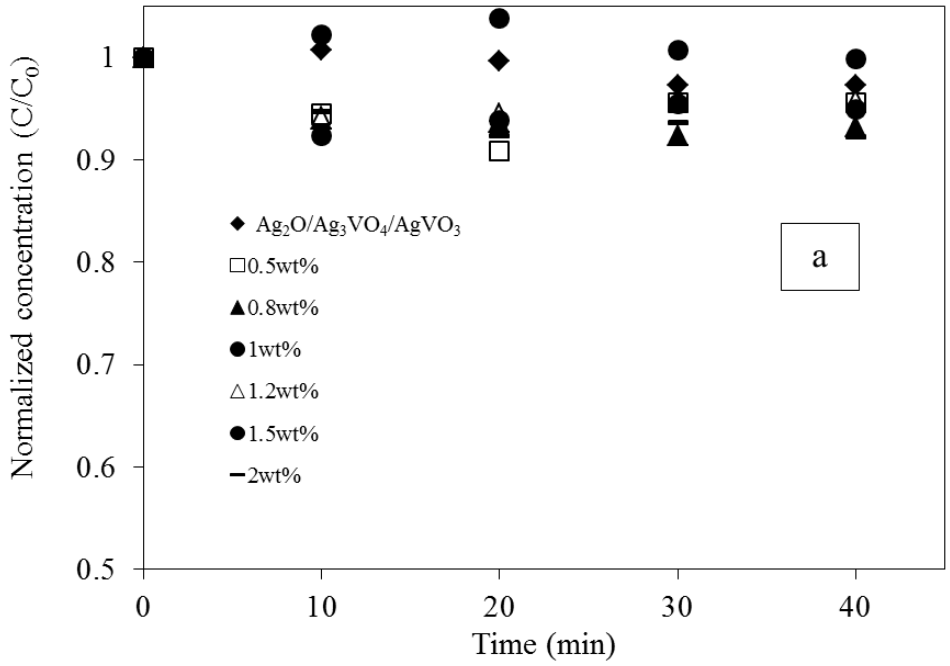

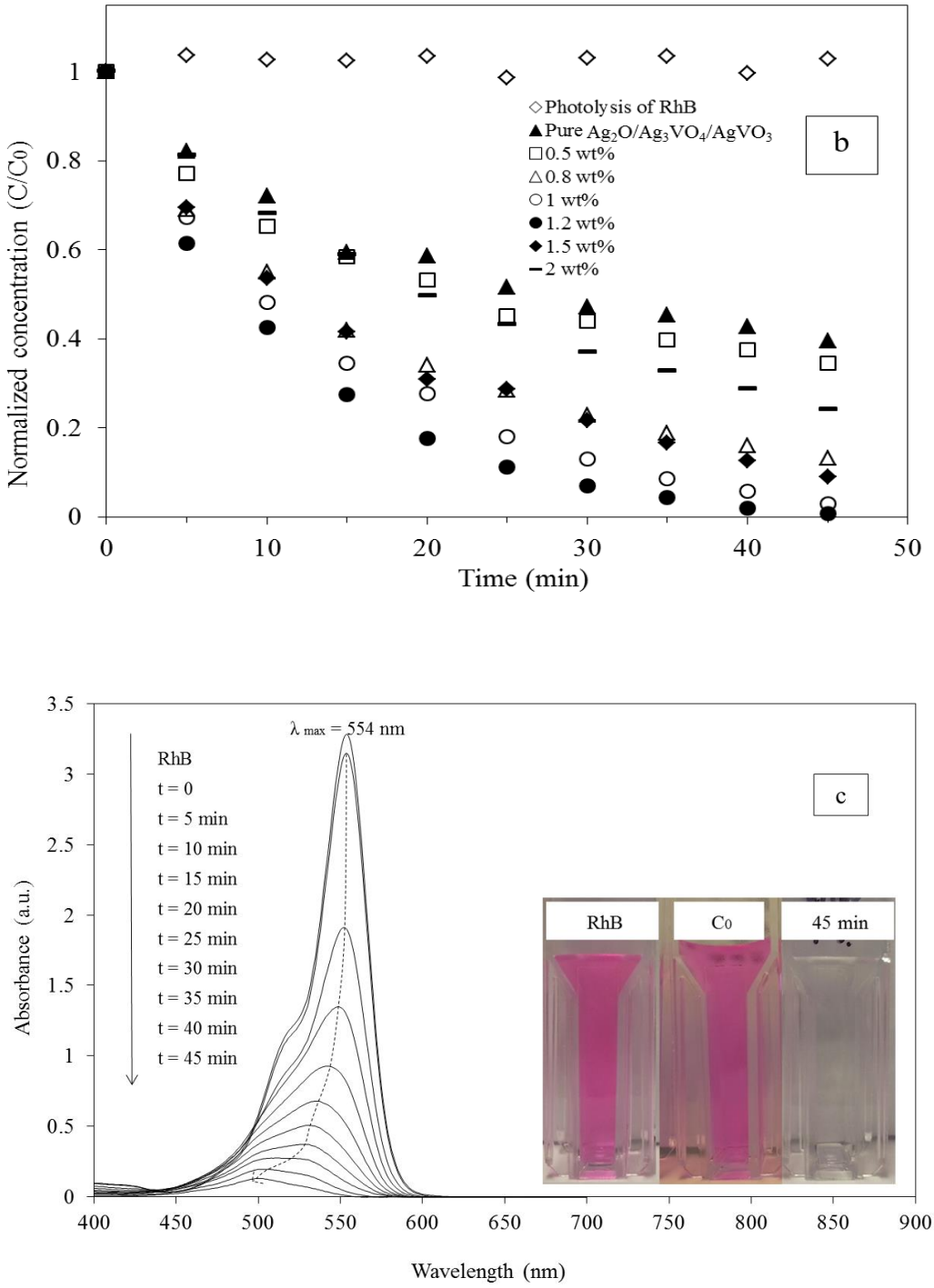

Figure 5.6: (a): adsorption reaction of RhB in the presence of various GO assisted silver species samples in the absence of light over 40 min; (b): the subsequent photocatalytic degradation of RhB (15 mg·L^{-1}) in the presence of various GO weight ratio samples, as well as the photolysis of RhB under VLI over 45 min, respectively; (c) UV-Vis spectra of RhB as a function of irradiation time over 1.2 wt% GO-$Ag_2O/Ag_3VO_4/AgVO_3$.

To achieve adsorption-desorption equilibration, the adsorption reaction of RhB in the presence of various GO-assisted silver species samples was performed over 40 min in the absence of light, the results of which are shown in Figure 5.6a. It can be seen that adsorptions of 2.7%, 4.7%, 6.8%, 0.2%, 4.1%, 5% and 7.9% onto photocatalysts corresponding to $Ag_2O/Ag_3VO_4/AgVO_3$, as well as 0.5 wt%, 0.8 wt%, 1 wt%, 1.2 wt%, 1.5 wt% and 2 wt% GO-assisted particles, respectively.

As shown in Figure 5.6b, the adsorption process was carried out in the absence of light for 40 min with minimal concentration changes, reaching an adsorption-desorption equilibrium before visible light irradiation. Compared to the pure multi-phase composite, samples containing GO exhibited higher photocatalytic activities towards RhB degradation. Of the GO samples, 1.2 wt% GO-$Ag_2O/Ag_3VO_4/AgVO_3$ exhibited the highest photocatalytic activity, resulting in the photodegradation of 99.2% RhB in 45 min. This indicates that photocatalytic activity towards RhB degradation is proportional to the quantity of added GO in the as-prepared samples. Such photocatalytic activity was observed to decrease when the quantity of GO exceeded 1.2 wt%. As seen in Figure 5.6b, the degradation of RhB using 1.5 wt% and 2.0 wt% GO samples was found to decrease, and the photocatalytic activities were similar to those which were seen in the 0.8 wt% and 0.5 wt% GO samples, respectively.

As seen in Figure 5.6c, the decline of RhB at the maximum absorption wavelength of 554 nm was mainly due to cleavage of the whole conjugated chromophore structure of RhB under VLI [39, 40], with slightly progressive hypochromatic shifts of the absorption bands from 554 nm to 500 nm. This decomposition of RhB was verified by the change in colour of the RhB supernatant from pink to colourless, which occurred after 45 min, shown in the inset of Figure 5.6c. Therefore, the high photocatalytic performance of GO-assisted $Ag_2O/Ag_3VO_4/AgVO_3$ was attributed to the synergetic effects of the adsorptivity of functionalized GO and multi-morphological features of heterogeneous photocatalysts.

5.3.6.2 Photodegradation of MO

To investigate the optimal GO-assisted sample which exhibits a high photocatalytic performance towards the degradation of organic dyes under VLI, different types of dyes were applied to the degradation process. MO was used as a control to confirm that the photo-induced degradation

process of different dyes was achieved using the 1.2 wt% GO-$Ag_2O/Ag_3VO_4/AgVO_3$ composite. The adsorption-desorption equilibration of the photosystem was attained after 45 min in the absence of light followed by the light reaction, which is shown in Figure 5.7a. The results of visible-light-induced photocatalytic performance towards MO in the absence and presence of photocatalysts are shown in Figure 5.7b, and the absorption spectra of the MO aqueous solution under VLI for different time periods are shown in Figure 5.7c.

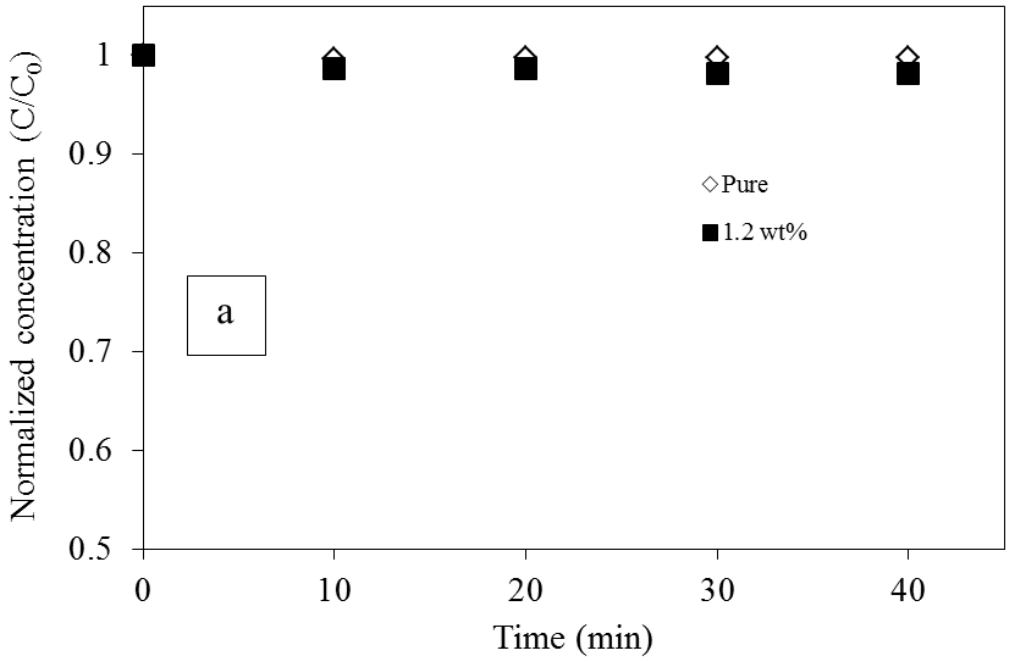

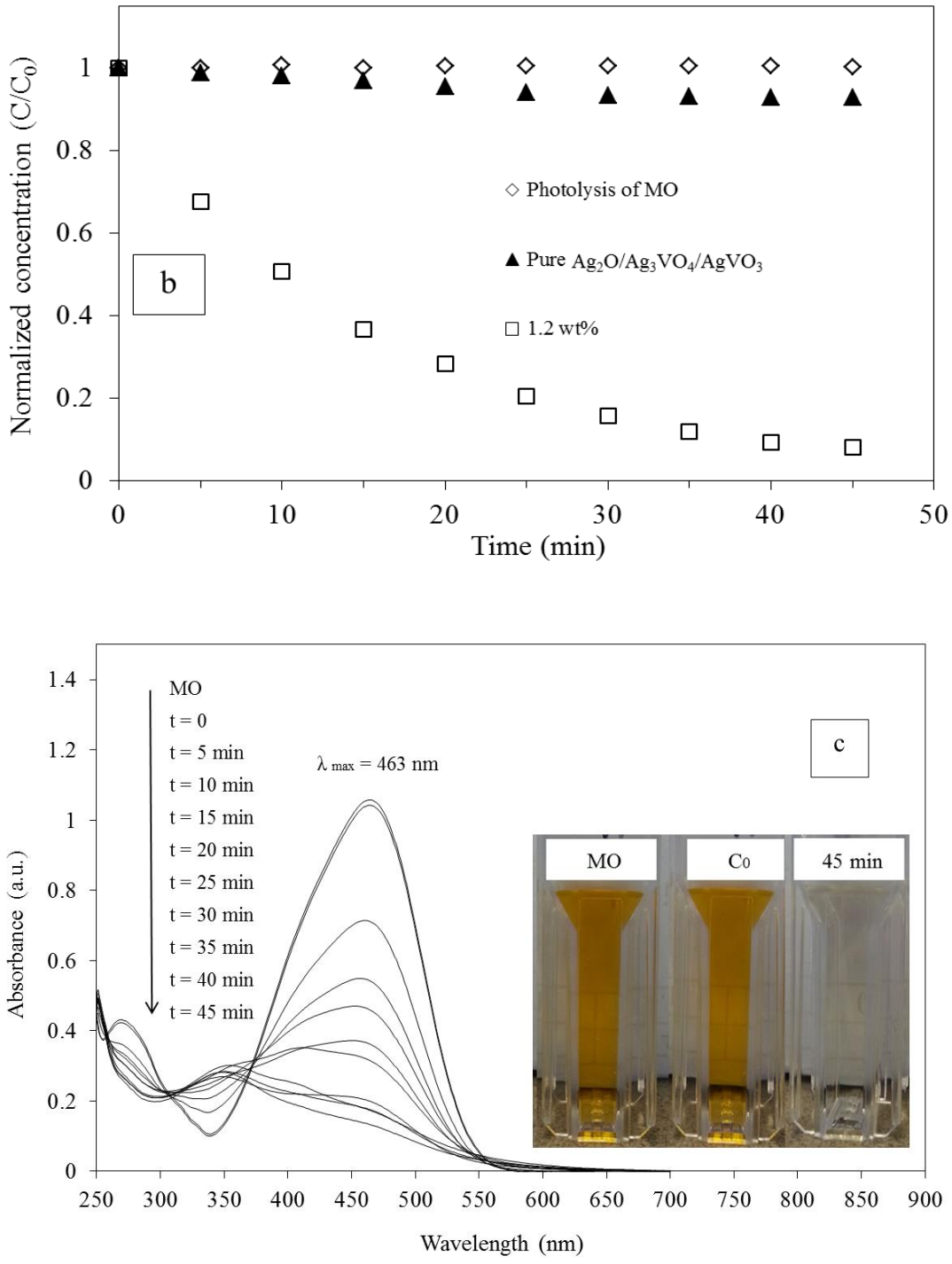

Figure 5.7: (a): adsorption reaction of MO in the presence of pure and 1.2 wt% GO-assisted silver composites in the absence of light over 40 min; (b): the subsequent photocatalytic degradation of MO (15 mg·L^{-1}) in the presence of pure and 1.2 wt% GO-$Ag_2O/Ag_3VO_4/AgVO_3$ composites, as well as the photolysis of MO under VLI over 45 min, respectively; (c) UV-Vis spectra of MO as a function of irradiation time using the 1.2 wt% GO sample.

To achieve adsorption-desorption equilibration, the adsorption reaction of MO in the presence of pure and 1.2 wt% GO-assisted silver composites was performed over 40 min in the absence of light, the results of which are shown in Figure 5.7a. It can be seen that adsorptions of 0.29% and 1.8% onto photocatalysts corresponded to $Ag_2O/Ag_3VO_4/AgVO_3$ and 1.2 wt% GO-assisted particles, respectively.

A comparison of the performance of degradation of RhB and MO is shown in Figures 5.6b and 5.7b, respectively. The concentration of MO was allowed to reach an adsorption-desorption equilibration in the absence of light over a period of 40 min. The photocatalytic activity towards the degradation of MO with pure $Ag_2O/Ag_3VO_4/AgVO_3$ decreased to 7% degradation under VLI over 45 min. However, 1.2 wt% GO-$Ag_2O/Ag_3VO_4/AgVO_3$ exhibited an enhanced photocatalytic performance with 92% degradation of MO under VLI over 45 min.

As shown in Figure 5.7c, the maximum absorption of MO at a wavelength of 463 nm declined under VLI in the presence of 1.2 wt% GO, suggesting that the chromophoric structure of MO was decomposed [41, 42]. This decomposition of MO was verified by the colour change of the MO supernatant from yellow to colourless observed after 45 min, and is shown in the inset of Figure 5.7c. Hence, the GO-assisted multi-phase photocatalysts exhibited high photo-induced degradations of different dyes under VLI.

5.3.7 Stability of graphene oxide-$Ag_2O/Ag_3VO_4/AgVO_3$

To investigate the stabilities of multi-phase, pure and the multi-phase GO-assisted $Ag_2O/Ag_3VO_4/Ag_4V_2O_7$ photocatalysts over the course of photocatalytic reactions, a number of characterization techniques and investigations were studied. The post-use characterization results are discussed in subsequent sections.

5.3.7.1 Post-use XRD analysis

In order to further investigate changes to the crystal structures of multi-phase pure and GO-assisted $Ag_2O/Ag_3VO_4/AgVO_3$ composites upon exposure to the photoactivity system, XRD analysis was performed on the recycled samples. The post-use patterns obtained for pure and 1.2 wt% GO samples as representatives are shown in Figure 5.8:

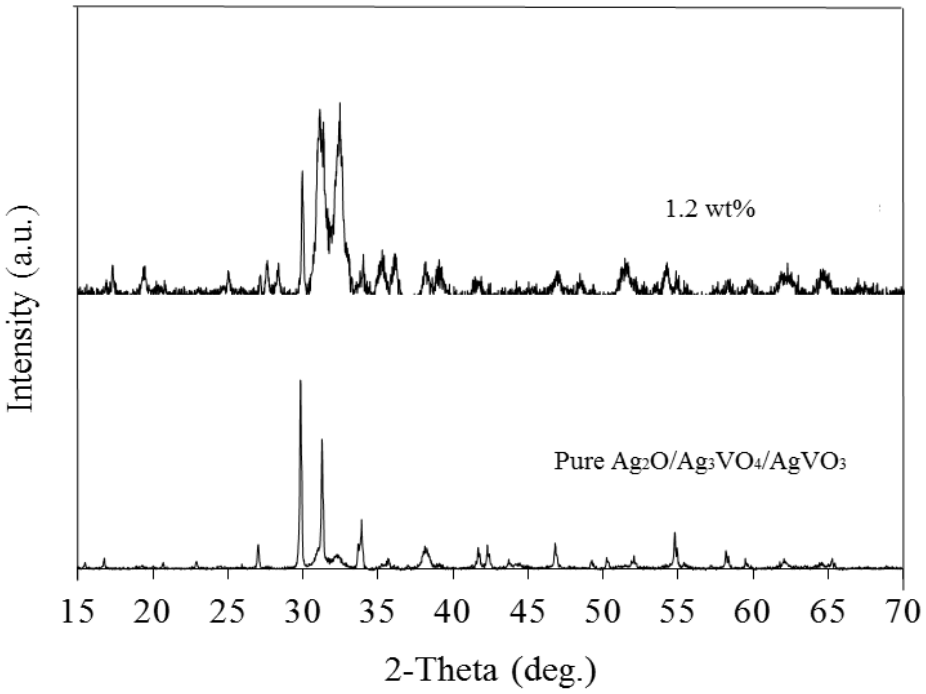

Figure 5.8: XRD patterns of post-use pure and 1.2 wt% GO-$Ag_2O/Ag_3VO_4/AgVO_3$ samples.

By comparing the corresponding fresh and post-use samples in Figure 5.1 and Figure 5.8, XRD patterns observed from the recovered post-use of pure $Ag_2O/Ag_3VO_4/AgVO_3$ and 1.2 wt% GO samples showed different structural changes. As shown in Figure 5.8, the declines of major peak intensities in the pure sample occurred at 30.96° and 32.42°, which is evidence that the loss of crystallinity of α-Ag_3VO_4 occurred during the photocatalytic activity. Compared to the corresponding fresh sample, the major peak intensities of β-$AgVO_3$ and Ag_2O increased at 29.84°and 33.48°, as well as 38.03° and 54.88° respectively, suggesting that the crystallinities of β-$AgVO_3$ and Ag_2O were increased in the photosystem due to photocorrosion of α-Ag_3VO_4 during photocatalytic operation. The reaction is shown in the following equation:

$$\alpha\text{-}Ag_3VO_4 \xrightarrow{VLI} \beta\text{-}AgVO_3 + Ag_2O \qquad (5.2)$$

According to this hypothesis, XRD patterns from the post-use pure sample can be explained sensibly without the necessity for the formation of new phases in the system. However, no changes of peak intensity were observed from the comparison with the fresh and post-use 1.2 wt% GO samples, which can most likely be attributed to the silver species samples protected

from photocorrosion by GO during photocatalytic reactions under VLI. This result agrees with reports that GO serves as a protective substrate which partially inhibits the photocorrosion of photocatalysts containing silver species [18, 43].

5.3.7.2 Post-use SEM analysis

In order to explore the microstructure and morphology changes which occurred, the morphologies of the synthesized multi-phase pure $Ag_2O/Ag_3VO_4/AgVO_3$ photocatalyst and the as-prepared composite in the presence of 1.2 wt% GO were investigated by SEM after photocatalytic reactions. The images that were obtained are shown in Figure 5.9.

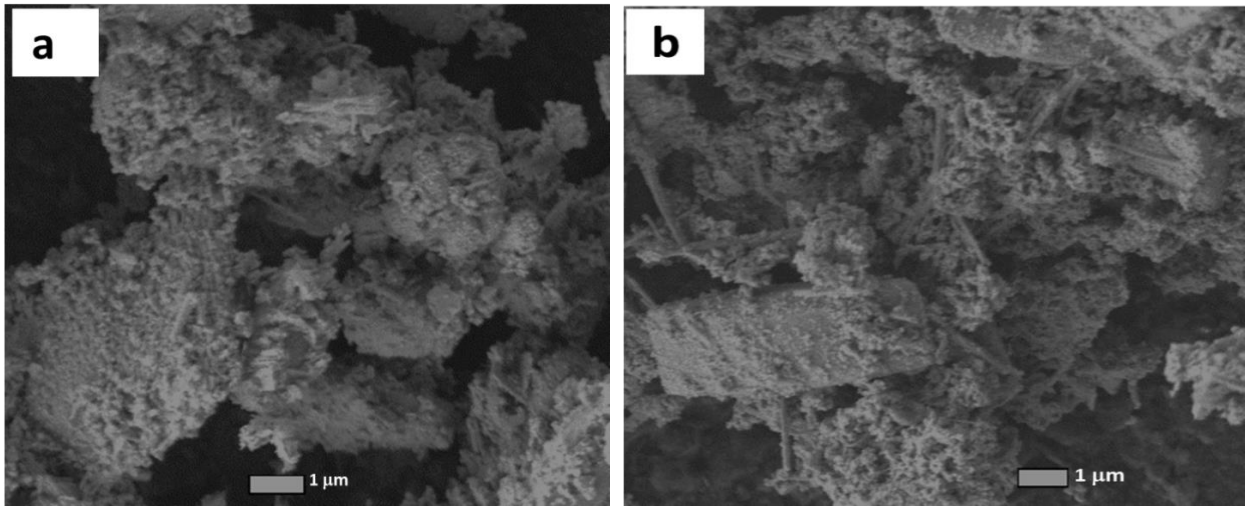

Figure 5.9: SEM images of post-use composites. (a) pure $Ag_2O/Ag_3VO_4/AgVO_3$; (b) 1.2 wt % GO-$Ag_2O/Ag_3VO_4/AgVO_3$.

As shown in Figure 5.9, SEM images from the recovered post-use of multi-phase pure $Ag_2O/Ag_3VO_4/AgVO_3$ and 1.2 wt% GO-assisted samples showed different structural changes. Comparing Figure 5.2a and Figure 5.9a, dendritic-like plates disappeared while elongated cylindrical-like structures and nanoparticles were formed after photocatalytic reactions under VLI. In addition, crystals which were unobstructed by nanoscale granular particles before VLI were subsequently encrusted completely by these cylindrical structures and nanoparticles after exposure to VLI, agreeing well with the post-use XRD results. However, no significant morphological changes were observed when comparing Figure 5.2e5and Figure.9b, indicating that the photocatalytic performance towards the degradation of dyes was unable to strongly impact the morphologies of as-prepared GO-assisted composites. This is most likely due to GO

as the sacrificial reagent protecting the multi-phase $Ag_2O/Ag_3VO_4/AgVO_3$ from photocorrosion under VLI. Therefore, the multi-morphological features of multi-phase composites could be partially maintained by GO to keep the photocatalytic activities of functionalized GO-assisted photocatalysts high in regards to the degradation of organic dyes under VLI.

5.3.7.3 Post-use XPS analysis

In order to further investigate the chemical and electronic states of the post-use pure and 1.2 wt% GO-assisted composites after photocatalytic reactions, XPS analysis was performed and the obtained results are shown in Figures 5.10a-i and 5.10a-ii, 5.10b-i and 5.10b-ii, 5.10c-i and 5.10c-ii, as well as 5.10d-i and 5.10d-ii for Ag 3d, V 2p, O 1s and C 1s states, respectively. The binding energies obtained via XPS analysis were calibrated by referencing C 1s at 285 eV.

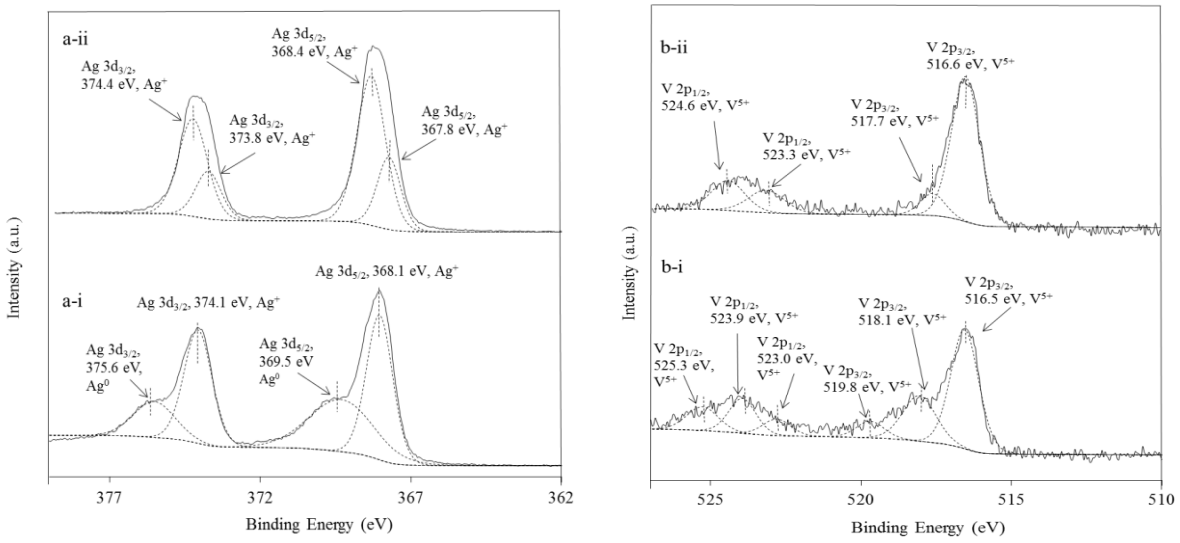

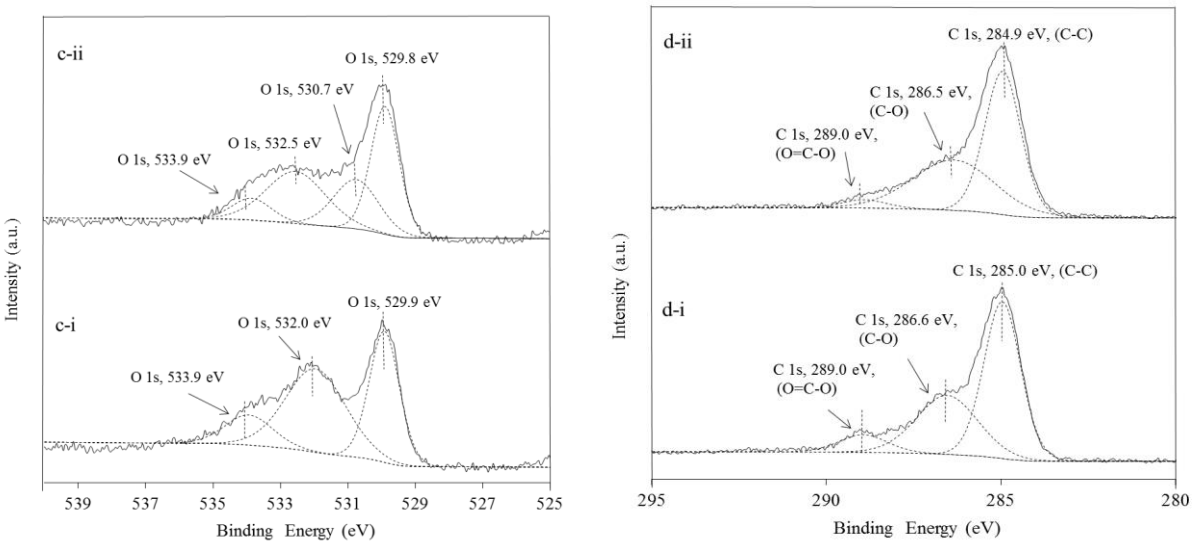

Figure 5.10: High-resolution XPS spectra of post-use, multi-phase pure (a-i, b-i, c-i and d-i) and 1.2 wt% GO-$Ag_2O/Ag_3VO_4/AgVO_3$ (a-ii, b-ii, c-ii and d-ii) composites; (a-i and a-ii): Ag 3d; (b-i and b-ii): V 2p; (c-i and c-ii): O 1s; (d-i and d-ii): C 1s.

Comparing Ag 3d spectra in Figure 5.4 and Figure 5.10, the observed Ag 3d spectra of post-use samples had changed noticeably. The devolution which occurred in Ag 3d was assigned to two couples of peaks centered at 368.1 eV and 369.5 eV as well as 374.1 eV and 375.6 eV (dashed lines in Figure 5.10a-i), attributed to the binding energies of Ag $3d_{5/2}$ and Ag $3d_{3/2}$, respectively. Of these four peaks, the peaks at 368.1 eV and 374.1 eV were ascribed to Ag^+, and the peaks at 369.5 eV and 375.6 eV were ascribed to Ag^0 [44]. However, no significant differences in the Ag 3d spectra were observed between Figure 5.4a-ii and Figure 5.10a-ii, indicating that two couples of peaks observed centered at 367.8 eV and 368.4 eV as well as 373.8 eV and 374.4 eV (dashed lines in Figure 5.10a-ii) were assigned to Ag $3d_{5/2}$ and Ag $3d_{3/2}$ orbits, respectively. Each of these peaks were ascribed to Ag^+, indicating that a minimal quantity of silver species was reduced to Ag^0 during photocatalytic performance in the form of dye degradation under VLI, indicating that GO, as the protective substrate, partially prevented the photocatalytic reduction of Ag^+.

Comparing V 2p spectra in Figure 5.4 and Figure 5.10, some changes to V $2p_{3/2}$ and V $2p_{1/2}$ spectra which occurred in Figure 5.10b-i were thought to be deconvoluted into three pairs of individual peaks centered at 516.5 eV&523.0 eV, 518.1 eV&523.9 eV, and 519.8 eV&525.3 eV (dashed lines in Figure 5.10b-i), which corresponds to V^{5+}. The shifts of peaks may be the result of changes to the states of vanadate ions in the crystal structures of multi-phase composites

following photocatalytic performance. No differences in V 2p spectra were observed between Figure 5.4b-ii and Figure 5.10b-ii, indicating that the states of vanadate ions were stable in photocatalytic reactions under VLI, which agrees well with the XRD analyses from post-use samples.

In a comparison of O 1s and C 1s in Figure 5.4 and Figure 5.10, photocatalytic reactions also influence the chemical and electronic states of oxygen and carbon. As seen in Figure 5.10c-i and Figure 5.10c-ii, the observed deconvoluted peaks were centered at 532.0 eV and 532.5 eV ascribed to oxide ions (e.g. O^{2-}), indicating the states of oxygen species in composites changed following photocatalytic reactions. From Figures 5.10d-i and 5.10d-ii, no major changes occurred in C 1s spectra compared to such spectra in fresh samples (Figures 5.4d-i and 5.4d-ii), the peak at 289.0 eV, which was originally assigned to C=O shown in Figure 5.4d-i, was assigned to be O=C-O after photocatalytic reactions. This was thought to be due to mineralized species from decomposed dye solutions which adhered to the post-use composites. Furthermore, an effective reduction from GO to reduced-GO (RGO) using the 1.2 wt% GO sample under VLI was confirmed by XPS data, in terms of the increased C/O atomic ratio from 1.5 to 2.7 (fresh sample vs. post-use sample) after photocatalytic performance, which was in agreement with the results reported by Zhang et al. [24]. Hence, GO could serve as a promising protective substrate to inhibit the photocorrosion of photocatalysts containing silver species in photosystems subjected to VLI.

5.3.7.4 Post-use optical properties

Further investigation of the UV-Vis diffuse reflectance spectra of post-use pure and 1.2 wt% GO-assisted samples resulted in the intrinsic absorption under VLI shown in Figure 5.11.

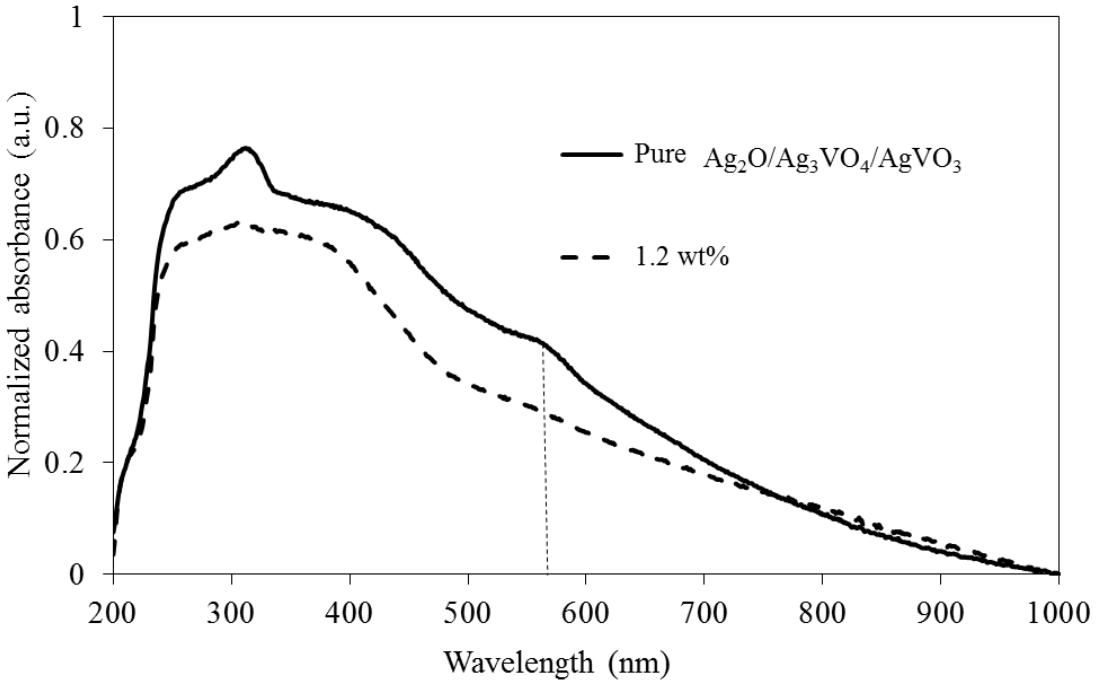

Figure 5.11: UV-Vis DRS of post-use pure and 1.2 wt% GO-$Ag_2O/Ag_3VO_4/AgVO_3$ samples.

As shown in Figure 5.11, no major differences in the intrinsic absorption were revealed in the post-use 1.2 wt% GO sample. However, a tail absorption peak at around 565 nm was observed in the absorption spectrum for the used pure sample, and was ascribed to the increased generation of metallic silver (Ag^0) present in the composite without the addition of GO [45]. This indicates that Ag^+ ions may be reduced by accepting photogenerated electrons in the absence of sacrificial reagents under VLI [7]. Therefore, comparison of the intrinsic absorption in the post-use samples after photocatalytic reactions under VLI showed that the GO sample was more resistant to photocorrosion under VLI than the pure sample, which is in agreement with the XRD and SEM results shown in previous sections.

5.3.8 Role of reactive species testing in RhB and MO

In order to investigate the mechanism of the photocatalytic degradation of organic dyes, it is important to note that the role of the reactive species in photocatalysis serves as a significant clue towards unlocking the machinery of the photoactive performance, and must be explored. Therefore, quenching tests as diagnostic tools were involved in the dye degradation studies. It is

well known that reactive species such as hole (h^+), electrons (e^-), hydroxyl radicals (•OH) and superoxide radicals (O_2•$^-$) play important roles in the photodegradation of organic pollutants [46-48]. The adsorption-desorption equilibration of RhB and MO onto photocatalysts was achieved over 40 min in the absence of light, which was followed by the quenching tests of various reactive species scavengers (including BQ, AO and TBA) for the photodegradation of RhB and MO, the results of which are shown in Figures 5.12a-d.

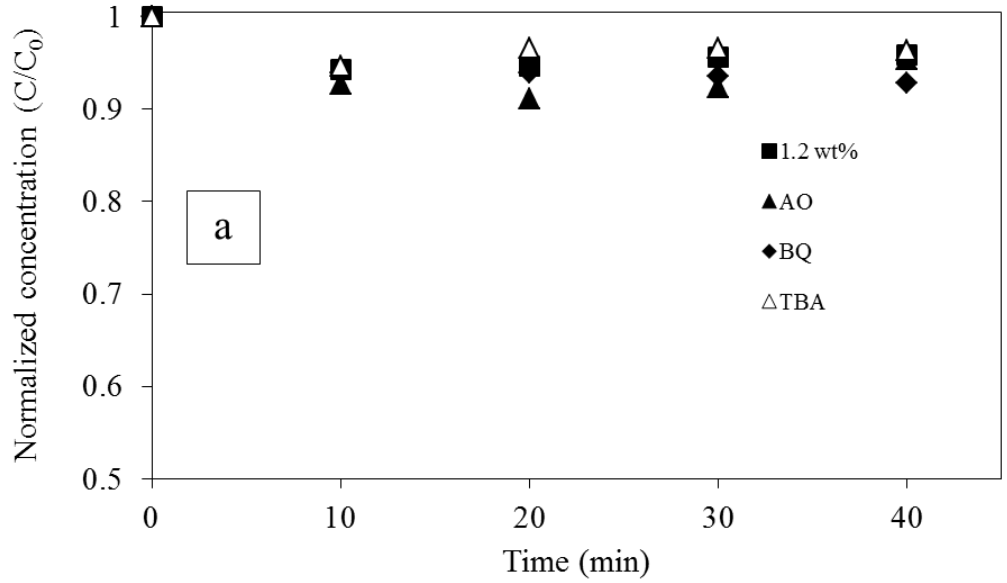

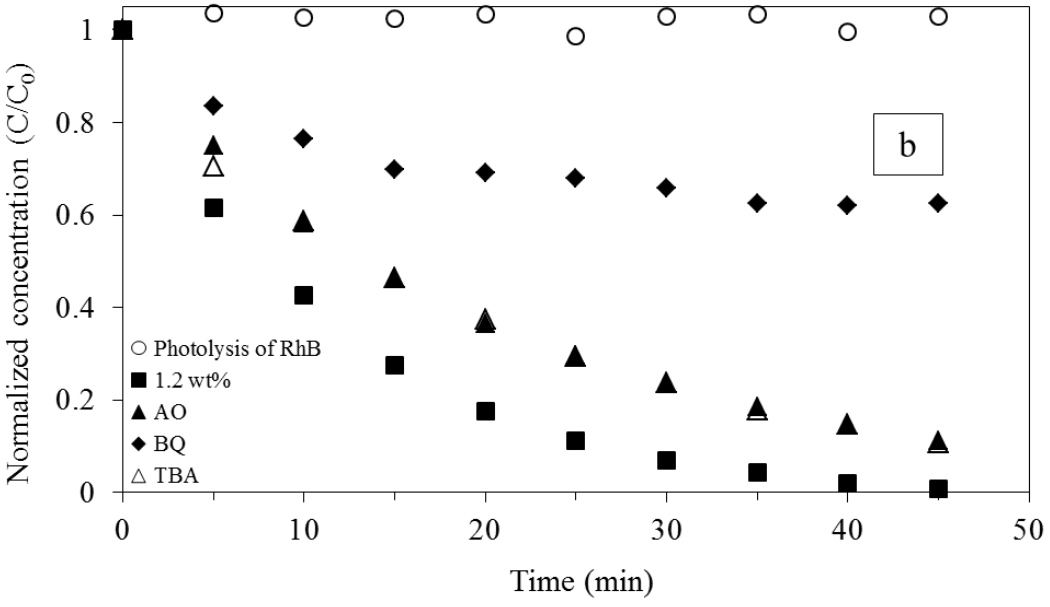

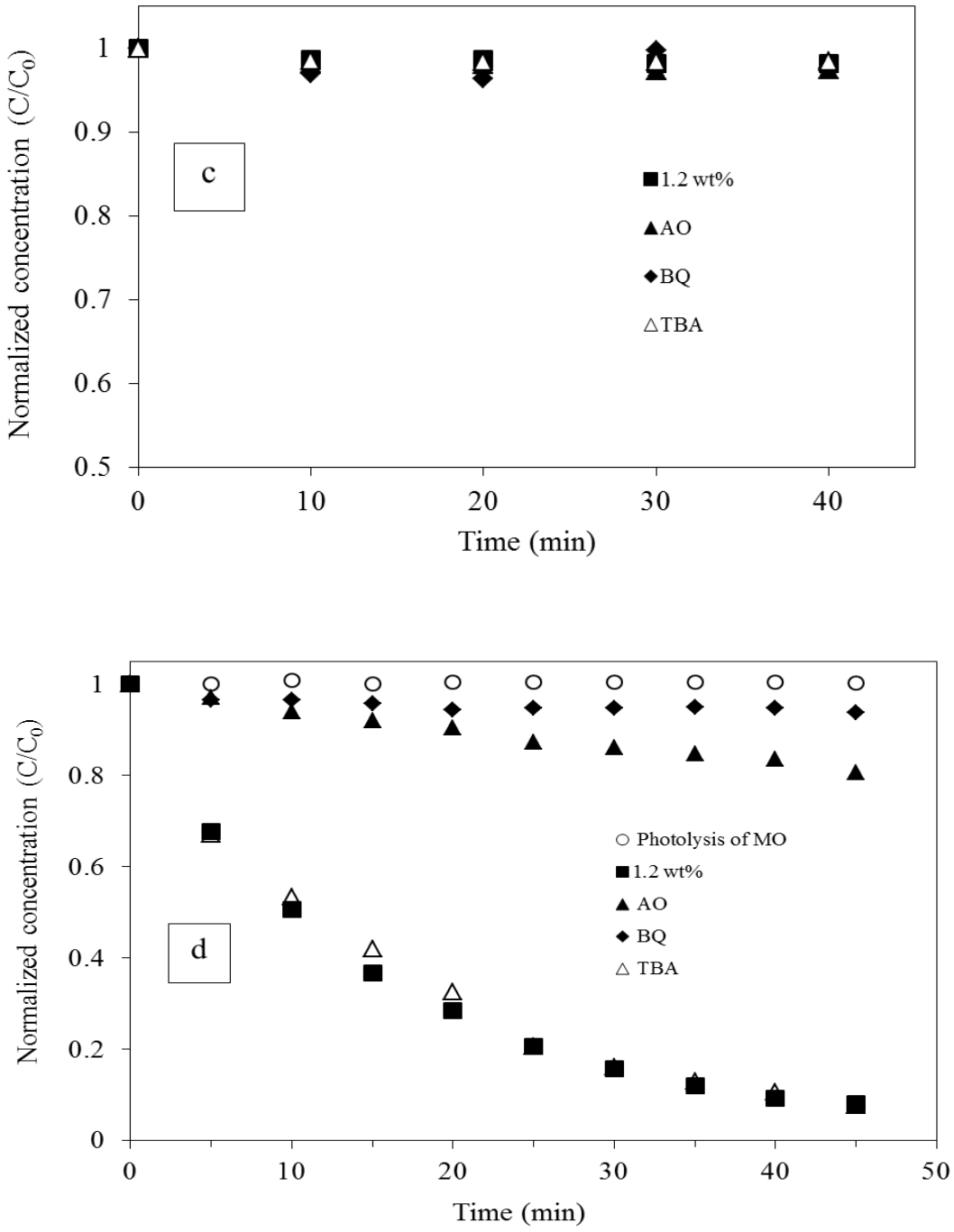

Figure 5.12: (a): adsorption reaction of RhB over 40 min in the absence of light; (b): quenching tests for photocatalytic degradation for RhB over 1.2 wt% GO-$Ag_2O/Ag_3VO_4/AgVO_3$ under different conditions with VLI; (c): adsorption reaction of MO over 40 min in the absence of light; (d): quenching tests for photocatalytic degradation of MO over 1.2 wt% GO-$Ag_2O/Ag_3VO_4/AgVO_3$ under different conditions with VLI.

To achieve adsorption-desorption equilibration, adsorption reactions of RhB and of MO in the presence of 1.2 wt% GO-$Ag_2O/Ag_3VO_4/AgVO_3$ composites were performed over 40 min in the

absence of light, the results of which are shown in Figure 5.12a and Figure 5.12c respectively. This adsorption-desorption process resulted in the adsorptions of 4.1%, 4.6%, 7.1% and 3.6% onto photocatalysts shown in Figure 5.12a, corresponding to a no-scavenger system, as well as the scavengers of AO, BQ and TBA used in the quenching tests, respectively. As shown in Figure 5.12c, the adsorption-desorption process also gave rise to the adsorptions of 1.8%, 2.6%, 2.4% and 1.6% onto photocatalysts shown in Figure 5.12c, corresponding to a no-scavenger system, as well as the scavengers of AO, BQ and TBA used in the quenching tests, respectively.

As shown in Figure 5.12b, employing BQ as a scavenger for O_2•$^-$ [49, 50] successfully resulted in suppression of the degradation of RhB under VLI, reducing the degradation of RhB to 38% after 45 min. Using AO as a scavenger for h^+ [51, 52] and TBA as a scavenger for •OH [46] showed almost identical results in regards to the suppression of RhB degradation, both of which reduced the degradation of RhB to 89% after 45 min. In addition, as can be seen in Figure 5.12d, BQ also played a major role in the degradation mechanism for MO, reducing the degradation of MO to 6% after 45 min, and AO showed excellent suppression towards the degradation of MO as well with 19% MO degradation after 45 min. No major differences were observed following addition of TBA, indicating that •OH is less likely to be restricted by TBA in the presence of MO in the photosystem. From these results, it can be concluded that oxygen plays a significant role in the photocatalytic oxidation of organic dyes (RhB and MO) on the surface of the GO-assisted $Ag_2O/Ag_3VO_4/AgVO_3$ photocatalysts.

5.3.9 Mechanism of photocatalytic activity

The photodegradation pathways of the dyes (RhB and MO) in the presence of the 1.2 wt% GO-$Ag_2O/Ag_3VO_4/AgVO_3$ composite were investigated under VLI. Given the results obtained from the photolytic and photocatalytic degradation studies, as well as from the quenching tests, the possible reactions are proposed as follows:

$$Ag_2O + VLI \rightarrow Ag_2O\ (h^+ + e^-) \qquad (5.3a)$$

$$Ag_3VO_4 + VLI \rightarrow Ag_3VO_4\ (h^+ + e^-) \qquad (5.3b)$$

$$AgVO_3 + VLI \rightarrow AgVO_3\ (h^+ + e^-) \qquad (5.3c)$$

$$h^+ + e^- \rightarrow \text{Heat} \quad (5.4)$$

$$AgVO_3\ (e^-) + GO \rightarrow AgVO_3 + GO_{(injected\ e^-)} \quad (5.5a)$$

$$GO_{(injected\ e^-)} + Ag_2O \rightarrow GO + Ag_2O_{(injected\ e^-)} \quad (5.5b\text{-}i)$$

$$GO_{(injected\ e^-)} + Ag_3VO_4 \rightarrow GO + Ag_3VO_4\ (injected\ e^-) \quad (5.5b\text{-}ii)$$

$$AgVO_3\ (e^-) + Ag_2O \rightarrow AgVO_3 + Ag_2O_{(injected\ e^-)} \quad (5.5c\text{-}i)$$

$$AgVO_3\ (e^-) + Ag_3VO_4 \rightarrow AgVO_3 + Ag_3VO_4\ (injected\ e^-) \quad (5.5c\text{-}ii)$$

$$Ag_2O_{(injected\ e^-)} + GO \rightarrow Ag_2O + GO_{(injected\ e^-)} \quad (5.5d)$$

$$Ag_3VO_4\ (injected\ e^-) + GO \rightarrow Ag_3VO_4 + GO_{(injected\ e^-)} \quad (5.5e)$$

$$Ag_3VO_4\ (h^+) + Ag_2O \rightarrow Ag_3VO_4 + Ag_2O\ (h^+) \quad (5.6a)$$

$$Ag_2O\ (h^+) + AgVO_3 \rightarrow Ag_2O + AgVO_3\ (h^+) \quad (5.6b)$$

$$AgVO_3\ (h^+) + GO \rightarrow AgVO_3 + GO\ (h^+) \quad (5.6c)$$

$$e^-_{(on\ AgVO3\ and\ GO)} + O_2 \rightarrow O_2\bullet^- \quad (5.7a)$$

$$O_2\bullet^- + H^+ \rightarrow HO_2\bullet \quad (5.7b)$$

$$HO_2\bullet + 2e^- + H^+ \rightarrow \bullet OH + OH^- \quad (5.7c)$$

$$GO_{(injected\ e^-)} + VLI \rightarrow RGO \quad (5.7d)$$

$$h^+ + H_2O \rightarrow \bullet OH + H^+ \quad (5.8a)$$

$$4\ h^+ + 2\ H_2O \rightarrow 4\ H^+ + O_2 \quad (5.8b)$$

$$4\ h^+ + 2\ OH^- \rightarrow O_2 + 2\ H^+ \quad (5.8c)$$

$$RhB_{ads} \text{ or } MO_{ads} + VLI \rightarrow RhB^{*}_{ads} \text{ or } MO^{*}_{ads} \qquad (5.9a)$$

$$RhB^{*}_{ads} \text{ or } MO^{*}_{ads} - e^{-} \rightarrow MO^{+}_{ads} \text{ or } RhB^{+}_{ads} + \bullet OH \rightarrow \text{intermediates} \rightarrow CO_2 + H_2O \qquad (5.9b)\ [40, 47]$$

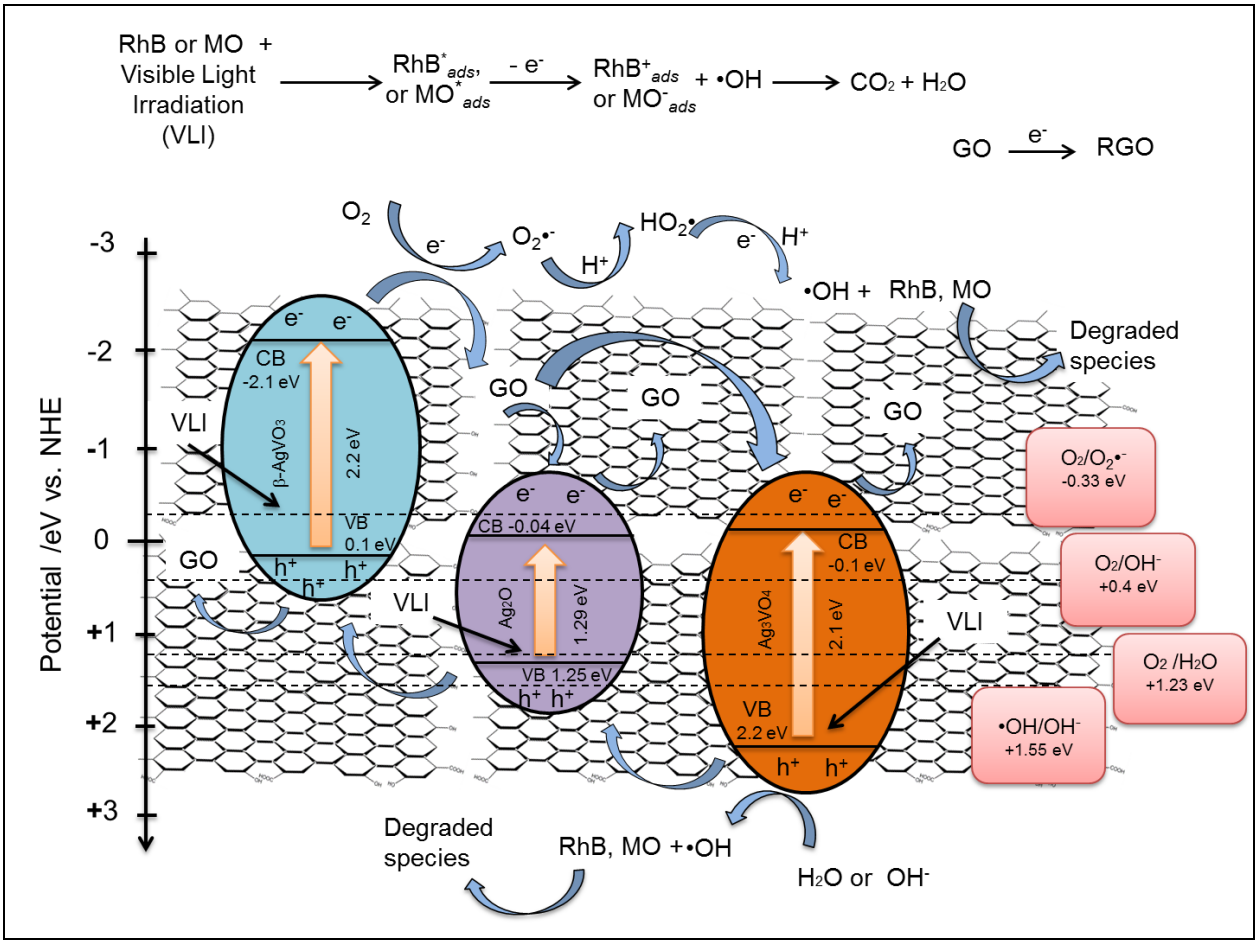

Figure 5.13: Photocatalytic mechanism of the degradation of organic components (RhB and MO) on 1.2 wt% GO-$Ag_2O/Ag_3VO_4/AgVO_3$ composite (white and hexagonal sheets represented GO in the diagram) under VLI.

The energy bands of Ag_2O, Ag_3VO_4 and $AgVO_3$ were identified using results reported in literature [9, 32, 53]. As shown in Figure 5.13, multi-phase heterogeneous $Ag_2O/Ag_3VO_4/AgVO_3$ particles are distributed on GO sheets, and the photocatalytic activity is initiated by the absorption of photons with wavelengths in the visible light region and energies larger than those of Ag_2O, Ag_3VO_4 and $AgVO_3$ with respect to reactions 5.3a, 5.3b, and 5.3c, respectively.

In these reactions, the photogenerated e^--h^+ pairs form in the photocatalysts, then either separate and move freely onto the surface of composites. That is to say that photo-excited electrons jump to the conduction band (CB) while holes remain on the valence band (VB) or are recombined as energy emissions under the internal electric field due to the characteristics of the components, in according with reaction (5.4). Upon successful separation of the photo-excited e^--h^+ pair, a series of photocatalytic reactions would occur in a particular sequence (from reaction 5.5 to reaction 5.9). The distribution of Ag_2O, Ag_3VO_4 and $AgVO_3$ particles on GO sheets can be separate or intimate. For the separated Ag_2O, Ag_3VO_4 and $AgVO_3$ particles exposed to VLI, the photo-excited electrons on the CB of $AgVO_3$ are transferred to GO sheets which serve as bridges to facilitate interfacial charge transmission. As such, electrons are transferred to the CB of Ag_2O or Ag_3VO_4 along the GO sheets (reactions 5.5a, 5.5b-i and 5.5b-ii). For the closely connected Ag_2O, Ag_3VO_4 and $AgVO_3$ particles exposed to VLI, the photogenerated electrons are directly transferred from the CB of $AgVO_3$ to those of Ag_2O and Ag_3VO_4 (reactions 5.5c-i and 5.5c-ii).

The photo-excited electrons on the CBs of Ag_2O and Ag_3VO_4 are transferred to GO sheets (reactions 5.5d and 5.5e) next. This step serves as an alternative to the accumulation of electrons in the conduction bands which results in the photocorrosion of Ag^+ in silver species composites, or to being trapped by adsorbed molecular oxygen (O_2) due to the increased positive CB potentials of Ag_2O and Ag_3VO_4 relative to the standard redox potential of $O_2/O_2\bullet^-$ (-0.33 eV vs. NHE). These electrons which are transferred to GO sheets are trapped by the adsorbed O_2 on the photocatalysts to eventually produce $O_2\bullet^-$. The photo-excited electrons left on the CB of $AgVO_3$ are also captured by adsorbed O_2 to produce $O_2\bullet^-$. Subsequently, hydroxyl radicals (•OH) are eventually generated after a series of reactions with the photo-excited electrons and protons (H^+), in accordance with reactions 5.7a, 5.7b and 5.7c [54]. The generated $O_2\bullet^-$ was confirmed to be the key reactive species, playing a significant role in the degradation of organic dyes (RhB and MO) under VLI. In addition, GO sheets with an excess of electrons could be reduced to RGO under VLI (reaction 5.7d), indicating that GO as the protective substrate could be employed to avoid photocorrison in heterogeneous $Ag_2O/Ag_3VO_4/AgVO_3$ composites [18, 43].

Holes on the VB of Ag_3VO_4 can be trapped by adsorbed H_2O or OH^- ions formed from the hydrolysis of H_2O on the surface of photocatalysts, yielding •OH, H^+ and O_2 in accordance with reactions 5.8a, 5.8b and 5.8c. Holes on the VB of Ag_2O can react with H_2O and OH^- giving rise

to reactions 5.8b and 5.8c, according to the internal electric field that is present. Moreover, the transfer of holes from the VB of Ag_3VO_4 to that of Ag_2O, then to that of $AgVO_3$ is enhanced with the assistance of GO sheets. The photo-excited holes transferred to the VB of $AgVO_3$ are shifted to GO sheets rather than captured by the adsorbed H_2O and OH^- ions on the surface to give •OH, H^+ and O_2, due to the increased negative potential of the VB of $AgVO_3$ with respect to the standard redox potentials of •OH/OH^- (1.55 eV vs. NHE) (reaction 5.8a), O_2/H_2O (1.23 eV vs. NHE) (reaction 5.8b) and O_2/OH^- (0.4 eV vs. NHE) (reaction 5.8c) [55]. Subsequently, holes shifted to GO sheets may eventually react with the reactive species.

During the overall photocatalytic degradation process, photogenerated electrons play a key role in the production of O_2•$^-$ radicals, resulting in the generation of strong •OH radicals. These subsequently give rise to the direct oxidization of RhB and MO (reactions 5.9a and 5.9b) [56] on the surface of GO-$Ag_2O/Ag_3VO_4/AgVO_3$ composites. Therefore, functional GO sheets facilitate the separation of photogenerated e^--h^+ pairs by shifting the charges in order to inhibit the recombination of e^--h^+ pairs. In turn, this allows GO sheets to be completely involved in the complete photocatalytic reaction series describing the degradation of organic pollutants (RhB and MO) under VLI, resulting in an enhanced photocatalytic performance.

5.4 Conclusions

Novel multi-phase $Ag_2O/Ag_3VO_4/AgVO_3$ photocatalysts in the presence of various quantities of GO were synthesized using a facile method at room temperature. Characterization results indicated that observable changes in multi-morphological features occurred in the multi-phase composites, and that photocorrosion of silver species composites was partially inhibited with the addition of GO. The high photocatalytic activity with regards to the decomposition of organic dyes under VLI was attributed to the synergetic effects between the absorbability of functionalized GO and the multi-morphological features of heterogeneous photocatalysts. The amount of GO in the photocatalysts worked in conjunction with the crystallinity of crystal structures and morphologies to increase photocatalytic efficiency. In addition, the optimum quantity of GO was investigated and determined to be 1.2 wt% combined with high-crystallinity heterogeneous $Ag_2O/Ag_3VO_4/AgVO_3$ composites. This gave rise to the most optimal photocatalytic performance with regards to the degradation of organic dyes, demonstrating

99.2% degradation of RhB and 92% degradation of MO after 45 min under VLI. This study may provide a new photocatalytic perspective on the facilitation of the practical applications of photocatalysts in environmental issues.

5.5 Acknowledgments

This work was funded by the Natural Sciences and Engineering Research Council of Canada (NSERC). The authors would like to thank Dr. Alexander Mommers and Dr. Yun Liu at the Center for Catalysis Research and Innovation, and the Department of Earth Sciences at the University of Ottawa, as well as Dr. Jianqun Wang at Carleton University for their help with sample characterization. The authors would also like to thank the China Scholarship Council for their financial support.

5.6 References

[1] A. Kudo, Y. Miseki, Chem. Soc. Rev. 38 (2009) 253-278.

[2] A.J. Nozik, R. Memming, J. Phys. Chem. 100 (1996) 13061-13078.

[3] M.G. Walter, E.L. Warren, J.R. McKone, S.W. Boettcher, Q. Mi, E.A. Santori, N.S. Lewis, Chem. Rev. 110 (2010) 6446-6473.

[4] R. Konta, H. Kato, H. Kobayashi, A. Kudo, Phys. Chem. Chem. Phys. 5 (2003) 3061-3065.

[5] X. Tao, Q. Hong, T. Xu, F. Liao, J. Mater. Sci.-Mater. Electron. 25 (2014) 3480-3485.

[6] X. Lin, J. Xing, W. Wang, Z. Shan, F. Xu, F. Huang, J. Phys. Chem. C 111 (2007) 18288-18293.

[7] P. Dong, Y. Wang, B. Cao, S. Xin, L. Guo, J. Zhang, F. Li, Appl. Catal., B 132-133 (2013) 45-53.

[8] Y. Bi, S. Ouyang, J. Cao, J. Ye, Phys. Chem. Chem. Phys. 13 (2011) 10071-10075.

[9] W. Jiang, X. Wang, Z. Wu, X. Yue, S. Yuan, H. Lu, B. Liang, Ind. Eng. Chem. Res. 54 (2015) 832-841.

[10] G. Dai, J. Yu, G. Liu, J. Phys. Chem. C 116 (2012) 15519-15524.

[11] C. Belver, C. Adán, S. García-Rodríguez, M. Fernández-García, Chem. Eng. J. 224 (2013) 24-31.

[12] D.R. Dreyer, S. Park, C.W. Bielawski, R.S. Ruoff, Chem. Soc. Rev. 39 (2010) 228-240.

[13] V. Singh, D. Joung, L. Zhai, S. Das, S.I. Khondaker, S. Seal, Prog. Mater Sci. 56 (2011) 1178-1271.

[14] Q. Xiang, J. Yu, M. Jaroniec, Chem. Soc. Rev. 41 (2012) 782-796.

[15] Z. Ji, X. Shen, J. Yang, Y. Xu, G. Zhu, K. Chen, Eur. J. Inorg. Chem. (2013) 6119-6125.

[16] Q. Liang, Y. Shi, W. Ma, Z. Li, X. Yang, Phys. Chem. Chem. Phys. 14 (2012) 15657-15665.

[17] Y. Ao, P. Wang, C. Wang, J. Hou, J. Qian, Appl. Surf. Sci. 271 (2013) 265-270.

[18] C. Dong, K.L. Wu, X.W. Wei, X.Z. Li, L. Liu, T.H. Ding, J. Wang, Y. Ye, CrystEngComm 16 (2014) 730-736.

[19] Y. Song, J. Zhu, H. Xu, C. Wang, Y. Xu, H. Ji, K. Wang, Q. Zhang, H. Li, J. Alloys Compd. 592 (2014) 258-265.

[20] M. Zhu, P. Chen, M. Liu, ACS Nano 5 (2011) 4529-4536.

[21] M. Zhu, P. Chen, M. Liu, Langmuir 28 (2012) 3385-3390.

[22] B.F. Machado, P. Serp, Catal. Sci. Technol. 2 (2012) 54-75.

[23] L. Han, P. Wang, S. Dong, Nanoscale 4 (2012) 5814-5825.

[24] H. Zhang, X. Fan, X. Quan, S. Chen, H. Yu, Environ. Sci. Technol. 45 (2011) 5731-5736.

[25] G.-T. Pan, M.-H. Lai, R.-C. Juang, T.-W. Chung, T.C.K. Yang, Ind. Eng. Chem. Res. 50 (2011) 2807-2814.

[26] Q. Yu, Z.R. Tang, Y.J. Xu, J. Energy Chem. 23 (2014) 564-574.

[27] W. Zhou, H. Liu, J. Wang, D. Liu, G. Du, J. Cui, ACS Appl. Mater. Interfaces 2 (2010) 2385-2392.

[28] B. Yao, M. Liu, Z. Ma, C. Wang, Synthesis and characterization of hollow core-shell ZrO_2@void@$BiVO_4$ visible-light photocatalyst, Adv. Mater. Res., 2011, pp. 1331-1338.

[29] J. Zhou, G. Tian, Y. Chen, Y. Shi, C. Tian, K. Pan, H. Fu, Sci. Rep. 4 (2014) 4027.

[30] R.E. Dinnebier, A. Kowalevsky, H. Reichert, M. Jansen, Zeitschrift für Kristallographie-cryst. Mater. 222 (2007) 420-426.

[31] C.-M. Huang, G.-T. Pan, Y.-C.M. Li, M.-H. Li, T.C.K. Yang, Appl. Catal., A 358 (2009) 164-172.

[32] H. Shi, C. Zhou, C. Zhang, Res Chem Intermed (2014) 1-13.

[33] K.S. Raju, M.K. Pour Seydei, S.A. Suthanthiraraj, Mater. Lett. 19 (1994) 65-68.

[34] W.-S. Wang, H. Du, R.-X. Wang, T. Wen, A.-W. Xu, Nanoscale 5 (2013) 3315-3321.

[35] D. Courcot, A. Ponchel, B. Grzybowska, Y. Barbaux, M. Rigole, M. Guelton, J.P. Bonnelle, Catal. Today 33 (1997) 109-118.

[36] Z. Sun, J. Guo, S. Zhu, L. Mao, J. Ma, D. Zhang, Nanoscale 6 (2014) 2186-2193.

[37] D. Krishnan, F. Kim, J. Luo, R. Cruz-Silva, L.J. Cote, H.D. Jang, J. Huang, Nano Today 7 (2012) 137-152.

[38] E.-Y. Choi, T.H. Han, J. Hong, J.E. Kim, S.H. Lee, H.W. Kim, S.O. Kim, J. Mater. Chem. 20 (2010) 1907-1912.

[39] Z. He, C. Sun, S. Yang, Y. Ding, H. He, Z. Wang, J. Hazard. Mater. 162 (2009) 1477-1486.

[40] T. Wu, G. Liu, J. Zhao, H. Hidaka, N. Serpone, J. Phys. Chem. B 102 (1998) 5845-5851.

[41] R. Zha, R. Nadimicherla, X. Guo, J. Mater. Chem. A 3 (2015) 6565-6574.

[42] Z. Wang, L. Yin, Z. Chen, G. Zhou, H. Shi, J. Nanomater. 2014 (2014) 6.

[43] M. Cao, P. Wang, Y. Ao, C. Wang, J. Hou, J. Qian, Int. J. Hydrogen Energy 40 (2015) 1016-1025.

[44] M.S.A.S. Shah, M. Nag, T. Kalagara, S. Singh, S.V. Manorama, Chem. Mater. 20 (2008) 2455-2460.

[45] G. Li, K.H. Wong, X. Zhang, C. Hu, J.C. Yu, R.C.Y. Chan, P.K. Wong, Chemosphere 76 (2009) 1185-1191.

[46] J. Wang, X. Yang, J. Chen, J. Xian, S. Meng, Y. Zheng, Y. Shao, D. Li, J. Am. Ceram. Soc. 97 (2014) 267-274.

[47] J. Zhao, C. Chen, W. Ma, Top. Catal. 35 (2005) 269-278.

[48] J. Wang, P. Wang, Y. Cao, J. Chen, W. Li, Y. Shao, Y. Zheng, D. Li, Appl. Catal., B 136-137 (2013) 94-102.

[49] M. Stylidi, D.I. Kondarides, X.E. Verykios, Appl. Catal., B 47 (2004) 189-201.

[50] P. Raja, A. Bozzi, H. Mansilla, J. Kiwi, J. Photochem. Photobiol., A 169 (2005) 271-278.

[51] H. Lin, H. Ye, S. Chen, Y. Chen, RSC Adv. 4 (2014) 10968-10974.

[52] W. Li, D. Li, W. Zhang, Y. Hu, Y. He, X. Fu, J. Phys. Chem. C 114 (2010) 2154-2159.

[53] G. Trimarchi, H. Peng, J. Im, A.J. Freeman, V. Cloet, A. Raw, K.R. Poeppelmeier, K. Biswas, S. Lany, A. Zunger, Phys. Rev. B: Condens. Matter 84 (2011).

[54] S. Horikoshi, H. Hidaka, N. Serpone, Environ. Sci. Technol. 36 (2002) 1357-1366.

[55] A.J. Bard, R. Parsons, J. Jordan, Marcel Dekker: New York (1985).

[56] Q. Zhu, W.S. Wang, L. Lin, G.Q. Gao, H.L. Guo, H. Du, A.W. Xu, J. Phys. Chem. C 117 (2013) 5894-5900.

SECTION III: CONCLUSIONS

Chapter 6

Discussion and conclusions

6.1 Introduction

The development of the utilization of solar energy applied to photocatalysis reactions for the degradation of organic pollutants requires an improvement of practical techniques of these processes, and an enhancement of functional materials in real-world photocatalytic applications. The necessity for functional materials requires desirable characteristics such as a highly efficient solar utilization, a high crystallinity in crystal structures, a high efficiency of charge separation, a large surface area, an accessible activity for degradation of organic pollutants, and the stability and reusability of materials. This necessity emerged as an issue in practical photocatalytic techniques, and has been energized by Fujishima's famous study on photoelectrochemical water splitting [1]. The photocatalysis application has drawn plenty of attention using these solar-light-induced functional materials to practices such as the detoxification of effluents, the destruction of microorganisms including bacteria, the inactivation of cancer cells, superhydrophilic self-cleaning, the production of hydrogen fuel including photo-splitting of water to produce hydrogen gas, the elimination of inorganic/organic gaseous pollutants or odour control, the fixation of nitrogen, and the synthesis of organic fuels [2]. As such, multi-functional materials in photocatalytic applications exhibit the potentials for use in waste water treatment and environmental remediation.

6.2 Discussion

In this thesis, a series of novel photocatalyst materials were designed and synthesized by applying diverse strategies. In addition, the experimental investigation of material characterization, photocatalytic performances with respect to the degradation of model organic pollutants, the stability and reusability of materials used in photocatalysis and the relevant mechanisms of individual photosystems were implemented. The comparison of photocatalytic performances among various photocatalysts is presented in this section.

The as-prepared photocatalysts in the project were categorized into two main classes, namely bismuth-based and silver-based multi-phase heterogeneous photocatalysts. In the bismuth-based ternary metal-oxide photocatalysts, monoclinic $BiVO_4$ as the host material was modified through different synthesis processes and prepared via a novel route using potassium metavanadate (KVO_3) followed by hydrothermal treatment. The photocatalytic performance for the degradation of model organic pollutants was improved in the presence of $BiVO_4$ particles under VLI, which can be attributed to a lower band gap energy, a high crystallinity of the crystal structure and the multi-morphological features of as-prepared particles, resulting in the enhancement of visible-light absorption characteristics, less defects in crystals and an increase in the surface areas of composites. This suggests that a highly efficient visible-light-driven photocatalytic activity was facilitated and accomplished through improving the crystallinity of crystal structures and by increasing the specific surface areas of the composites based on their single phase crystal structures.

Single-phase photocatalysts may increase the recombination rate of photogenerated charge carriers due to defects of grain boundaries serving as the recombination centres to impede the separation of charge species [3-5]. Silver-based ternary metal-oxide photocatalysts have attracted considerable attention due to the high removal rate of pollutants and the synergistic effect among different silver species in the photosystem. A multi-phase silver species ($Ag_2O/Ag_3VO_4/Ag_4V_2O_7$) photocatalyst was synthesized by adjusting the molar ratio of silver to vanadium (Ag to V) via the hydrothermal method. The stability of as-prepared silver species composites in regards to changes in the crystal structure during photocatalytic reactions was further investigated. Modification of silver-based heterogeneous photocatalysts increased the

photocatalytic activity attributed to the matched band potentials among each phase, as well as high transfer efficiencies of charges at the interface [6]. This implies that the inhibition of defects in single phase, as well as the separation and the transfer of photoexcited electrons and holes during visible-light-induced photocatalytic activity were achieved using multi-phase heterogeneous silver-based photocatalysts.

Photocorrosion of silver-based ternary metal-oxide composites has been raised as an issue recently. The instability of silver species photocatalysts manifested in the form of photocorrosion of the composites during photocatalytic performances under VLI. This could be ascribed to the interstitial silver ions (Ag^{+}) combining with electrons in the absence of sacrificial reagents under VLI [7], resulting in the decrease of visible-light-driven photodegradation of organic pollutants. Efforts have been made to improve the stability of silver species applied to the degradation of organic pollutants. GO as a highly oxidative form of graphene consisting of a variety of oxygen functionalities could serve as the protective substrate that partially inhibits the photocorrosion of silver species. Multi-phase silver species composites assisted with graphene oxide (GO-Ag_2O/Ag_3VO_4/$AgVO_3$) were synthesized at room temperature, and exhibited high visible-light-driven photocatalytic activities with regards to the degradation of model organic pollutants, and demonstrated the anti-photocorrison capabilities of GO sheets to protect silver species.

6.3 Conclusions

Bismuth-based and silver-based oxide visible-light-driven photocatalysts, and the modified relevant silver species composites presented in Chapters 3-5 were synthesized, characterized, and experimentally investigated and mechanistic considerations were proposed. Results based on the objectives of the project are listed as follows:

- **Development and experimental investigation of novel single phase crystal structure based on bismuth ternary metal-oxide photocatalyst-$BiVO_4$.** The visible-light-driven monoclinic $BiVO_4$ photocatalyst was synthesized and characterized, and the photocatalytic degradation of Rhodamine B (RhB) under VLI was investigated. The experimental investigation of crystal structure details and the relevant mechanism of photocatatlysis were proposed. The results indicate that $BiVO_4$ particles showed excellent

visible-light-induced photocatalytic activity due to the improvement of crystallinity in the crystal structures and the increase of specific surface areas.

- **Development and experimental investigation of novel multi-phase silver species ($Ag_2O/Ag_3VO_4/Ag_4V_2O_7$) photocatalyst.** The photocatalyst prepared by adjusting the molar ratio of silver to vanadium (Ag to V) via the hydrothermal method was explored. The as-synthesized multi-phase $Ag_2O/Ag_3VO_4/Ag_4V_2O_7$ composites giving rise to a dominant, higher photocatalytic degradation of RhB under VLI were investigated. The stability of as-prepared silver species composites regarding changes to crystal structure during photocatalytic reactions was studied, and the mechanism in this photosystem was also discussed.

- **Development and experimental investigation of novel multi-phase silver ($Ag_2O/Ag_3VO_4/AgVO_3$) photocatalysts incorporated with graphene oxide sheets.** The composites were synthesized, characterized and investigated, and the removal of organic pollutants (RhB and MO) over GO-$Ag_2O/Ag_3VO_4/AgVO_3$ under VLI was studied. The effect of graphene oxide addition on visible-light-driven photoactivity and on the photocorrosion of silver species composites with respect to the degradation of organic compounds was studied, and an acceptable mechanism for this photosystem was proposed.

6.4 Publications

This thesis was shared with academic peers and has yielded three publications in peer-reviewed journals, which are included in Chapters 3-5 of this work.

6.5 Suggestions for future work

Some specific advice based on the current research discussed in this thesis is proposed for future work:

- The photocatalytic performance of as-prepared monoclinic $BiVO_4$ in regards to the degradation of organic pollutants could be enhanced to better improve the adsorption-

desorption equilibrium in dark and photocatalytic processes under light, which could take full advantage of the functional materials of photoactivity. The acceptable approaches with respect to high photocatalytic activity could be achieved using templates or specific methods, such as ultrasonic spray pyrolysis reported by Scott S. Dunkle et al. [8] which could better control the structures and morphologies of materials, resulting in high photocatalytic activities.

- More cycling experiments demonstrating the stability of the as-prepared photocatalysts may be needed as supportive evidence for reusability, such as adding more cycling tests with prolonged irradiation. In addition, cycling tests with washed samples may facilitate the reusability of photocatalysts due to a number of unblocked active sites released in the photocatalyst, which may keep the adsorption-desorption equilibrium in dark and photosystem. Therefore, cycling experiments need to be done in the future as the supportive evidence for the stability of photocatalysts.

- The detailed selection study for optimum conditions using KVO_3 should be further investigated to gather supporting evidence for the enhancement of photocatalytic activity. Conditions of interest include factors such as temperature and time in hydrothermal processes, which could be used to optimize photocatalytic behaviours and to increase the efficiency of photocatalytic activity.

- Morphology and particle size of silver species composites ($Ag_2O/Ag_3VO_4/Ag_4V_2O_7$) should be modified and fine-tuned to study multi-morphological features and smaller sizes in order to achieve a highly efficient adsorption-desorption equilibrium in dark and light processes. For example, nanostar and nanoflower morphologies of α-Ag_3VO_4 were achieved and reported by Li et al. [9] using n-butylamine (n-BA) as a precipitant and complexing agent, resulting in a better photocatalytic performance in regards to the degradation of RhB.

- Equal distribution of multi-phase silver species composites ($Ag_2O/Ag_3VO_4/AgVO_3$) onto GO sheets should be further optimized to obtain smaller particle sizes of each discussed

phase. This is necessary to increase the surface area of materials and to equalize the adsorption rates of organic molecules onto photocatlysts, resulting in the maximum degradation of RhB during photocatalytic reactions.

6.6 References

[1] A. Fujishima, K. Honda, Electrochemical photolysis of water at a semiconductor electrode, Nature, 238 (1972) 37-38.

[2] H. Changseok, A. Joel, C.P. Suresh, F. Rachel, F. Polycarpos, J.A. Byrne, S.M.D. Patrick, C. Hyeok, J. Wenjun, O.S. Kevin, D.D. Dionysios, Chapter green nanotechnology: Development of nanomaterials for environmental and energy applications, in, J. Am. Chem. Soc., 2013, pp. 201-229.

[3] A. Kudo, Y. Miseki, Heterogeneous photocatalyst materials for water splitting, Chem. Soc. Rev., 38 (2009) 253-278.

[4] R. Konta, H. Kato, H. Kobayashi, A. Kudo, Photophysical properties and photocatalytic activities under visible light irradiation of silver vanadates, Phys. Chem. Chem. Phys., 5 (2003) 3061-3065.

[5] X. Tao, Q. Hong, T. Xu, F. Liao, Highly efficient photocatalytic performance of graphene-Ag_3VO_4 composites, J. Mater. Sci.-Mater. Electron., 25 (2014) 3480-3485.

[6] X. Lin, J. Xing, W. Wang, Z. Shan, F. Xu, F. Huang, Photocatalytic activities of heterojunction semiconductors $Bi_2O_3/BaTiO_3$: A strategy for the design of efficient combined photocatalysts, J. Phys. Chem. C, 111 (2007) 18288-18293.

[7] P. Dong, Y. Wang, B. Cao, S. Xin, L. Guo, J. Zhang, F. Li, Ag_3PO_4/reduced graphite oxide sheets nanocomposites with highly enhanced visible light photocatalytic activity and stability, Appl. Catal., B, 132-133 (2013) 45-53.

[8] S.S. Dunkle, R.J. Helmich, K.S. Suslick, $BiVO_4$ as a visible-light photocatalyst prepared by ultrasonic spray pyrolysis, J. Phys. Chem. C, 113 (2009) 11980-11983.

[9] D. Li, X. Duan, Q. Qin, H. Fan, W. Zheng, Facile synthesis of novel α-Ag_3VO_4 nanostructures with enhanced photocatalytic activity, CrystEngComm, 15 (2013) 8933-8936.

SECTION IV: APPENDICES

Appendix A

Hypothesis flow chart

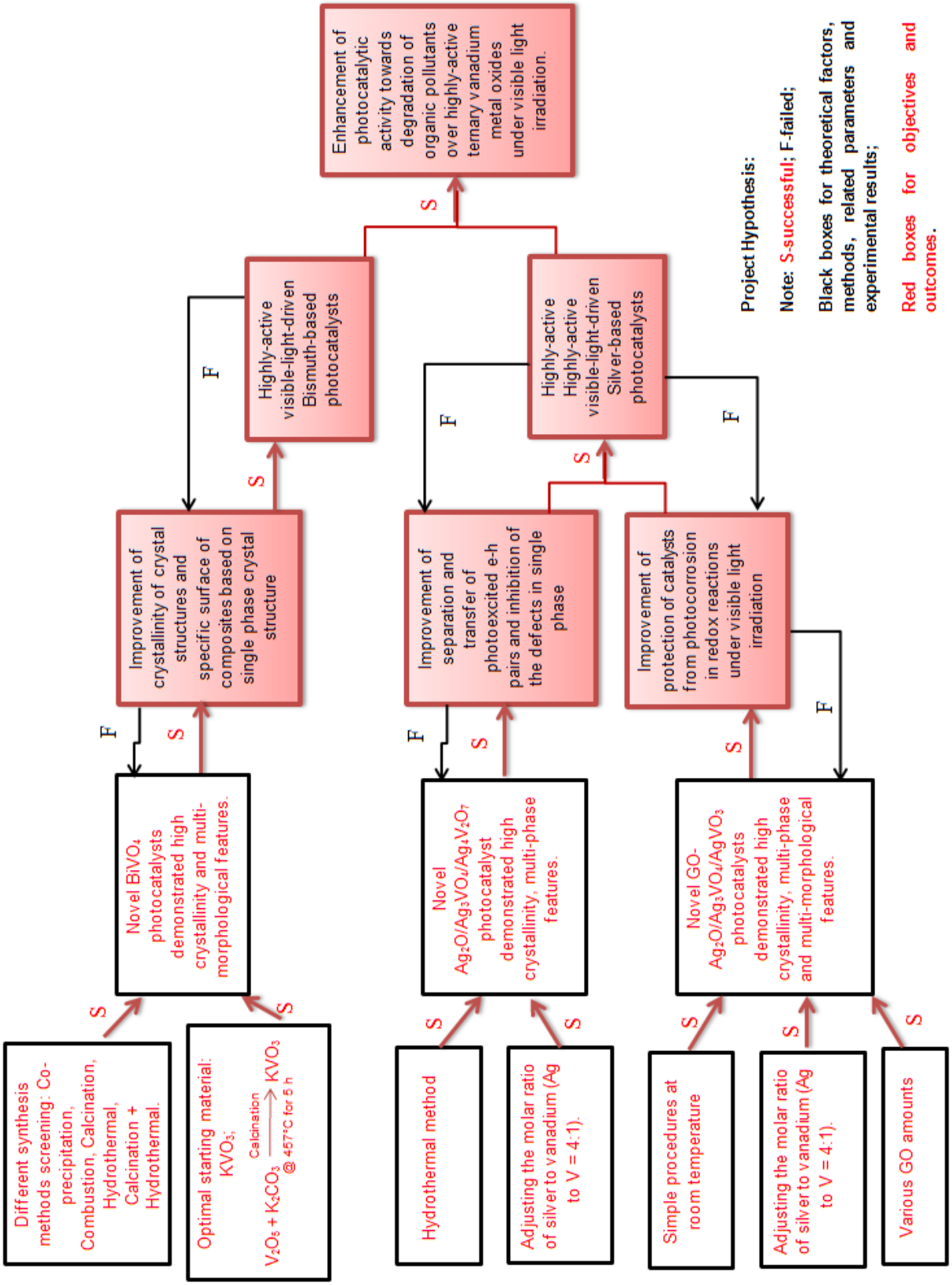
Enhancement of photocatalytic activity towards degradation of organic pollutants over highly-active ternary vanadium metal oxides under visible light irradiation.
Highly-active visible-light-driven Bismuth-based photocatalysts
Highly-active Highly-active visible-light-driven Silver-based photocatalysts
Improvement of crystallinity of crystal structures and specific surface of composites based on single phase crystal structure
Improvement of separation and transfer of photoexcited e-h pairs and inhibition of the defects in single phase
Improvement of protection of catalysts from photocorrosion in redox reactions under visible light irradiation
Novel $BiVO_4$ photocatalysts demonstrated high crystallinity and multi-morphological features.
Novel $Ag_2O/Ag_3VO_4/Ag_4V_2O_7$ photocatalyst demonstrated high crystallinity, multi-phase features.
Novel GO-$Ag_2O/Ag_3VO_4/AgVO_3$ photocatalysts demonstrated high crystallinity, multi-phase and multi-morphological features.
Different synthesis methods screening: Co-precipitation, Combustion, Calcination, Hydrothermal, Calcination + Hydrothermal.
Optimal starting material: KVO_3; $V_2O_5 + K_2CO_3 \xrightarrow{\text{Calcination}} KVO_3$ @ 457°C for 5 h
Hydrothermal method
Adjusting the molar ratio of silver to vanadium (Ag to V = 4:1).
Simple procedures at room temperature
Adjusting the molar ratio of silver to vanadium (Ag to V = 4:1).
Various GO amounts
S
F
Project Hypothesis:
Note: S-successful; F-failed;
Black boxes for theoretical factors, methods, related parameters and experimental results;
Red boxes for objectives and outcomes.

Appendix B

Terminologies used in photocatalysis

B.1 Solar radiation spectrum

Sunlight is a portion of the electromagnetic radiation given off by the sun, and is composed of particularly ultraviolet, visible, and infrared light. The solar radiation spectrum is shown in Figure. B.1.

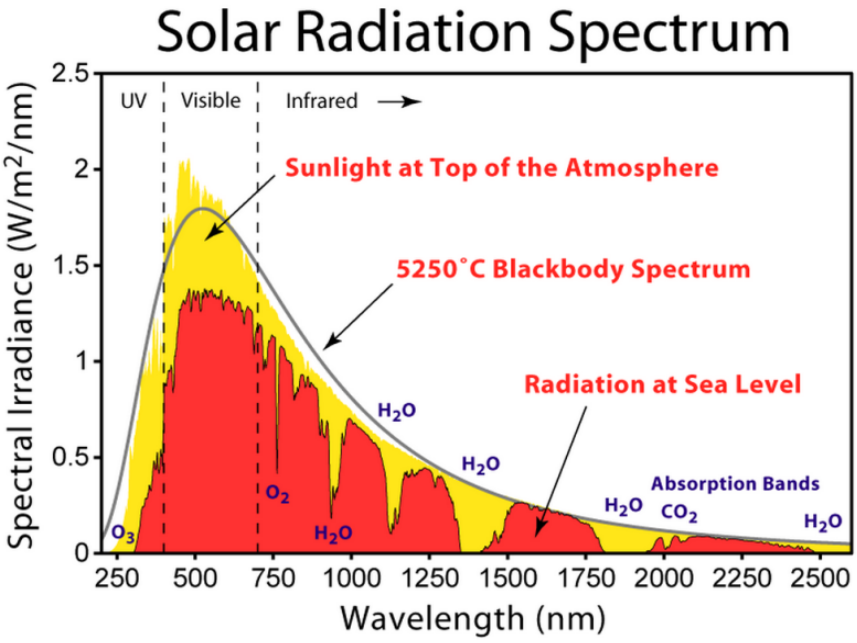

Figure B.1 Solar radiation spectrum [1]

As shown in Figure. B.1, ultraviolet (UV) light possesses wavelengths shorter than those of visible light, and is in the range between 100 nm and 400 nm which accounts for 3% of the energy from sunlight at the ground level. Visible light wavelengths range from 380 nm to

approximately 700 nm and accounts for 44% of the energy from sunlight. Infrared (IR) light possesses longer wavelengths, extending from the nominal red edge of the visible spectrum at 700 nm to 1 mm and accounts for 53% of that energy from sunlight. In the three projects, monoclinic $BiVO_4$ (m-$BiVO_4$) is the host material in Chapter 3 with highly-active visible-light-induced properties, indicating that $BiVO_4$ is photosensitive under visible light irradiation, due to its band gap energy of approximately 2.4 eV. This band gap corresponds to the absorption of light with wavelengths of approximately 518 nm. The heterogeneous multi-phase $Ag_2O/Ag_3VO_4/Ag_4V_2O_7$ is a photocatalyst is visible-light-induced photocatalyst in Chapter 4 with a maximum wavelength of absorption at approximately 625 nm. In addition, graphene oxide-assisted, heterogeneous multi-phase and multi-morphological $Ag_2O/Ag_3VO_4/AgVO_3$ photocatalysts (GO-$Ag_2O/Ag_3VO_4/AgVO_3$) in Chapter 5 are visible-light-driven photocatalysts with a maximum wavelength of absorption at approximately570 nm (1.2 wt% GO-$Ag_2O/Ag_3VO_4/AgVO_3$).

B.2 Mole of photons

One mole (6.022×10^{23}) of photons is identified as a unit. Specifically, Einstein is the unit for a mole of photons. In extension of this, Einsteins per square metre is a measure of irradiance.

B.3 Radiation intensity

Radiation intensity is the amount of energy passing through a given area perpendicular to the direction of light propagation in a given unit of time. In these three projects, a 300-W ELH tungsten halide bulb (Ushio) was used as a light source with a 410 nm cut-off filter (Kenko Zeta; $\lambda>$ 410 nm, transmittance >90%) to provide visible light irradiation. The projector lamp is shown in Figure B.2.

Figure B.2: 300-W ELH tungsten halide bulb (Ushio)

The relative parameters of the Ushio ELH 300-W lamp are shown in the following: Tungsten Halogen Lamps: Watts: 300; Volts: 120; Dimensions: Diameter (mm) 50.67; Reflector Type: Stippled; Working Distance (mm): 154.3; Average Life (h): 35; Color Temp (Kev): 3350.

B.4 The irradiation intensity of 300-W ELH tungsten halide bulb (Ushio)

The irradiation of the 300-W tungsten halide light source was measured using a quantum meter (Biospherical QSL-2100; 400 nm < λ < 700 nm), and was found to be approximately 10^{-3} Einstein·m^{-2}·s^{-1} at a distance of 15 cm from top of the slurry (under the filter). The distribution of intensity of light irradiation over 22 h is shown in Figure B.3.

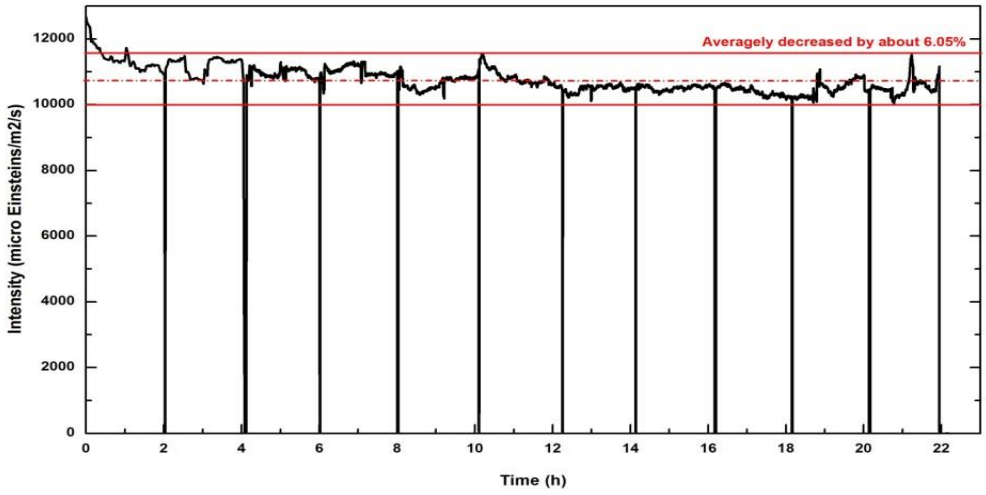

Figure B.3: The distribution of intensity of light irradiation for 22 h.

The flux of photons (intensity, J) was obtained by using a quantum meter working under a 300-W ELH tungsten halide bulb (Ushio) with irradiation lasting an average 22 h until the bulb ceased to function properly. A balance could be obtained after first 2 h, and it decreased by 6% on average, which is acceptable during the photocatalytic process. Therefore, the irradiation was kept as a constant from the second hour of irradiation until the end of the bulb's lifetime, which was up to 22 h with continuous irradiation under experimental test.

B.5 The spectral distribution of 300-W ELH tungsten halide bulb (Ushio)

The colour temperature of the 300-W ELH tungsten halide bulb (Ushio) is 3350 Kev according to the parameters mentioned above, which belong to the studio lamp. The spectral distribution of luminous flux for the studio lamp is shown in Figure B.4.

Figure B.4: Spectral distribution of luminous flux (lumens) for typical studio lamp [2].

According to the spectral distribution of luminous flux shown in Figure B.4, the spectral distribution of the Ushio ELH 300-W lamp is between 400 nm to 700 nm, and the maximum relative luminous flux is observed around 570 nm, which is between yellow and green visible light wavelengths.

B.6 The selection of the distance in photoreactor

The distance of 15 cm from the top of the slurry (under the filter) was selected in the photoreaction system. This was an optimal parameter obtained after multi-time tests by co-workers in the catalysis lab (D510). According to research from 'Photocatalytic Radiation Engineering' from Dr. M. Salaices' Ph.D. Dissertation at the University of Western Ontario, 2002, this distance could be arbitrary within the bounds of 8–30 cm. In thesis bounds, the tendency of the radiative flux was found to be comparatively smooth. The typical asymmetrical radiative flux axial distribution of a lamp is shown in Figure B.5.

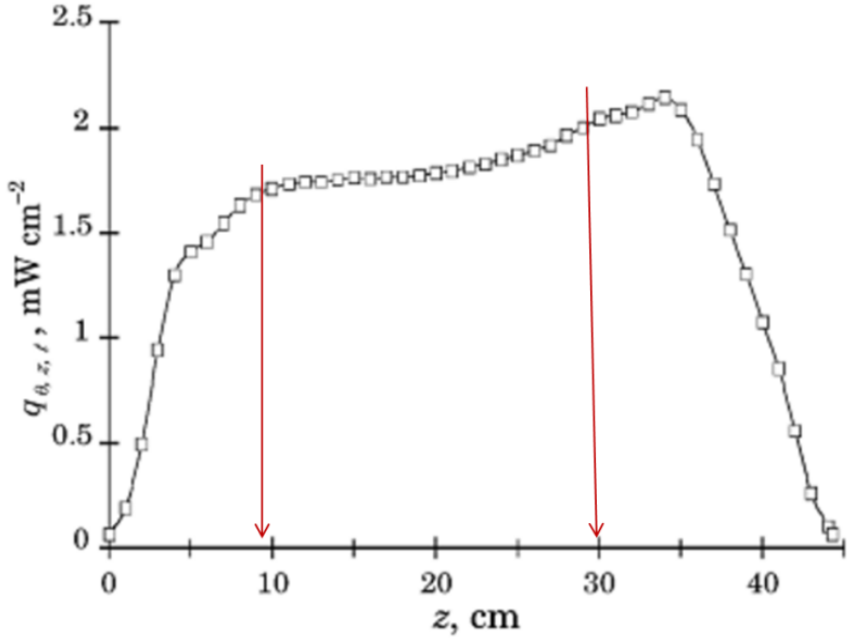

Figure B.5: The typical asymmetrical radiative flux axial distribution of a lamp.

B.7 Apparent photonic efficiency

ξ is calculated as the ratio of the number of molecules of reactant consumed per unit time to the number of photons incident in the reactor. The apparent photonic efficiency is different from the quantum yield (Φ), which is the ratio of the number of reacted molecules consumed per unit time to the number of photons absorbed by the photocatalyst (e.g. $BiVO_4$) per unit time. The value of Φ is higher than ξ, and the difference in their magnitude is a function of light scattering in the photocatalytic reactor [3]. In this thesis, apparent photonic efficiency is a useful approach which

can be applied to measuring photocatalytic activities. The application for calculation of apparent photonic efficiency was proposed in Chapter 3 and is shown in Appendix C.

B.8 Band gap

In solid-state physics, a band gap is an energy range in a solid where no electron states can exist. It generally refers to energy difference (in electron volts) between the top of the valence band and the bottom of the conduction band in insulators and semiconductors (e.g. $BiVO_4$ with a band gap of 2.4 eV; $Ag_2O/Ag_3VO_4/Ag_4V_2O_7$ with a band gap of 1.98 eV; 1.2 wt% GO-$Ag_2O/Ag_3VO_4/AgVO_3$ with a band gap of 2.18 eV). This is equivalent to the energy required to free an outer shell electron from its orbit about the nucleus to becoming a mobile charge carrier, able to move freely within the solid material. Therefore, the band gap is a major factor determining the electrical conductivity of a solid. Metals are not of widespread interest as photocatalysts because they can easily become oxidized or photocorroded in photocatalytic systems due to the abundance of radical species in their systems.

B.9 Valence band and conduction band

In solids, the valence band is the highest range of electron energies in which electrons are normally present at a temperature of absolute zero. The conduction band is the range of electron energies enough to free an electron from binding with the electron's atom to move freely within the atomic lattice of the material, which is identified as a 'delocalized electron'. For instance, the valence and conduction bands of $BiVO_4$ refer to VB at Bi 6s–O 2p, with an energy band edge at 2.73 eV, and the CB at V 3d, given by an energy band edge at -0.33eV, and therefore the estimated band gap is 2.40 eV [4]. For Ag_3VO_4, its VB at Ag 4d–O 2p possesses an energy band edge around 2.20 eV, and the conduction band refers to V 3d, with an energy band edge of -0.10 eV, with an estimated band gap of 2.10 eV [5].

B.10 Heterojunction

Heterojunction refers to the interface that occurs between two layers or regions of dissimilar crystalline semiconductors, such as the p-n heterojunction of $Co_3O_4/BiVO_4$ photocatalysts. In this composite, the heterojunction is formed at the interfaces of Co_3O_4 and $BiVO_4$. Herein, Co_3O_4 has

been reported as a p-type semiconductor, which is deficient of electrons in the crystal lattice, whereas holes act as the major charge carriers [4]. On the contrary, $BiVO_4$ is a n-type semiconductor having an excess of electrons in the crystal lattice, which act as charge carriers [6].

B.11 Graphene oxide (GO)

Graphene oxide is an amorphous material and its expected peak is 10.5°~10.7° [7]. A comparison of diffraction peaks for graphite, graphene oxide, graphene and functionalised graphene is shown in Figure B.6. And the diffraction peak of GO was barely visible in the XRD patterns of as-prepared samples when hybridized with inorganic components, due to the low diffraction intensity of GO [8].

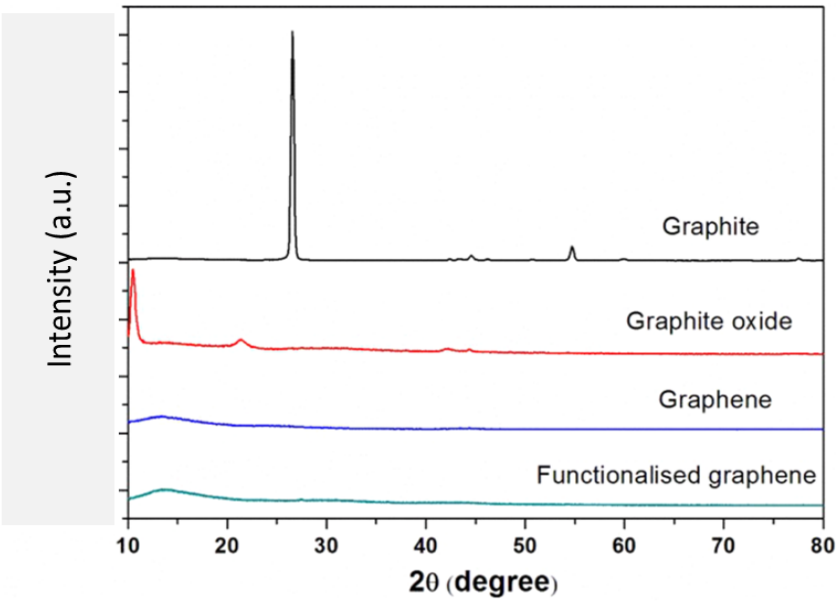

Figure B.6:The diffraction peaks for different carbon species.

GO is a highly oxidative form of graphene consisting of a variety of oxygen functionalities [9] shown in Figure B.7.

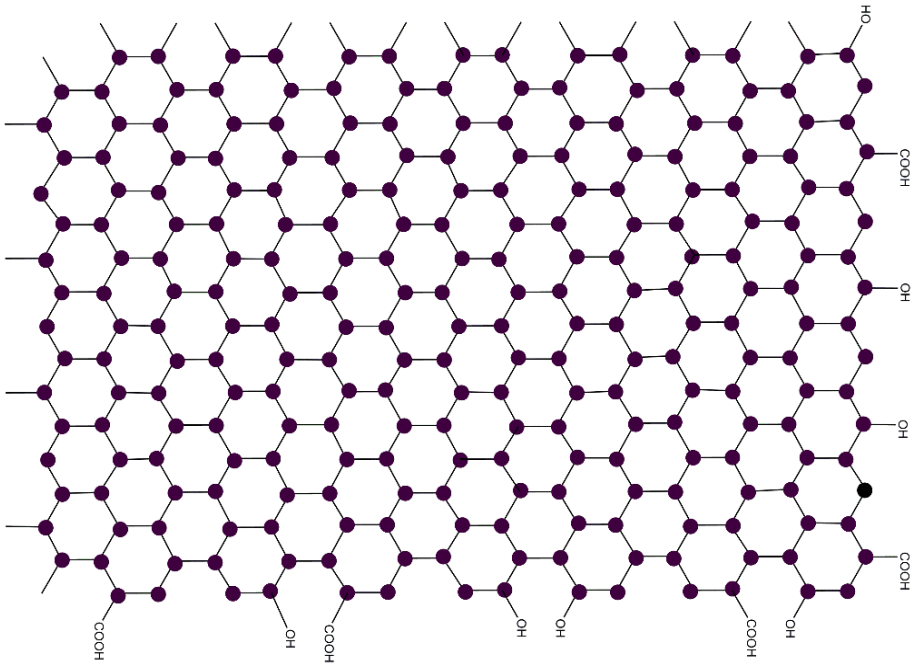

Figure B.7: GO sheet with oxygen functional groups.

As seen from Figure B.7, the carbon plane in GO is decorated with hydroxyl and epoxy (1,2-ether) functional groups, carboxylic acids as well as organic carbonyl defects [10, 11]. These functional groups of GO disrupt the sp2 bonding network, resulting in the electrical insulating characteristics of GO [12]. However, the conductivity can be partially recovered by restoring the π-network via chemical, thermal, or electrochemical reduction of GO to obtain reduced graphene oxide (RGO) [11].

B.12 Host materials

In this thesis, promising ternary photosensitive semiconductors were selected as the host materials, in which Bismuth-based semiconductor $BiVO_4$ was selected as the host material in Chapter 3. Meanwhile silver-based semiconductor $Ag_2O/Ag_3VO_4/Ag_4V_2O_7$ and multi-phase & multi-morphology GO-$Ag_2O/Ag_3VO_4/AgVO_3$ particles were selected as the host materials in Chapter 4 and Chapter 5, respectively.

Some different phases of silver-based host materials were observed in Chapter 4 and Chapter 5 due to the changes of synthesis methods. Because the GO structure is destroyed under the hydrothermal method, it may react with silver species particles, resulting in the loss of highly-

active characteristics such as large specific surface areas, strong absorption capabilities, and the abundance of reactive sites for surface modification reactions. Therefore, the synthesis method was changed to a simple mixing procedure at room temperature in order to maintain the integrities of the structures of GO and highly-active visible-light-driven silver species particles. The alternative synthesis caused the crystal structure phases to change slightly, which may be attributed to the different synthesis conditions, such as various different temperatures and pressures during the synthesis process, influencing the formation of phases in crystal structures of composites. However, the changed phases didn't harm the photocatalytic performance; it promoted the improvements of the activity with less energy inputs.

B.13 References

[1] ASTM Standard C33, Specification for concrete aggregates, (2003).

[2] Spectrum – The GE lighting lamp catalogue, GE, 2002.

[3] L.-H.X. Byung-Chul Choi, Hyung-Taek Kim†, and Detlef W. Bahnemann, Photocatalytic characteristics on sintered glass and micro reactor, J. Ind. Eng. Chem., 12 (2006) 663-672.

[4] M. Long, W. Cai, J. Cai, B. Zhou, X. Chai, Y. Wu, Efficient photocatalytic degradation of phenol over $Co_3O_4/BiVO_4$ composite under visible light irradiation, J. Phys. Chem. B, 110 (2006) 20211-20216.

[5] G. Trimarchi, H. Peng, J. Im, A.J. Freeman, V. Cloet, A. Raw, K.R. Poeppelmeier, K. Biswas, S. Lany, A. Zunger, Using design principles to systematically plan the synthesis of hole-conducting transparent oxides: Cu_3VO_4 and Ag_3VO_4 as a case study, Phys. Rev. B: Condens. Matter, 84 (2011).

[6] I.C. Vinke, J. Diepgrond, B.A. Boukamp, K.J. Vries de, A.J. Burggraaf, Bulk and electrochemical properties of $BiVO_4$, Solid State Ionics, 57 (1992) 83-89.

[7] M. Naebe, J. Wang, A. Amini, H. Khayyam, N. Hameed, L.H. Li, Y. Chen, B. Fox, Mechanical property and structure of covalent functionalised graphene/epoxy nanocomposites, Sci. Rep., 4 (2014).

[8] Z. Ji, X. Shen, J. Yang, Y. Xu, G. Zhu, K. Chen, Graphene oxide modified Ag_2O nanocomposites with enhanced photocatalytic activity under visible-light irradiation, Eur. J. Inorg. Chem., (2013) 6119-6125.

[9] S. Chowdhury, R. Balasubramanian, Recent advances in the use of graphene-family nanoadsorbents for removal of toxic pollutants from wastewater, Adv. Colloid Interface Sci., 204 (2014) 35-56.

[10] A. Lerf, H. He, M. Forster, J. Klinowski, Structure of graphite oxide revisited, J. Phys. Chem. B, 102 (1998) 4477-4482.

[11] D.R. Dreyer, S. Park, C.W. Bielawski, R.S. Ruoff, The chemistry of graphene oxide, Chem. Soc. Rev., 39 (2010) 228-240.

[12] D. Krishnan, F. Kim, J. Luo, R. Cruz-Silva, L.J. Cote, H.D. Jang, J. Huang, Energetic graphene oxide: Challenges and opportunities, Nano Today, 7 (2012) 137-152.

Appendix C

Sample calculations

The related sample calculations mentioned in the thesis and Appendix B are given in this section, which are involved in experimental results from previous studies discussed in the three research articles present in Chapter 3, Chapter 4 and Chapter 5 respectively.

C.1 Photo energy calculation

The energy of a photon is equal to the light frequency, v (s^{-1}) multiplied by Planck's constant, h (J·s); while the speed of light in a vacuum, c (m/s) is equal to the light wavelength λ (nm) multiplied by the light frequency, v (s^{-1}). Therefore, the photoenergy calculations are as follows:

$$E_{photon} = h\,v = h\,c/\lambda \quad \text{(C.1)}$$

Where $h = 6.63 \times 10^{-34}$ (J·s); $c = 3.00 \times 10^{8}$ m/s; λ is the specific light wavelength (nm).

In the proposed projects, we apply the photoenergy calculation to estimate the band gap energy for the specific photocatalysts, where the band gap energy has units of electron volts (eV).

Herein, $J = 6.24150974 \times 10^{18}$ (eV).

Taking $BiVO_4$ and Ag_3VO_4 as examples, the maximum absorption wavelength of $BiVO_4$ is 518 nm, and 600 nm is the minimum absorption wavelength for Ag_3VO_4.

E_{bg} ($BiVO_4$) =

6.63×10^{-34}(J·s) $\times 3.00 \times 10^{8}$ (m/s) $\times$ $6.24150974 \times 10^{18}$ (eV/J)/(518×10^{-9}) (m) ≈ 2.40 (eV);

E_{bg} (Ag_3VO_4) =

6.63×10^{-34}(J·s) $\times 3.00 \times 10^{8}$ (m/s) $\times$ $6.24150974 \times 10^{18}$ (eV/J)/(600×10^{-9}) (m) ≈ 2.10 (eV).

C.2 Langmuir-Hinshelwood (L-H) kinetics

To investigate the kinetics of model pollutants' degradation, Langmuir-Hinshelwood (L-H) kinetics can be used to quantitatively approximate the reaction. When the initial concentration is sufficiently small, L-H expression reduces to pseudo-first order kinetics; the kinetic constants are calculated according to Equation (3.6) in Chapter 3. Taking data in Chapter 3 as an example, this data is from screening studies performed to investigate the optimized synthesis of $BiVO_4$, and photocatalytic degradation of rhodamine B in the presence of $BiVO_4$ particles. Herein, the initial 20 minutes of RhB degradation are taken into account (t = 20 min), due to the initial reaction within 20 min considered to be linear with changing concentration of model pollutants. The comparison of rate constants obtained is given in Table C.1.

Table C.1: Pseudo-first order rate constants *k'* using Langmuir–Hinshelwood kinetics with respect to $BiVO_4$ samples

Sample (various methods)	Degradation rate constants $k'(min^{-1})$
$BiVO_4$ (Co-pre-350-24)	0.00102
$BiVO_4$ (Comb-500-3)	-0.00149
$BiVO_4$ (Calc-450-5)	0.00219
$BiVO_4$ (H-140-8)	0.00260
$BiVO_4$ (C+H-200-24)	0.0142

As seen from Table C.1, according to the data given by pseudo-first order rate constants *k'*, samples fabricated from five different synthesis methods (i.e. co-Precipitation, combustion, calcination, hydrothermal and calcination+ Hydrothermal methods, denoted by $BiVO_4$ (Co-pre-350-24), $BiVO_4$ (Comb-500-3), $BiVO_4$ (Calc-450-5), $BiVO_4$ (H-140-8) and $BiVO_4$ (C+H-200-24), respectively) are seen to display photocatalytic activity to some extent for the degradation of RhB. Of these prepared samples, $BiVO_4$ (C+H-200-24), referring to starting materials obtained via calcination method at 457°C (730K) for 5 h, and the precursor of m-$BiVO_4$ treated in a hydrothermal process at 200°C for 24 h, showed the highest degradation rate of $k' = 0.0142$ (min^{-1}).

C.3 Apparent photonic efficiency

Apparent photonic efficiency is a useful approach which can be applied to measuring photocatalytic activities. The results from Chapter 3, the initial reaction within 20 min is considered to be linear with changing concentration of RhB. Accounting for this, photonic efficiency at 20 min is taken as the reference for comparsion of photocatalytic activities among $BiVO_4$ samples. The formula for apparent photonic efficiency is given according to the following [64]:

$$\xi = \frac{V \Delta C}{J A \Delta t} \qquad \text{(C.2)}$$

Where ξ is the apparent photonic efficiency (mol/Einstein), V is the solution volume (m^3), ΔC is the change in the concentration (mol/m^3), J is the flux of photons ($Einstein/m^2 \cdot s$), A is the illuminated area (m^2) and Δt is the change in time (min). The calculated values of apparent photonic efficiencies for $BiVO_4$ particles, using five different synthesis conditions (i.e. co-precipitation, combustion, calcination, hydrothermal and calcination + hydrothermal reactions) are shown in Table C.2. The photonic efficiency results agreed well with the first order kinetic constants obtained by Langmuir–Hinshelwood analysis shown in Table C.1. $BiVO_4$(C+H-200-24), and were found to possess superior photonic effiency to the other samples, with the maximum photonic efficiency of 1.31×10^{-2} mol/Einstein.

Table C.2: Apparent photonic efficiency of $BiVO_4$ samples prepared via various synthesis methods.

Sample	Apparent photonic efficiency ξ (mol/Einstein)
$BiVO_4$ (Co-pre-350-24)	0.04×10^{-2}
$BiVO_4$ (Comb-500-3)	0.08×10^{-2}
$BiVO_4$ (Calc-450-5)	0.16×10^{-2}
$BiVO_4$ (H-140-8)	0.28×10^{-2}
$BiVO_4$ (C+H-200-24)	1.31×10^{-2}